ANGULAR DISTRIBUTIONS OF MOLECULES EFFUSING FROM CONICAL ORIFICES

By

RUTH CAMPBELL ERBAR

Bachelor of Science
Oklahoma State University
Stillwater, Oklahoma
1958

Master of Science
Oklahoma State University
Stillwater, Oklahoma
1960

Submitted to the Faculty of the Graduate College
of the Oklahoma State University
in partial fulfillment of the requirements
for the Degree of
DOCTOR OF PHILOSOPHY
August, 1969

OKLAHOMA
STATE UNIVERSITY
LIBRARY

NOV 5 1969

ANGULAR DISTRIBUTIONS OF MOLECULES EFFUSING

FROM CONICAL ORIFICES

Thesis Approved:

Robert Freeman
Thesis Adviser

J. Paul Hewlin

Tom E. Moore

Clarence M. Cunningham

William J. Lewis

D. D. Durham
Dean of the Graduate College

729924

ACKNOWLEDGEMENTS

The author thanks Dr. Robert D. Freeman for his invaluable advice and counsel during the course of this research.

The help initially given by Dr. J. G. Edwards in becoming familiar with the experimental apparatus is appreciated.

Discussions with other people in this laboratory, especially Dr. K. C. Wang and Dr. R. E. Gebelt, were most helpful.

The fine craftsmanship of the staff of the Physics-Chemistry Shop is much appreciated. Mr. Heinz Hall contributed significantly to the design of parts of the system.

Financial support was provided in part by USAF Contract AF33(657)-8767.

TABLE OF CONTENTS

Chapter		Page
I.	INTRODUCTION AND DISCUSSION OF THE LITERATURE	1
	Applications of the Knudsen Effusion Method	3
	Theoretical Extensions to Knudsen's Ideal Orifice Treatment	4
	Angular Distribution Experiments	5
II.	DISCUSSION OF EDWARDS AND FREEMAN'S THEORETICAL ANALYSIS OF MOLECULAR FLOW THROUGH CONICAL ORIFICES	8
III.	THE EXPERIMENTAL METHOD	17
	The Apparatus	18
	The Main Vacuum Chamber	21
	The Gas Reservoir	23
	The Chopper Chamber	25
	The Detector Chamber	27
	The System Electronics	31
	The Experiment	31
	Alignment of Orifices	31
	Preparation for a Run	38
	Making a Run	39
	Miscellaneous Observations	40
IV.	DISCUSSION OF EXPERIMENTAL RESULTS AND COMPARISON WITH THEORETICAL ANALYSIS	43
	The Data Range	43
	The General Differences Between Experiment and Theory	50
	General Treatment of Experimental Data	63
	Probable Sources of Differences Between Theory and Experiment	66
	Surface Diffusion	84
	Specular Reflection	88
	Pressure Effects	90
	Velocity Distribution Distortion	93
	Geometry Effects	94
	Development of Expressions for the Deviations	97
	Angular Velocity Selection Simulation	98
	Surface Diffusion Approximation	99

Chapter | Page

IV. (Continued)

Pressure Effect Modification 101
Comparison of Experimental Data with Modified Analysis 102
The Diverging Orifices 104
The Converging Orifice 106
The Cylindrical Orifices 106
Summary of Modification Effects 108

V. CONCLUSIONS AND RECOMMENDATIONS 110

SELECTED BIBLIOGRAPHY 112

APPENDIX

A. EXPRESSIONS FOR $\underline{A}(D_x, D_L)$ 116

B. THE DEFINITION OF $\underline{\psi}(\underline{x})$ 122

C. THE TRANSMISSION COEFFICIENT, $\underline{W}$ 123

D. THE EXPERIMENTAL DATA 124

LIST OF TABLES

Table		Page
I.	Pressure Range of Experiments	44
II.	Normalized Intensities for Orifice No. 1	45
III.	Normalized Intensities for Orifice No. 2	46
IV.	Normalized Intensities for Orifice No. 3	47
V.	Normalized Intensities for Orifice No. 4	48
VI.	Normalized Intensities for Orifice No. 5	49

LIST OF FIGURES

Figure		Page
1.	Knudsen Cells with Various Orifices	2
2.	Schematic of Experimental Apparatus	19
3.	Rotating Effusion Cell	22
4.	Valve for First Collimating Orifice	24
5.	Chopper Chamber	26
6.	Beam Chopper Power Supply	27
7.	Beam Ionizer	30
8.	Beam Ionizer Power Supply	32
9.	Preamplifier	32
10.	Orifice Alignment Schematic	34
11.	Orifice Nesting Schematic	37
12.	Normalized Theoretical (Q_n Cos θ) and Experimental (I (θ)) Intensities for He from Orifice 1	51
13.	Normalized Theoretical (Q_n Cos θ) and Experimental (I (θ)) Intensities for N_2 from Orifice 1	52
14.	Normalized Theoretical (Q_n Cos θ) and Experimental (I (θ)) Intensities for N_2O from Orifice 1	53
15.	Normalized Theoretical (Q_n Cos θ) and Experimental (I (θ)) Intensities for He from Orifice 2	50
16.	Normalized Theoretical (Q_n cos θ) and Experimental (I (θ)) Intensities for N_2 from Orifice 2	55
17.	Normalized Theoretical (Q_n cos θ) and Experimental (I (θ)) Intensities for N_2O from Orifice 2	56
18.	Normalized Theoretical (Q_n cos θ) and Experimental (I (θ)) Intensities for He from Orifice 3	57

Figure Page

19. Normalized Theoretical (Q_n Cos θ) and Experimental (I (θ)) Intensities for N_2 from Orifice 3 58

20. Normalized Theoretical (Q_n Cos θ) and Experimental (I (θ)) Intensities for N_2O from Orifice 3 59

21. Normalized Theoretical (Q_n Cos θ) and Experimental (I (θ)) Intensities for N_2 form Orifice 4 60

22. Normalized Theoretical (Q_n Cos θ) and Experimental (I (θ)) Intensities for He from Orifice 5 61

23. Normalized Theoretical (Q_n Cos θ) and Experimental (I (θ)) Intensities for N_2 from Orifice 5 62

24. Example of Plotting Program Output 67

25. ΔP(θ) for Orifice 1 with He 68

26. ΔP(θ) for Orifice 1 with N_2 69

27. ΔP(θ) for Orifice 1 with N_2O 70

28. ΔP(θ) for Orifice 2 with He 71

29. ΔP(θ) for Orifice 2 with N_2 72

30. ΔP(θ) for Orifice 2 with N_2O 73

31. ΔP(θ) for Orifice 3 with He 74

32. ΔP(θ) for Orifice 3 with N_2 75

33. ΔP(θ) for Orifice 3 with N_2O 76

34. ΔP(θ) for Orifice 4 with N_2 77

35. ΔP(θ) for Orifice 5 with He 78

36. ΔP(θ) for Orifice 5 with N_2 79

37. ΔP(θ) for Adams' Conical Orifice with CsCl 80

38. ΔP(θ) for Wang's Long Orifice with CsCl 81

39. ΔP(θ) for Wang's Intermediate Orifice with CsCl 82

40. ΔP(θ) for Wang's Short Orifice with CsCl 83

41. The Generalized Conical Orifice 117

Figure | Page

42. Projection at Angle $\underline{\theta}$ of the Disc $\underline{D}_x$ at $\underline{x}$ onto the Plane of the Disc $\underline{D}_L$ at $\underline{L}$ for the Case: $T < 0,\ 0 \le \theta \le |T|$ 118

43. Projection at Angle $\underline{\theta}$ of the Disc $\underline{D}_x$ at $\underline{x}$ onto Plane of the Disc $\underline{D}_L$ at $\underline{L}$ for the Case: $T > 0,\ \theta \le \theta \le |T|$ 118

44. Projection at Angle $\underline{\theta}$ of the Disc $\underline{D}_x$ at $\underline{x}$ onto the Plane of the Disc $\underline{D}_L$ at $\underline{L}$ for the Case: $T < 0,\ |T| \le \theta \le \tan^{-1} (r_L + r_x)/(L - x)$ 119

45. Projection at Angle $\underline{\theta}$ of the Disc $\underline{D}_x$ at $\underline{x}$ onto the Plane of the Disc $\underline{D}_L$ at $\underline{L}$ for the Case: $T > 0,\ |T| \le \theta \le \tan^{-1} (r_L + r_x)/(L - x)$ 119

46. Projection at Angle $\underline{\theta}$ of the Disc $\underline{D}_x$ at $\underline{x}$ onto the Plane of the Disc $\underline{D}_L$ at $\underline{L}$ for the Case: $T < 0,\ \tan^{-1} (r_L + r_x)/(L - x) \le \theta \le \pi/2$ 120

47. Projection at Angle $\underline{\theta}$ of the Disc $\underline{D}_x$ at $\underline{x}$ onto the Plane of the Disc $\underline{D}_L$ at $\underline{L}$ for the Case: $T > 0,\ \tan^{-1} (r_L + r_x)/(L - x) \le \theta \le \pi/2$ 120

48. Normalized Experimental Intensities for Run 111-59 125

49. Normalized Experimental Intensities for Run 113-58 126

50. Normalized Experimental Intensities for Run 121-55 127

51. Normalized Experimental Intensities for Run 122-54 128

52. Normalized Experimental Intensities for Run 123-50 129

53. Normalized Experimental Intensities for Run 124-56 130

54. Normalized Experimental Intensities for Run 125-53 131

55. Normalized Experimental Intensities for Run 126-52 132

56. Normalized Experimental Intensities for Run 127-51 133

57. Normalized Experimental Intensities for Run 131-64 134

58. Normalized Experimental Intensities for Run 132-63 135

59. Normalized Experimental Intensities for Run 133-65 136

60. Normalized Experimental Intensities for Run 134-62 137

61. Normalized Experimental Intensities for Run 135-66 138

Figure Page

62. Normalized Experimental Intensities for Run 211-70 139

63. Normalized Experimental Intensities for Run 212-69 140

64. Normalized Experimental Intensities for Run 213-68 141

65. Normalized Experimental Intensities for Run 214-67 142

66. Normalized Experimental Intensities for Run 221-75 143

67. Normalized Experimental Intensities for Run 222-74 144

68. Normalized Experimental Intensities for Run 223-73 145

69. Normalized Experimental Intensities for Run 224-72 146

70. Normalized Experimental Intensities for Run 225-71 147

71. Normalized Experimental Intensities for Run 231-80 148

72. Normalized Experimental Intensities for Run 232-79 149

73. Normalized Experimental Intensities for Run 233-78 150

74. Normalized Experimental Intensities for Run 234-77 151

75. Normalized Experimental Intensities for Run 235-76 152

76. Normalized Experimental Intensities for Run 311-83 153

77. Normalized Experimental Intensities for Run 312-82 154

78. Normalized Experimental Intensities for Run 313-81 155

79. Normalized Experimental Intensities for Run 321-87 156

80. Normalized Experimental Intensities for Run 322-86 157

81. Normalized Experimental Intensities for Run 323-85 158

82. Normalized Experimental Intensities for Run 324-84 159

83. Normalized Experimental Intensities for Run 331-91 160

84. Normalized Experimental Intensities for Run 332-90 161

85. Normalized Experimental Intensities for Run 333-89 162

86. Normalized Experimental Intensities for Run 334-88 163

87. Normalized Experimental Intensities for Run 421-15 164

Figure Page

88. Normalized Experimental Intensities for Run 422-13 165

89. Normalized Experimental Intensities for Run 423-14 166

90. Normalized Experimental Intensities for Run 424-17 167

91. Normalized Experimental Intensities for Run 425-16 168

92. Normalized Experimental Intensities for Run 426-18 169

93. Normalized Experimental Intensities for Run 511- 7 170

94 Normalized Experimental Intensities for Run 512- 8 171

95. Normalized Experimental Intensities for Run 521- 4 172

96. Normalized Experimental Intensities for Run 522- 5 173

97. Normalized Experimental Intensities for Run 523- 6 174

98. Normalized Experimental Intensities for Run 524- 2 175

99. Normalized Experimental Intensities for Run 52 - 1 176

100. Normalized Experimental Intensities for Run 526- 3 177

CHAPTER I

INTRODUCTION AND DISCUSSION OF THE LITERATURE

The various problems associated with rarefied gas flow through orifices have been studied by many investigators since Knudsen[29,30,31,32] first developed and showed the great value of the Knudsen effusion method as a means of measuring low vapor pressures. These problems are, by definition, confined to the "molecular flow" region of pressure. This is the pressure range in which the mean free path of a molecule is larger than the system (orifice) itself. In the molecular flow region a molecule can be considered to interact with the system only, rather than with other molecules.

Knudsen's "ideal orifice" treatment assumes that the orifice has infinitesimal length, i.e., it has no walls. The angular distribution from such an orifice is directly proportional to the cosine of the effusion angle. Many investigators have tried to approximate this condition by using cells with "knife-edged" orifices (Figure 1), but the error involved in using this method has not really been known. Others have used holes in "thin" films to simulate an ideal orifice. These papers are far too numerous to mention individually; the reader is referred to references 34 and 57 for reviews of and references to

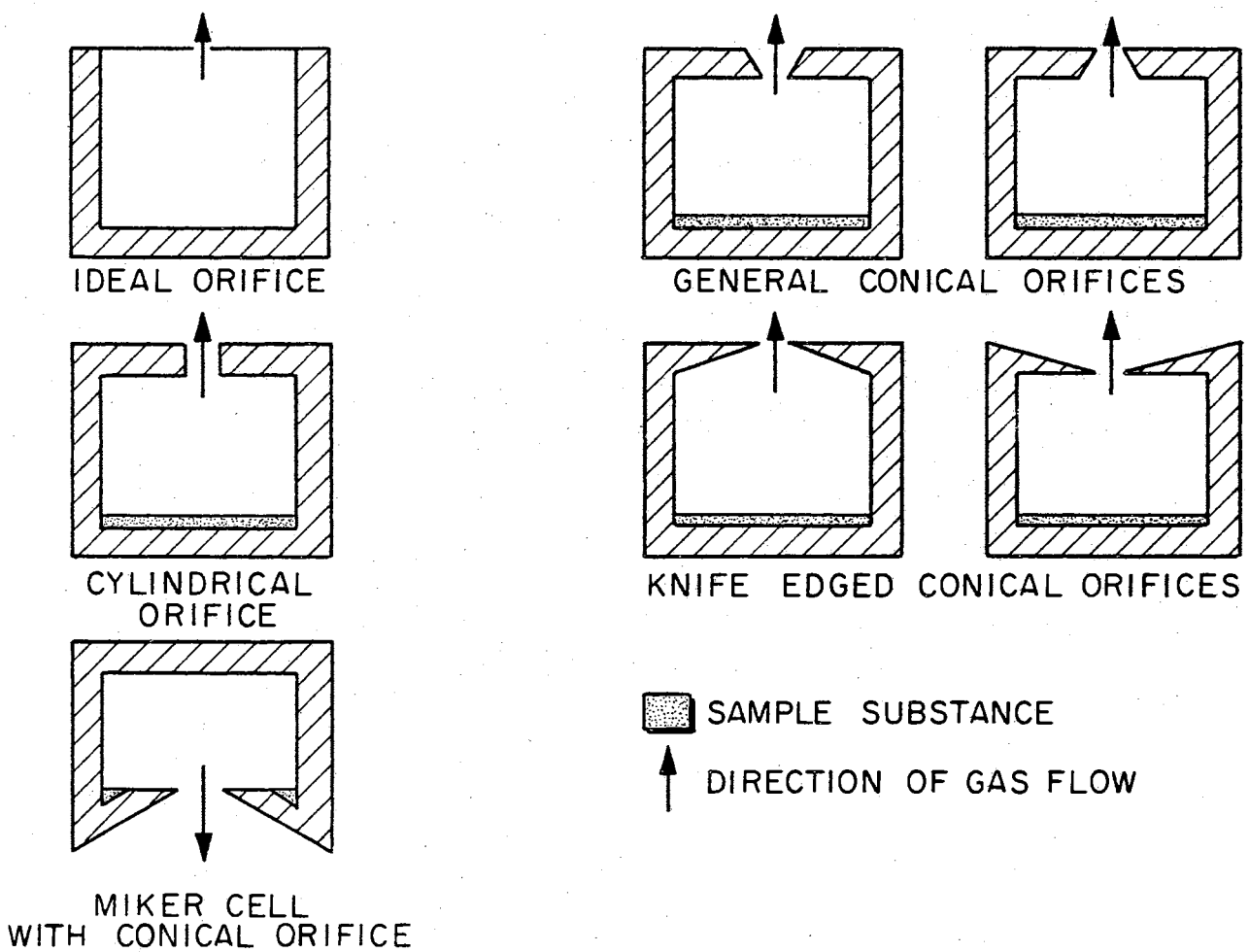

Figure 1. Knudsen Cells with Various Orifices

many of these experiments.

Applications of the Knudsen Effusion Method

The Knudsen effusion method is an extraordinarily useful means of measuring vapor pressures of materials which have low vapor pressures at the temperatures of interest. It has been used extensively[34,57] for this purpose since Knudsen's[31] experimental determination of mercury vapor pressures using the effusion method.

There is the possibility of using effusion experiments to accurately determine the average molecular weight of the vapor, hence, the composition of the effusing vapor.[37,45] This can be done only if one has a really good theoretical description of the system and processes.

A particularly interesting and potentially useful application of conical orifices in effusion experiments has been developed in this laboratory.[18,19] The MIKER technique uses an inverted Knudsen cell suspended from a microbalance in the vacuum system. The weight-loss per unit time is established and then the recoil force on the cell determined from the apparent weight change on rapid cooling of the cell. Since this cell has a conical orifice as its base, an accurate method of treating conical orifices is necessary before it can be used with confidence in determining vapor pressures or molecular weights.

A valid theoretical treatment for conical orifices will also allow a good estimate of possible errors in previous "knife edged" and other conical orifice experiments and would allow the data to be recalculated when necessary.

Theoretical Extensions to Knudsen's Ideal Orifice Treatment

Clausing[6-9] was the first investigator to make a reasonably rigorous theoretical analysis of rarefied gas flow through an actual orifice, i.e., one of finite length. In this work, he developed the equations used to describe the theoretical angular distribution of molecules effusing through cylindrical orifices. Clausing's equations, which were solved using numerical approximations, yield the transmission coefficient, W, as a function of the orifice geometry, i.e., L/r. W is the fraction of the molecules entering the orifice which subsequently escape rather than being returned to the cell; hence, W has values between 0.0 and 1.0. The "ideal orifice" of Knudsen has a W of 1.0 as there are no walls to participate in returning the molecules to the cell. Because of Clausing's original work in this area, the transmission coefficients is often referred to as the "Clausing factor."

Demarcus[12,13] has also treated the cylindrical orifice theoretically and has solved Clausing's equations for more exact values of W. These values are tabulated in the open literature[15] and provide a means of correcting total flow data taken using cylindrical orifices.

The theoretical molecular flow problem for conical orifices was investigated and solved concurrently by Edwards[16] and Freeman and Edwards[21,22] and by Iczkowski, Margrave and Robinson.[26] An approximate analysis had been done earlier by Balson.[4] However, only Freeman and Edwards have described the angular distribution of molecules effusing from the orifice and the application of the distribution to calculation of the recoil force. The testing of the angular distri-

bution portion of the Edwards-Freeman method against experimental data for conical orifices has not been possible because experimental data[2,3] existed for only one conical orifice of rather extreme geometry.

Angular Distribution Experiments

The angular distribution of molecules effusing from cylindrical orifices has been the subject of many investigations.

Knauer and Stern[28] and then Johnson[27] measured the effusion rate of collimated beams from slits at the normal to the orifice face, i.e., 0° off-axis angle, as a function of source cell pressure. While these were not angular distributions, they were the first angular measurements made. Mayer[35,36] measured the angular distribution of momentum using a torsion balance as the beam detector. He used slits and holes in thin films to confirm Knudsen's cosine law at low pressures for the angular distribution of momentum. The cosine law did not hold for long tubes.

Günther[23] used an interferometric method to measure the effusion of SiO vapor through cylindrical graphite orifices. His data are limited to the region from 0° to 50° off-axis angles. Interferometry has also been used as the detection method in studies of cylindrical orifices by Rohn[41] and by Clower[10], Hopkins[24] and Walbeck[52] with Phipps. These data, along with those of Günther, are of historical interest but presently of limited use, since the detection system limits data to 40° to 50° off-axis angle. In addition, Hopkins and Clower used orifice shapes which have not been treated mathematically.

Streekanth[48,49] has used a pressure probe to measure some cross-sections of intensities of molecular beams from two cylindrical ori-

fices. The data are primarily in the transition region of pressure using N_2 as the effusing gas at room temperature.

Angular distributions for series of cylindrical orifices of varying length to radius ratios have been measured by several investigators. Naumov[38] used NH_3 as the effusing gas and an ionization gauge as the detector. Cook and Richley[11] and Stickney, et. al.[51] used surface ionization detectors to measure the angular distribution of effusing cesium.

Ward[58-62] measured the angular distributions of plutonium and gold at extremely low pressures - such that only molecular flow occurred in the source cell itself as well as in the orifice. These results show cell, sample and orifice geometry effects. The orifice was a -75°, knife edged orifice.

Adams[2] with Phipps used a surface ionization detector to measure angular distributions of CsCl molecules from two cylindrical orifices and one conical orifice (15.93° orifice angle, $L/r_o = 58.8$). His work represents the first published data of angular distributions of molecules from a conical orifice.

Wang[54] and Wang and Walbeck[55,56] also used a surface ionization detector in studying the effusion of CsCl through three cylindrical orifices. Wang measured both number and velocity angular distributions.

The intense interest in, and great usefulness of the Knudsen effusion method is indicated by the many investigations[34,40,57] that have been made in addition to the selected angular distribution experiments mentioned above. Velocity distributions, total flow measurements, and unusual orifice shapes (ovals, right angle bends, etc.)

have been studied to add to the understanding of the molecular flow and transition regions of pressure in the effusion process.

However, even though numerous and extensive investigations have been made on cylindrical orifices, these data are not sufficient to test the theory of Edwards and Freeman. The cylindrical orifice is only a limiting case of the general conical orifice.

Experimental data on angular distributions of molecules effusing from four conical orifices and one cylindrical orifice are presented in this thesis. These data are used to evaluate the basic theoretical treatment of Freeman and Edwards.

CHAPTER II

DISCUSSION OF EDWARDS AND FREEMAN'S THEORETICAL ANALYSIS OF MOLECULAR FLOW THOUGH CONICAL ORIFICES

Edwards and Freeman's analysis has been reported[16,18-22] in great detail and covers many aspects of the molecular flow problem. The portions discussed here are those pertinent to the angular distribution of the effusing molecules.

The analysis is based on the following assumptions:

(1) The pressure is low enough that only molecular flow need be considered. Collisions among molecules have such low probability as to be negligible compared to collisions between molecules and the system (orifice); molecular interactions can therefore be ignored.

(2) No chemical reactions occur between the walls of the system and the molecules of the gas; hence, there is no change in number of molecules as the gas effuses and no reaction rate or enthalpy of reaction effects.

(3) The orifice and effusing gas are in thermal equilibrium. The velocity distribution of the molecules does not change due to orifice collisions and the possibility of incomplete thermal accommodation is avoided.

(4) No significant surface diffusion occurs through the orifice. Molecules do not collide with the orifice wall, stick, and move along the orifice wall before being remitted.

(5) Only cosine law reflection occurs, i.e., the momentum transfer coefficient is unity so specular reflection does not occur.

(6) Molecules entering the orifice are distributed according to the cosine law.

(7) The molecular flux is measured at a point far enough away from the orifice that the orifice may be considered a point source.

The validity of assumptions (1), (2), and (3) are dependent entirely on the experimental conditions. Therefore, the experimenter can determine a priori whether his data can be analyzed using the Edwards-Freeman method. There is evidence[43,63,64] in some cases that assumption (4), no surface diffusion, may not apply. This condition is partially under the experimenters control by the choice of orifice geometry and material, gas species, and temperature, though more data are needed on surface diffusivities to aid in making such choices.

Assumption (5), cosine law reflection, has been shown to be valid over a wide range of conditions. It is basic to both Clausing's[6-9] work and this work. There are many specialized situations where specular reflection has been observed.[25,40,44] These conditions are seldom duplicated in Knudsen effusion cells, particularly if the experiment is designed so that assumption (3), thermal equilibrium, applies.

Assumptions (6) and (7) are basic to Knudsen's "ideal" orifice treatment, Clausing's work, the analysis of Iczkowski, et. al. and this treatment. These assumptions have been shown to be generally true[23,32,55] though in specialized experiments[58-62] the cell geometry

and pressure conditions may invalidate assumption (6). Measuring the effusion intensity very close to the orifice might invalidate assumption (7). The experimental conditions again determine the applicability of the method.

The angular distribution of molecules effusing through a conical orifice is made up of two parts if assumptions (1), (2) and (4) are valid; one - those molecules which travel directly through the orifice without colliding with the walls and, two - those molecules which collide with the walls one or more times before leaving the orifice.

Then, the number of molecules which travel per second from the orifice into an incremental volume $\underline{dV_\theta}$ is given by equation 1.

$$dN_\theta(L) = dN_\theta(D_o,D_L) + \int_{x=0}^{x=L} dN_\theta(x,D_L), \qquad (1)$$

where θ = the off-axis angle - the angle between the orifice axis and the molecular trajectory,

L = axial length of the orifice,

$dN_\theta(D_o,D_L)$ = number of molecules per second which travel from the disc at $\underline{0}$ to the disc at $\underline{L}$ (0,L = extremes of the orifice) and into the incremental volume $\underline{dV_\theta}$ (Figure 41, Appendix A),

$dN_\theta(x,D_L)$ = number of molecules per second which leave an incremental ring at some distance $\underline{x}$ along the orifice wall and travel through the disc at $\underline{L}$ into $\underline{dV_\theta}$. (Figure 41, Appendix A).

The first part of equation 1 follows from Knudsen's cosine law - the number $\underline{\delta N_\omega}$ of molecules which leave an incremental plane surface

per second and go into an incremental solid angle, $d\omega$, at angle θ is proportional to the cosine of θ.

$$\delta N_{\omega} = \frac{dn}{\pi} \cos \theta \, d\omega \tag{2}$$

where dn = the number of molecules per second leaving the incremental surface.

Converting to spherical coordinates, $d\omega = \sin \theta \, d\theta \, d\phi$ and integrating equation 2 over $0 \leq \phi \leq 2\pi$ yields

$$\delta N_{\theta} = dn \; 2 \sin \theta \cos \theta \, d\theta \; . \tag{3}$$

The molecular flux is considered at a distance far enough away that the orifice can be considered a point source, assumption (7). Integration of equation 3 over the orifice area yields

$$dN_{\theta} = 2\mu_o \pi r^2 \sin \theta \cos \theta \, d\theta \tag{4}$$

where r = radius of the orifice,

μ_o = number of molecules per second striking a unit area in the source chamber, hence, entering through a unit area of the orifice from the source chamber,

dN_{θ} = number of molecules per second which enter the orifice and go into the incremental solid angle between θ and $\theta + d\theta$.

At this point assumption (6) has been included since molecules are considered to be passing from the source chamber through an orifice with cosine distribution rather than leaving a surface. For the "ideal" orifice - one which has no thickness - equation 4 is correct as it stands for all θ from 0 to π. However, for an actual orifice that does have thickness, equation 4 does not describe all contributions to flow through the orifice. Nor does it apply to certain effusion angles depending on orifice geometry since a molecule cannot

pass straight through the orifice without encountering a wall at these angles.

For those molecules which do not encounter a wall, we still may write

$$dN_\theta\ (D_o,\ D_L) = 2\mu_o \pi r^2 \sin\theta \cos\theta\ d\theta. \tag{5}$$

The second part of equation 1, in the limit where the ring at x becomes incremental, becomes

$$dN_\theta(x,D_L) = \left| \lim_{x \to x'} [dN_\theta(D_x,D_L) - dN_\theta(D_{x'},D_L)] \right|$$

$$= \frac{d}{dx}\ [dN_\theta(D_x,D_L)]\ dx. \tag{6}$$

Assuming the cosine law applies - assumptions (5) and (6) - then $\underline{dN_\theta}\ (D_x,D_L)$ is assumed to be proportional to cos $\underline{\theta}$, to $\underline{d\omega}$ and to the area, $\underline{A}(D_x,D_L)$, of the part of $\underline{D_x}$ which can be traversed by a molecule on a direct trajectory through $\underline{D_L}$ into $\underline{d\omega}$ at $\underline{\theta}$. Let $\underline{Y}$ be the proportionality constant.

Then

$$dN_\theta(D_x,D_L) = Y \cos\theta\ d\omega\ A(D_x,D_L). \tag{7}$$

Converting $\underline{d\omega}$ to spherical coordinates and integrating over $0 \le \phi \le 2\pi$ yields

$$dN_\theta(D_x,D_L) = Y2\pi A(D_x,D_L) \cos\theta \sin\theta\ d\theta. \tag{8}$$

For L = 0 (an "ideal" orifice) $A(D_x,D_L) = \pi r^2$, then

$$dN_\theta(D_x,D_L)_{ideal} = Y2\pi(\pi r^2) \cos\theta \sin\theta\ d\theta \tag{9}$$

which must be the same as equation 4. Then $Y = \mu_o/\pi$ and equation 9 becomes

$$dN_\theta(D_x,D_L) = 2\mu_o A(D_x,D_L) \cos\theta \sin\theta\ d\theta. \tag{10}$$

The expression for $\underline{dN_\theta}(L)$ is then obtained by substituting equations

5, 6, and 10 into Equation 1

$$dN_\theta(L) = 2\mu_o \pi r_o^2 \sin\theta \cos\theta \, d\theta$$

$$+ \int_{x=0}^{x=L} d/dx \, (2\mu_x A(D_x, D_L) \cos\theta \sin\theta \, d\theta. \qquad (11)$$

Since the parts of equation 11 contribute differently in the three ranges of θ (Appendix A), the detailed solution is rather conveniently broken up according to these ranges by substituting equations A-1 into 11.

Range 1: $0 \leq \theta \leq |T|$

A. $T < 0$

All $\underline{D_o}$ contributes to $\underline{dN_\theta}(L)$ in this range.

No part of the orifice wall contributes.

$$dN_\theta(L) = dN_\theta(D_o, D_L) = 2\mu_o \pi r_L^2 \sin\theta \cos\theta \, d\theta \qquad (12)$$

B. $T \geq 0$

All $\underline{D_o}$ contributes to $\underline{dN_\theta}(L)$ in this range.

All parts of the orifice walls contribute.

$$dN_\theta(L) = 2\mu_o \pi r_o^2 \sin\theta \cos\theta \, d\theta +$$

$$\int_{x=0}^{x=L} \frac{d}{dx} (2\mu_x \pi r_x^2 \sin\theta \cos\theta \, d\theta) dx$$

$$= 2\mu_o \pi r_o^2 \sin\theta \cos\theta \, d\theta +$$

$$\int_0^L 4 \tan T \mu_x \pi r_x \sin\theta \cos\theta \, d\theta \, dx$$

$$= 2\mu_o \pi \sin\theta \cos\theta \, d\theta (r_o^2 + 2 \tan T \int_0^L r_x \psi(x) dx) \qquad (13)$$

where $\psi(x)$ is defined as μ_x/μ_o (Appendix B).

Range 2: $|T| \leq \theta \leq \tan^{-1} \frac{r_L+r_x}{L-x}$

Only part of $\underline{D}_o$ contributes to $\underline{dN}_\theta(L)$ in this range.

All parts of the walls contribute.

$$dN_\theta(L) = 2\mu_o\pi \sin\theta \cos\theta \, d\theta$$

$$\left\{ \left\langle \frac{-t_1(0)}{4\tan^2\theta}\left[4r_L^2\tan^2\theta - \left(t_1(0)\right)^2\right]^{\frac{1}{2}} \right.\right.$$

$$-r_L^2 \sin^{-1}\left[\frac{t_1(0)}{2r_L^2\tan\theta}\right] + \tfrac{1}{2}\pi\,(r_L^2+1)$$

$$-\frac{t_2(0)}{4\tan^2\theta}\left[4r_o^2\tan^2\theta - \left(t_2(0)\right)^2\right]^{\frac{1}{2}}$$

$$\left. -r_o^2 \sin^{-1}\left[\frac{t_2(0)}{2r_o\tan\theta}\right] \right\rangle_{ORIF}$$

$$+\int_o^L \left\langle \frac{\tan^2\theta-\tan^2 T}{2\tan^2\theta}\left[4r_L^2\tan^2\theta - \left(t_1(x)\right)^2\right]^{\frac{1}{2}} \right.$$

$$+\frac{\tan^2\theta+\tan^2 T}{2\tan^2\theta}\left[4r_x^2\tan^2\theta - \left(t_2(x)\right)^2\right]^{\frac{1}{2}}$$

$$\left.\left. -2r_x\tan T\sin^{-1}\left[\frac{t_2(x)}{2r_x\tan\theta}\right] + \pi r_x\tan T \right\rangle_{WALLS} \psi(x)\,dx \right\} \qquad (14)$$

where

$$t_1(x) = (L-x)\tan^2\theta + (r_x + r_L)\tan T$$

and

$$t_2(x) = (L - X)\tan^2\theta - (r_x + r_L)\tan T.$$

Range 3: $\tan^{-1}\dfrac{r_L + r_x}{L - x} \le \theta \le \dfrac{\pi}{2}$

No contribution from $\underline{D_o}$ to $\underline{dN_\theta}(L)$ in this range.

Only parts of the orifice walls contribute.

The orifice walls contribute only when

$$x > \left(\frac{L\tan\theta - r_L - 1}{\tan\theta + \tan T}\right) = x'$$

So $dN_\theta\,(D_o, D_L) = 0$, $\underline{dN_\theta}(x, D_L)$ is the same as for Range 2 and

$$dN_\theta(L) = 2\mu_o\pi\sin\theta\cos\theta\,d\theta\left\{0 + \int_{x'}^{L}\left\langle\frac{\tan^2\theta - \tan^2 T}{2\tan^2\theta}\left[4r_L^{\,2}\tan^2\theta - \left(t_1(x)\right)^2\right]^{\frac{1}{2}}\right.\right.$$

$$+ \frac{\tan^2\theta + \tan^2 T}{2\tan^2\theta}\left[4r_x^{\,2}\tan^2\theta - \left(t_2(x)\right)^2\right]^{\frac{1}{2}}$$

$$\left.\left. - 2r_x\tan T\sin^{-1}\left[\frac{t_2(x)}{2r_x\tan\theta}\right] + \pi r_x\tan T\right\rangle_{\text{WALLS}}\psi(x)dx\right\}. \qquad (15)$$

Define $\underline{Q_n}$ as the coefficient of $(2\pi\mu_o\sin\theta\cos\theta\,d\theta)$ in the expression for $\underline{dN_\theta}(L)$ in the $\underline{n}$th range. Then

$$Q_n = \left(\frac{dN_\theta(L)}{2\pi\mu_o\sin\theta\cos\theta\,d\theta}\right)_{\text{range } n} \qquad (16a)$$

and

Range 1: A. $$Q_1 = r_L^2 \tag{16b}$$

B. $$Q_1 = r_o^2 + 2 \tan T \int_o^L r_x \psi(x) dx \tag{16c}$$

Range 2: $$Q_2 = \langle\ \rangle_{ORIF} + \int_o^L \langle\ \rangle_{WALLS} \psi(x) dx \tag{16d}$$

Range 3: $$Q_3 = \int_{x'}^L \langle\ \rangle_{WALLS}\ \psi(x) dx \quad . \tag{16e}$$

Qn is normalized with respect to the number of molecules entering the orifice, $\mu_o \pi r_o^2$, and is dependent only on θ and the geometry of the orifice. The incremental solid angle from θ to $\theta + d\theta$ is $2\pi \sin \theta\ d\theta$. Therefore, of those $\mu_o \pi r_o^2$ molecules per second which enter the orifice, the fraction which traverses the orifice and enters the angle $d\omega$ at θ is $Q_n \cos \theta$, and equations 17 with equations 13, 14, 15 and 16 provide a convenient way of expressing this angular distribution.

$$dN_\theta(L) = Q_n\ 2\pi\ \mu_o \sin \theta \cos \theta\ d\theta \tag{17}$$

$$= Q_n \cos \theta\ 2\pi\ \mu_o \sin \theta\ d\theta$$

or

$$Q_n \cos \theta = \frac{dN_\theta(L)}{\mu_o\ \pi r_o^2\ 2 \sin \theta\ d\theta} \quad .$$

The quantity $Q_n \cos \theta$ has been measured experimentally and compared with the theoretical value of $Q_n \cos \theta$ in the discussion section.

CHAPTER III

THE EXPERIMENTAL METHOD

The design of the apparatus to measure the angular distribution of molecules effusing from various orifices provides for a rotatable simulated Knudsen cell which incorporates the orifice under study. A constant pressure gas reservoir supplies gas to the cell. Collimating orifices generate a molecule beam from the effusate from the orifice. A chopper modulates the beam at 170 Hz. A beam ionizer-detector generates a signal which is proportional to the beam intensity.

A large volume gas reservoir (10 liters) is filled with the gas to be used in the experiment. The gas feeds into a hemicylinder containing the experimental orifice in its face. A large ring nut, simulating the Knudsen cell is placed inside the hemicylinder and behind the orifice. The hemicylinder is situated in an evacuated chamber so the gas in the cell at some pressure is emitted into a vacuum approximating zero pressure (actually $\sim 10^{-6}$ Torr).

A second orifice is situated about 10-cm. from the source orifice. The gas which is emitted from the source orifice and passes through the second orifice constitutes the molecular beam. As the beam passes through this second orifice into the "chopper chamber" it is modulated

at 170 Hz. The chopper chamber pumping system removes the scattered portion of the beam and the rest of it continues as a pulsed molecular beam through a third orifice into the detector chamber. As the chopped beam passes along the 4.2-cm. length of the detector, it is bombarded by electrons. Positive ions are formed which are extracted and collected. The resulting ion current is amplified and measured.

The hemicylinder can be rotated through 180° around an axis through the center of the face of the source orifice. A molecular beam can be generated from the orifice effusate at any desired angle by rotating the hemicylinder to the proper position. The source orifice can have any desired geometry (within reason!) and any gas compatible with the system materials at room temperature can be used.

The Apparatus

The major portion of the apparatus used in this research was designed and assembled by Dr. J. G. Edwards under the direction of Dr. R. D. Freeman. Edwards has described the system in great detail.[16] This chapter, therefore, will describe briefly the overall system and provide details only for those parts which have been modified for various reasons.

The major parts of the system (Figure 2) are (1) <u>The Main Vacuum Chamber</u> containing the rotating effusion cell (a) and first collimating orifice (b), which can be opened and closed with external controls; (2) <u>The Gas Reservoir</u>, a large chamber from which gas at constant pressure is supplied to the effusion cell; (3) <u>The Chopper Chamber</u>, a small independently pumped chamber which encloses the beam chopper (c) and is separated from the main chamber by the first collimating ori-

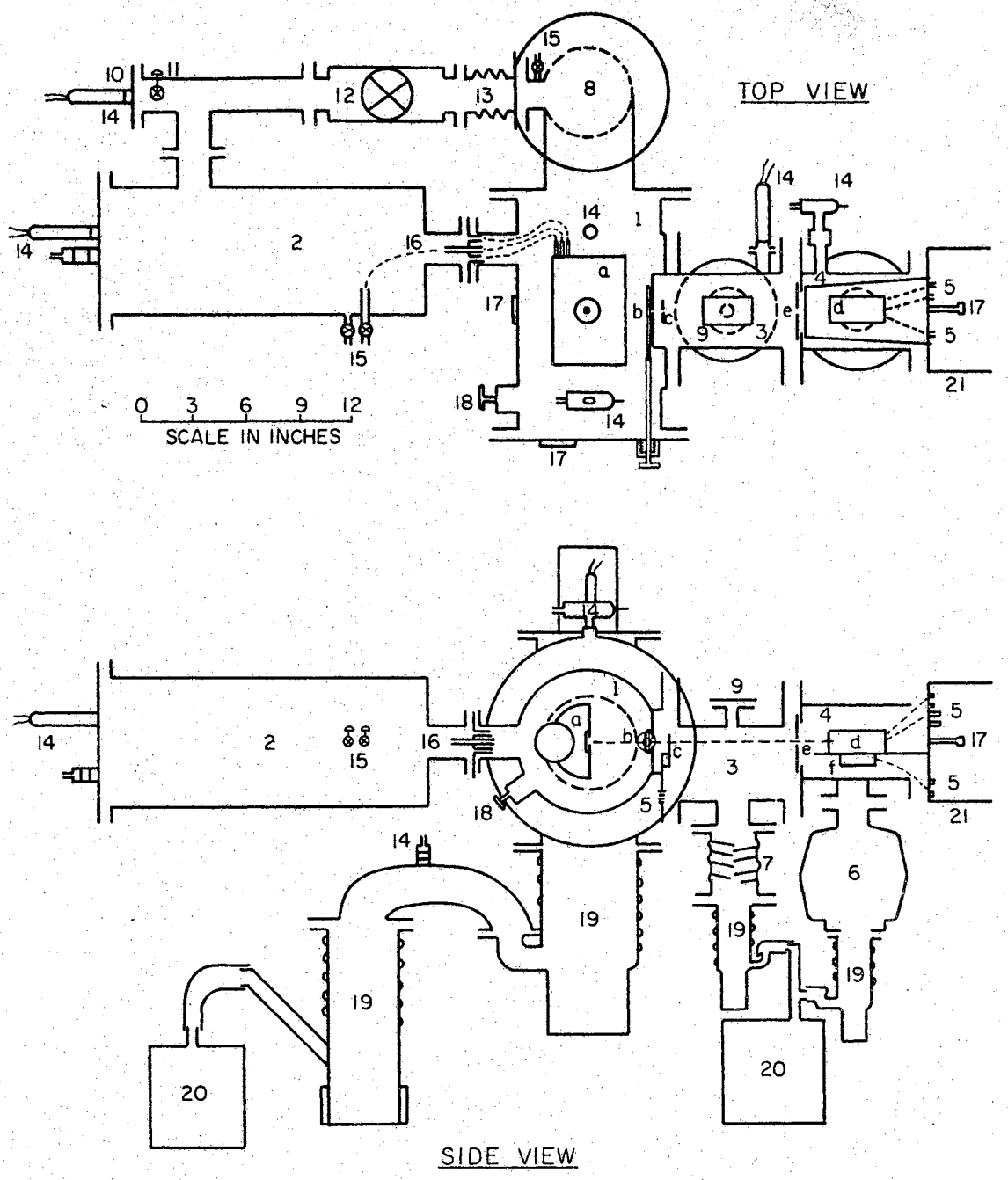

Figure 2. Schematic of Experimental Apparatus

References to Numbers in Figure 2

1. Main Vacuum Chamber
   a. Rotating Effusion Cell
   b. First Collimating Orifice and Its Valve
2. Gas Reservoir
3. Chopper Chamber
   c. Beam Chopper
4. Detector Chamber
   d. Beam Ionizer and Detector
   e. Second Collimating Orifice
   f. Preamplifier
5. Electrical and Water Feed-throughs
6. Granville-Phillips Liquid Nitrogen Trap
7. Water-cooled Baffle
8. Liquid Nitrogen Trap or Blank-off Plate
9. Port for Attaching Helium Leak Detector
10. Port for Attaching 45-liter Stainless Steel Tank
11. Valve for Introducing Effusant Gas
12. Globe Valve
13. Brass Bellows
14. Fittings for Attaching Veeco, Cold-cathode or Hastings Pressure Gauges
15. Connections to Equibar Pressure Meter
16. Connectors for Tygon Tubing which Carries Gas from Reservoir to Rotating Cell
17. Glass Windows
18. Rotary Vacuum Seal though Which the Cell is Rotated
19. Oil Diffusion Pumps
20. Welch Mechanical Pumps
21. Aluminum Shield

fice (b); (4) The Detector Chamber, an independently pumped, bakeable, well-trapped section contains the electron-impact molecular beam detector (d) and is separated from the Chopper Chamber by the second collimating orifice (e); (5) The System Electronics which consist of power supplies for the beam ionizer and chopper, a preamplifier (f), a lock-in amplifier and a recorder for the beam signal.

The Main Vacuum Chamber

This chamber is 12-in. long and made of nickel-plated, cold-rolled seamless pipe, 7.5-in. i.d. with 0.25-in. walls.

The rotating effusion cell (Figure 3) is mounted on a x-y table in this chamber. Four Tygon tubes from the gas reservoir connect to the hemicylinder to provide source gas. A replaceable orifice is held in place on the face of the hemicylinder by a large ring nut which simulates the Knudsen cell. The hemicylinder, hence the orifice face, is rotated externally through a vacuum seal on the chamber wall.

The chamber is pumped by a CVC PMC-720 diffusion pump connected to the lower flange of a 5-in. i.d. steel "Tee". A liquid nitrogen trap or blank-off plate fits on the top flange. A CVC MB-110 diffusion pump backs the PMC-720, and a Welch 1402-B mechanical pump provides for vacuum for the MB-100 pump. A 1.5-in. connection to the "Tee" provides for evacuation of the gas reservoir. A 0.25-in. copper line to the evacuated, reference side of the Equibar is also attached to the "Tee".

As originally designed, the chopper chamber was welded to the main vacuum chamber. However, the original chopper chamber was replaced. The new chamber connects to a stainless steel flange welded

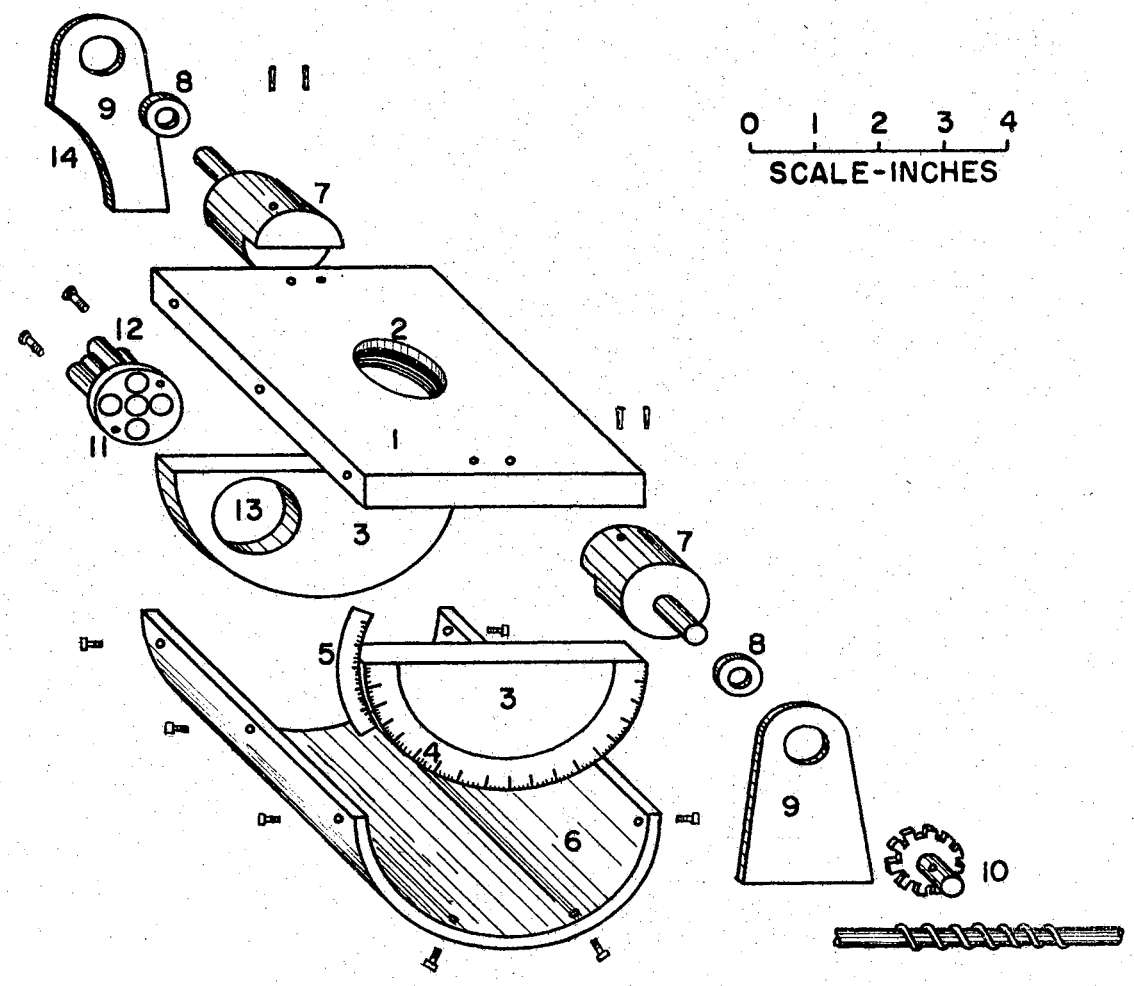

1. Steel Face-Plate
2. Hole for Orifice-Plate
3. Brass End-Plates
4. Calibrated Dial
5. Venier Scale
6. Plexiglass Hemicylinder
7. Brass Axles
8. Ball Bearings
9. Steel Supports
10. Worm Gear
11. Brass Plate
12. Connectors for Tygon Tubes
13. Port for Introduction of Effusant Gas
14. Cutaway to Increase Range of Rotation

Figure 3. Rotating Effusion Cell

to the main vacuum chamber. The first collimating orifice is located just inside the main chamber prior to this flange. This orifice can be closed by a sliding, O-ring-sealed valve, mechanically linked to the front plate of the main chamber (Figure 4). The valve handle can be uncoupled from the slide and the main chamber opened while the chopper and detector chambers remain under vacuum. The O-ring operates properly only when lubricated with molybdenum disulfide. The valve design was adapted from Sheffield[46] by Mr. Heinz Hall.

The Gas Reservoir

This chamber and its associated connections remain essentially as described by Edwards.[16] The reservoir is a nickel-plated, 18-in. long, steel cylinder, 6-in. i.d. Connections are provided for the following items.

(1) The gas source. The gas cylinder to be used is connected by copper tubing to the stainless steel "Tee" using a Granville-Phillips variable leak to regulate flow. No additional regulator other than that on the gas cylinder was necessary.

(2) The PMC-720 pump. A 1.5-in. Kinny bellows valve separates the stainless steel "Tee" on the gas reservoir from the connection to the "Tee" on the PMC-720 pump.

(3) The Transonics 120 Differential Static Equibar. Two 0.25-in. copper tubing connections are made from the reservoir wall to the Equibar. Either the pressure in the reservoir or that in the hemicylinder can be measured.

(4) Cold-Cathode, Veeco and/or Hastings gauges. Two condulet

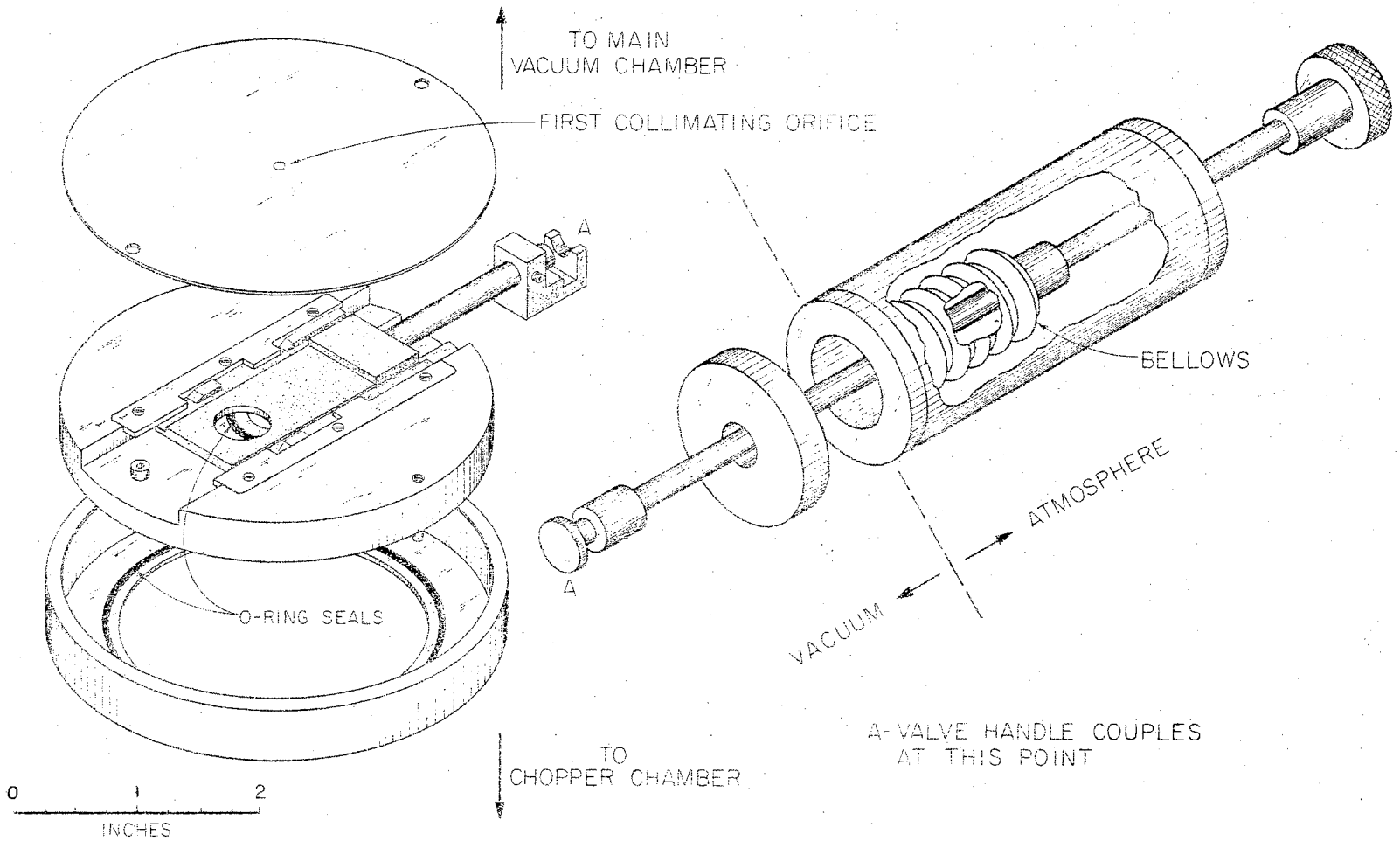

Figure 4. Valve for First Collimating Orifice

fittings in the end plates of the reservoir itself and in the stainless steel "Tee" will accommodate any desired combination of the gauges.

(5) The hemicylinder. Four copper tubes in the plate separating the gas reservoir from the main chamber connect to Tygon tubing going to the hemicylinder. The fifth tube connects the hemicylinder through the plate to the Equibar.

The Chopper Chamber

The original chopper chamber[16] was welded to the main chamber. The original chopper was an angled chopper wheel with teeth, rotated through magnetic coupling by a 180 RPM synchronous motor. This chopper was used in runs series 400 and 500.

The new chamber (Figure 5) is made entirely of 304 stainless steel, the envelope is 6.75-in. long, 4.0-in. i.d. pipe, 0.25-in. thick, welded to 0.75-in. flanges, 8-in. in diameter. Aluminum foil seals[5] are used at both ends of the chamber. This sealing method is extraordinarily good, very easy to use, and the seals made of standard aluminum cooking foil are always available. A 1-inch flanged pipe is welded in the top of the chamber for attaching the helium leak detector or a blank-off plate. A 2.0-in. flanged pipe is welded in the bottom of the chamber and connects to a CVC BW-40 water cooled baffle to provide trapping between the chamber and the CVC PMC-115 diffusion pump. The PMC-115 is charged with Convelex-10 pump fluid and has fore vacuum provided by a Welch 1402-B mechanical pump.

The chopper wheel described by Edwards has been replaced by a Bulova American Time Products timing fork chopper - Type 40 - CHOP(C),

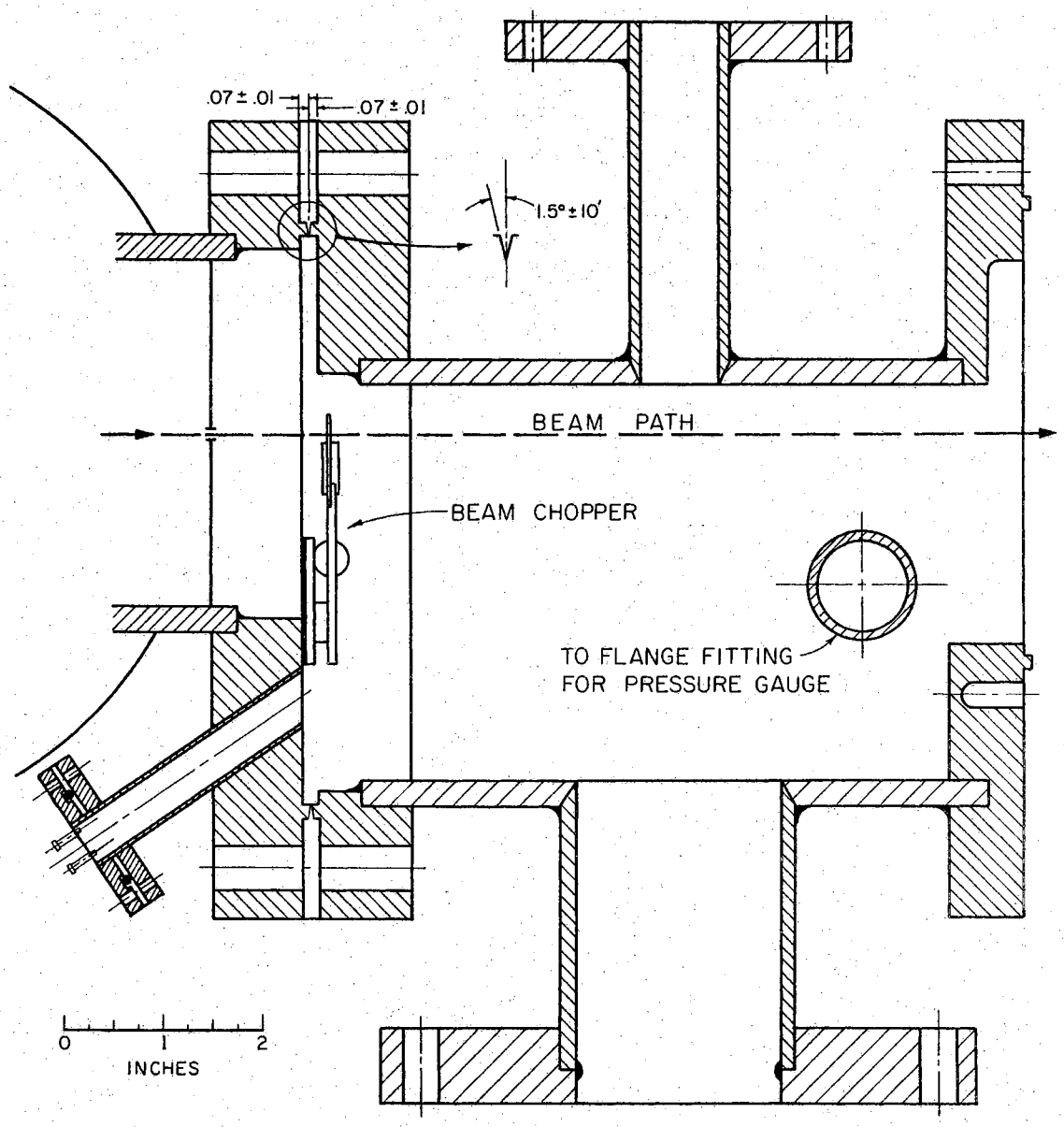

Figure 5. Chopper Chamber

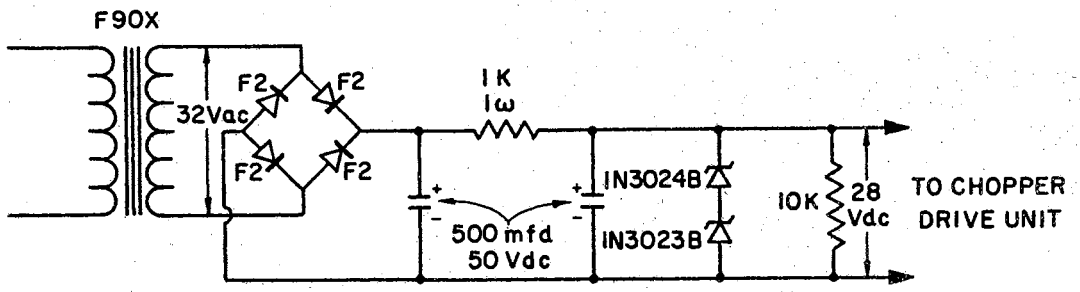

Figure 6. Beam Chopper Power Supply

170 Hz. This chopper eliminated the noise generated by the motor, magnets and bearings in the original system. The chopper is mounted on the flange of the main vacuum chamber near the first collimating orifice, but is enclosed by the chopper chamber. The electrical connections for the chopper are made using an Advac feed-through in the stainless steel flange on the main vacuum chamber. The chopper is adjusted to just cover the orifice when closed and to pass the entire beam when full open. The chopper drive unit also generates a reference signal which has the same frequency as the chopper and which is compatible with the PAR lock-in amplifier. The 28 volt dc power supply for the chopper was designed and built by Dr. R. E. Gebelt, Figure 6.

The Detector Chamber

The new detector chamber attaches to the chopper chamber and has 5/8-inch thick aluminum foil seal flanges on both ends. It is made of 7.0-in. long, 4.0-in. i.d., 0.25-in. thick 204 stainless steel pipe. A flanged section of 2.0-in. i.d. stainless steel pipe is welded into the bottom of the chamber and connects to a Granville-Phillips liquid

nitrogen trap. A CVC PMC-115 diffusion pump filled with Convelex 10 is mounted beneath the trap. Fore vacuum for the diffusion pump is provided by the same Welch 1402-B mechanical pump that is used for the chopper chamber fore vacuum. The O-rings for seals both above and below the cold trap are United Aircraft Products' Self-energized Teflon coated steel O-rings. An RCA demountable connector is attached to a section of 0.84-in. stainless steel tubing welded in the side of the chamber. The connector provides means of attaching the Veeco RG-75 or RG-75 K vacuum gauge using either neoprene and indium O-rings or a gold O-ring.

The chamber is wrapped with an 8-ft. strip of heating tape connected to a variac for bakeout. A thermometer was attached to the top of the chamber with a "liquid aluminum" adhesive when temperatures produced by the heating tape were initially determined. The chamber and tape are wrapped in aluminum foil to provide a stable air space for heating. The chamber is heated for about 3 hours at 100-200°C to reduce the background gases. Teflon in the system limits the bakeout temperature to 200°C. The indium and neoprene O-rings are water cooled during heating.

Connections made through the end plate all use Advac's ceramic to A grade nickel feed-throughs, silver soldered to the stainless steel flange.

Electrical connections are made to #14 copper wire pins silver-soldered into the feed-through tubes. The leads are supported outside the system by attaching plugs through an aluminum shield which is wrapped around the end plate of the detector chamber. This shield also serves to protect the glass window.

The glass window is made from a Pyrex to Kovar tube. The glass end is sealed by a flat glass plate and the Kovar end is silver soldered into an Advac feed-through in the end plate. The water connections are made through nylon Swaglok fittings between Tygon tubing and heavy-duty Advac feed-throughs.

The beam ionizer is mounted on a 0.25-in. stainless steel plate attached to the end plate. The ionizer has been described in detail by Edwards[16] and is nearly identical to that described by Aberth.[1] In general, (Figure 7) a Phillips Metalonics type B (barium aluminate impregnated) tungsten cathode, the electron source, is supported in a molybdenum channel. The cathode is heated with a six-loop insulated tungsten filament which fits inside the channel. A molybdenum heat shield and grid fit around the channel and cathode and are supported in a molybdenum block. An adjustable, water cooled molybdenum anode is screwed to the block and thermally insulated from the block with quartz washers.

The anode is clamped in a water cooled copper plate which is clamped into a groove in a second copper plate. The second plate is attached to a 0.25-in. teflon plate which is mounted with adjusting screws on the stainless steel plate attached to the end flange. Teflon and mica insulate the copper clamps on the heater leads from the rest of the components. Aluminum rods hold the repression plate, extraction grid and collector plate in place. The above physical mounting for the beam ionizer has been changed slightly from Edwards' design to reduce outgassing and shorting problems and to make the ionizer easier to disassemble when replacement of various parts is necessary.

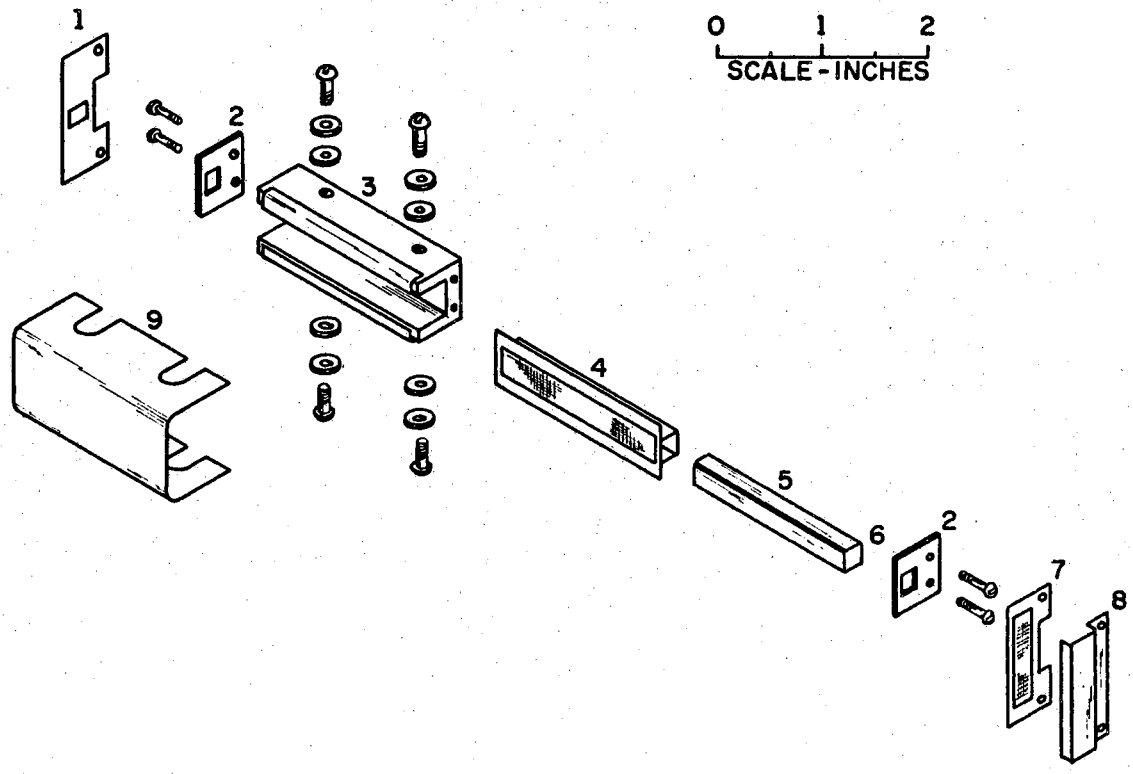

1. Ion-Repression Plate
2. Alumina Support
3. Molybdenum Block
4. Grid and Heat Shield
5. Cathode
6. Slots in Alumina Supports Accommodate Cathode
7. Ion-Extraction Grid
8. Ion Collector
9. Anode

Figure 7. Beam Ionizer

The ion current preamplifier is mounted beneath the stainless steel plate.

The System Electronics

The cathode heater current is supplied by two 12-volt storage batteries. These batteries are kept at peak performance by continuous charging, when not in use, with a 12-volt battery charger connected to the laboratory ac line or with the laboratory dc lines. The laboratory dc lines could not be used to supply the heater power because the 60 cycle ripple completely swamped the beam signals. All other dc voltages in the system are supplied by various dry cell batteries. The current preamplifier and the ionizer power supply are shown in Figures 8 and 9 have been discussed in detail by Edwards.[16] The capacitor and diode were added to the beam signal to protect the lock-in amplifier from large voltages (greater than 20 volts above ground).

The PAR JB-5 Lock-in Amplifier amplifies the final beam signal. It amplifies only the part of the signal matching (in frequency and phase) a specified reference signal. The reference signal in this system is provided by the chopper drive unit. The output of the lock-in is recorded using a Brown Model No. 153 x IIV-X-F 10-mv strip chart recorder equipped with a Cahn 1491 recorder control

The Experiment

Alignment of Orifices

System alignment was checked each time a new orifice was used. The system alignment was so stable, however, that repetition of the complete alignment procedure was required only when a major change had

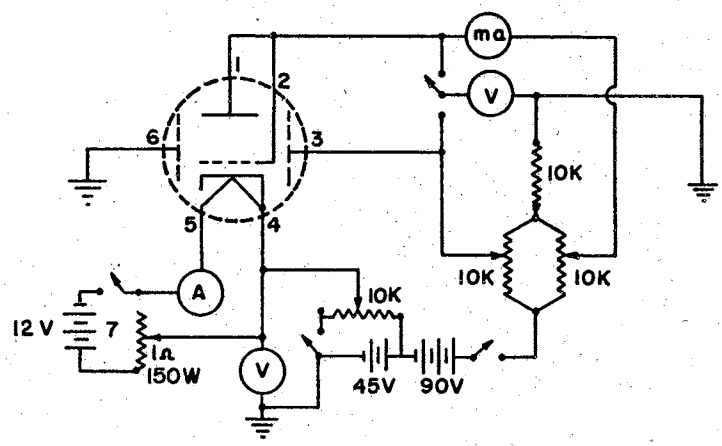

1. Anode
2. Electron Grid
3. Repression Plate
4. - 5. Cathode and Heater
6. Extraction Grid
7. Heater Power Supply

Figure 8. Beam Ionizer Power Supply

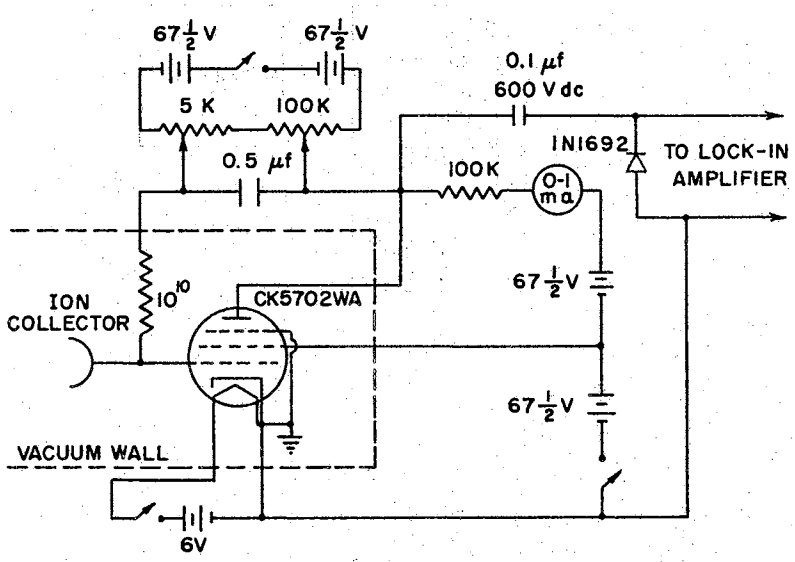

Figure 9. Preamplifier

been made - such as removing and replacing the chopper and detector chambers.

Assume that the hemicylinder has been removed, a new orifice installed, the hemicylinder replaced and that a new cathode has been installed. The alignment must be completely checked according to the following procedure. Numbers refer to Figure 10, which shows the relative positions of pertinent parts.

1. A 25-watt light bulb placed in the main chamber between the hemicylinder (3) and the first collimating orifice (2) provides the necessary illumination. A Gaetner Scientific Corporation cathetometer telescope is used for the major alignment. The optical axis of the telescope is located so that the first collimating orifice (2) is centered in the field of view through the detector chamber window and its tubular mount (1). The optical axis of the telescope so located defines the molecular beam axis on which other components are to be aligned. The first collimating orifice and the detector chamber window are not adjustable; their relative positions are determined by the accuracy of machining and fabrication.

2. The source orifice (3) in the hemicylinder and the second collimating orifice (4) are aligned with now established beam axis. When the hemicylinder is being aligned, the light bulb is moved outside the window on the main vacuum chamber. The light passes through the chamber window and the plexiglass of the hemicylinder to illuminate the source orifice. The hemicylinder mount is adjusted so that the source orifice is centered in the nest of orifices.

3. The (tuning-fork) chopper is mounted on the flange (between the main chamber and the chopper chamber) which also bears the first

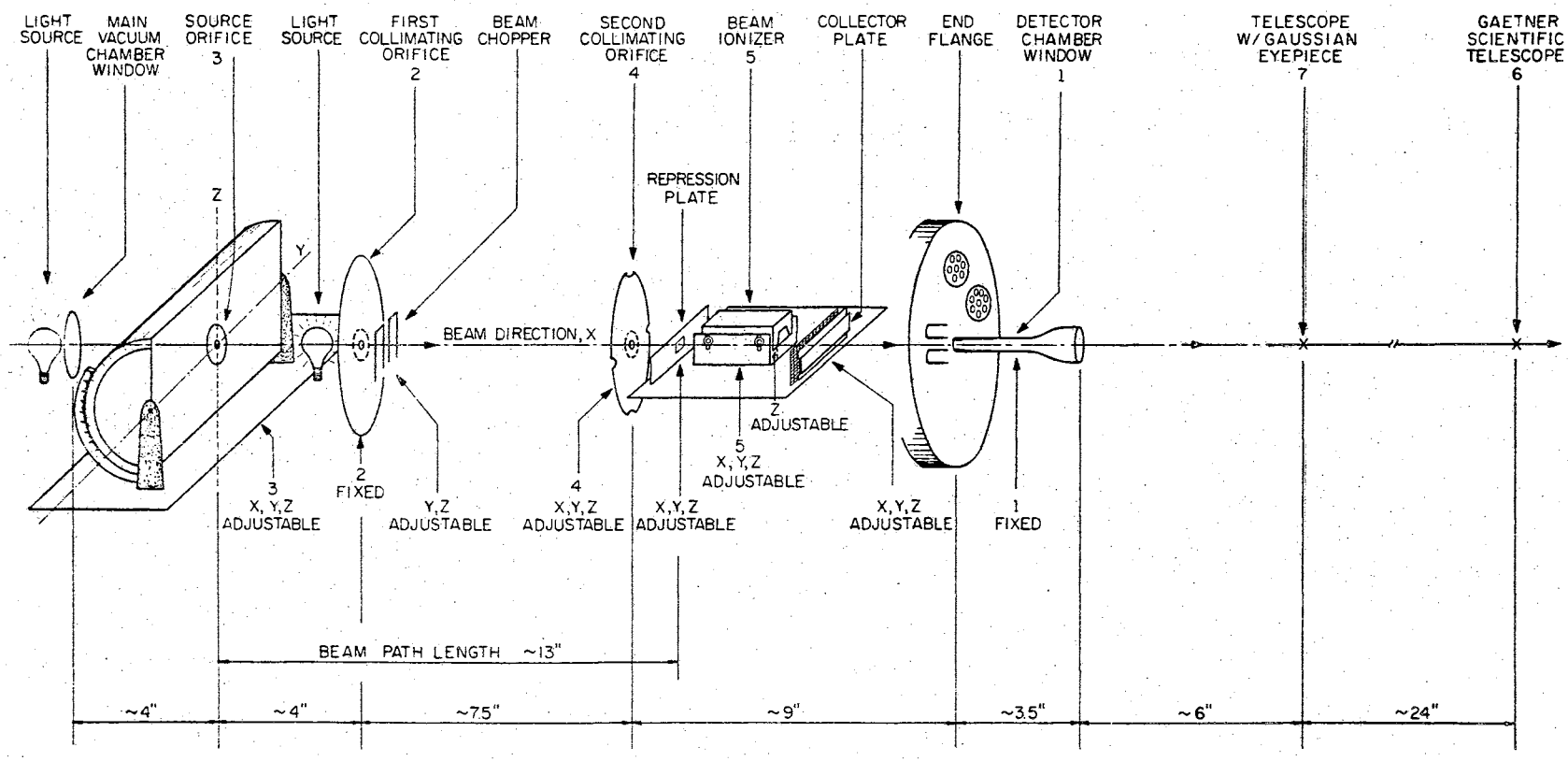

Figure 10. Orifice Alignment Schematic

collimating orifice. The chopper position must be adjusted to provide the desired full open - full closed view of the first collimating orifice from the detector (i.e., through the aligning telescope), but this position is stable and, once established, is ordinarily not adjusted during the alignment procedure. In their equilibrium, nonenergized position the chopping vanes obscure the view of the first collimating orifice from the detector (or through the telescope); hence, the chopper is energized and operating throughout the alignment procedure.

4. The second collimating orifice (4) is adjusted next. This adjustment requires removing the detector end plate with the attached detector assembly. Locating pins in the detector chamber flange and corresponding holes in the detector chamber end plate permit one to remove and replace the end plate with no apparent change in position.

5. The various components, other than the detector, are now nominally aligned. However, through the telescope it is difficult to be sure the axes of the various orifices are precisely aligned with the optical axis of the telescope, i.e., that the face of each orifice plate is precisely perpendicular to the established beam axis. The required perpendicularity is established using a second telescope fitted with a Gaussian eyepiece.

Perpendicularity of an orifice to the beam axis is established when the stationary eyepiece crosshairs are superimposed on their image reflected from a small front-surfaced mirror mounted flat on the orifice face. The orientation of the source orifice around its Z-axis is very stable. Even after the hemicylinder has been removed to insert a new orifice, locating pins in the hemicylinder x-y table allow perfect repositioning. In the new system, the first and second colli-

mating orifices are perpendicular to the beam parth when they are screwed tightly in place. This perpendicularity was checked using the mirror and telescope-crosshairs before the run series 100, 200, and 300 were made. In run series 400 and 500 (with the old chopper and detector chambers) the second collimating orifice had to be braced tightly against the adjusting pins to hold it in the perpendicular position under vacuum.

6. The system, other than the beam ionizer, is considered to be aligned when all orifices appear through the cathetometer to be perfectly nested (Figure 11) both before and after checking for perpendicular positioning of the source orifice. At first, this part of the alignment may take a full day or more, but as one becomes more adept and familiar with it, the time involved is reduced to about one or two hours.

7. The detector assembly, i.e., ion repression plate, cathode and anode, is aligned roughly outside the system by viewing the positions relative to the detector chamber window. The opening in the positive ion repression plate is fixed with respect to the cathode. The cathode, hence the repression plate opening, is adjustable with respect to the anode. The cathode is positioned so that the entire beam as defined by the second collimating orifice and the repression plate opening is admitted to the region between anode and cathode. This adjustment in the Z direction is done outside the system, as is the X direction positioning of the repression, extraction and collection plates. The beam ionizer is put back onto the supporting plate if it has been removed, and adjustments are made in the Z and Y directions for the detector assembly as a whole. The detector assembly and

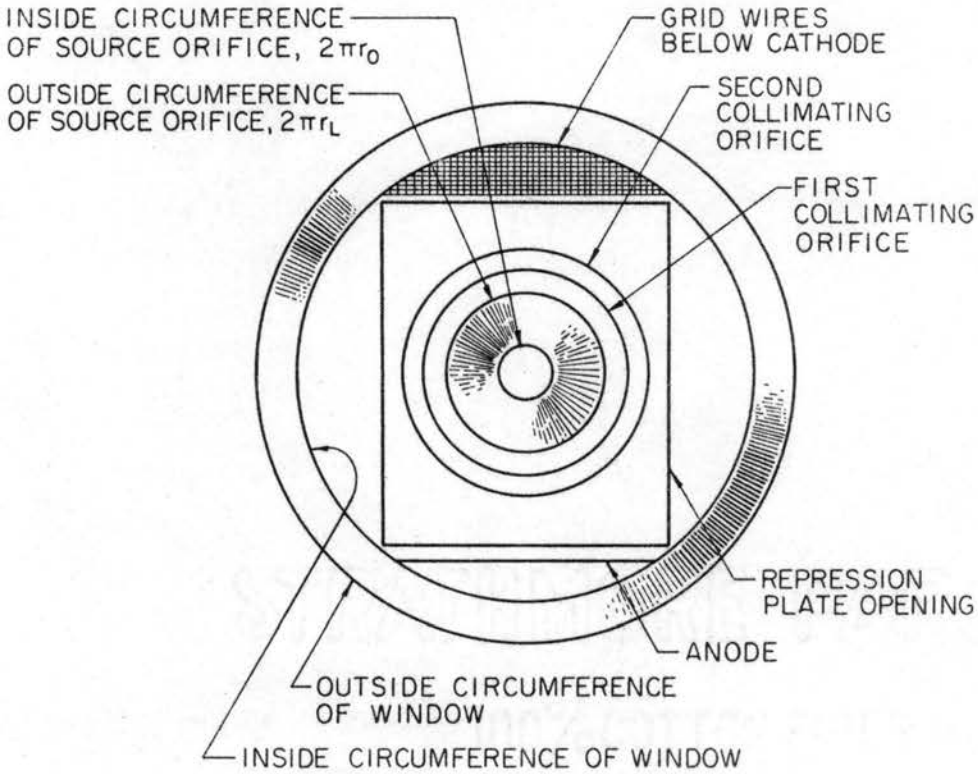

Figure 11. Orifice Nesting Schematic

end plate are replaced in the detector chamber and the alignment of the detector assembly with the various orifices is checked with the telescope. If necessary, the detector assembly is removed, adjusted for better alignment, replaced, and the alignment rechecked. The repression plate opening and the free space between the anode and cathode must fit properly into the nest of orifice openings (Figure 11). As mentioned earlier, locating pins allow replacing the end flange in the same position with no apparent error.

8. The vernier setting used for reading the angles of rotation for the source orifice is the weakest point in the alignment system. It is set to read "0" when the source orifice face is aligned perpendicular to the beam path. If the vernier is tightened too much, it may slip during the tightening, if too little, the vernier may shift to a new position when the mechanical pumps are first turned on. For this reason the zero degree point is best found by finding the maximum effusion current. This method was also used by Wang[54] and by Adams[2] to determine the zero degree angle. During runs, readings were taken for both positive and negative angles at 5° or 10° intervals to determine the zero angle and to check for any alignment failure that might occur during a run. This procedure was found to be extremely valuable as it did show one alignment failure. The system was checked, the source of failure determined and corrected. The system was then realigned, and the runs redone.

Preparation for a Run

After the alignment has been completed the system is closed and allowed to pump down at least 8 hours. The liquid nitrogen traps are

filled and the detector chamber heated at 100-200°C for at least three hours. During this time, the cathode heater is turned on for a few seconds at a time without water-cooling to prevent the beam ionizer area from acting as a gas trap. When the pressures have dropped to 10^{-6} Torr in the empty gas reservoir, 10^{-7} Torr in the main and chopper chambers and 10^{-8} Torr in the detector chamber without the cathode heater on, preparations for the run begin. The gas reservoir is filled and flushed with the gas to be used, filled again and the flow adjusted to hold the cell pressure constant at the desired level. The cathode heater and cooling water to the beam ionizer assembly are turned on. When the pressure in the detector chamber has stabilized, the heating tape around the outside of the chamber is turned off. When the detector chamber pressure has dropped to 2-4x10^{-7} Torr, the beam ionizer is turned on and the voltages adjusted. The chopper is turned on, the valve in front of the first collimating orifice opened and beam ionizer and preamplifier voltages adjusted for the particular beam intensity resulting from the established cell pressure. The settings needed are functions of cathode age, beam gas and pressure. Generally, a beam ionizer plate current of 10-20 ma is best. The reference signal and beam signal controls on the lock-in amplifier are adjusted. The recorder controls are set and the run is ready to be made and recorded.

Making a Run

For each run the hemicylinder with source orifice is first rotated from 0° to + and - 90° to establish the base line (at 90°) and maximum intensity (at 0°) on the recorder chart. The hemicylinder is

then rotated in 5° or 10° increments from 0° to + and - 90°+. During each set of 90° readings, the beam intensity at 0° is occasionally rechecked so that any changes in the maximum reading may be noted. These changes, or drifts, do occur in some runs and are linear with time. As runs with nitrous oxide show the largest changes, the drift is probably due to continuous cathode poisoning by oxygen. (See Miscellaneous Observations.) Checks are also occasionally made on the base line (90°) reading. Changes here seldom occur, the maximum recorded drift being 0.5% over the total time period required to scan through 0° to $+90^{\circ}$ and 0° to -90°.

Miscellaneous Observations

The limiting factor in the number of scans at various pressures which can be made at one time is the capacity of the 12-volt storage batteries; the cathode heater current must be quite stable. Between runs the batteries are recharged on the laboratory dc lines or by a standard 12-volt battery charger operating off the ac lines.

The pressure in the source chamber is measured by a Trans-Sonics Equibar. The readings are pressure differences, the reference pressure being measured near the main chamber, about 10^{-7} Torr. The other pressure can be measured either in the gas reservoir of the hemicylinder. The gas flow is considered to be constant when both readings are constant and very nearly equal. The pressure recorded for each run is, of course, that in the hemicylinder.

The Philips Cathodes used in our experiments had an operating life in the old system of about 300 hours, although they are "expected" to last from 6,000 to 70,000 hours.[39] This short life probably

resulted from several things - comparatively high background pressure in the old system (10^{-6} Torr when cathode heater was on); periodic or continuous exposure to cathode poisons - carbon, water, oxygen; and because the cathodes could not be "activated" and aged as recommended.[39] This detector assembly is not designed to carry the current (18 A) that would be generated even at zero field during the recommended activation and aging procedure.[39] The activation and aging temperatures required are also too high for some of the materials used. The cathode life in the new system is not known.

The pressure ranges of the experimental runs were determined by the pumping system and the beam signal detecting system. The maximum usable hemicylinder pressure is about 0.7 Torr. For higher pressures the gas through-put exceeds the capacity of the MB-100 diffusion forepump and the main chamber pumping system fails. Helium causes pump failure at slightly lower hemicylinder pressures than does N_2 or N_2O.

The minimum pressure that can be measured with the Equibar is 0.001 Torr. Experimental runs were usually limited to a minimum pressure of about 0.007 Torr however. At 0.002 Torr the output of the beam signal became so noisy that differences in signal level from one 5° increment to the next were difficult to observe. Some of the noise is probably due to (1) the background pressure becoming relatively larger in proportion to the beam pressure, (2) a short section of unshielded cable, and (3) several electrical connections made between the beam collector and recorder output.

Helium, the most difficult of the three gases to ionize, produced the noisest signals at low pressures and was limited to about 0.02 Torr as a minimum pressure. Both N_2 and N_2O showed less noise

at a given pressure than did He. The least noisy signals at a given pressure were produced by N_2O, the most readily ionized component used. The N_2 signals were nearly as good as those of N_2O over the whole range. Occasionally N_2O runs could not be made at 0.007 Torr. It is believed that the poisoning effect of oxygen on the cathode was too great relative to the number molecules going through the ionizer. The maximum (0°) signal deteriorated with time until noise swamped meaningful recorder readings.

The major assumption in using positive ion current as a measure of the beam intensity is that the fraction of beam molecules which are ionized and collected is constant over the pressure range. Several tests of intensity versus cell pressure were made for the different gases. The assumption is valid for this ionization system as pressure as a function of intensity was found to be approximately linear.

CHAPTER IV

DISCUSSION OF EXPERIMENTAL RESULTS AND COMPARISON WITH THEORETICAL ANALYSIS

The Data Range

Experimental angular distribution data were taken for 5 orifices - one cylindrical ($L/r = 2.439$, $T = 0.0^{o}$, $\theta^{*} = 39.352^{o}$), three diverging ($L/r_o = 1.987$, $T = 27.98^{o}$, $\theta^{*} = 56.996^{o}$; $L/r_o = 4.010$, $T = 25.65^{o}$, $\theta^{*} = 44.393^{o}$; $L/r_o = 10.076$, $T = 8.50^{o}$, $\theta^{*} = 19.185^{o}$), and one converging ($L/r_m = 11.009$, $T = -58.93^{o}$, $\theta^{*} = 61.497^{o}$) - and three gases (helium, nitrogen, and nitrous oxide) over a wide range of pressures (Table I). The "raw" intensity data, as obtained from the recorder charts but normalized to 1.000 at 0.0^{o}, are shown in Appendix D, Figures 48 thrugh 100. From smooth curves drawn through these original data points values were read at 5.0^{o} intervals. These "5.0^{o} points" are listed in Tables II through VI for each run. Each of these tables provides orifice geometry details, i.e., the quantities length ($\underline{L}$) and diameters ($\underline{D}_o$, $\underline{D}_L$) and the values of orifice angle ($\underline{T}$, $\underline{\theta}^{*}$) and $\underline{L/r}_o$. The values of $\underline{W}$ and $\underline{Q}_1$ are taken from theoretical calculations using the method of Edwards and Freeman. Molecular mass and diameters are standard values with the exception of N_2O whose "diameter" is estimated. The Run Number is assigned with orifice number as the first digit, component number (He-1; N_2-2; N_2O-3) as the second digit and order of the run in the pressure range as the third digit. The

TABLE I

PRESSURE RANGE OF EXPERIMENTS

ORIFICE			GAS	SERIES	PRESSURES MICRONS Hg									
Number	Angle	L/r_m												
1	25.65°	4.010	He	110			20.0				70.2			
			N_2	120		7.00	20.2	27.5	41.0		72.7		200.	670.
			N_2O	130		6.90	22.0		45.0		69.0		195.	
2	8.50°	10.076	He	210			21.0		41.5		71.0		190.	
			N_2	220		7.00	22.0				70.0		210.	660.
			N_2O	230		6.20	20.0		41.5		70.1		207.	
3	-58.93°	11.009	He	310					41.5		74.0		220.	
			N_2	320			14.0				66.0		180.	700.
			N_2O	330			24.0				69.0		200.	790.
4	27.98°	1.987	N_2	420			24.0		40.0		73.0	91.0	120.	126.
5	0.00°	2.439	He	510			33.0		45.0					
			N_2	520		8.70	20.0	23.5	46.0	50.0	70.0			

TABLE II

NORMALIZED INTENSITIES FOR ORIFICE NO. 1

$I_\theta^+/I_o^+ = I(\theta)$

$T = 25.65^\circ$ $L/r_o = 4.010$ $\theta^* = 44.393^\circ$ $W = 0.87395$ $Q_1 = 1.655707$

$L = 0.1803$ cm $D_L = 012634$ cm $D_o = 0.0902$ cm

	HELIUM Diam. = 2.650 Å Mass = 4.003		NITROGEN Diam. = 3.150 Å Mass = 28.013							NITROUS OXIDE Diam. = 3.300 Å Mass = 43.013				
Pressure, Microns Hg	20.2	70.2	7.00	20.2	27.5	41.0	72.7	200.	670.	6.90	22.0	45.0	69.0	195.0
Run No.	111	113	121	122	123	124	125	126	127	131	132	133	134	135
Exp. No.	59	58	55	54	50	56	53	52	51	64	63	65	62	66
Angle														
0°	1000	1000	1000	1000	1000	1000	1000	1000	1000	1000	1000	1000	1000	1000
5	996	993	993	989	991	994	994	995	995	996	997	996	995	994
10	973	969	969	972	973	976	975	977	982	980	982	976	978	972
15	939	934	936	944	946	949	946	945	953	952	956	946	949	938
20	898	892	897	912	910	911	906	902	909	912	919	907	906	890
25	851	842	847	868	863	863	859	892	846	858	870	858	849	827
30	785	773	766	796	792	791	780	765	758	787	807	790	773	746
35	645	638	637	664	671	662	670	657	630	652	653	660	644	636
40	422	432	424	445	475	475	523	485	500	455	450	475	466	494
45	264	274	275	295	275	300	342	345	379	277	286	305	299	360
50	178	187	188	202	200	215	234	244	265	205	197	214	204	258
55	127	134	137	143	148	159	175	178	186	150	147	156	146	182
60	089	097	104	102	111	117	133	129	129	106	111	115	103	129
65	062	069	078	071	082	082	099	093	085	072	083	082	071	091
70	042	048	057	049	058	057	072	066	055	048	060	057	049	063
75	027	031	040	032	040	038	050	044	034	028	042	038	031	041
80	016	018	025	024	024	022	031	026	019	013	025	022	022	024
85	007	007	012	008	010	010	010	012	008	004	012	009	007	010
90	000	000	000	000	000	000	000	000	000	000	000	000	000	000

TABLE III

NORMALIZED INTENSITIES FOR ORIFICE NO. 2

$I_\theta^+/I_o^+ = I(\theta)$

$T = 8.50^\circ$ $L/r_o = 10.076$ $\theta^* = 19.185^\circ$ $W = 0.53366$ $Q_l = 1.926066$

$L = 0.4557$ cm $D_L = 0.2271$ cm $D_o = 0.0907$ cm

	HELIUM Diam. = 2.65 Å Mass = 4.003				NITROGEN Diam. = 3.150 Å Mass = 23.013					NITROUS OXIDE Diam. = 3.300 Å Mass = 43.013				
Pressure, Microns Hg	21.0	41.5	71.0	190.0	7.00	22.0	70.0	210.0	660.0	6.20	20.0	41.5	70.1	207.0
Run No.	211	212	213	214	221	222	223	224	225	231	232	233	234	235
Exp. No.	70	69	68	67	75	74	73	72	71	80	79	78	77	76
Angle														
0°	1000	1000	1000	1000	1000	1000	1000	1000	1000	1000	1000	1000	1000	1000
5	993	993	986	988	991	990	995	993	996	991	989	992	992	992
10	950	950	940	958	943	950	949	960	973	940	937	965	969	970
15	718	737	736	784	718	763	790	875	927	675	735	800	825	894
20	475	507	514	580	468	500	576	725	860	400	464	587	641	794
25	342	342	361	434	350	371	425	587	765	268	326	423	500	675
30	265	263	272	334	286	294	328	472	652	200	254	328	392	569
35	203	210	226	267	239	238	263	376	543	149	201	267	317	470
40	173	169	182	217	201	197	211	305	444	110	158	220	258	388
45	142	134	144	177	169	163	169	248	355	075	124	180	210	318
50	116	107	116	142	141	134	135	197	275	051	097	147	170	256
55	095	084	093	114	115	110	107	153	207	035	075	118	135	200
60	077	066	074	091	092	088	084	117	148	025	068	095	105	151
65	061	050	060	070	071	068	062	085	102	017	043	073	080	114
70	046	036	048	052	053	051	044	059	068	012	030	054	059	084
75	033	024	036	036	037	035	027	040	043	008	019	038	042	059
80	021	014	024	022	023	022	015	024	025	005	011	023	026	037
85	011	007	012	010	011	011	006	012	010	003	004	010	012	017
90	000	000	000	000	000	000	000	000	000	000	000	000	000	000

TABLE IV

NORMALIZED INTENSITIES FOR ORIFICE NO. 3

$I_\theta^+/I_o^+ = I(\theta)$

$T = 58.93^\circ$ $L/r_o = 11.009$ $\theta^* = 61.497^\circ$ $W = .99485$ $Q_1 = 1.0000$

$L = 0.3160$ cm $D_L = 0.0574$ cm $D_o = 1.1067$ cm

	HELIUM Diam. = 2.6050 Å Mass = 4.0026			NITROGEN Diam. = 3.150 Å Mass = 28.0134				NITROUS OXIDE Diam. = 3.300 Å Mass = 43.0[illegible]			
Pressure, Microns Hg	41.5	74.0	220.0	14.0	66.0	180.0	700.0	24.0	69.0	200.0	690.0
Run No.	311	312	313	321	322	323	324	331	332	333	334
Exp. No.	83	82	81	87	86	85	84	91	90	89	88
Angle											
0°	1000	1000	1000	1000	1000	1000	1000	1000	1000	1000	1000
5	998	996	998	997	992	992	990	989	995	993	982
10	989	979	978	986	972	972	960	971	979	968	947
15	968	949	927	964	944	939	912	943	949	930	898
20	936	903	868	929	905	893	844	906	909	882	837
25	888	844	801	879	858	843	750	859	856	824	769
30	826	779	728	817	802	783	697	802	795	756	694
35	758	710	648	741	739	716	610	739	729	682	613
40	687	636	563	665	669	641	520	667	658	603	528
45	612	559	473	585	593	561	431	593	584	525	449
50	534	479	380	503	510	478	350	514	507	447	374
55	455	397	291	418	423	396	275	437	426	371	305
60	373	311	213	325	340	317	208	361	344	295	243
65	291	222	146	238	258	247	151	287	261	226	188
70	205	144	087	164	175	180	104	216	186	164	140
75	128	085	042	104	106	122	068	148	123	113	100
80	069	042	014	056	055	073	040	078	075	069	070
85	027	013	003	021	020	039	026	023	033	040	049
90	000	000	000	000	000	000	000	000	000	000	000

TABLE V

NORMALIZED INTENSITIES FOR ORIFICE NO. 4

$I_\theta^+/I_o^+ = I(\theta)$

$T = 27.98^\circ$ $L/r_o = 1.987$ $\theta^* = 56.966^\circ$ $W = .9049$ $Q_1 = 1.411233$

$L = 0.18694$ cm $D_L = 0.38710$ cm $D_o = 0.18821$ cm

	NITROGEN Diam. = 3.15 Å Mass = 28.013					
Pressure Microns Hg	24.0	40.0	73.0	91.0	120.0	126.0
Run No.	421	422	423	424	425	426
Exp. No.	15	13	14	17	16	18
Angle						
0°	1000	1000	1000	1000	1000	1000
5	999	991	993	994	990	995
10	988	969	973	977	963	977
15	962	938	940	947	926	946
20	924	896	894	901	876	903
25	869	841	833	838	812	844
30	796	760	753	752	733	767
35	704	664	653	648	635	664
40	598	564	543	545	525	555
45	469	462	433	442	416	443
50	337	356	320	339	308	332
55	249	247	224	237	218	237
60	178	157	157	163	149	160
65	126	109	110	112	098	108
70	088	075	075	074	064	069
75	059	050	049	047	041	042
80	036	029	028	026	023	022
85	017	013	013	011	010	008
90	000	000	000	000	000	000

TABLE VI

NORMALIZED INTENSITIES FOR ORIFICE NO. 5

$I_\theta^+/I_o^+ = I(\theta)$

$T = 0.0^o$	$L/r = 2.439$		$\theta^* = 39.352^o$		$W = 0.97470$		$Q_1 = 1.0000$	
	$L = 0.19202$ cm		$D_L = 0.15748$		$D_o = 0.15748$ cm			
	HELIUM Diam. = 2.65 Å Mass = 4.003		NITROGEN Diam. = 3.150 Å Mass = 28.013					
Pressure, Microns Hg	33.0	45.0	8.70	20.0	23.5	46.0	50.0	70.0
Run No.	511	512	521	522	523	524	525	526
Exp. No.	7	8	4	5	6	2	1	3
Angle								
0°	1000	1000	1000	1000	1000	1000	1000	1000
5	964	957	951	964	961	959	966	980
10	911	902	893	913	910	911	919	942
15	835	833	826	848	844	851	860	886
20	750	753	752	761	766	785	788	808
25	661	660	667	666	676	709	704	709
30	571	561	575	573	571	625	614	613
35	482	473	477	488	478	535	524	521
40	410	397	390	411	409	450	440	444
45	345	332	330	344	349	373	363	373
50	288	279	282	286	295	301	293	306
55	235	230	237	237	244	238	231	246
60	185	185	198	193	198	184	176	192
65	138	143	161	151	151	137	131	145
70	096	105	126	122	120	096	096	106
75	060	071	093	078	073	061	067	074
80	032	042	061	046	041	032	042	046
85	011	019	031	019	016	012	019	021
90	000	000	000	000	000	000	000	000

Experiment Number reflects the chronological order of the various experiments and refers to the original strip chart recordings.

The smooth experimental curves for each orifice and gas over the pressure range used are shown along with the theoretical curve for the orifice in Figures 12 through 23.

The General Differences Between Experiment and Theory

The variations of molecular beam intensity with source pressure are revealed very clearly in Figures 12 through 23. In general, the beam intensities at lower pressures are in better over all agreement with the theoretical curve; at higher pressures the discrepancies become progressively larger.

The major differences between the theoretical and experimental $\underline{I(\theta)}$ values occur in the region near $\underline{\theta}^*$, the division between the ranges 2 and 3 defined in the theoretical treatment. At angles greater than $\underline{\theta}^*$, a molecule can not enter at one edge of the orifice and exit at the opposite edge without encountering the wall.

Not nearly so large as the differences around $\underline{\theta}^*$, but real and consistent, are the differences between theoretical and experimental intensities, at angles near the orifice angle $\underline{T}$. $\underline{T}$ is the point of division between the ranges 1 and 2 of the theoretical analysis. There is a small pressure effect in these differences and they are always in the same direction.

There are also differences among the three gases used in this study. N_2O exhibits a greater pressure effect at the higher pressures than do the other two gases. N_2 exhibits a greater pressure effect than does He.

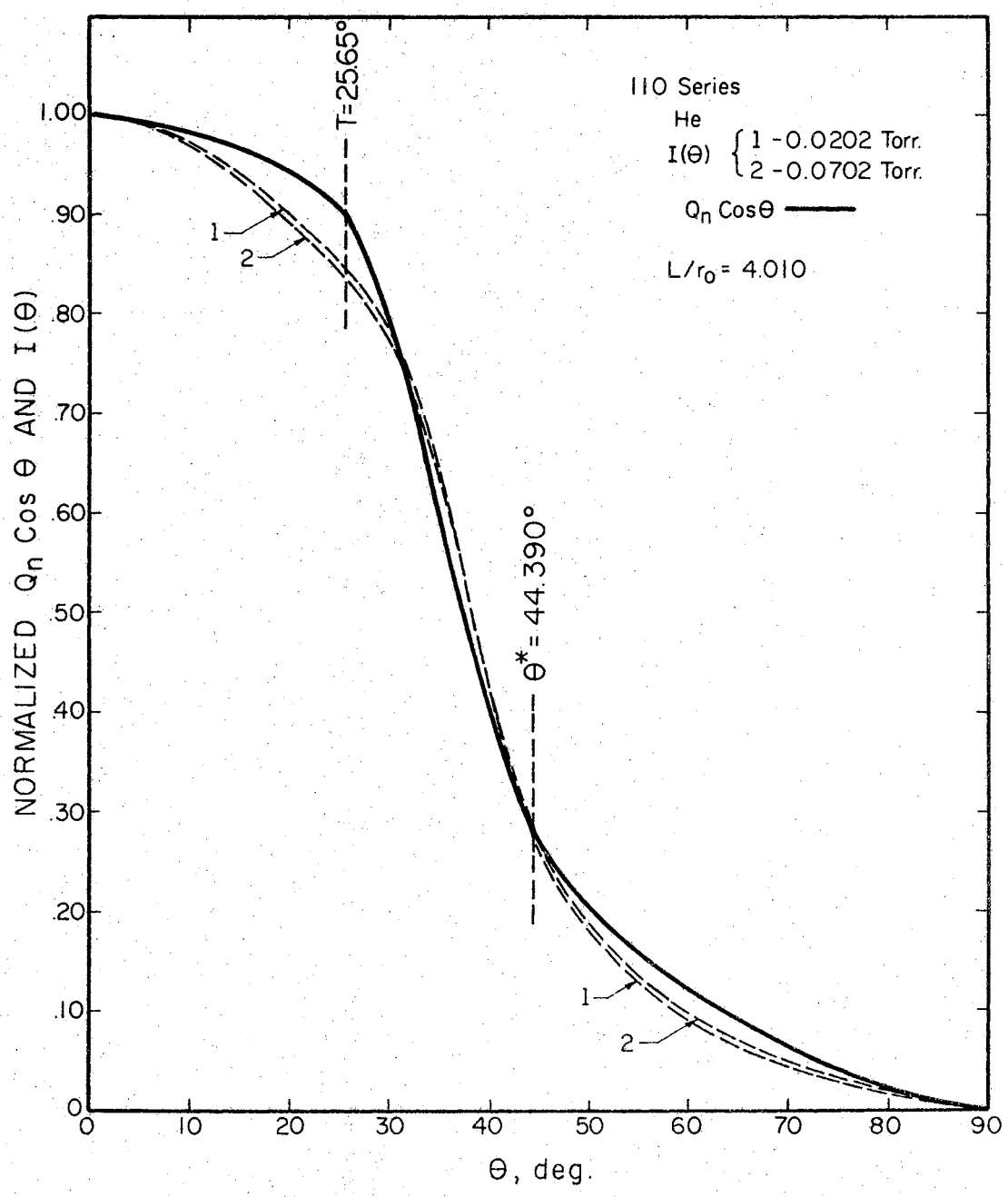

Figure 12. Normalized Theoretical (Q_n Cos θ) and Experimental (I (θ)) Intensities for He from Orifice 1

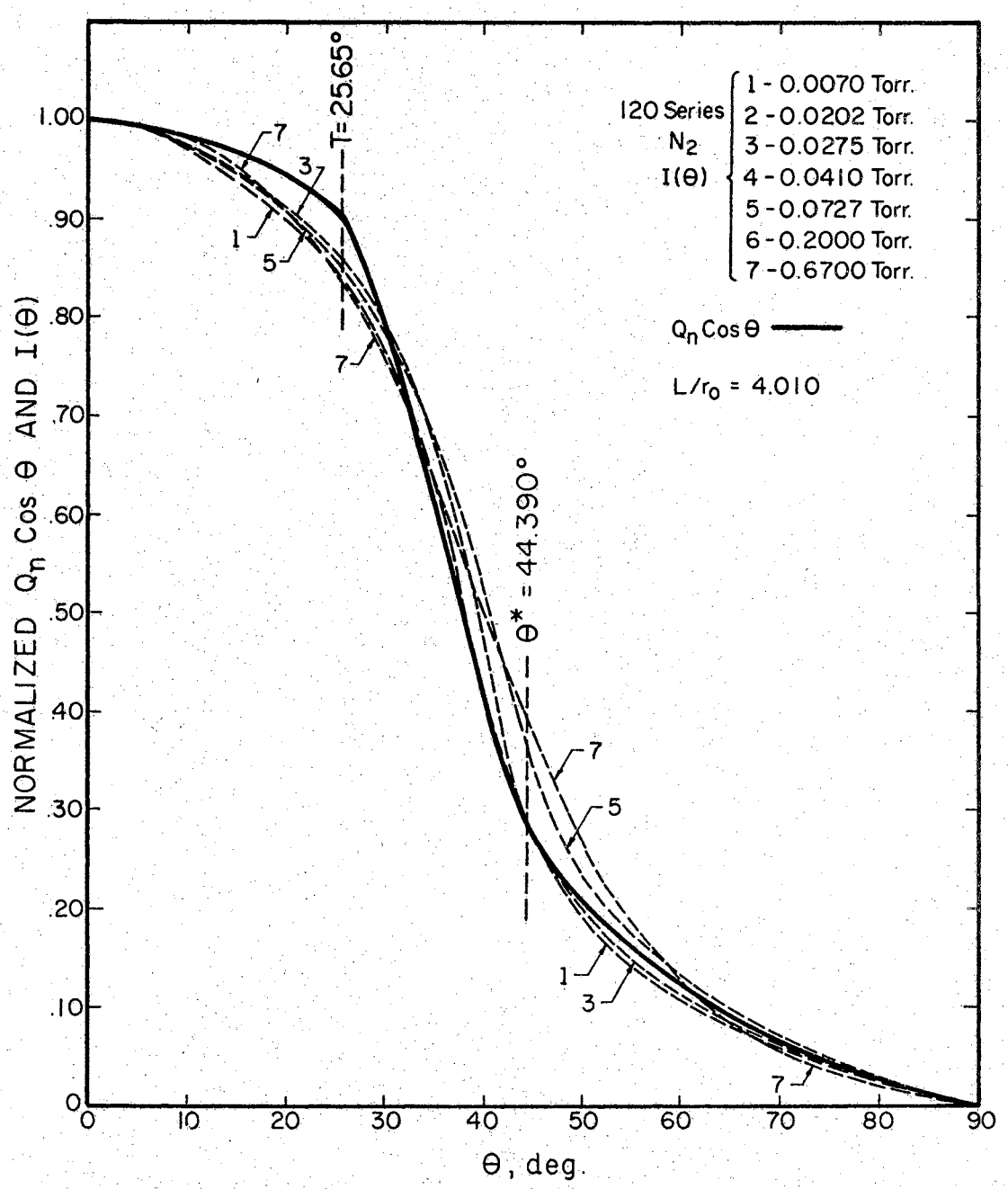

Figure 13. Normalized Theoretical (Q_n Cos θ) and Experimental (I (θ)) Intensities for N_2 from Orifice 1

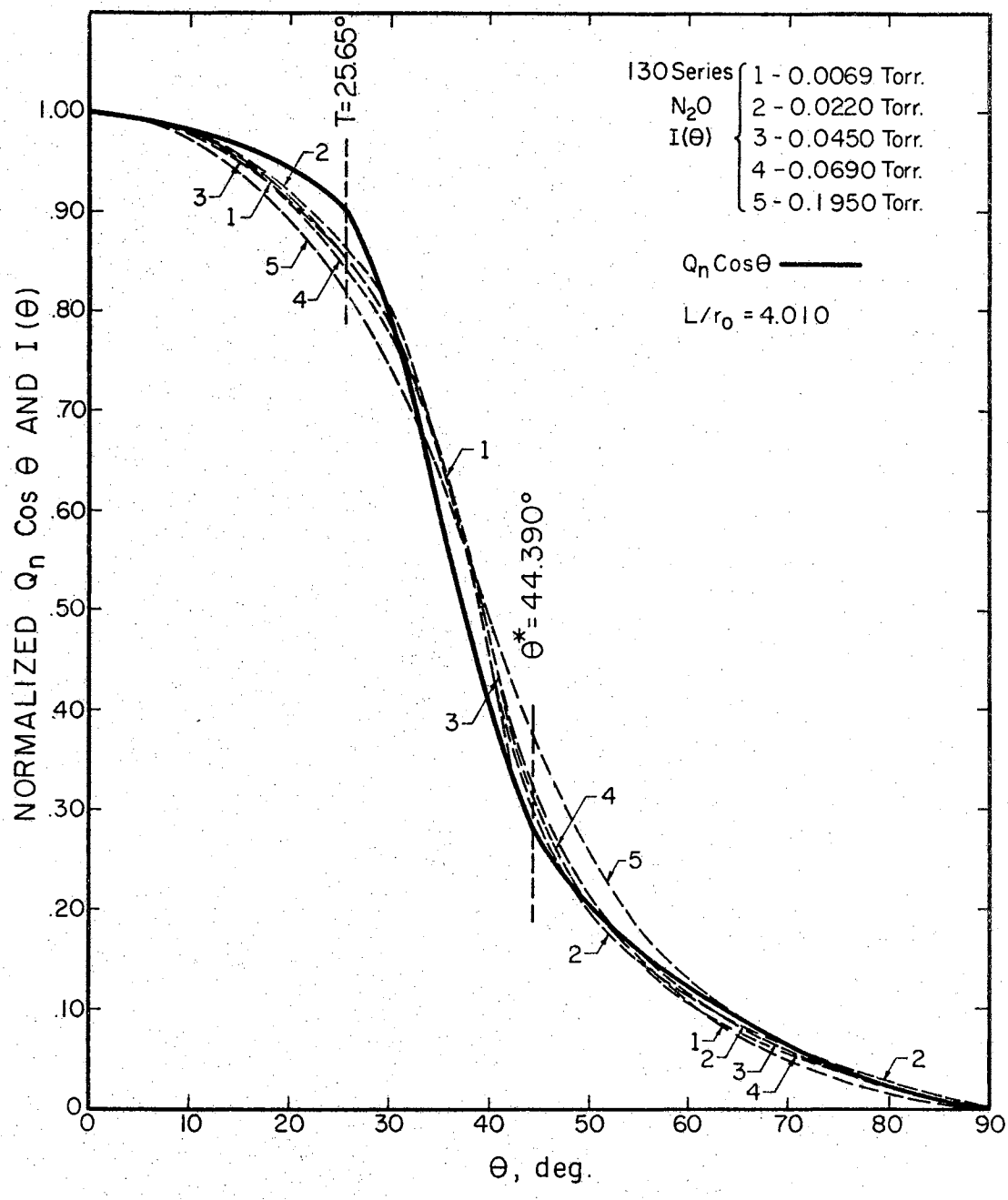

Figure 14. Normalized Theoretical (Q_n Cos Θ) and Experimental (I (Θ)) Intensities for N_2O from Orifice 1

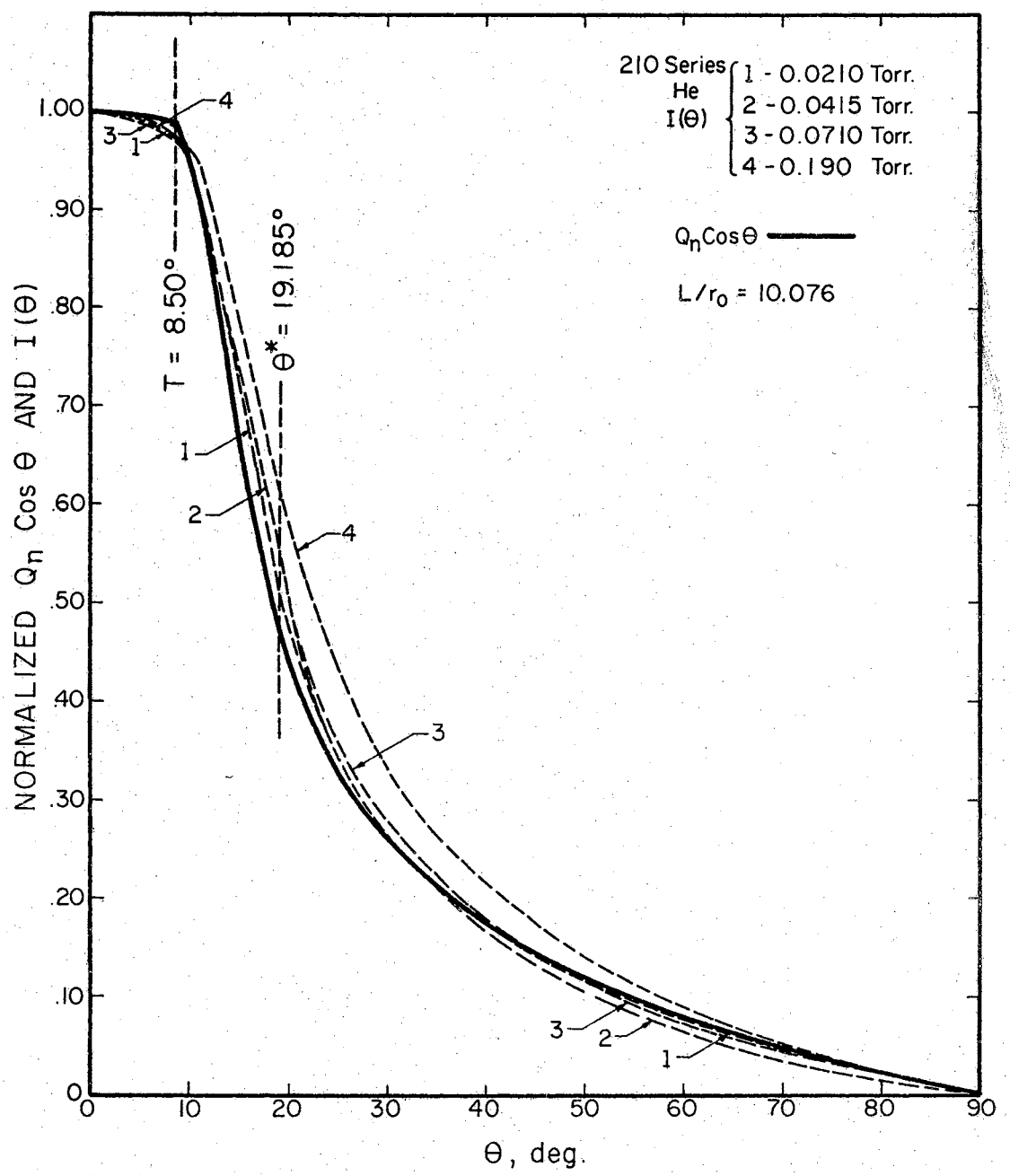

Figure 15. Normalized Theoretical (Q_n Cos Θ) and Experitmental (I (Θ)) Intensities for He from Orifice 2

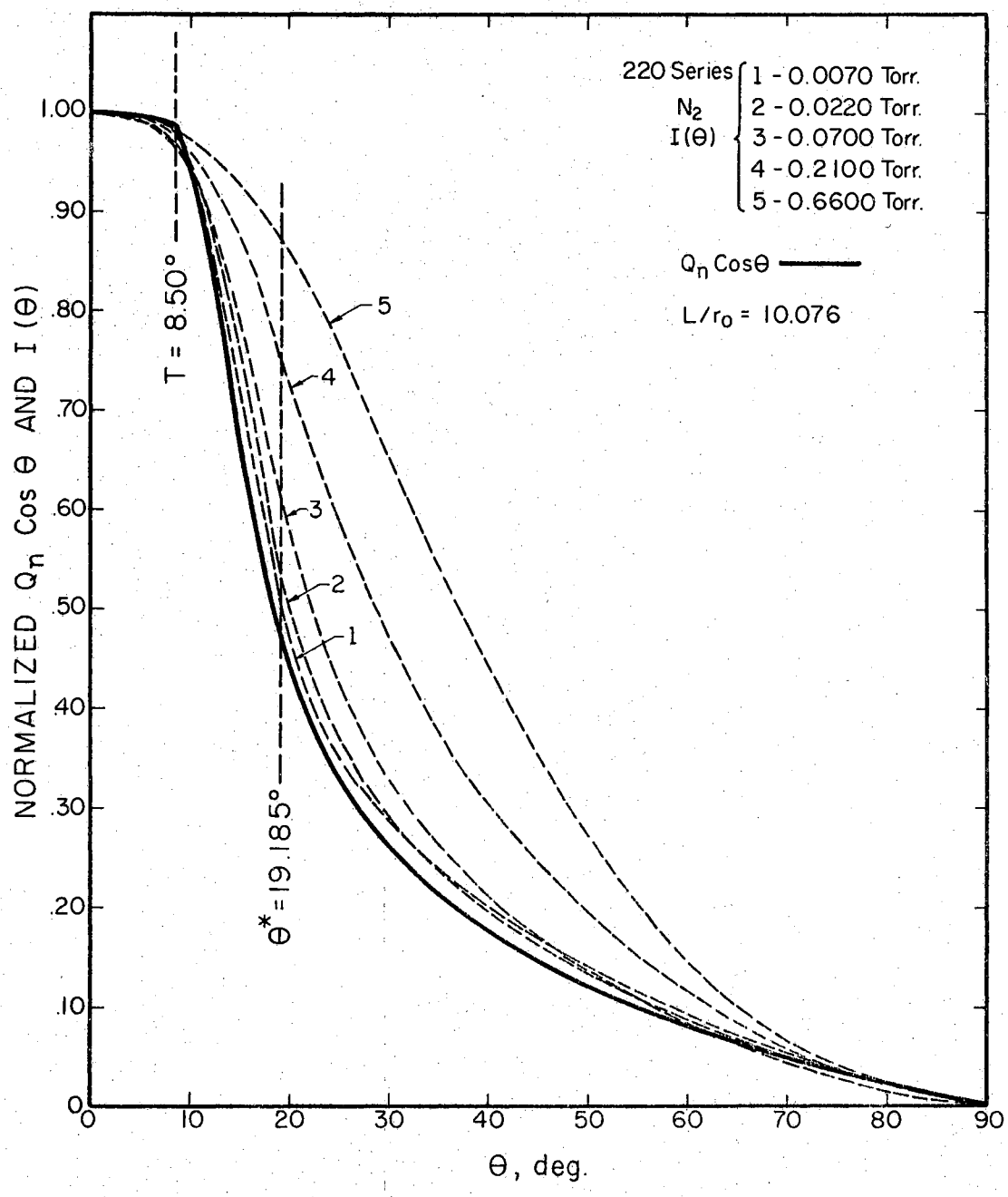

Figure 16. Normalized Theoretical (Q_n Cos θ) and Experimental Intensities for N_2 from Orifice 2

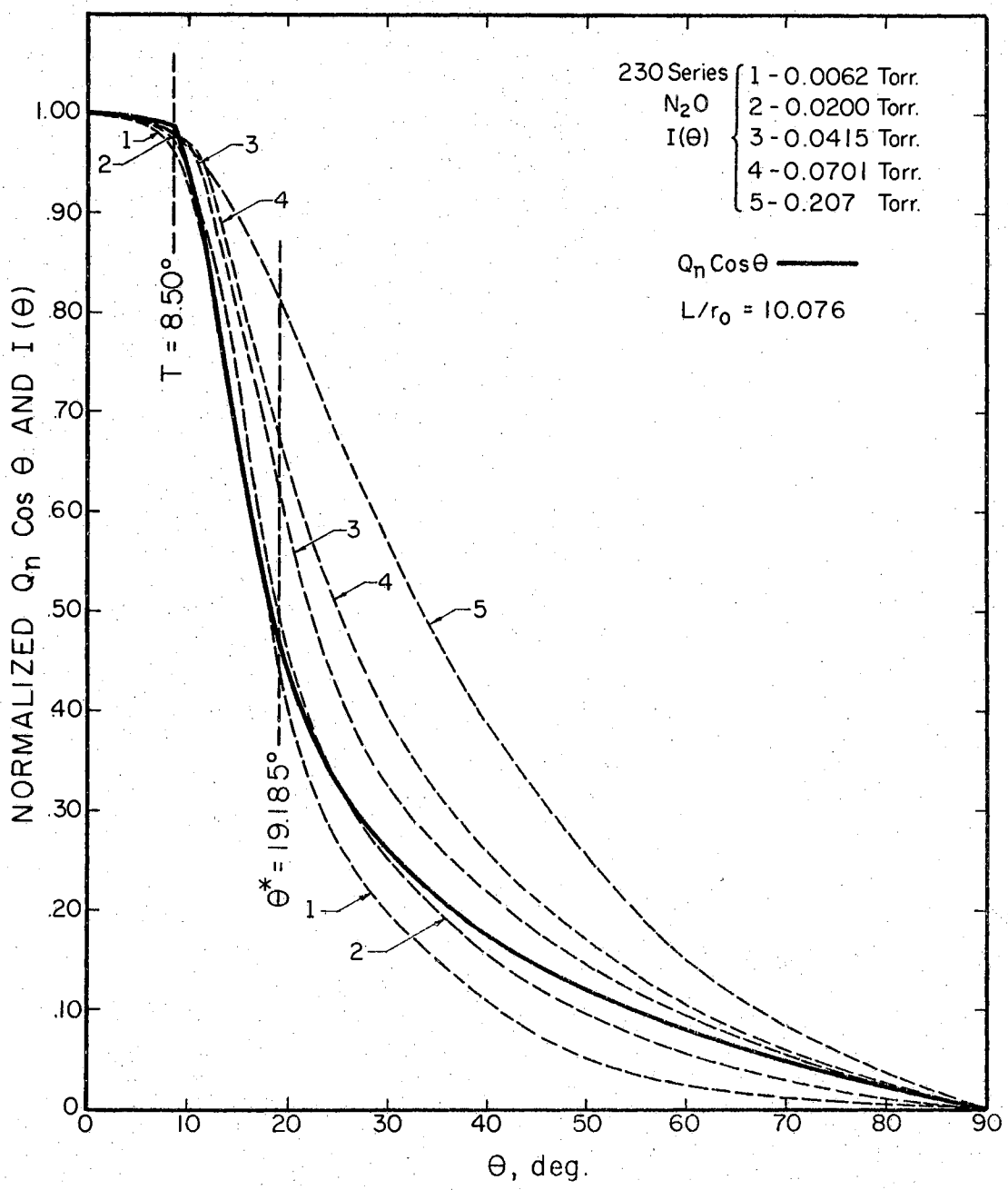

Figure 17. Normalized Theoretical (Q_n Cos θ) and Experimental (I (θ)) Intensities for N_2O from Orifice 2

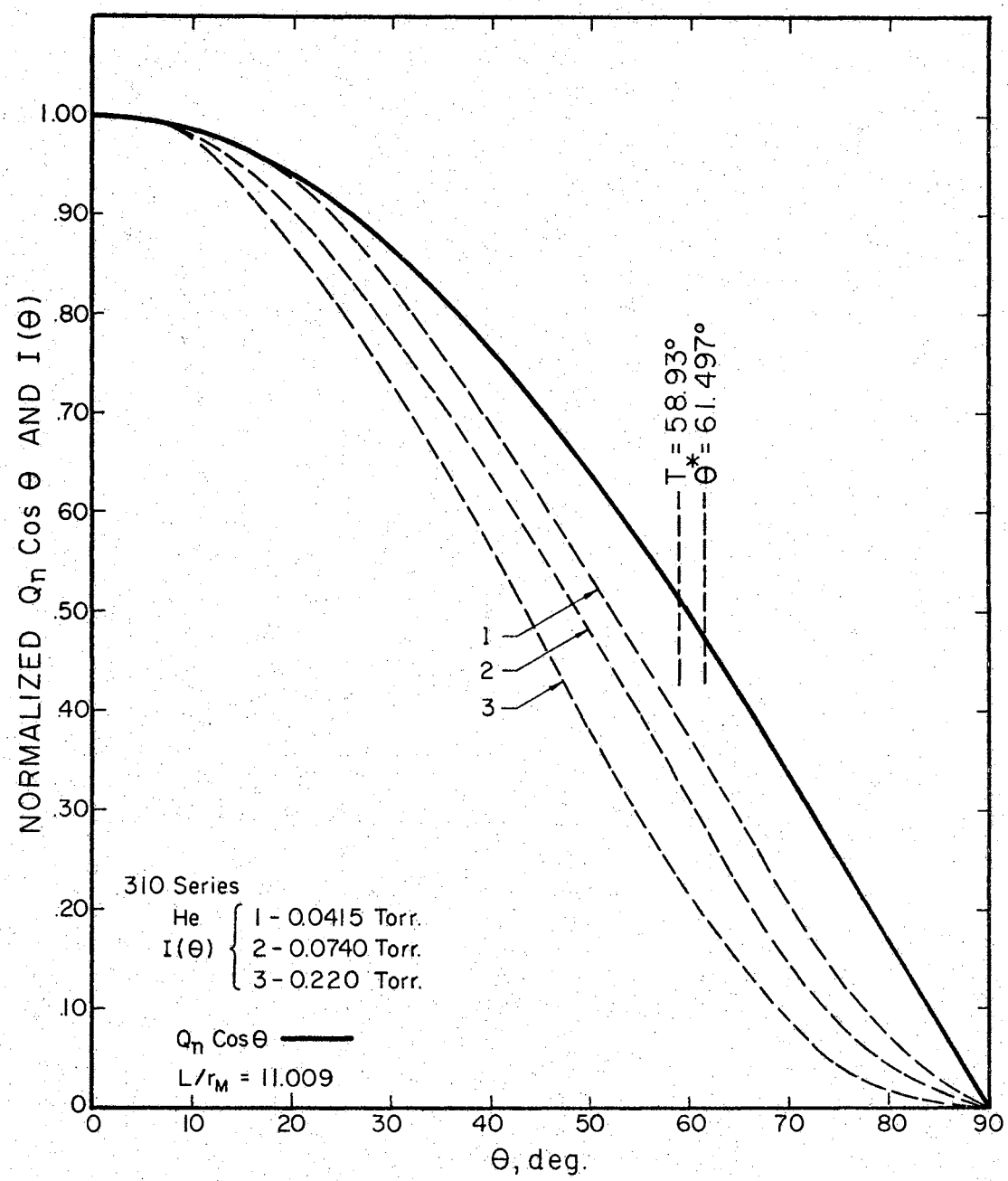

Figure 18. Normalized Theoretical (Q_n Cos θ) and Experimental (I (θ)) Intensities for He from Orifice 3

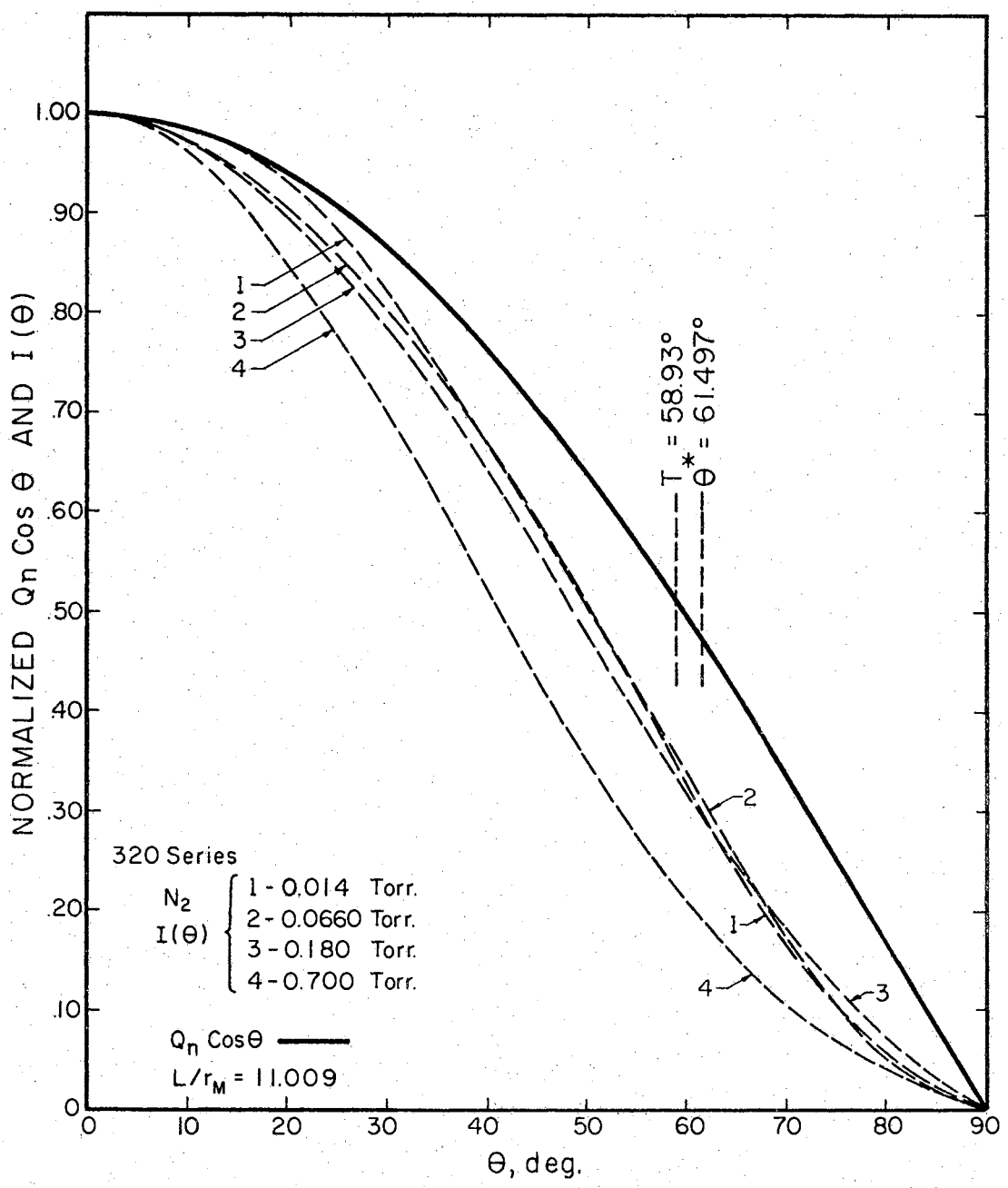

Figure 19. Normalized Theoretical (Q_n Cos θ) and Experimental (I (θ)) Intensities for N_2 from Orifice 3

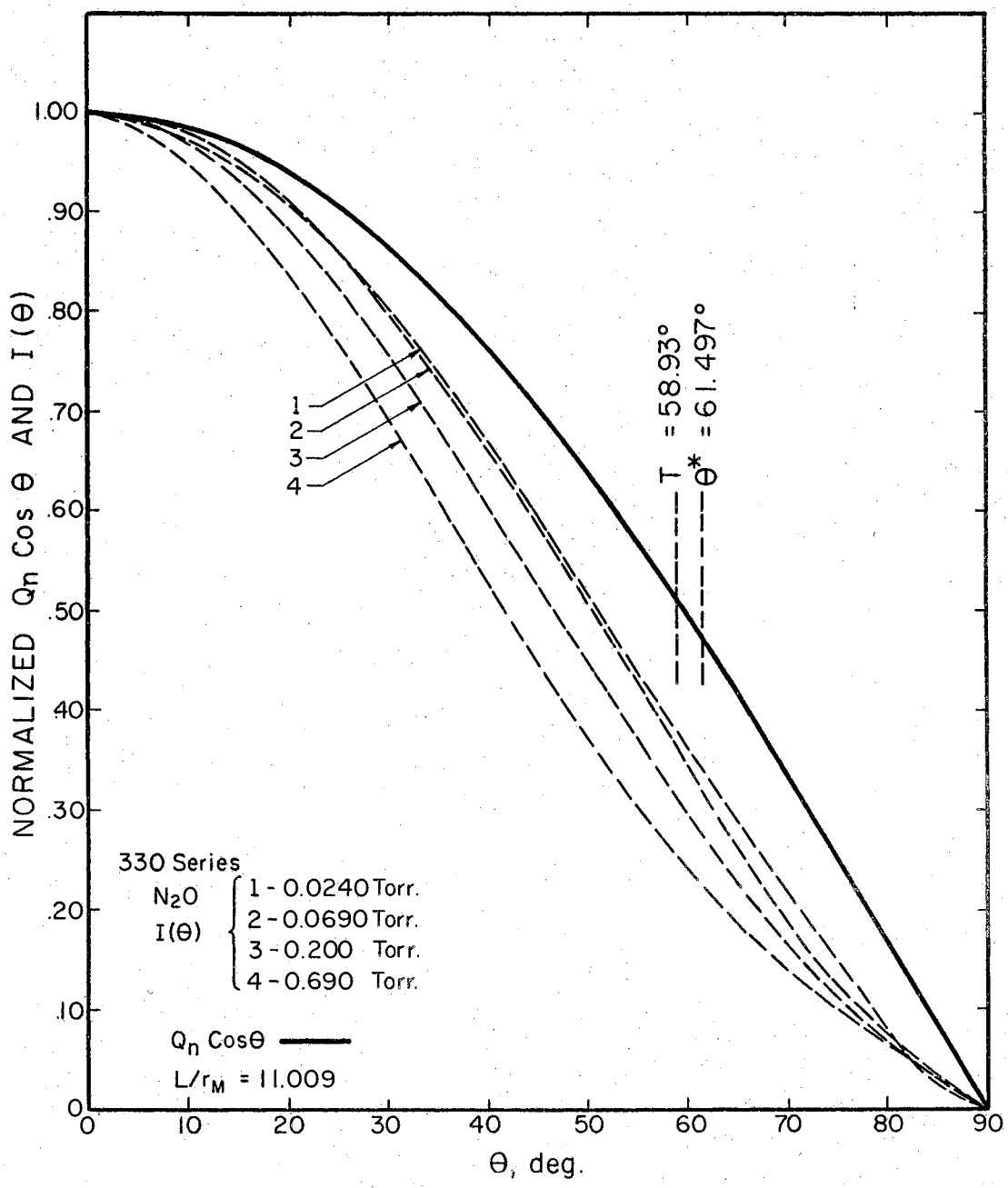

Figure 20. Normalized Theoretical (Q_n Cos Θ) and Experimental (I (Θ)) Intensities for N_2O from Orifice 3

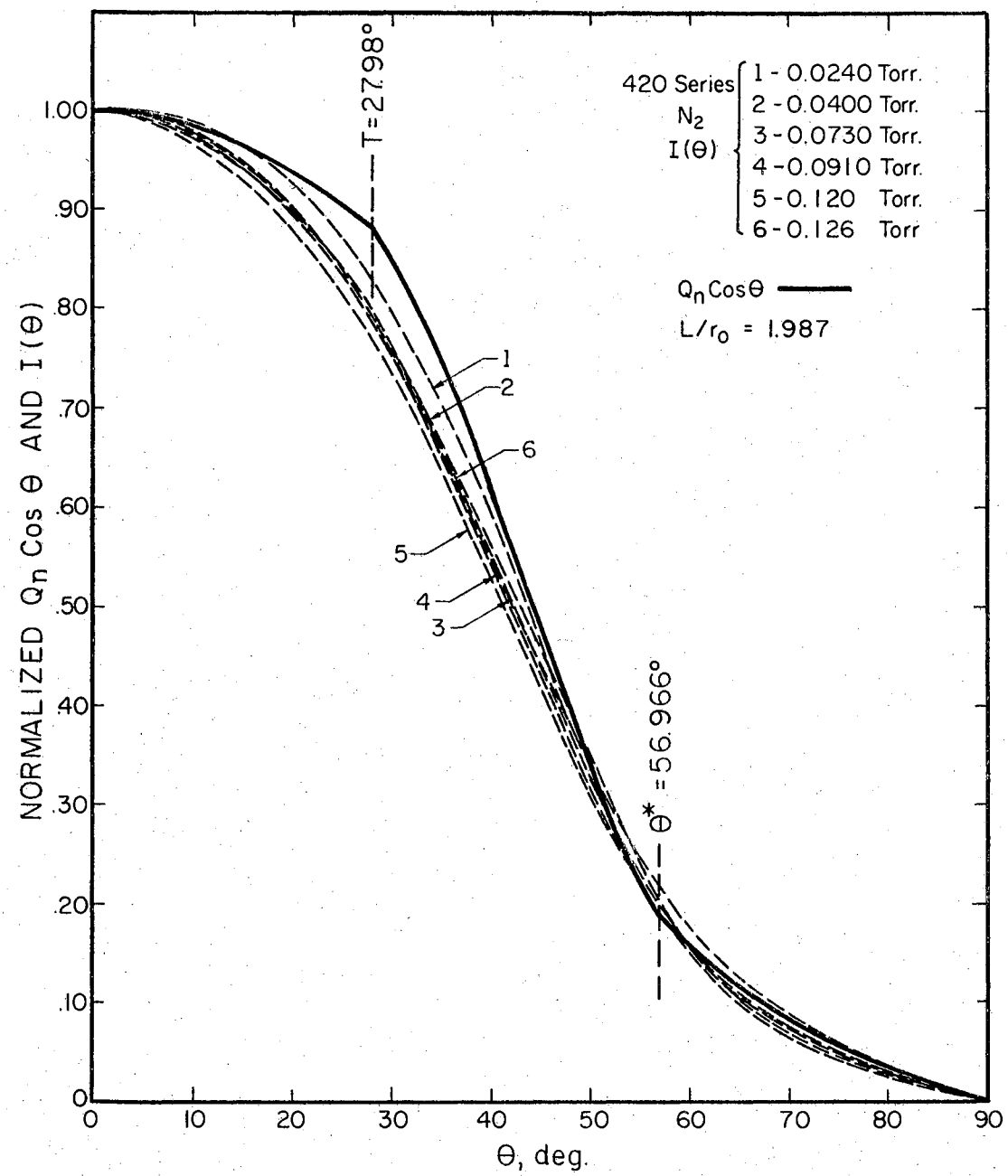

Figure 21. Normalized Theoretical (Q_n Cos θ) and Experimental (I (θ)) Intensities for N_2 from Orifice 4

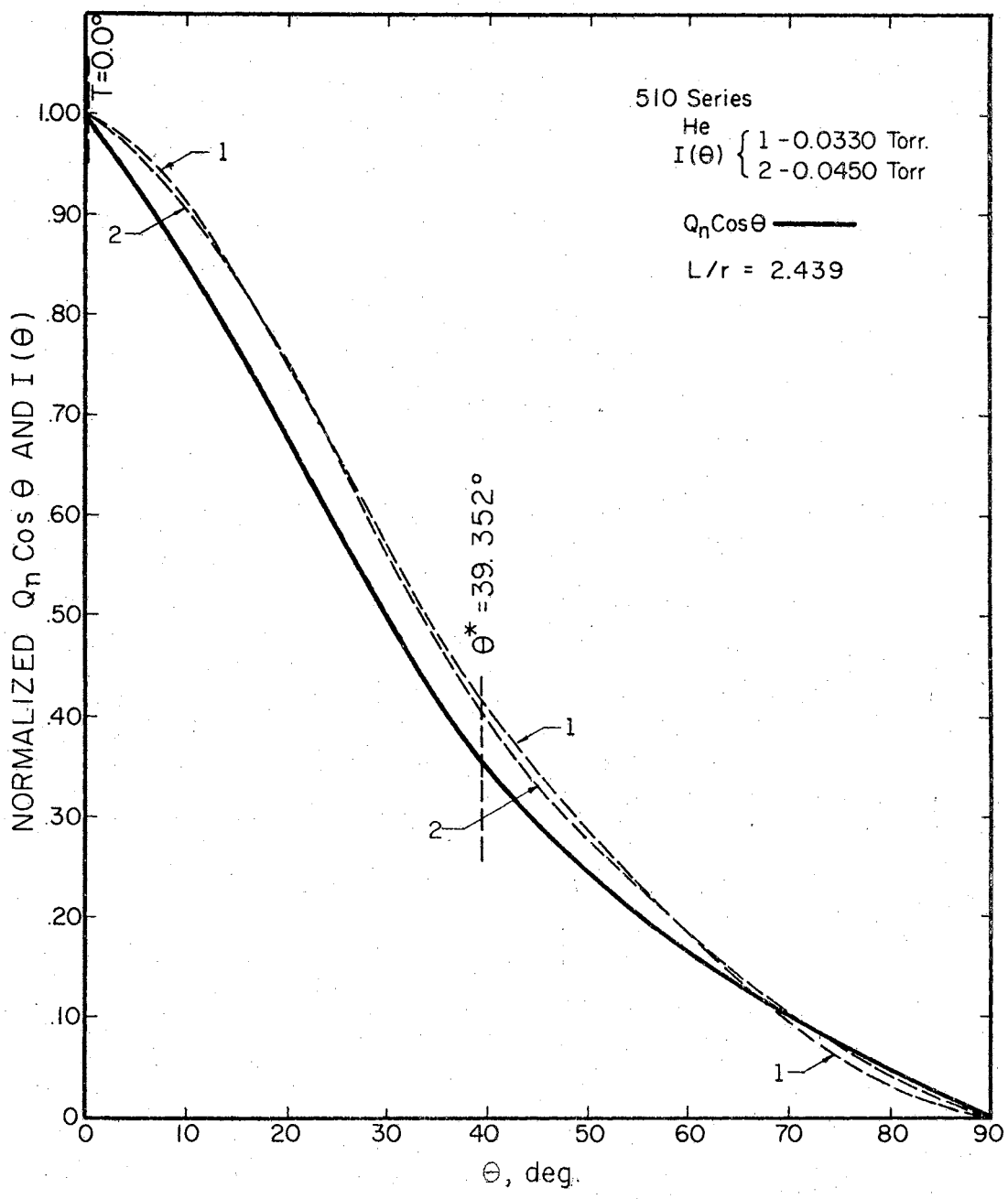

Figure 22. Normalized Theoretical (Q_n Cos θ) and Experimental (I (θ)) Intensities for He from Orifice 5

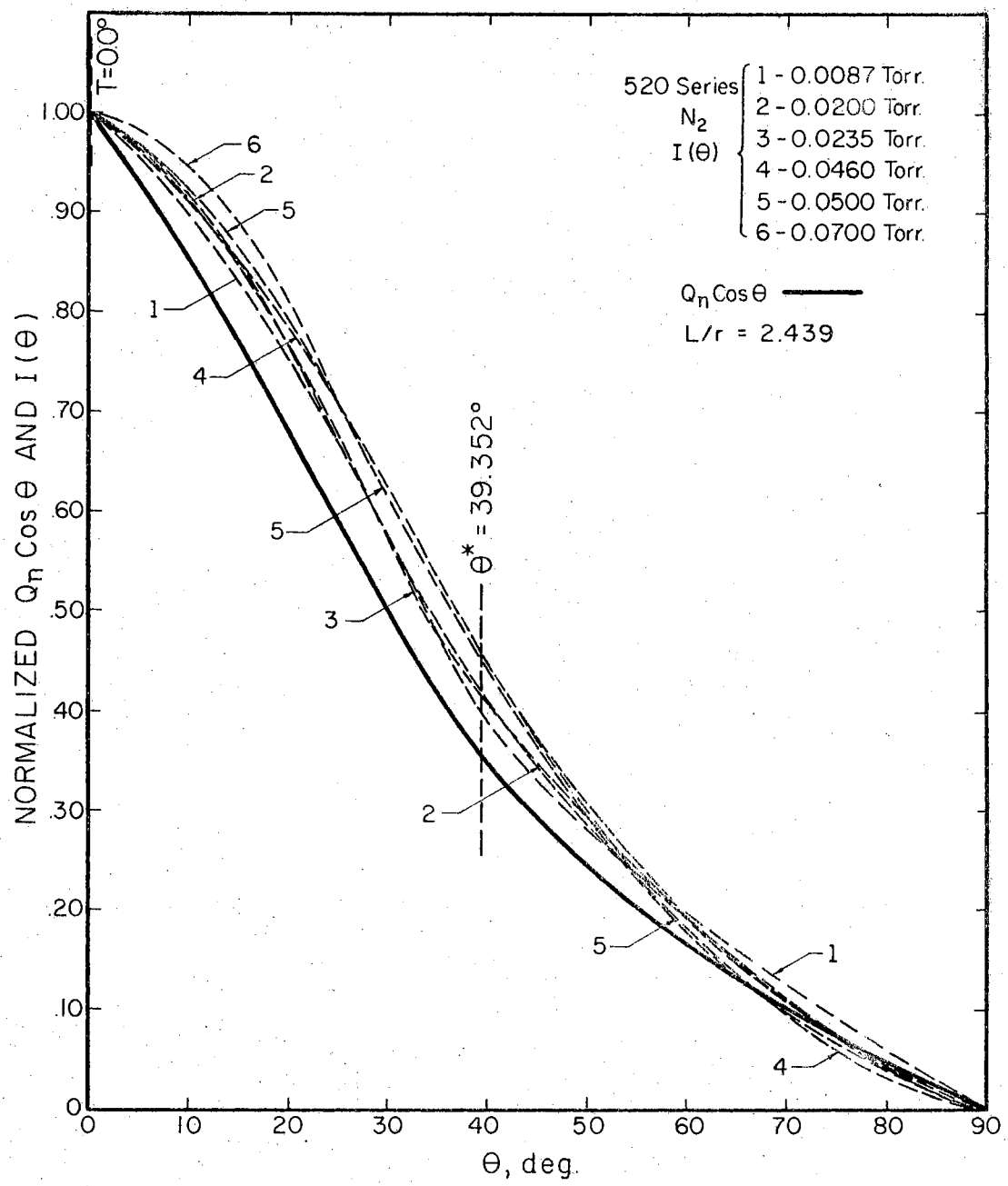

Figure 23. Normalized Theoretical (Q_n Cos θ) and Experimental (I (θ)) Intensities for Orifice 5 with N_2

In the region of $\underline{\theta}^*$ for the long diverging orifice the experimental intensity values for N_2O at a given high pressure are larger than those of N_2 or He at the same pressure. For example, in Figures 15, 16 and 17 the intensity values for N_2O at 0.207 Torr fall between the values for N_2 at 0.210 Torr and 0.66 Torr. The intensities for N_2O at 0.0415 Torr are virtually identical to those for N_2 at 0.070 Torr and for He at 0.190 Torr. In addition, the lowest pressure runs on He and N_2O have intensities lower than the theoretical values in the region between $\underline{\theta}^*$ and 90°. Similar behavior is observed with Orifice 1 for the three gases though the differences are not nearly so great as with Orifice 2.

In Orifice 3 pressure differences between N_2O and N_2 are not very great, but He at 0.220 Torr shows differences similar to those of N_2 and N_2O at 0.70 Torr. In this orifice the major difference among the gases appears to be the overall shape of the $\underline{I(\theta)}$ curve. The data indicate that the He beam is more collimated than is the N_2 beam, which in turn is more collimated than that of N_2O.

Though these component differences seem large, they are small compared to the differences exhibited by each gas at the angles $\underline{T}$ and $\underline{\theta}^*$.

General Treatment of Experiment Data

Probability density function calculations have been used along with intensity data because of the additional flexibility they provide. The normalized angular intensities can only be properly compared with a normalized angular distribution. As this experimental system only allows measurement of relative intensities and cannot be used to count

molecules, the theoretical angular distribution must also be normalized. A comparison of normalized $\underline{Q_n \cos\theta}$ with normalized experimental intensities forces agreement at $\theta = 0.0^{\circ}$. There is also agreement at $\theta = 90.0^{\circ}$, but this agreement is real for the data in this study. The intensity at 90.0° can be compared with and is the same as (1) the intensity at $\approx 95.0^{\circ}$ (detector can no longer "see" the orifice) and (2) the intensity when gas flow is shut off. Since there is real agreement at $\theta = 90.0^{\circ}$ and normalization forces agreement at $\theta = 0.0^{\circ}$, any differences that occur are forced to appear spread over the intermediate angles. The probability density function, first used by Walbeck[52] and later by Adams[2] and Wang,[54] allows differences at $\theta = 0.0^{\circ}$ to appear.

The probability density function, $\underline{P(\theta)}$, is defined as the fraction of effusing molecules which flow per stearadian at $\underline{\theta}$. Then the experimental probability density function is

$$P(\theta) = I_{\theta}^{+} \Big/ \int_{0}^{\pi/2} I_{\theta}^{+}\, 2\pi \sin\theta d\theta \qquad (18)$$

where $\underline{I_{\theta}}^{+}$ is the experimental positive ion current at θ.

Normalizing $\underline{I_{\theta}}^{+}$ to 1.0 at $\theta = 0.0^{\circ}$ yields

$$P(\theta) = I(\theta) \Big/ \int_{0}^{\pi/2} I(\theta)\, 2\pi \sin\theta d\theta \qquad (19)$$

where $\underline{I(\theta)}$ is the normalized intensity at $\underline{\theta}$; hence, at $\theta = 0.0^{\circ}$

$$P(0) = 1.0 \Big/ \int_{0}^{\pi/2} I(\theta) 2\pi \sin\theta d\theta. \qquad (20)$$

Then, from equations (19) and (20) we may write

$$P(\theta) = I(\theta)\ P(0) \tag{21}$$

and $\underline{P(\theta)}$ differs from $\underline{I(\theta)}$ by the constant $\underline{P(0)}$. However, $\underline{P(0)}$ is not a fixed constant among runs, so $\underline{P(0)}$ is not self-normalizing and can show differences among runs at $\theta = 0^{o}$. Any corrections that make the entire range of $\underline{I(\theta)}$ equal among runs will do the same for $\underline{P(0)}$ since identical $\underline{I(\theta)}$ curves yeild equal $\underline{P(0)}$.

Returning to the definition of $\underline{P(\theta)}$ and substituting the theoretical values from Chapter II and Appendix C, one has the theoretical expression for $\underline{P}(\theta)$:

$$P^{t}(\theta) = \frac{Q_n \cos\theta}{\pi\ r_o^{\ 2}\ W}. \tag{22}$$

Since $\underline{r_o}^{2}$ is 1.0 by definition, we have

$$P^{t}(\theta) = \frac{Q_n \cos\theta}{\pi\ W} \tag{23}$$

and for $\theta = 0$

$$P^{t}(0) = \frac{Q_1 \cos(0)}{\pi\ W} = \frac{Q_1}{\pi\ W} \tag{24}$$

Combination of equations 23 and 24 yields

$$P^{t}(\theta) = P^{t}(0)\ \frac{Qn \cos\theta}{Q_1} = P^{t}(0)\ (Qn \cos\theta)_{normalized} \tag{25}$$

where P(0) is not constant from orifice to orifice.

An additional useful piece of information can be obtained by rearranging equation 24:

$$W = \frac{Q_1}{\pi\ P(0)} \tag{26}$$

$\underline{P}(\underline{0})$ experimental can be used in equation 26 to indicate in one number the overall direction and size of the differences in the experimental and theoretical distributions.

Fortran program was written to plot for each run the differences between the theoretical and experimental angular intensity distributions as a means of seeing the differences more clearly. The probability density function, $\underline{P}(\underline{\theta})$, was also calculated for both the theoretical and experimental curves and the differences $\underline{\Delta P(\theta)} = P_\theta^x - P_\theta^t$ calculated and plotted. An example of the computer output difference plots is shown in Figure 24. Plots of $\underline{\Delta P(\theta)}$ for all the experimental runs are shown in Figures 25 through 36. Figure 37 shows $\underline{\Delta P(\theta)}$ for Adams' conical orifice and Figures 38, 39, and 40 are for Wang's cylindrical orifices.

Probable Sources of Differences Between Theory and Experiment

The differences between the theoretical and the experimental values of $\underline{I(\theta)}$ and $\underline{P(\theta)}$ indicate that several different processes or phenomena may be occuring. The most obvious possiblilities are surface diffusion, specular reflection, viscous flow (pressure effect due to being in the transition flow region between free molecular and viscous flow), angular velocity selection and a geometry effect. There are many factors to be considered both for and against each or any

20.32056 HRS 06/11/69

BASE(THEO,EMP) RUN 100- 0- 0- 0
COMP(EMP,EXP) RUN 131- 0- 0- 0-13164

T =	25.650	Q1 =	1.65572	TEMP,K =	300.00
L/R =	4.0100	DIMOD =	0.0	P,MM HG =	0.00690
T* =	44.390	W =	0.87396	P,MUBAR =	9.199
		WMOD =	0.0		
MFP,CM =	0.9305	MASS =	43.013	DIAMOL,A =	3.3000
DOD,IN =	0.03550	OLD,IN =	0.10370	LEN,IN =	0.07100
DOD,CM =	0.09017	OLD,CM =	0.26340	LEN,CM =	0.18034
K,DD =	10.319	K,OL =	3.533	K,LN =	5.160

NITROUS OXIDE

A	I(A)/I(0)	P(A)	P(A)TH	DEL P	DEL I
0.	1.0000	0.615529	0.603037	0.012492	0.0
5.	0.9960	0.613067	0.600742	0.012324	-0.000160
10.	0.9800	0.603218	0.593875	0.009343	-0.004770
15.	0.9520	0.585983	0.582489	0.003494	-0.013920
20.	0.9120	0.561362	0.566669	-0.005307	-0.027660
25.	0.8580	0.528124	0.546537	-0.018413	-0.048270
30.	0.7870	0.484421	0.475308	0.009113	-0.001190
35.	0.6520	0.401325	0.363493	0.037832	0.049230
40.	0.4550	0.280066	0.248065	0.032000	0.043640
45.	0.2770	0.170501	0.162796	0.007706	0.007040
50.	0.2050	0.126183	0.124015	0.002169	-0.000650
55.	0.1500	0.092329	0.095045	-0.002715	-0.007610
60.	0.1060	0.065246	0.072165	-0.006919	-0.013670
65.	0.0720	0.044318	0.053682	-0.009364	-0.017020
70.	0.0480	0.029545	0.038504	-0.008959	-0.015850
75.	0.0280	0.017235	0.025870	-0.008635	-0.014900
80.	0.0130	0.008002	0.015450	-0.007448	-0.012620
85.	0.0040	0.002462	0.006899	-0.004437	-0.007440
90.	0.0	0.0	0.0	0.0	0.0

WEXP = 0.8562256

DELP = P(A) - P(A)TH, P(A)TH = Q*COS(A) / PI*4.
DELI = I(A)/I(0) - Q(A)*COS(A) / Q(0).

T = 25.650 EL = 4.010 T* = 44.390 06/11/69

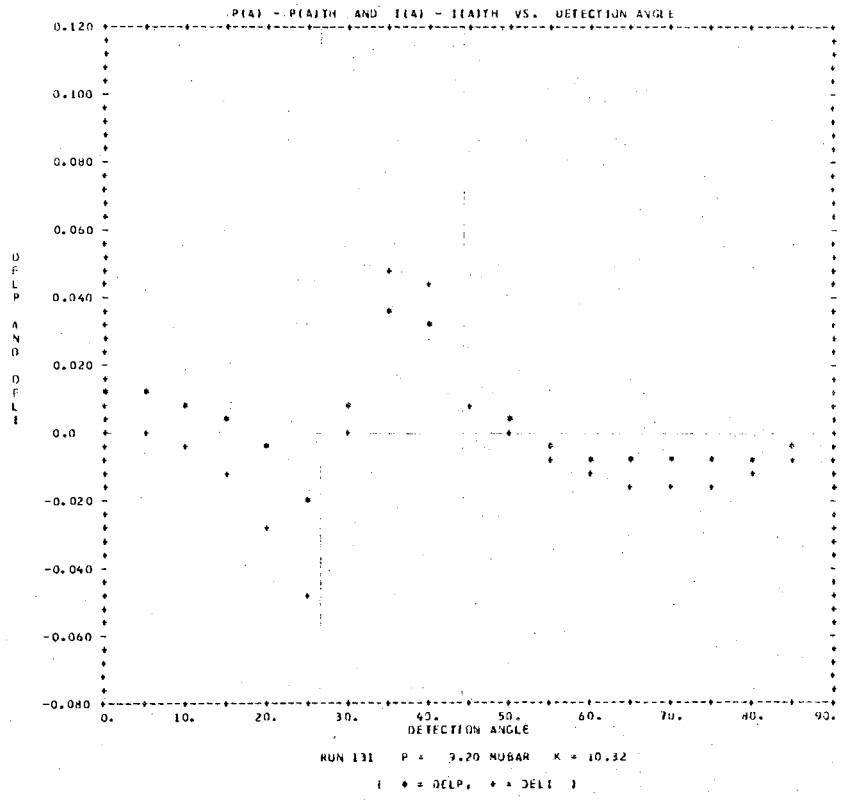

Figure 24. Example of Plotting Program Output

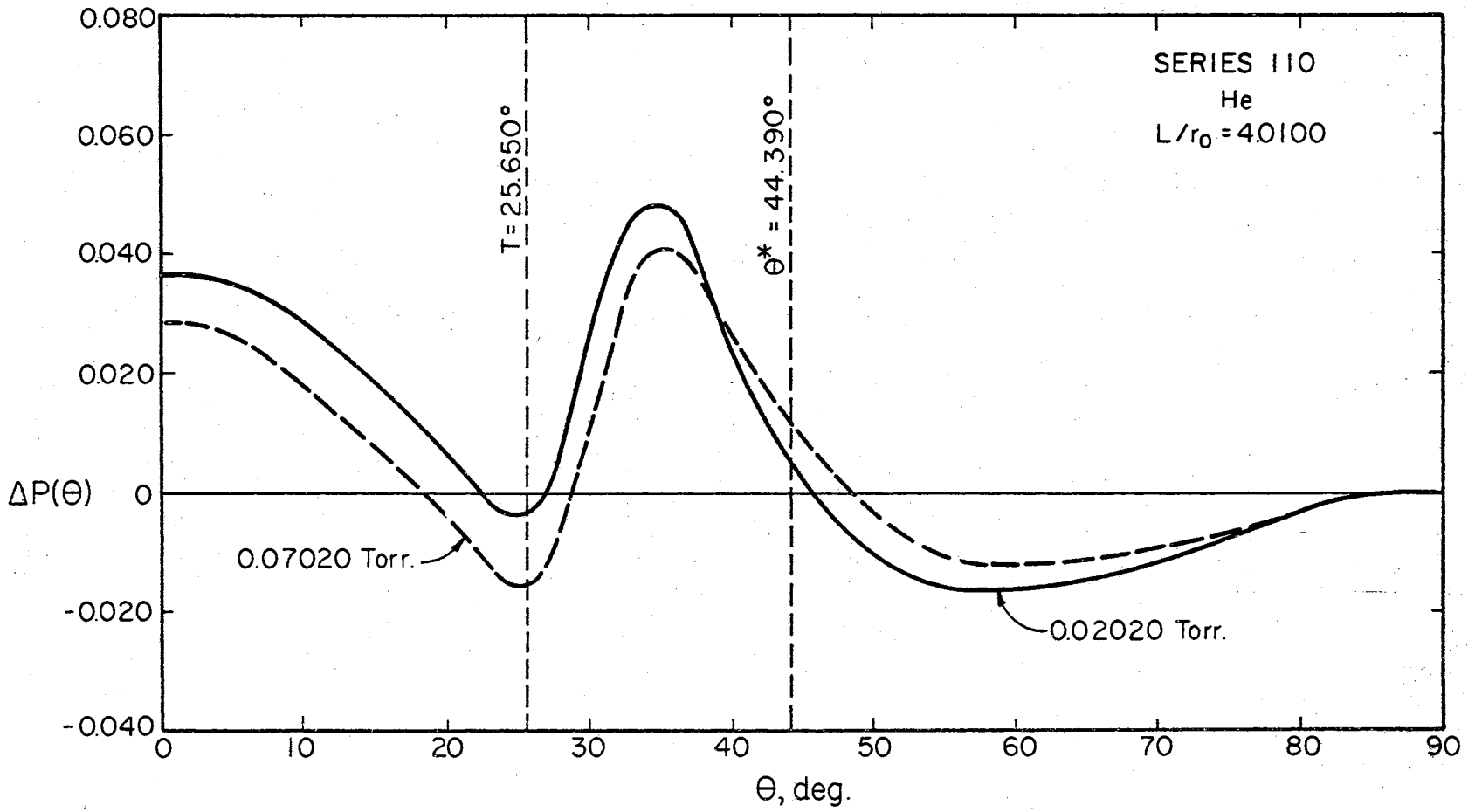

Figure 25. $\Delta P(\theta)$ for Orifice 1 with He

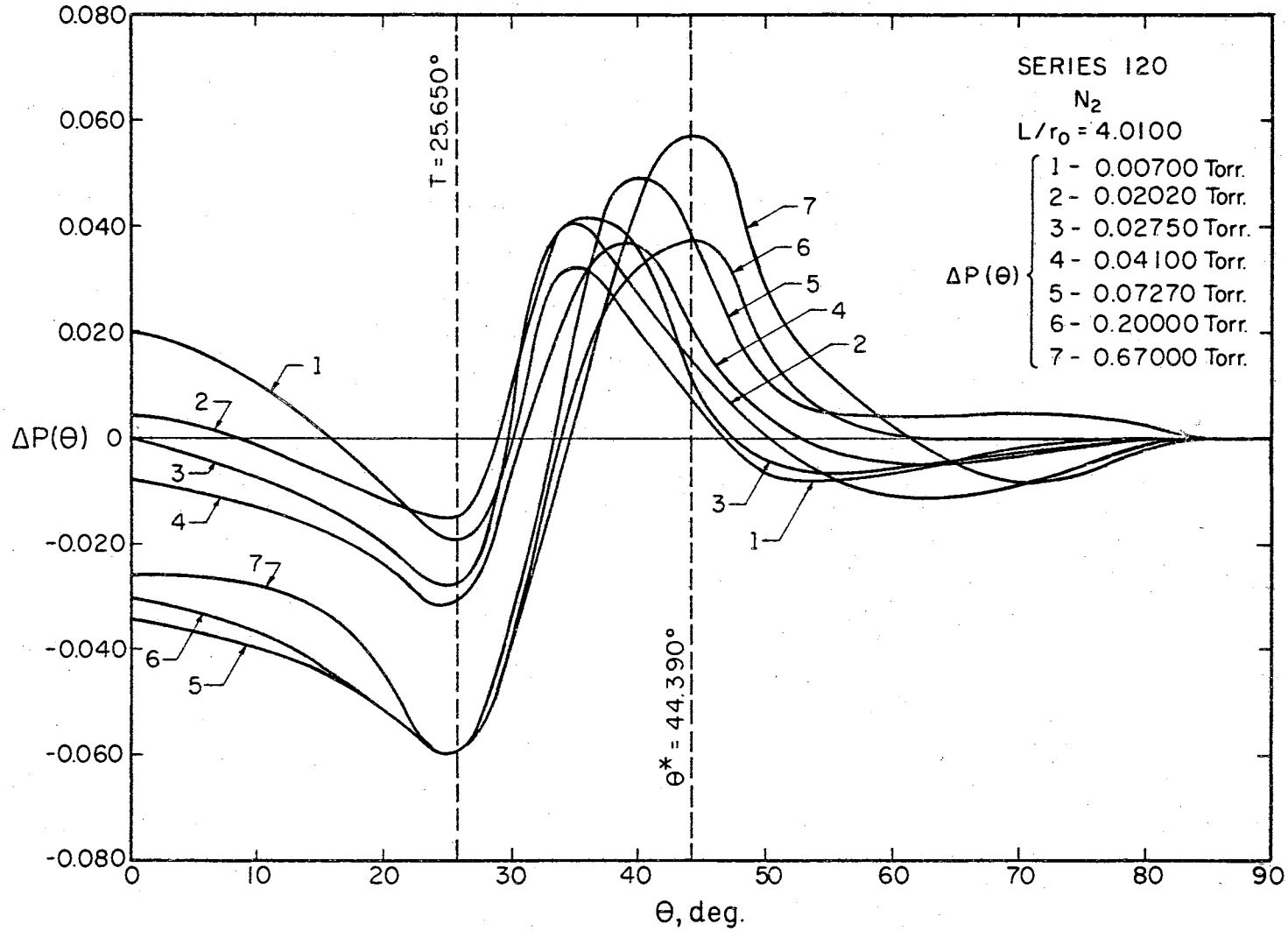

Figure 26. $\Delta P(\Theta)$ for Orifice 1 with N_2

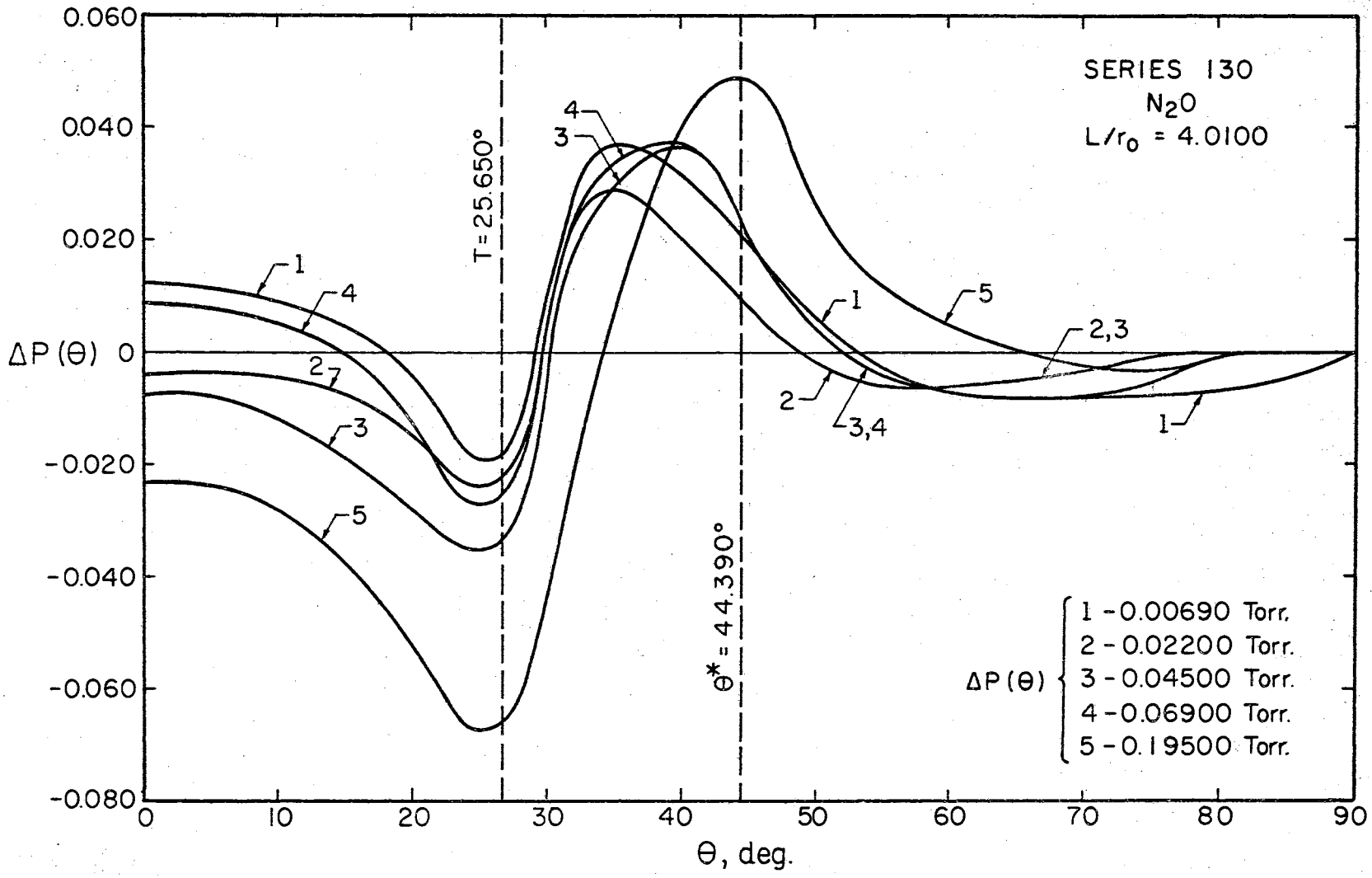

Figure 27. $\Delta P(\theta)$ for Orifice 1 with N_2O

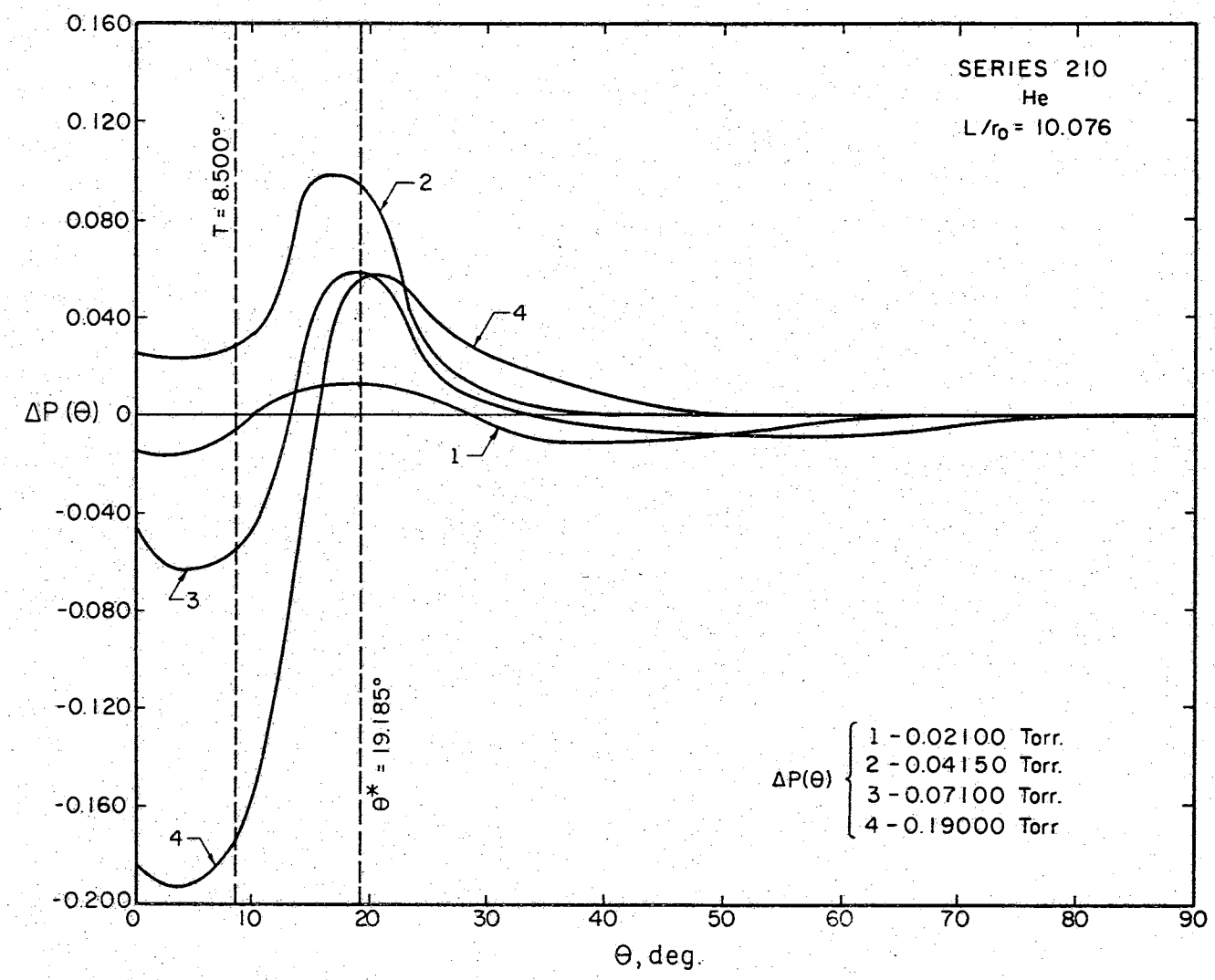

Figure 28. $\Delta P(\theta)$ for Orifice 2 with He

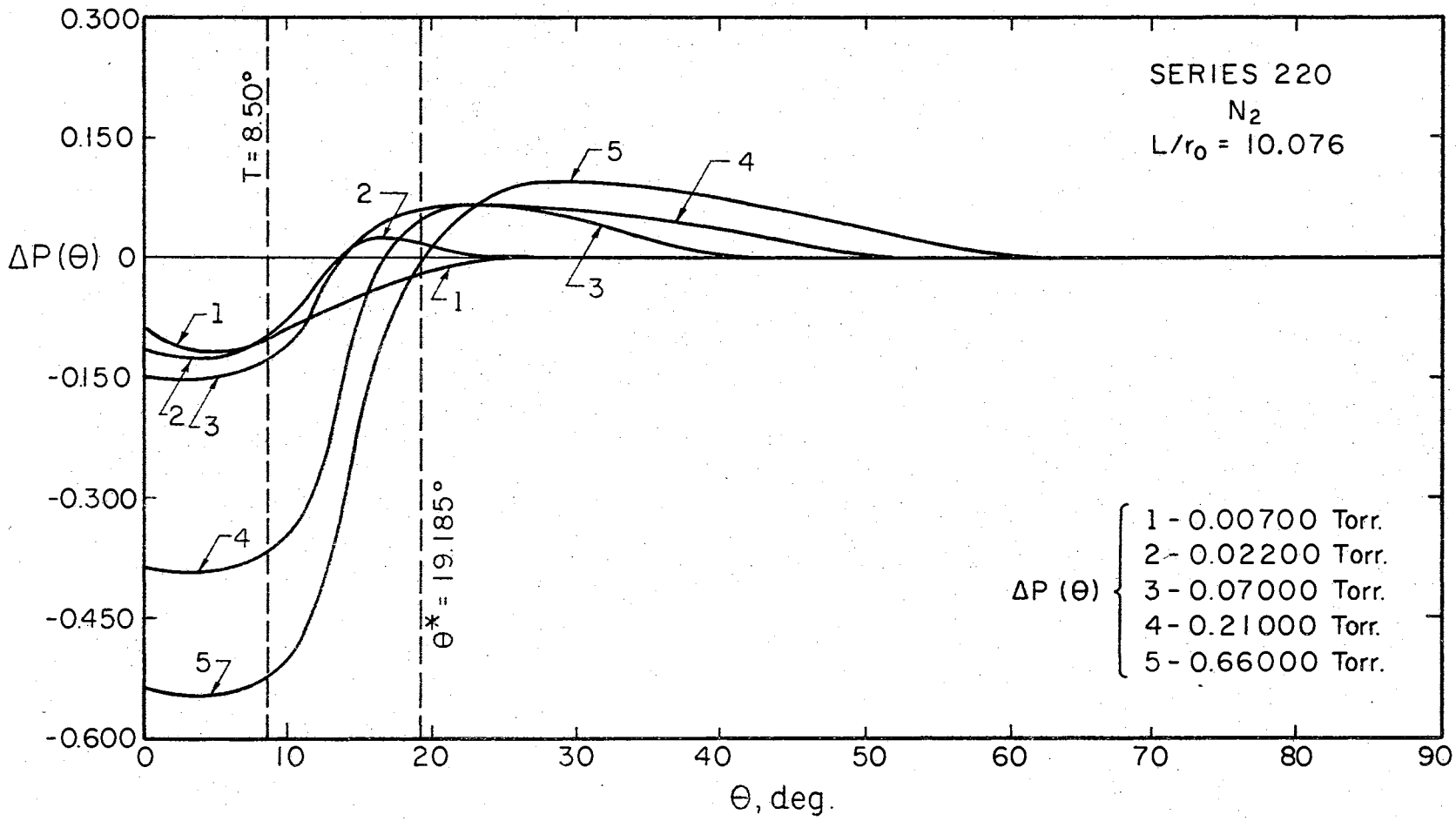

Figure 29. $\Delta P(\theta)$ for Orifice 2 with N_2

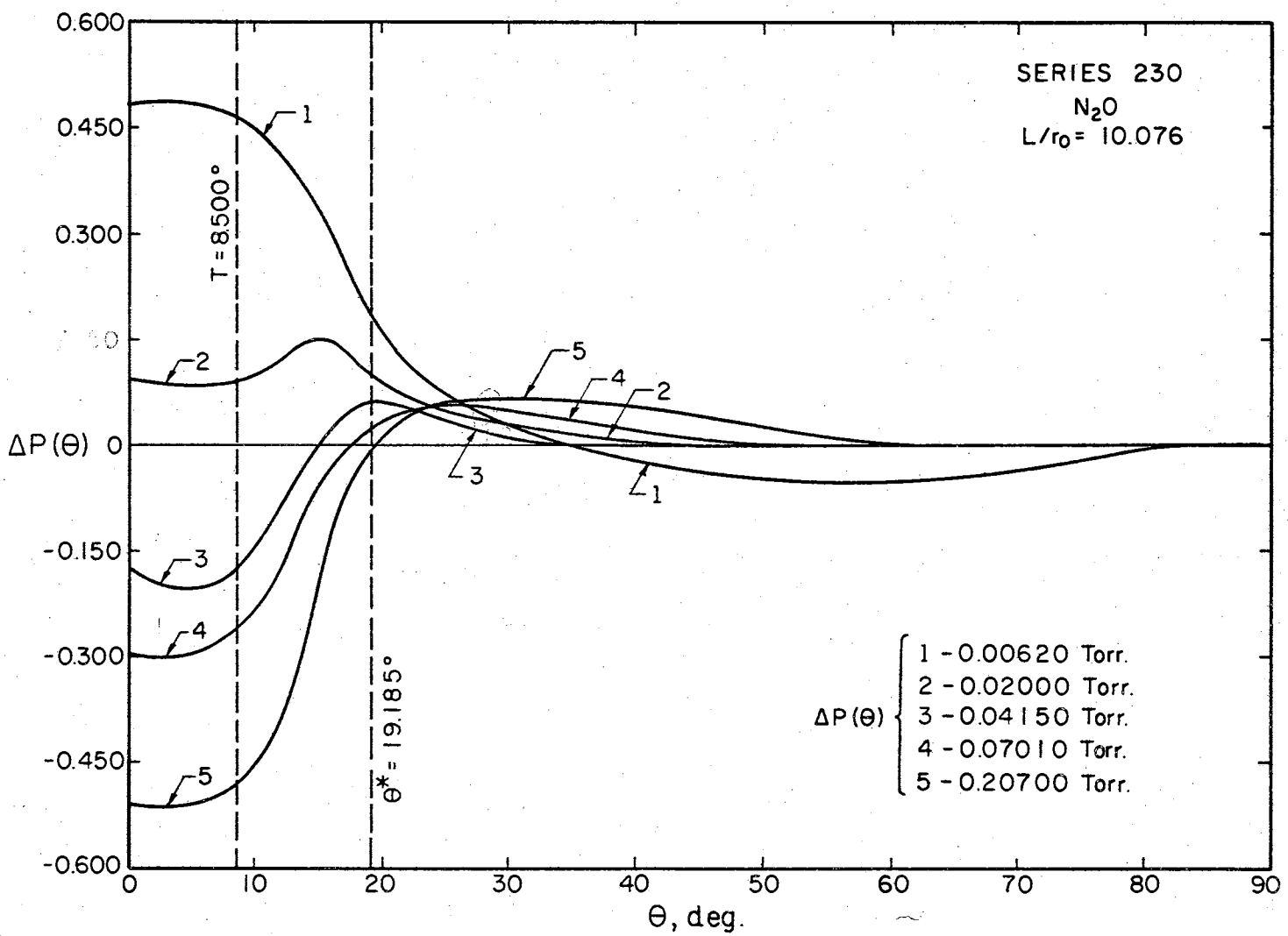

Figure 30. $\Delta P(\theta)$ for Orifice 2 with N_2O

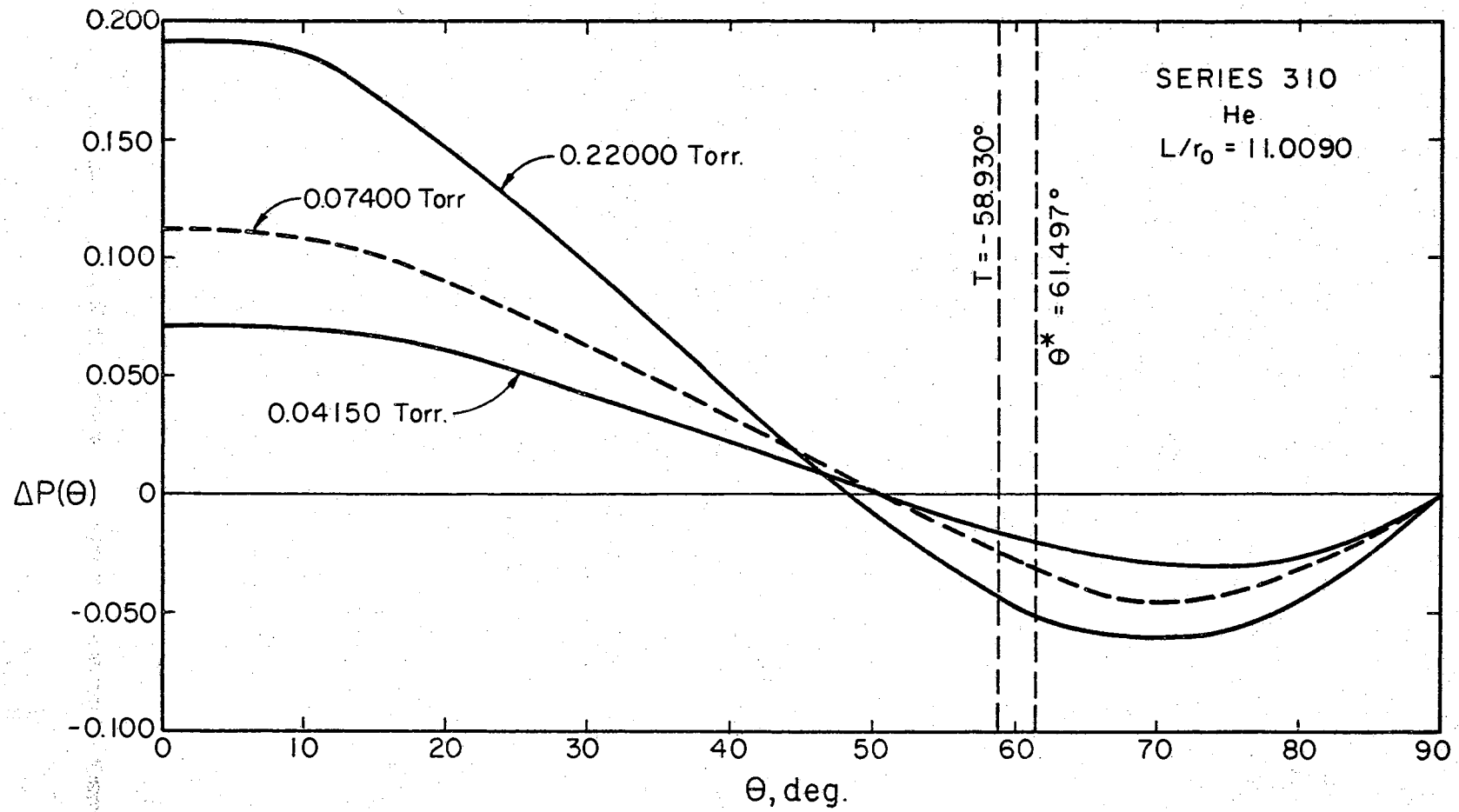

Figure 31. $\Delta P(\theta)$ for Orifice 3 with He

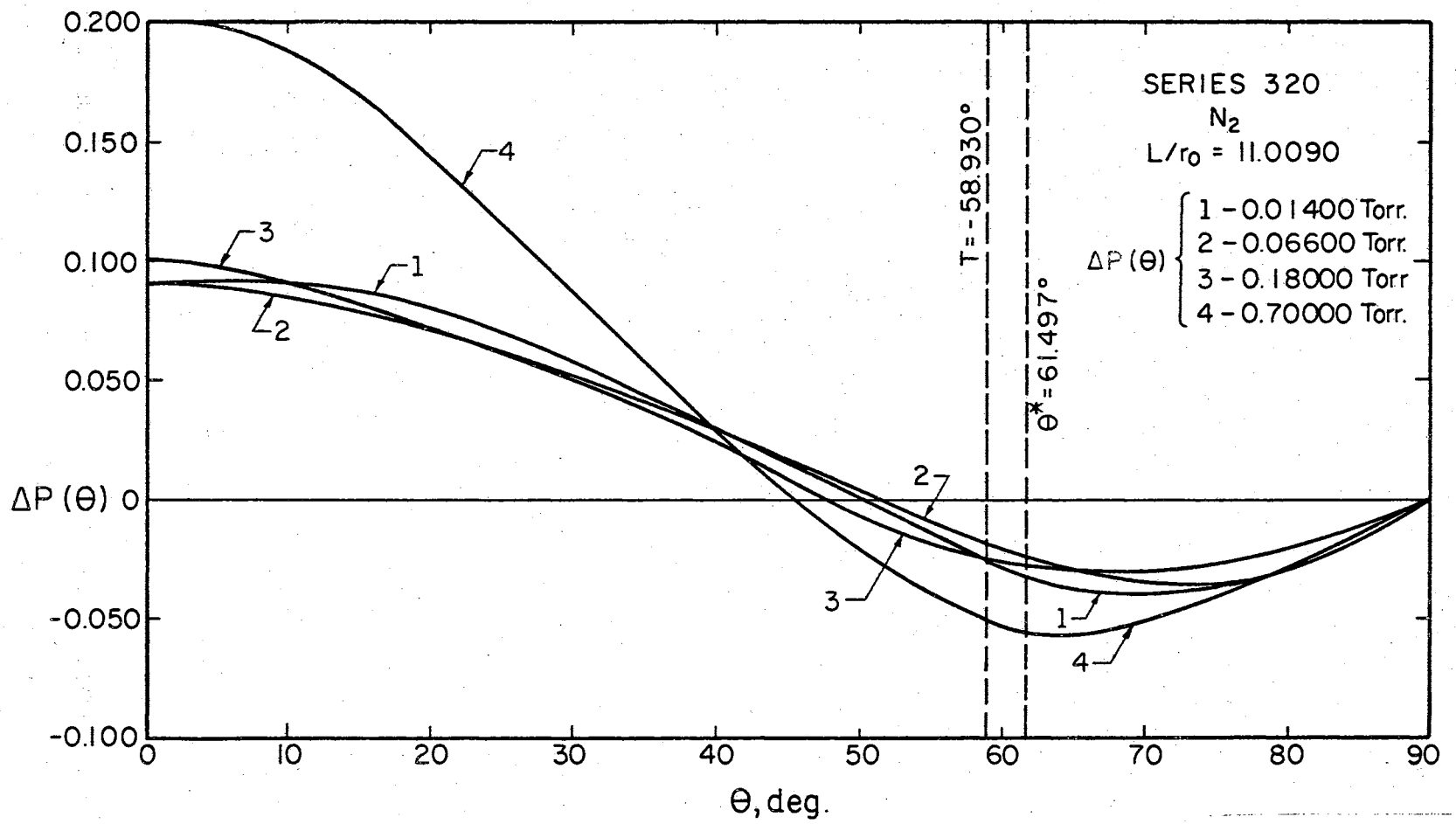

Figure 32. $\Delta P(\theta)$ for Orifice 3 with N_2

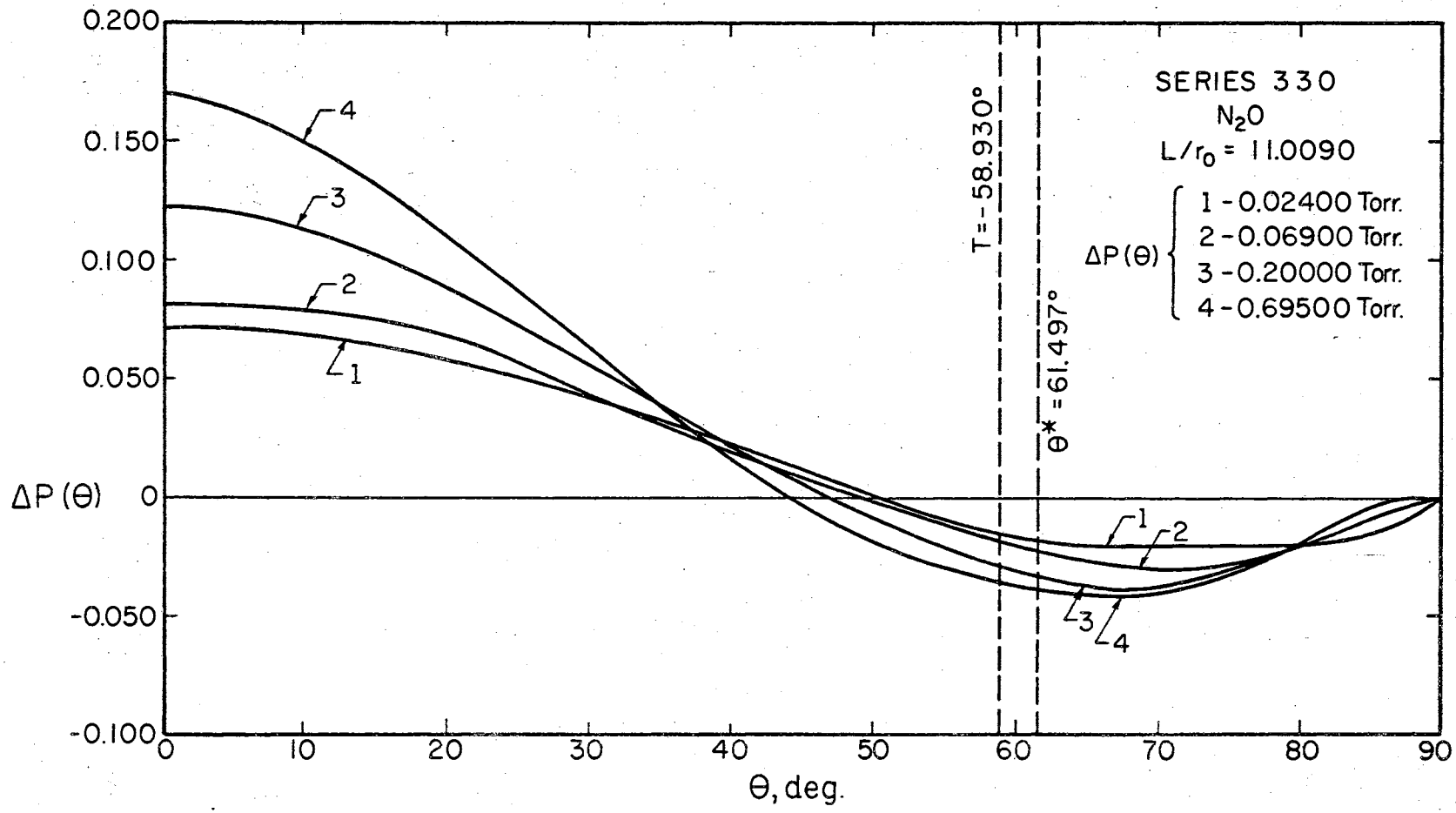

Figure 33. $\Delta P(\theta)$ for Orifice 3 with N_2O

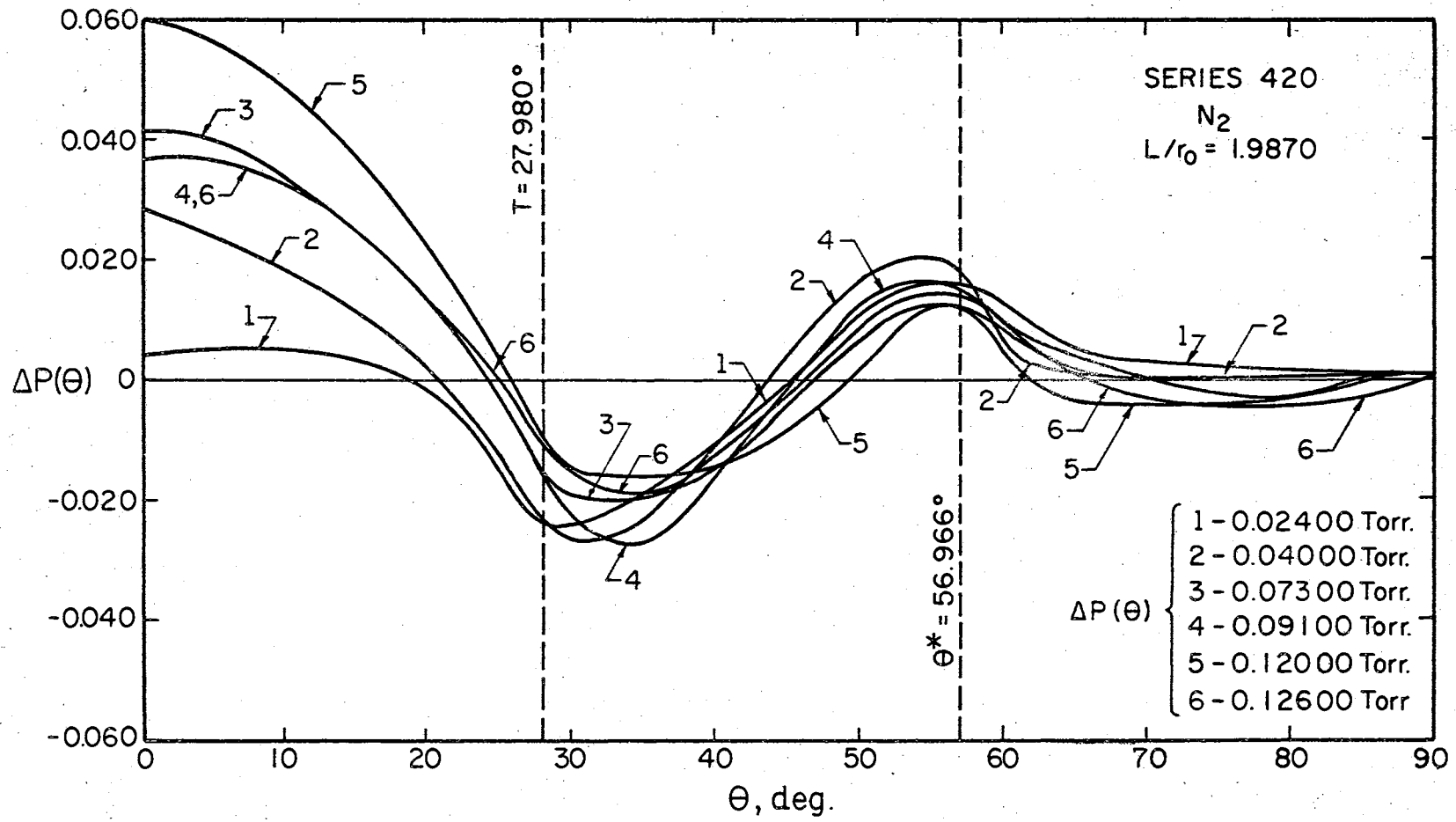

Figure 34. $\Delta P(\theta)$ for Orifice 4 with N_2

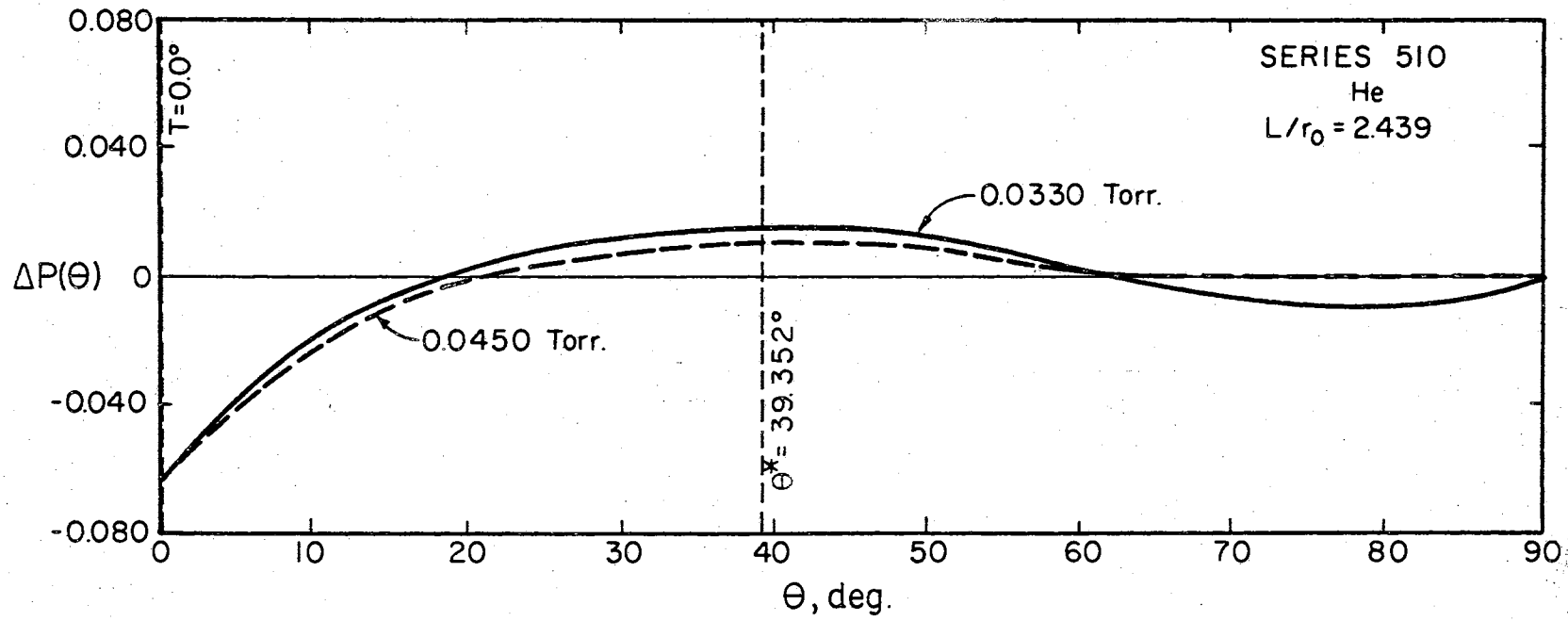

Figure 35. $\Delta P(\theta)$ for Orifice 4 with H_2

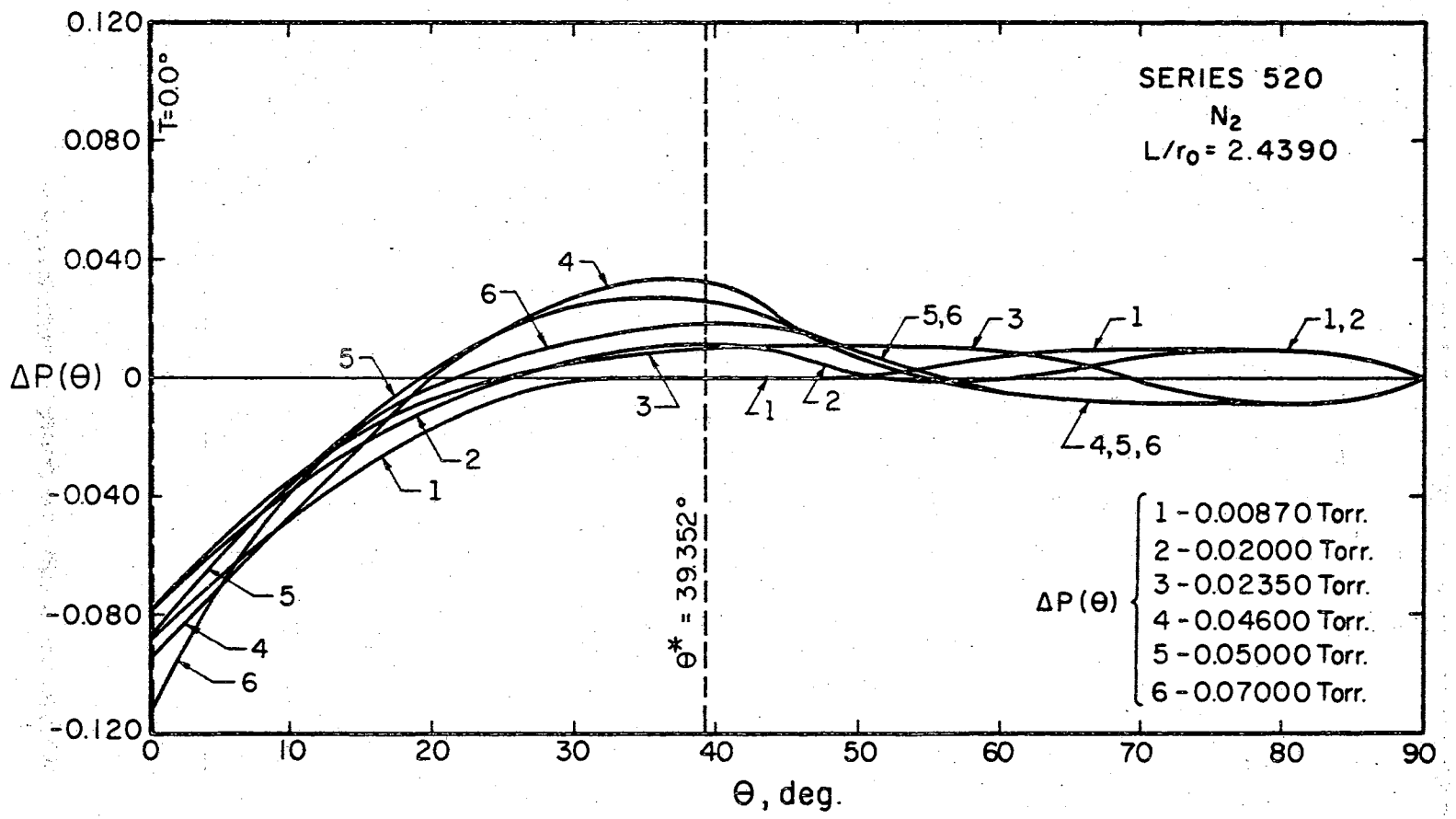

Figure 36. $\Delta P(\theta)$ for Orifice 5 with N_2

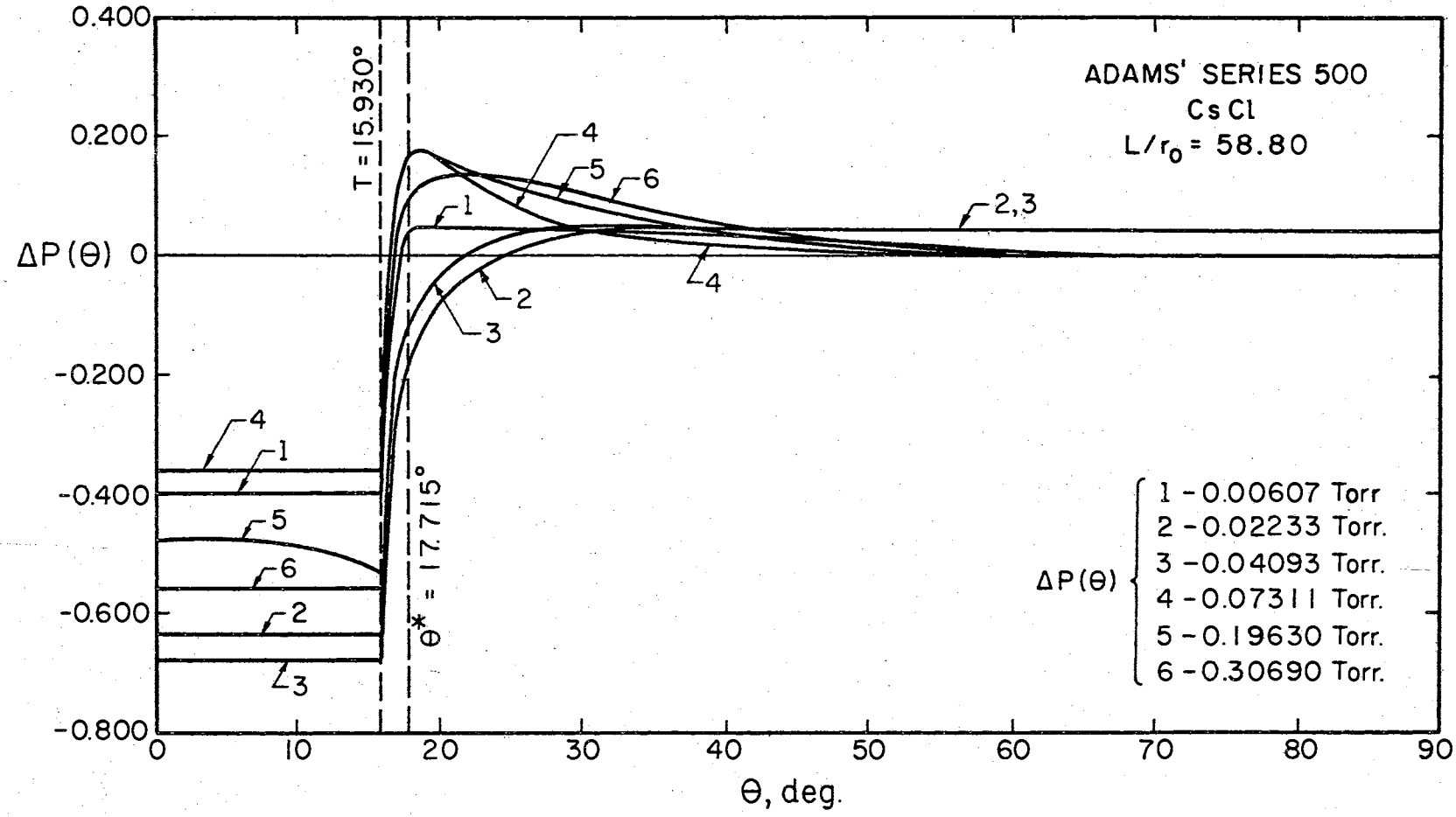

Figure 37. $\Delta P(\theta)$ for Adams' Conical Orifice with CsCl

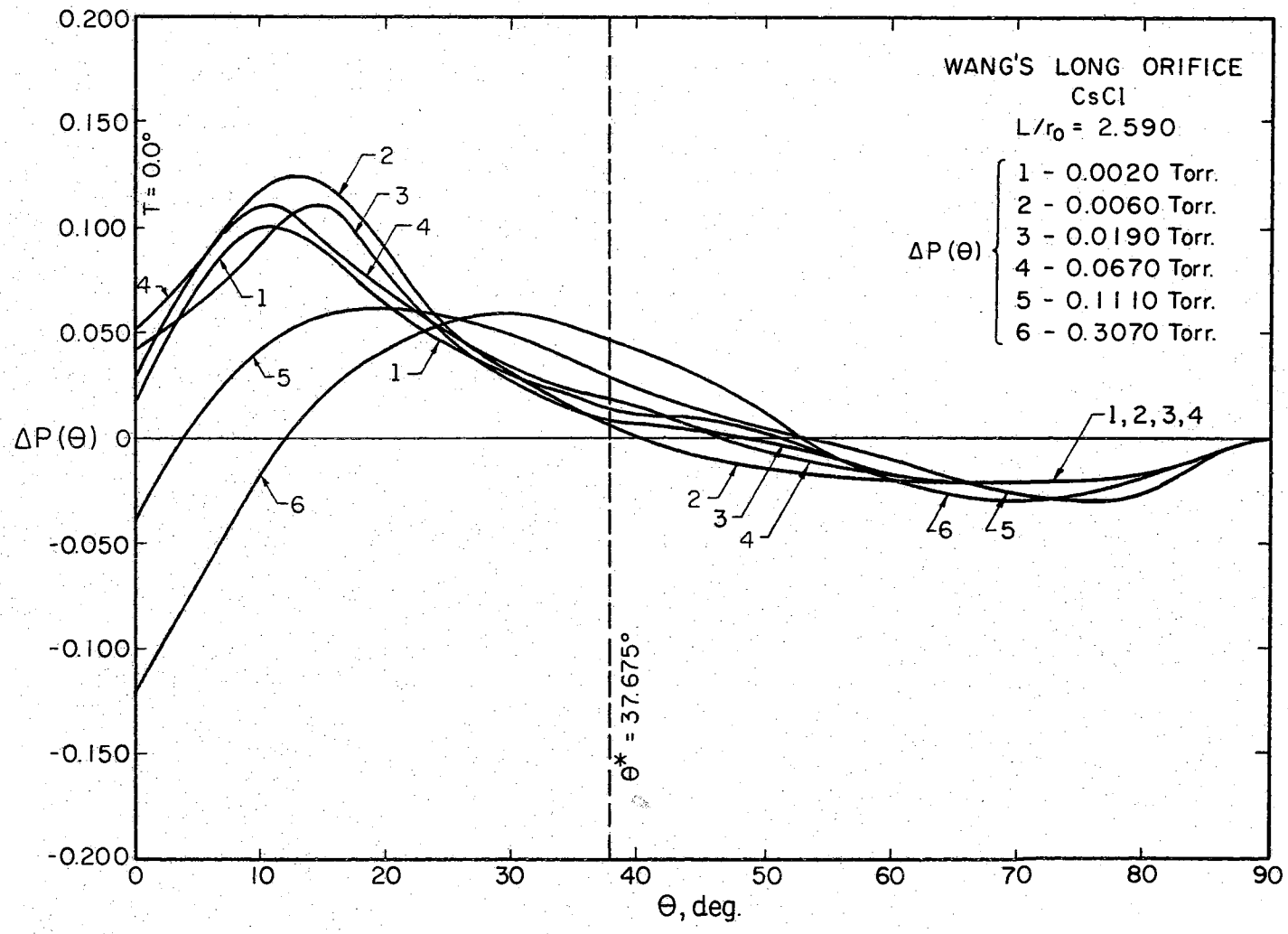

Figure 38. ΔP(Θ) for Wang's Long Orifice with CsCl

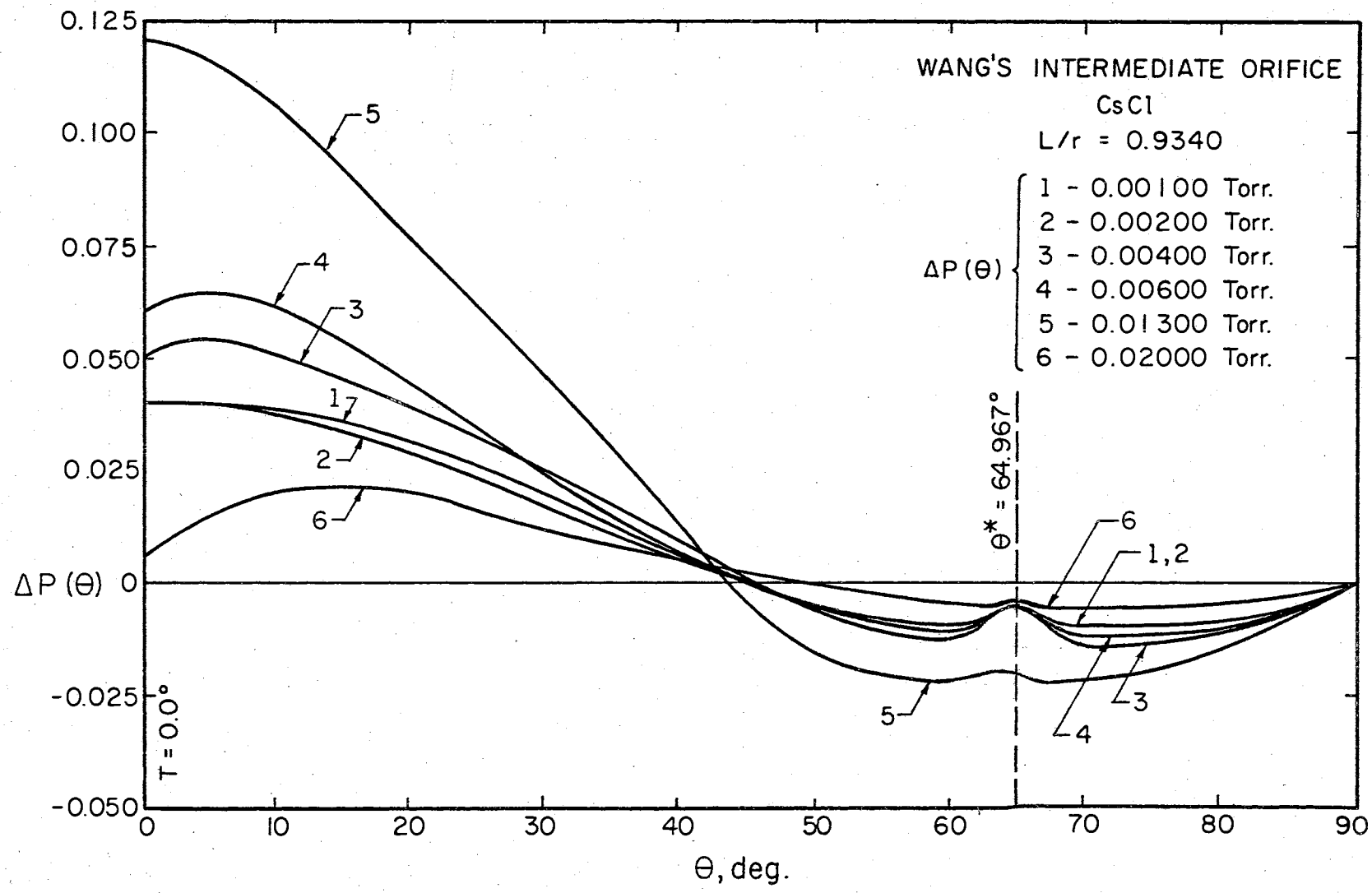

Figure 39. ΔP(θ) for Wang's Intermediate Orifice with CsCl

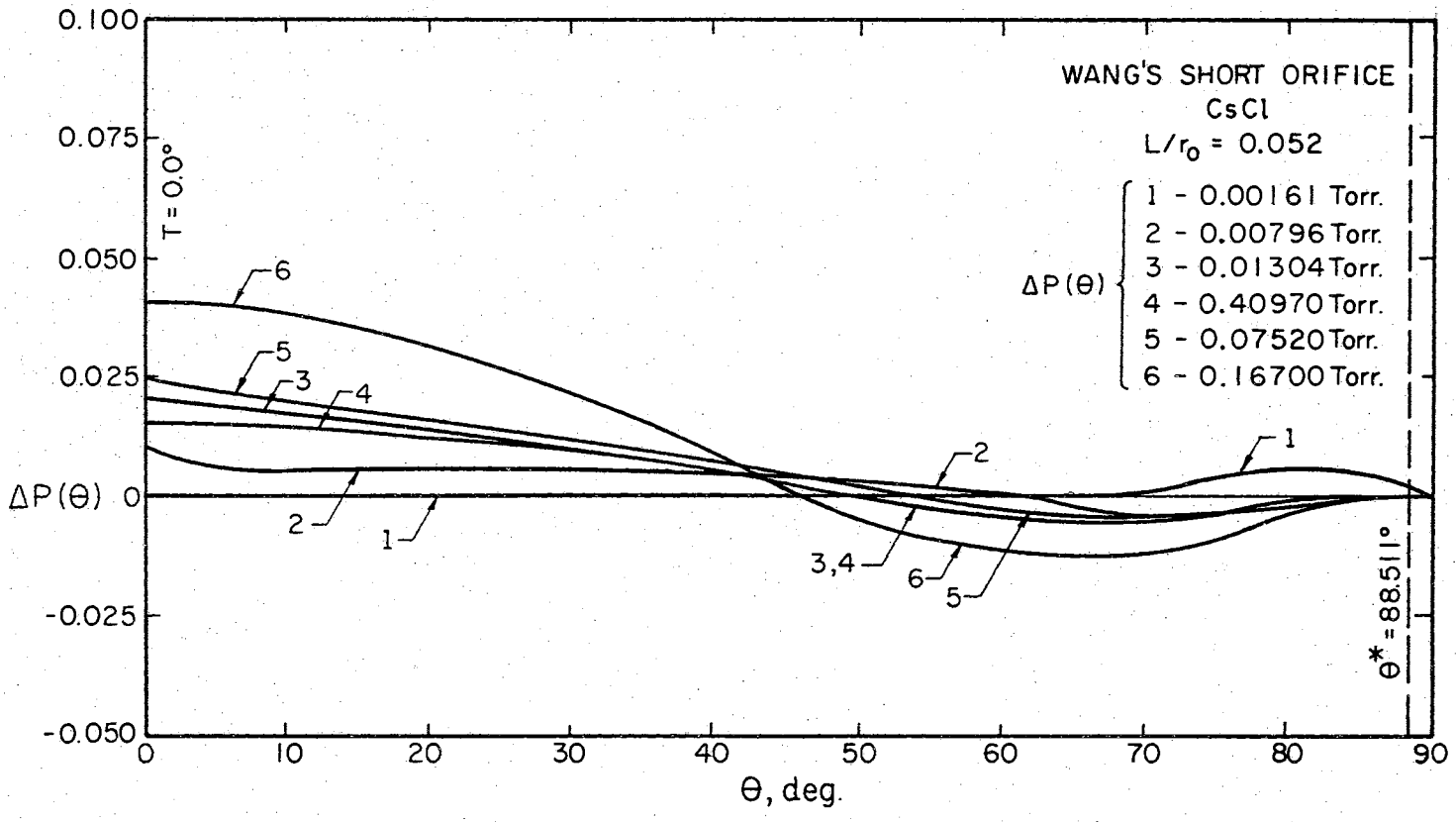

Figure 40. ΔP(θ) for Wang's Short Orifice with CsCl

combination of these effects being a source of the deviations.

Surface Diffusion

The theoretical description of surface diffusion occurring in a cylindrical orifice of a Knudsen cell was first described by Winterbottom and Hirth,[65] Ruth and Hirth,[42] and Ruth, Winterbottom and Hirth[43] and then extended by Winterbottom.[63,64] Dunham and Hirth[14] have extended the treatment to the general conical orifice.

Calculations made by the above authors show that for a given set of vapor-solid surface diffusion parameters, surface diffusion becomes relatively more important

(1) at lower pressures,

(2) in orifices with smaller L/r_o values,

(3) and in orifices with the larger values of T.

Therefore, surface diffusion has the greatest relative effect in the most nearly ideal system - a very thin, or knife-edged, orifice with very low pressure gas effusing.

Ward[61] has simulated surface diffusion in a Knudsen cell with a cylindrical orifice using a Monte Carlo technique. His results agree with those cited above.

The general result of surface diffusion is to force the angular distribution for a cylindrical or diverging orifice toward a more nearly cosine law distribution. When surface diffusion occurs there is an increased concentration of molecules on the walls of the orifice, especially near the entrance of the orifice. This concentration increase makes the wall contribution to the angular distribution relatively more important than it is when surface diffusion does not

occur. The angles of effusion in range 3 ($\underline{\theta}^*$ to 90.0°) can receive molecules only from the walls; range 2 angles ($\underline{T}$ to $\underline{\theta}^*$) are supplied with molecules from the walls in increasing numbers as $\underline{\theta}^*$ is approached. At $\underline{\theta}^*$ the number contribution from the walls to the angular distribution is greatest. Then, when surface diffusion makes the wall contribution more important, the effect will be most noticible in region of $\underline{\theta}^*$ and will increase the relative intensity in this region causing the distribution to be distorted toward the cosine law distribution. At present, applying theory rigorously to an actual experiment is seldom possible as the required data (surface diffusivity, vibrational frequency, desorption energy and root-mean-square diffusion distance) for a given vapor-solid system are usually not available.

The increased wall concentration resulting from surface diffusion would help explain the deviations in the vicinity of $\underline{\theta}^*$ in the data presented here. If surface diffusion occurs, there are (1) molecules which migrate along the surface from the inside of the cell into the orifice itself, (2) molecules which strike the wall, stick and move along the orifice wall before being remitted, and (3) molecules which travel over the outer edge of the orifice onto the face of the orifice plate. These molecules change the wall density to increase the relative numbers emitted in vicinity of $\underline{\theta}^*$ making the angular distribution less geometry dependent for cylindrical and diverging orifices.

Maxima in the region between T and just past $\underline{\theta}^*$ are seen readily in the $\underline{\Delta P}(\theta)$ plots for orifices 1, 2, 4 and 5, for Adam's conical orifice and for Wang's 3 cylindrical orifices. The large differences in Wang's orifices are not centered around $\underline{\theta}^*$ but more nearly around 15°. It is felt these maxima at 15° are due to some process other

than surface diffusion. Note that in Wang's intermediate orifice there is a second maximum in the difference curves at $\underline{\theta}^*$.

However, surface diffusion should not affect the normalized angular distribution in the region between 0° and $\underline{T}$ as the cosine law is applicable in this region for a diverging orifice even with surface diffusion. The data show a marked deviation from the theoretical curve in this region. More importantly, there should be deviations at very large angles due to molecules that slide over the lip of the orifice onto the flat plate and are emitted from the orifice face rather than from the interior. The hemicylinder can be rotated past 90° in both positive and negative directions and in all runs the value of intensity drops to the base zero line at 90° and past. There are four runs in the 53 total that do show peculiar behavior at angles just prior to 90°. These are 323, 324, 333 and 334, the high pressure N_2 and N_2O runs on orifice number 3 (Figures 81, 82, 85 and 86). It does not occur in the lower pressure runs on these gases nor in any of the helium runs. If the effect is surface diffusion it should have the greatest relative effect at the lowest pressure. This is not the case for the experimental data given here. Significant surface diffusion at room temperature for helium, nitrogen, or nitrous oxide on aluminum is very unlikely; however, since the hemicylinder and, hence, the orifice are not baked out prior to a run, it is possible that an oil film is present on the orifice and acts as a trapping medium, simulating surface diffusion to some extent.

In summary, if surface diffusion occurs we should expect and do find:

(1) The effect to be most noticeable at lower pressures; none of

the discrepancies between theory and experiment found in these data increase with decreasing pressure,

(2) The deviation at $\underline{\theta}^*$ to be relatively greater for <u>shorter</u> orifices; comparing deviations at $\underline{\theta}^*$ for orifices 1 and 4, we find that the difference at $\underline{\theta}^*$ is relatively greater for the <u>longer</u> orifice

(3) The differences at $\underline{\theta}^*$ to be in a positive direction, raising the experimental intensity curve; this is consistantly found to be the case in our data.

(4) The effect to be greater for orifices with large angles; there are not enough data on different orifices to comment on this.

(5) The effect to be most noticible in systems where the gas used is readily adsorbed onto the solid used; significant adsorption of He, N_2, or N_2O on aluminum seems unlikely, however, an oil film could be present on the orifice to act as the trapping medium.

(6) No effect on the normalized intensities in the region 0° to $\underline{T}$; there is a major deviation in this region in our data.

(7) An increase in intensity in the region of $\theta = 80\text{-}90^o$ that is significantly greater than Edwards and Freeman predict; four of 53 runs show such a deviation and surface diffusion is not an acceptable explanation in these cases.

Therefore, we cannot conclude that surface diffusion does not occur in this experimental system. However, we may and do conclude that the major trends in the data are opposite to those predicted by the surface diffusion model and that surface diffusion makes minor to

insignificant contribution to the effusive flux.

Specular Reflection

The phenomenon of specular reflection has been studied by a great many investigators.[25,40,44,50] Experiments have been made with a variety of gases on many different surfaces. Specular reflection, or at least directed reflection rather than diffuse (cosine law) scattering, is observed to some extent only when the solid surface is very clean and smooth - such as the surface exhibited by crystals cleaved in vacuum, by metal films at high temperatures or by single metal crystals grown in vacuum.

The reflection angle of the beam is more nearly equal to the angle of incidence when there is a large temperature difference between the beam and solid. At a constant solid temperature the reflected beam moves closer to the specular angle as the beam temperature is increased. For a given beam temperature, lowering the surface temperature results in a greater number of particles diffusely scattering but the angle of maximum intensity usually moves toward the specular angle. This increase in diffuse scattering at lower solid temperatures is thought to be due to adsorption of gases on the surface, resulting in a surface that is no longer clean and smooth. Specular reflection from a metal surface has a low temperature limit in the vicinity of 200°C. As the metal temperature is lowered to this region specular reflection disappears entirely. The phenomenon is reversible and as the temperature of the solid is increased again specular reflection begins to occur. The only reported case in which this effect has not been observed was in an ultrahigh vacuum system

(10^{-10}-10^{-9}Torr) where the background gas particles are so few that contamination of the surface with adsorbed particles would be very slow.[47]

The specularly reflected molecules have also been found to be the higher energy molecules in the beam. Specular reflection occurs more readily in beams striking at small incident angles.[44] There has been much work done on the theoretical treatment of specular reflection; however, no quantitatively correct method has been reported.

Specular reflection occurring to any marked extent would account for the deviations in vicinity of $\underline{T}$ in the experimental data reported here. That is, specular reflection occurs more readily at small incident angles, so a molecule hitting the wall at about 15° incident angle would be reflected at about $15\text{-}25^{\circ}$ from the wall. For an orifice with $T = 25^{\circ}$ the particle would then escape at $\theta = 0 - 10^{\circ}$. This same molecule, if diffusely scattered, could escape into any incremental solid angle between $\theta = 0$ to at least $\theta = T$. Therefore, if specular reflection occurs, it tends to remove molecules from the entire angular distribution, but particularly from the region between $\theta = 0^{\circ}$ and $\theta = T^{\circ}$ and to add all these particles to the region around 0°. For a diverging orifice the effect would be to decrease the intensity at $\underline{T}$ relative to the intensity at 0°. One would expect the cylindrical orifice also to show a relative decrease at $\underline{T}$ (0.0° in this case) with these molecules being reflected to increase the intensity at larger angles up to the region of $\underline{\theta}^{*}$. This effect should show up more readily in longer orifices since a larger proportion of the effusing molecules have an opportunity to strike the wall and, hence, have occasion to be specularly reflected. The data in this study and Wang's data do show

such deviations. However, for the two very similar orifices (Orifice 5, L/r = 2.439 and Wang's Long Orifice, L/r = 2.59) the positions of the maximum deviations are very different. Wang's data show maxima generally around 15°; the maxima for Orifice 5 are around $35\text{-}40^{o}$ (θ^{*} = 39.352). Wang's deviations may be partially due to an effect of system geometry and those of orifice 5 might be better explained by surface diffusion or pressure effects.

The converging orifice should also show a relative decrease at $\underline{T}$ and an increase in the region of $\underline{\theta}^{*}$ and larger angles. The data for this orifice do not show such a deviation, though $\underline{T}$ and $\underline{\theta}^{*}$ are so nearly equal it might not show up readily.

However, specular reflection requires a smooth, very clean surface, is most often observed for large temperature differences between the beam and the solid and has not been reported for metal solids at room temperature with background pressures less than 10^{-9} torr. The aluminum orifices used in this study were used "as machined" and at room temperature with the effusing gas at room temperature. Specular reflection has not been reported for conditions even mildly similar.

Pressure Effects

The molecular flow region is that range of pressure in which collisions among molecules are negligible compared to collisions between molecules and the system. The transition region covers the range where collisions between molecules must be considered, but they are still relatively small in number compared to the number in the region of viscous flow. In the region of viscous flow collisions between molecules are so numerous that the fluid is treated a

continuum rather than as a collection of individual molecules. In this region the flow pattern through a tube is streamline with the highest velocity along the axis and with velocity decreasing in a parabolic manner to a "zero velocity" boundary layer at the interface of the fluid and solid. The axial velocity gradually increases with increasing pressure up to a second transition region between viscous and turbulent flow.

There is obviously a pressure effect in the data reported here. The deviations are more pronounced as pressure increases, i.e., mean free path decreases and progress is made toward the viscous flow region of pressure and away from the molecular flow region.

The higher axial velocity in viscous flow might account for the relative increase at 0° over that at $\underline{T}$ for the diverging and converging orifices. It might also be an adequate explanation for the relative increase in intensity at angles close to 0° for the cylindrical orifice reported here and for Wang's cylindrical orifice. In all the orifices the normalized intensities between 0° and $\underline{T}$ for diverging, and between 0° and $\sim 50^{\circ}$ for the cylindrical and converging orifices, decrease more rapidly than the cosine law. In the cylindrical and converging orifices the intensity also decreases less rapidly than the geometry dependent molecular flow treatment predicts.

If molecules collide often with each other in the orifice, the effect is that of having a shorter orifice. Collisions among molecules tend to destroy the effect of orifice geometry, yielding a more nearly cosine distribution of paths in the orifice interior than can occur if there are no intermolecular collisions. If a number of intermolecular collisions interrupt the flight path of a molecule before it leaves

the orifice, the geometry dependent trajectory is not present to be measured, but has been replaced by a random one. This removes the effect of a particular wall collison from the final angular distribution, just as if the orifice were shorter and the wall collision had not occurred. The shorter the orifice the more nearly the angular distribution should approach the cosine law distribution. This reasoning could account for the deviation occurring in the vicinity of $\underline{\theta}^*$, which increases with pressure toward the cosine distribution.

In summary, transition region effects:

(1) Should increase with increasing cell pressure; the differences between theory and experiment at both $\underline{T}$ and $\underline{\theta}^*$ in the runs reported here become greater with increasing pressure,

(2) Should change the angular distribution for cylindrical and diverging orifices from the theoretical shape given by the Edwards-Freeman treatment to a distribution more nearly cosine in shape between $\underline{T}$ and 90°; this effect is observed in these data in the region of $\underline{\theta}^*$,

(3) Might tend to increase the intensity at 0° relative to $\underline{T}$ for both converging and diverging orifices; the intensity at 0° is increased relative to $\underline{T}$ for these data,

(4) Might tend to increase the intensities near 0° over the theoretical values for a cylindrical orifice; the near 0° intensities are larger than predicted,

(5) Should be greater at a given pressure for larger molecules since the mean free path becomes smaller as the effective diameter increases; in general, N_2O shows greater deviations than N_2 and N_2 shows greater deviations than He,

(6) Should become unimportant in the low pressure runs; the deviations are smaller at low pressures but do not disappear.

A pressure or mean free path effect does account for many of the effects we observe. However, it alone does not account for the deviations at $\underline{\theta}^*$ and at $\underline{T}$ at low pressures nor does it explain the angular shift toward $\underline{\theta}^*$ in the deviations of this region.

Velocity Distribution Distortion

The frequency (170 Hz) of the chopper used in these experiments is such that velocity selection of the beam by the chopper does not occur. However, Wang has found that molecules effusing at small angles from the orifice axis tend to have somewhat higher average velocities than those effusing at larger angles. The longer orifices and higher pressures increase this angular dependence of velocity. If the velocity difference is great enough then an effect of this angular selection is also a possible explanation for the relative increase in intensity at 0° over $\underline{T}^o$.

However, the differences in average velocities reported by Wang were very small and were found in a system operating at high temperatures with a small but real temperature difference between the orifice and gas - a system in which specular reflection might possibly be occurring for the high speed molecules. The runs reported here are all at room temperature so there is little or no thermal accommodation problem. Specular reflection is an unlikely explanation for an angular velocity selection in these runs.

The effect of longer orifice increasing the angular dependence of velocity is not shown in these data. Orifices 1 and 4 have very

similar orifice angles but different L/r values. The longer orifice, 1, has the smaller intensity differences at T relative to 0°. This can be seen readily by comparing the differences at T between the experimental and theoretical curves in Figures 12, 13 and 14 with Figure 21.

In summary, the angular velocity distributions reported by Wang show unexpected results that are pertinent to a possible explanation of the differences from theory found in our experimental data.

(1) The average velocity of the molecules effusing at angles close to 0° is greater than that of those effusing at large angles and this angular velocity dependence increases with orifice length and pressure. Our data show too great a relative intensity at 0° compared with that at T for both converging and diverging orifices. The cylindrical orifice shows relative intensities greater than theoretical over both small and large angles. All orifices show increasing differences with increasing pressure.

(2) The angular dependence of velocity in Wang's data has been interpreted as being a product of specular reflection. Specular reflection is highly unlikely in our experimental system.

Geometry Effects

Ward[58,62] has shown that at very low pressures the geometry of the cell and source material can greatly affect the shape of the angular distribution. His experiments were made at pressures so low that the source cell itself was in the molecular flow region. He found that the orifice acted much like a pinhole camera, reflecting

geometry of the sample and cell interior.

The deviations in the data presented here are functions of the orifice geometry rather than of the source cell geometry. It is possible that the maxima in the data for Wang's orifices are at least partially dependent on source cell geometry. The angle from the orifice to the edge of the baffle plate in his front oven is 10 to 15°.[20,54] In our system the only discontinuity "seen" by the detector looking through the orifice is the edge of the simulated Knudsen cell. The detector can "see" this discontinuity only at $\theta \cong 25^{o}$.[16,20] Orifices 1 and 4 have orifice angles, $\underline{T}$, in this region so any source effect would be difficult to separate from an orifice effect. However, the data from orifices 2, 3 and 5 show no maxima or mimima in the region of $\theta = 25^{o}$. In all the data the deviations occur only in the regions around $\underline{T}$ and $\underline{\theta}^{*}$-orifice, not source cell, parameters. In addition, the runs are made at pressures higher than those in which Ward observed these effects. The cell is never in the molecular flow region of pressure. The source cell pressure also is one reason to reject source geometry as an explanation of Wang's 15° maxima, although in his lower pressure runs the pressure inside the cell is approaching the molecular flow region.

Geometry effects in the rest of the system along the beam path are also very unlikely. The orifice face is flush with the face of the hemicylinder so there is no edge to scatter molecules effusing at large angles back into a trajectory toward the detector. The plate containing the first collimating orifice (Figure 4) is smooth and the edge drops toward the vacuum chamber wall leaving no rim to deflect molecules back into the beam path.

The diameter of the valve opening just past the first collimating orifice is large compared to the diameter of the collimated beam. (Figure 4) Scattered molecules from the walls of the main vacuum chamber that pass through the first collimating orifice are the main source of particles striking the valve opening. The collimated molecular beam will not spread to such a large diameter in only a one-half inch path length.

The chopper vanes are the next obstructions to the beam. The particles scattered when the vanes are closed would have to rebound from the first collimating orifice face at very nearly 90° to the face in order to enter the beam path and be measured. Any such effect would be directly proportional to the beam intensity.

The next six inches of the beam path are unobstructed. The beam then passes through the second collimating orifice into the beam ionizer. The detector chamber is at such low pressure (10^{-7} torr) that possible effects of beam ionizer geometry are not expected to be observable.

In summary, any geometry effect of the system should show up at a constant angle in all the distributions, and should be independent of orifice parameters.

No evidence for such effects has been observed in the data.

Combination of Effects

The major deviation, that at $\underline{\theta}^{*}$, can be partially explained by surface diffusion or pressure effects or both - surface diffusion being more important at low pressures and decreased mean free path more important at high pressures. The other difference, that at $\underline{T}$, can be

explained by specular reflection, angular velocity selection or viscous flow effects. However, in this system if surface diffusion occurs, it is probably due to an oil film, in which case specular reflection is very unlikely. Therefore it appears most probable that the differences are due to mean free path pressure effects and/or surface diffusion effects coupled with a velocity distribution distortion effect which is not due to specular reflection but is perhaps due to viscous flow effects.

Development of Expressions for the Deviations

The basic theoretical treatment of Freeman and Edwards had been written in Fortran. This program has been modified to allow arbitrary functions to be added to the calculation of many of the expressions - such as $\underline{Q}_1, \underline{Q}_2, \underline{Q}_3$ and $\underline{\psi(x)}$ - to approximate the effects of surface diffusion, specular reflection, angular velocity distribution distortion, and pressure.

Three correction functions were developed. One function simulates surface diffusion by changing the wall density as a function of total orifice length, distance along the axis and pressure (Appendix B). A second function simulates specular reflection and/or angular velocity selection by increasing the intensity at 0° relative to that at $\underline{T}$. The third function was introduced to simulate a transition region pressure effect.

No correction for cell and source geometry was attempted as no such effect in the data could be seen. In addition the correction functions contain no terms dependent on the effusing gas itself. There are differences among the three gases used, but they are small compared

to the geometry-pressure dependent intensity differences.

Angular Velocity Selection Simulation

$$A_{corr} = A\left(1 + (1 - \frac{\theta}{T}) \frac{0.26}{(L/r_o \cdot L/r_L)}\right) \tag{27a}$$

$$A_{corr} = A\left(1 + (1 - \frac{\theta}{T}) \frac{0.24}{(L/r_o \cdot L/r_L)} (1 + 5P^{\frac{1}{4}})\right) \tag{27b}$$

where $A = Q_{1_{WALL}} \cos \theta$

The term $Q_{1_{WALL}} \cos \theta$ is the theoretical intensity at θ in the range $0 \leq \theta \leq T$ arising from molecules that proceed from a collison with the orifice wall directly to the detector. $Q_{1_{WALL}}$ does not include those molecules that travel straight through the orifice without encountering the wall. (See equations 13 and 16c, Chapter II.)

These functions, 27a and 27b, are used to simulate the $I(\theta)$ deviations in the region 0° to T for conical orifices. These deviations are thought to be the result of an angular velocity selection possibly due to specular reflection or to a transition region effect extending for some presently unaccountable reason to low pressures. The correction is applied only to molecules leaving the orifice wall. If the deviations are due to specular reflection, they must originate from molecules that do encounter the walls. If the deviations are caused by a transition pressure effect then this reasoning is not correct. Intermolecular collisions are important, not wall collisions. However, since both parts of Q_1 are directly proportional to $\cos \theta$ only the value of the constant term need be changed to use equation 27a or 27b for either or both parts of Q_1.

We find the experimental-theoretical difference, $\Delta P(\theta)$, or the

equivalent $\Delta I(\theta)$ decreases rapidly from its value at 0° to a minimum at T; the difference curve then abruptly increases at angles just past T. The term $(1 - \theta/T)$ serves to make the correction largest at $\theta = 0^{\circ}$ and to reduce the correction to zero at $\theta = T$.

The difference at T, $\Delta I(T)$, is much greater for short, large angle orifices than for the long narrow orifice. The term $1/((L/r_o) \cdot (L/r_L))$ reflects this effect of orifice angle and length making the correction larger for the short wide orifice and smaller for the long narrow orifice.

The $\Delta P(\theta)$ in the region of 0° to T also has an increasingly negative slope. Multiplying the correction term by A is equivalent to including a cos θ term in the correction. Its inclusion provides an increasingly negative slope rather than the constant slope of the linear term, $(1 - \theta/T)$.

The difference at T is pressure dependent. The term $(1 + 5P^{\frac{1}{4}})$ is included in equation 27b in an attempt to describe the observed pressure effect. $P^{\frac{1}{4}}$ describes the pressure effects reasonably well, but is too large at high pressures as will be shown later. One is added to the pressure term so that at very low pressure the entire correction term does not go to zero.

Surface Diffusion Approximation

$$\psi(x)_{corr} = \psi(x)\left[1 + 0.6\ (1 - \frac{x}{L})\right] \tag{28a}$$

$$\psi(x)_{corr} = \psi(x)\left[1 + (1 - \frac{x}{L})L \cdot P^{\frac{1}{2}}\right] \tag{28b}$$

This function changes the density along the wall from the theoretical value; the density on the wall is also changed relative to the total molecules going straight through. Thus, it can be considered either a pressure or a surface diffusion effect. These functions are used to correct the $I(\theta)$ deviations found in the region around θ^*. As discussed earlier these deviations may be caused by surface diffusion and/or a transition region pressure effect. This correction will affect all effusion angles containing molecules emitted from the walls. Its effect will be greatest at the angles just preceding and up to θ^* as this is where the wall molecules give the greatest contribution.

The term $(1 - x/L)$ serves to place the largest increase in wall density at the orifice entrance, i.e., at $x = 0$. It also reduces the density increase to zero at $x = L$. This is the general effect surface diffusion has on the wall density although it does not cause a linear density change from entrance to exit. If surface diffusion occurs, the density change has a negative slope increasing to zero at the orifice exit. Multiplying to the correction term by $\psi(x)$ yields this kind of slope change in the density along the wall. This is necessary to make the "tail" (θ^* to 90°) of the corrected intensity curve, $(Q_n \cos \theta)_{corr}$, have the same slope changes found in $I(\theta)$. $(Q_n \cos \theta)_{corr}$ does not drop rapidly enough between θ^* and 90° if only a constant multiplier, instead of $\psi(x)$, is used. The terms L and $P^{\frac{1}{2}}$ are included in equation 28b to describe the length and pressure effects observed. The difference increases with length and pressure. However, as shown later an exponent of one on L is not large enough for extremely long orifices. An exponent of one-half

on $\underline{P}$ is too large at high pressures. In addition, pressure should probably be included in the form $(1 + \underline{P}^c)$ so that at low pressures the correction does not go to zero.

Pressure Effect Modification

$$B_{corr} = B\left(1 + 3(0.07 + \tan^2 T \cdot P^{\frac{1}{4}})\right) \tag{29}$$

where $B = Q_{n_{ORIF}}$

and $\underline{Q}_{n_{ORIF}}$ includes only those molecules going from the source cell straight through the orifice without encountering a wall. This means only $\underline{Q}_1$ and $\underline{Q}_2$ are included in this correction term; all molecules considered in $\underline{Q}_3$ (range 3; $\theta^* \leq \theta \leq 90^o$) must strike a wall to get out of the orifice at these angles.

This function was included originally as a general pressure effect. Some function was necessary at higher pressures to describe the collimation from 0° to $\underline{\theta}^*$ found in the experimental data particularly for the converging orifice. Some of the general increase observed in the cylindrical orifice also needed to be described. Equation 29 accomplishes this purpose quite well. However upon examining what this function really does we find that it is coupled with the $\underline{\psi(x)}$ correction. The $\underline{\psi(x)}$ correction increases the wall density, this increased wall density in turn adds molecules to the parts of the angular distribution receiving molecules from the wall. The $\underline{B}$ correction adds molecules from the orifice entrance to the distribution. Since the final distribution is normalized, the $\underline{B}$ correction serves to reduce the relative number of wall source molecules from what $\underline{\psi(x)}_{corr}$ alone predicts. Considering $\underline{B}_{corr}$ and

$\underline{\psi(x)}_{corr}$ together means that the wall density predicted by the combination is smaller and of slightly different shape than $\underline{\psi(x)}_{corr}$ alone predicts.

The term $\tan^2 \underline{T}$ is included to reflect the effect of orifice angle, which is most important for the large angled, converging orifice and of little relative significance in the diverging orifices. The constant term assures its application to the cylindrical orifice. $\underline{P}^{\frac{1}{4}}$ includes a small but necessary pressure effect.

This function, while useful at the present level of fitting, should probably be replaced by extensions to equations 27b and 28b when additional data are available.

Comparison of Experimental Data with Modified Analysis

The experimental work cited in Chapter I is generally only of historical interest for the purpose of comparison in this thesis. The data are on cylindrical orifices - and often limited in the range of effusion angle covered.

None of the data measured with interferometric methods will be used as they are limited to 40-50° off-axis angle. This is only the first half of the angular distribution and so, does not allow one to tie down the distribution at 90° and make valid comparisons with theory or other experimental data.

From the data on cylindrical orifices that are taken over the entire range of effusion angle, the data of Wang[54] have been chosen for comparison. His data for three cylindrical orifices cover an extensive pressure range and reasonable range of $\underline{L/r}$. The data appear to have few inconsistencies reflecting careful experimental

work. They are quite recent and readily available from his thesis. In addition Dr. Wang could be consulted immediately when questions arose concerning his experiments.

Adams'[2] conical orifice data are the only other data on a diverging orifice, in the open literature, of which this writer is aware. There is some doubt as to the validity of this data as there are a number of unexplained discontinuities with source pressure through the runs. In addition there is a fairly significant and fluctuating background pressure effect appearing at 90°. However, as these concial orifice data constitute the only available data for comparison they will be used. Although for the reasons cited above his cylindrical orifice data will not be considered.

In the following discussion $\underline{\Delta M}$ will be used to designate the differences between the modified and unmodified theoretical values of intensity. $\underline{\Delta I}$ will refer to the differences between experimental and unmodified theoretical intensity values.

$$\Delta M = \Delta M(\theta) = (Q_n \cos \theta)_{corr} - (Q_n \cos \theta)_{theo.}$$

$$\Delta I = \Delta I(\theta) = I(\theta) - (Q_n \cos \theta)_{theo.}$$

$(\underline{Q}_n \cos \underline{\theta})_{theo}$ are the normalized theoretical intensity values predicted by the Edwards-Freeman method (Equation 16, Chapter II). $(\underline{Q}_n \cos \underline{\theta})_{corr}$ are the normalized intensity values when the suggested modifications have been made in the theoretical calculations. $\underline{I(\theta)}$ is the normalized <u>experimental</u> intensity. In both $\underline{\Delta M}$ and $\underline{\Delta I}$ the $(\underline{\theta})$ has been removed for simplicity.

If the modifications to the Edwards-Freeman theoretical treatment were exact, then $(\underline{Q}_n \cos \underline{\theta})_{corr}$ would equal $\underline{I(\theta)}$, and $\Delta\underline{M}$ and $\Delta\underline{I}$ would be equal. The differences, $\Delta\underline{M}$ and $\Delta\underline{I}$, will be discussed in terms of intensity units. The intensity at $\theta = 0^{o}$ is defined as 100 intensity units. A difference between $\Delta\underline{M}$ and $\Delta\underline{I}$ of 1 intensity unit or less is considered excellent agreement; a difference of 2 to 3 intensity units is considered good agreement; differences greater than 3 intensity units, unless these are less than 20% of $\Delta\underline{I}$, are considered to indicate poor agreement.

The modifications were added to the Fortran program used to make the Edwards-Freeman calculation. The program is now set up so that all combinations of the modifications can be used. This allows one to see just what the effect of each function is and what combination provides the best description of the experimental results.

The correction functions were developed using the data in this study and then tested on the data of Adams and Wang. The modified theoretical results agree reasonably well with the experimental data.

The Diverging Orifices

The shape of $\Delta\underline{M}$ is in excellent agreement with $\Delta\underline{I}$. The minimum found in $\Delta\underline{I}$ at $\underline{T}$ appears also in $\Delta\underline{M}$ at $\underline{T}$. The $\Delta\underline{I}$ maximum in the region of $\underline{\theta}^*$ is present in $\Delta\underline{M}$ near $\underline{\theta}^*$.

(1) Orifice 4, $L/r_o = 1.987$, $T = 27.98^{o}$

At low pressures equations 28a and 27a produce $\Delta\underline{M}$ values at $\underline{T}$ and $\underline{\theta}^*$ of -10 and 1 intensity units, respectively, as compared with $\Delta\underline{I}$ values of -6 and 3 intensity units. At high pressures equations 28a and 27b yield $\Delta\underline{M}$ values equal

to ΔI.

(2) Orifice 1, $L/r_o = 4.010$, $T = 25.65^o$

At low pressures using equations 28a and 27a results in ΔM values at both T and θ^* that are smaller than the ΔI values by 1 intensity unit. At high pressures ΔM at θ^* is 3 intensity units larger than the ΔI value of 10 intensity units. At T the minimum in ΔM is -4 and in ΔI is -6 intensity units. Equations 28a and 27b were used.

(3) Orifice 2, $L/r_o = 10.076$, $T = 8.50^o$

Equations 28b and 27a at low pressures result in ΔM values at T and θ^* differing from those of ΔI by less than half an intensity unit. This is less than experimental error. At high pressures equations 28a and 27b yeild ΔM values at T differing from the ΔI values by less than half an intensity unit. At θ^* the ΔM value is 26 intensity units. ΔI has values of 13, 35, and 44 intensity units for He, N_2 N_2O respectively.

(4) Adams' Conical Orifice, $L/r_o = 58.80$, $T = 15.93^o$

Equations 27b and 28b were best for both high and low pressures. At low pressures ΔM at T was from less than 0.2 to 3 intensity units smaller than ΔI. The spread is due to intensity variations among Adams' low pressure runs. ΔM at θ^* had a value of only 6 intensity units while ΔI is 20 intensity units. At high pressures the maximum at θ^* is just over 7 intensity units for ΔM but ΔI is 34 to 36 intensity units. ΔI at T is -4 to -5 intensity units while the modifications yeild a negative ΔM of less than half

an intensity unit.

The Converging Orifice

The only converging orifice used, Orifice 3, has $T = -58.93^{\circ}$ and $L/r_o = 0.571$ ($L/r_m = 11.009$). The experimental data from this orifice are best described using only equation 27b to modify the theoretical calculations. The $\Delta\underline{M}$ and $\Delta\underline{I}$ curves have the same general shape over the range $0\text{-}90^{\circ}$ for both high and low pressures. However at both pressure extremes the $\Delta\underline{M}$ minimum is only about 30% of the $\Delta\underline{I}$ minimum and the position of the minima are different. At low pressures the minima in $\Delta\underline{I}$ are at ~ 70, 65 and 60° for He, N_2 and N_2O respectively. These minima are about -15 intensity units. $\Delta\underline{M}$ has the minimum at 50° with a value of -5 intensity units. At high pressures the position of the minima shift in the $\Delta\underline{I}$ curves by 10° to 60, 55 and 50° with values of about -29 intensity units. The minimum in $\Delta\underline{M}$ is still at 50° with a value of -10 intensity units.

The $\underline{\psi(x)}$ correction never improves the $\Delta\underline{M}$ values as it adds a positive "spike" at $\underline{T}$. Including equation 29 drops the minimum of $\Delta\underline{M}$ to -30 intensity units at low pressures and -37 intensity units at high pressures. This intensity change covers the 60° to 90° range only so the shape of $\Delta\underline{M}$ and $\Delta\underline{I}$ are no longer similar.

The Cylindrical Orifices

(1) Orifice 5, $L/r = 2.439$

The best fit to the experimental data is obtained using equations 28a and 29 at low pressure and 28b and 29 at high pressure. The agreement between $\Delta\underline{M}$ and $\Delta\underline{I}$ is excellent;

the overall $\Delta \underline{I}$ curve shape is reproduced by $\Delta \underline{M}$ and the maximum difference between the two is 1.5 intensity units. At low pressures the $\Delta \underline{I}$ maximum is 7 intensity units; the $\Delta \underline{M}$ maximum is 8.5 intensity units. At high pressures the $\Delta \underline{I}$ maximum is 11 intensity units, that of $\Delta \underline{M}$ is 10 intensity units. The "tails" ($40^{\circ} \leq \theta < 90^{\circ}$) of the $\Delta \underline{I}$ and $\Delta \underline{M}$ curves are also quite similar.

(2) Wangs' Long Orifice, L/r = 2.59

At low pressure using equation 28a yields a maximum $\Delta \underline{M}$ of 12 intensity units at 25-30°. The low pressure $\Delta \underline{I}$ maximum is 12 intensity units but at θ = 15-20°. At high pressure $\Delta \underline{I}$ is 20 intensity units at 30°; $\Delta \underline{M}$ is 19 intensity units at 30°. The minima occurring around 65° in $\Delta \underline{I}$ are not present in $\Delta \underline{M}$. Equation 29 does not have enough effect to produce a minimum in this orifice, but reduces the maxima by 25%.

(3) Wangs' Intermediate Orifice, L/r = 0.934

This orifice is best simulated using only equation 29. The $\Delta \underline{I}$ curves show a small maximum of less than one half to 3 intensity units at 10°, a large minimum of -4 to -12 intensity units at ~55°, and a secondary maximum of about -5 intensity units at $\underline{\theta}^{*}$. The ranges above are from low to high pressure. $\Delta \underline{M}$ has only a minimum of -1 intensity unit at low pressure and -3 intensity units at high pressure, about 25% of the $\Delta \underline{I}$ values. Adding equation 28a inserts a maximum at $\underline{\theta}^{*}$ but it is so large that the most important feature of the curve, the minimum at 55°, disappears.

(4) Wangs' Short Orifice, L/r = 0.052

ΔI curve at low pressure has a minimum of -1 to -2 intensity units at 40°; the minimum shifts at high pressures to $60\text{-}70^{\circ}$ and 8 intensity units. Equation 29 produces a minimum in ΔM in the region $70\text{-}85^{\circ}$ of less than half an intensity unit. This is certainly not adequate. This orifice is so short that equations 28, $\psi(x)$ corrections, cannot materially affect the ΔM curve.

Summary of Modification Effects

(1) $\psi(x)$ corrections, equations 28a and 28b, are reasonably good at producing the maxima in diverging orifices. Improvement in $\psi(x)$ corrections for very long (Adams', $L/r_o = 58.8$) and very short (Wang's, $L/r = 0.052$) orifices are needed to simulate well either surface diffusion or a transition region pressure effect in these extreme orifices. A component dependent term should also be included.

(2) The A correction term is vital to the simulation of the experimental data for both diverging and converging orifices. The pressure effect is not adequate over the whole pressure range although the correction is reasonably good with pressure included. The pressure term must be improved to simulate the effect in an orifice as long as Adams conical orifice and perhaps even the length effect term, $(1/(L/r_o) \cdot (L/r_L))$, improved. If additional development of the equations is undertaken provision should also be made to apply the A corrections to the cylindrical orifice - perhaps from T to Θ^*.

(3) The B correction was not necessary or even useful in the conical orifices but was significantly useful for the cylindrical cases. B corrections were too small for Wang's short and intermediate

orifices, about right for orifice 5, and too large for the converging orifice and Wang's long orifice. B corrections should probably be dropped as a separate function and incorporated into $\psi(x)$ and A corrections.

(4) From the above it appears that Wang's orifices and Orifice 5 have different processes occurring inside. Possibly Orifice 5 has "surface diffusion" on an oil film occuring and Wang's orifices have some specular reflection occurring. All four orifices show pressure effects becoming more significant at higher pressures.

(5) The ΔI curves of Adams' conical orifice are not predicted well by the correction functions used. The shape is good but ΔM is far too small at θ^*. The effect of the extremely long orifice is probably not being accounted for well.

(6) The agreement in shape and in most cases the actual values of the ΔM and ΔI curves for the orifices of this study indicate that the experimental processes are being accounted for by the modifications suggested. However, this agreement does not mean the deviations are actually due to the effects mentioned earlier - mass transport in an orifice oil film, transition region pressure effects, and an unexplained angular velocity selection - simply that a simulation of such effects does reproduce the deviations found experimentally.

CHAPTER V

CONCLUSIONS AND RECOMMENDATIONS

The theoretical predictions of Edwards and Freeman are verified generally by the experimental data. The overall shape of the intensity curves and the position of the cusps due to the geometry of the orifice are as predicted. However, even at low pressures, small deviations from theory are found. These may be due to (1) the assumption of no surface diffusion being invalid, (2) an angular velocity selection, or (3) some transition region pressure effect. In the higher pressure runs assumption (1), (no gas phase molecular collisions), is obviously invalid since these runs are in the transition region of pressure.

The theoretical predictions can be modified by adding effects due to pressure, wall density changes and orifice angle to yield more nearly the experimental results.

Data on these same orifices at even lower pressures should help show more definitely the source of the differences between $\underline{P^t(\theta)}$ and $\underline{P^x(\theta)}$. If the difference at $\underline{T}$ for the diverging orifices disappears at lower pressure, then the difference is probably a transition region effect. If the differences at $\underline{T}$ remain, then another explanation, perhaps velocity distribution distortion due to specular reflection, must be considered. If the differences at $\underline{\theta^*}$ remain at lower pressures, then surface diffusion becomes a very probable source of some of this discrepency; if the difference disappears, then it must be

solely a pressure effect.

A study of the angular distribution of velocities for these orifices and these gases over the reported pressure range would immediately show if there is, in fact, a distortion of the velocity distributions under these conditions.

A particularly useful set of data would be the transmission coefficients for these orifices and gases. This would show whether the apparent decrease in intensity at T is really a decrease or whether it is actually an artifact of the normalization procedure and represents an increase in intensity at 0°. In addition, major differences among gases would show up as variations in W. W might be different for each of the gases due to effect of surface diffusion or W might not become constant at the same pressure for the three gases due to the different mean free paths. Experimental values for W would also do away with the assumptions in the $P(\theta)$ calculations, that the transmission coefficient is constant with pressure and equal for all gases. The measurement of W for the five orifices used in the experiments reported in this thesis will soon be undertaken in this laboratory under the direction of Dr. R. D. Freeman.

To complete the analysis of the range of validity of Edwards and Freeman's theory, angular distribution data are needed for several additional orifices, particularly for 2 or 3 additional converging orifices. The one converging orifice studied is not sufficient to define the source of the deviations and cannot show variation of the deviations with T.

SELECTED BIBLIOGRAPHY

1. Aberth, W., Rev. Sci. Inst. 34, 298 (1963).

2. Adams, J. Q., Ph.D. Thesis, University of Illinois (1961).

3. Adams, J. Q., T. E. Phipps and P. G. Wahlbeck, J. Chem. Phys. 49, 1609 (1968).

4. Balson, E. W., J. Phys. Chem. 65, 1151 (1961).

5. Batzer, T. H. and J. F. Ryan, :Flange Design Using Aluminum Foil Flanges for UHV Application," Engineering Note, ENA-129, University of California Lawrence Radiation Laboratory, Livermore, California (1963).

6. Clausing, P., Versl. Afd. Nat. Kon. Akad. Wed. Amst. (Report of Natural Science Section, Royal Academy of Sciences, Amsterdam) 35, 1023 (1926).

7. Clausing, P., Physica 9, 65 (1929).

8. Clausing, P., Ann. Physik (5), 4, 533 (1930).

9. Clausing, P., Z. Physik 66, 471 (1930).

10. Clower, E. W., Ph.D. Thesis, University of Illinois (1954).

11. Cook, H. and E. A. Richley, NASA Technical Note, TN D-2480 (1964).

12. DeMarcus, W. C. and E. H. Hopper, J. Chem. Phys. 23, 1344 (1955).

13. DeMarcus, W. C., "The Problems of Knudsen Flow," Technical Report K-1302, Parts 1-6, Oak Ridge Gaseous Diffusion Plant, Oak Ridge, Tennessee (1957).

14. Dunham, T. E. and J. P. Hirth, J. Chem. Phys. 49, 4650 (1968).

15. Dushman, S. and J. M. Lafferty, "Scientific Foundations of Vacuum Technique," John Wiley and Sons, Inc., New York (1962).

16. Edwards, J. G., Ph.D. Thesis, Oklahoma State University (1964).

17. Freeman, R. D., Ph.D. Thesis, Purdue University (1950).

18. Freeman, R. D., "Molecular Flow and the Effusion Process in the Measurement of Vapor Pressures," Technical Report ASD-TDR-63-754, Pt. I (1963) (AD423140).

19. Freeman, R. D., "Molecular Flow and the Effusion Process in the Measurement of Vapor Pressures," Technical Report ASD-TDR-63-754, Pt. II (1965) (AD612958).

20. Freeman, R. D., "Molecular Flow and the Effusion Process in the Measurement of Vapor Pressures," Technical Report ASD-TDR-63-754, Pt. III (1967).

21. Freeman, R. D. and J. G. Edwards, "Condensation and Evaporation of Solids," Eds. E. Rutner, P. Goldfinger and J. P. Hirth, Gordon and Breach, Science Publishers, Inc., New York (1964).

22. Freeman, R. D. and J. G. Edwards, "The Characterization of High-Temperature Vapors," Ed. J. L. Margrave, John Wiley & Sons, Inc., New York (1967).

23. Günther, K. G., Z. Angew. Phys. 9, 550 (1957).

24. Hopkins, T. E., Ph.D. Thesis, University of Illinois (1956).

25. Hurlbut, F. C., "Current Developments in the Study of Gas-Surface Interactions," Report No. AS-66-10, College of Engineering, University of California, Berkeley, August (1966).

26. Iczkowski, R. P., J. L. Margrave and S. H. Robinson, J. Phys. Chem. 67, 229(1963).

27. Johnson, T. H., Phys. Rev. 31, 103 (1928).

28. Knauer, F. and O. Stern, Z. Physik 39, 764 (1926).

29. Knudsen, M., Ann. Physik 28, 75 (1909).

30. Knudsen, M., Ann. Physik 28, 999 (1909).

31. Knudsen, M., Ann. Physik 29, 179 (1909).

32. Knudsen, M., Ann. Physik 48, 1113 (1915).

33. Knudsen, M., "The Kinetic Theory of Gases," Methuen and Company, London (1950).

34. Margrave, J. L., Ed., "The Characterization of High-Temperature Vapors," John Wiley and Sons, Inc., New York (1967).

35. Mayer, H., Z. Physik 52, 235 (1928).

36. Mayer, H., Z. Physik 58, 373 (1929).

37. Mayer, H., Z. Physik 67, 240 (1931).

38. Naumov, A. I., Zh. Tekhn. Fiz. 33, 127 (1963), (Sov. Phys.-Tech. Phys. 8, 88 (1963)).

39. Philips Metalonics, "The Philips Impregnated Cathode," Technical Bulletin, PM 101 IMP 863, Mount Vernon, New York; Also Private Communication from R. M. Klein, Sales Manager (1964).

40. "Rarefied Gas Dynamics," Academic Press, Inc., New York, Vol. I (1960-63); Vol. II (1965-66).

41. Rohn, K., Z. Physik 126, 20 (1949).

42. Ruth, V. and J. P. Hirth, "Condensation and Evaporation of Solids," Eds. E. Rutner, P. Goldfinger and J. P. Hirth, Gordon and Breach, Science Publishers, Inc., New York (1964).

43. Ruth, V., W. L. Winterbottom and J. P. Hirth, Z. Angew. Phys. 16, 53 (1963).

44. Saltsburg, H., J. N. Smith and M. Rogers, Eds., "Fundamentals of Gas-Surface Interactions," Academic Press Inc., New York (1967).

45. Searcy, A. W. and R. D. Freeman, J. Am. Chem. Soc. 76, 5229 (1954).

46. Sheffield, J. C., Rev. Sci. Instr. 36, 1269 (1965).

47. Smith, J. N., Jr., and H. Saltsburg, "Fundamentals of Gas-Surface Interactions," Eds. H. Saltsburg, J. N. Smith and M. Rogers, Academic Press Inc., New York (1967).

48. Sreekanth, A. K., "Some Experiments on the Flow of a Rarefied Gas Through a Circular Orifice," Technical Report No. 86, Boeing Research Laboratories (1963) (AD614695).

49. Sreekanth, A. K., "Rarefied Gas Dynamics," Vol. II, Ed. J. A. Laurman, Academic Press Inc., New York (1964).

50. Stickney, R. E. and F. C. Hurlbut, "Rarefied Gas Dynamics," Vol. I., Ed. J. A. Laurman, Academic Press, Inc., New York (1963).

51. Stickney, R. E., R. F. Keating, S. Yamamoto and W. J. Hastings, J. Vac. Sci. Tech. 4, 10 (1967).

52. Wahlbeck, P. G., Ph.D. Thesis, University of Illinois (1958).

53. Wahlbeck, P. G., and T. E. Phipps, J. Chem. Phys. 49, 1603 (1968).

54. Wang, K. C., Ph.D. Thesis, Illinois Institute of Technology (1966).

55. Wang, K. C. and P. G. Wahlbeck, J. Chem. Phys. 47, 4799 (1967).

56. Wang, K. C. and P. G. Wahlbeck, J. Chem. Phys. 49, 1617 (1968).

57. Ward, J. W., "Use of the Knudsen Effusion Method - A Literature Survey," Report LA-3006, Los Alamos Scientific Laboratory of the University of California, Los Alamos, New Mexico (1964).

58. Ward, J. W., Ph.D. Thesis, University of New Mexico (1966).

59. Ward, J. W., J. Chem. Phys. 47, 4030 (1967).

60. Ward, J. W., J. Chem. Phys. 49, 5129 (1968).

61. Ward, J. W., "Monte Carlo Analysis of Specular and Surface-Diffusional Contributions to Flow from Knudsen Orifices," Presented at Fifth Annual Symposium, New Mexico Section, American Vacuum Society, Los Alamos, New Mexico, April (1969).

62. Ward, J. W., R. N. R. Mueford and M. Kohn, J. Chem. Phys. 47, 1710 (1967).

63. Winterbottom, W. L., J. Chem. Phys. 47, 3546 (1967).

64. Winterbottom, W. L., J. Chem. Phys. 49, 106 (1968).

65. Winterbottom, W. L. and J. P. Hirth, J. Chem. Phys. 37, 784 (1962).

APPENDIX A

EXPRESSIONS FOR $A(D_x, D_L)$

The symbols used are defined by Figure 41, which shows their relationship to the geometry of the generalized conical orifice. Coordinates $\underline{x}$ and $\underline{y}$ describe flow in a diverging orifice and $\underline{t}$, in a converging orifice. The circle represents an imaginary sphere circumscribed about coaxial discs $\underline{D}_x$ at $\underline{x}$ and $\underline{D}_y$ at $\underline{y}$.

The Figures 42-47 show the projections of the disc $\underline{D}_x$ at $\underline{x}$ onto the plane of the disc $\underline{D}_L$ at $\underline{L}$ for all possible cases in the conical orifice. The projection of the overlap of $\underline{D}_x$ onto $\underline{D}_L$ at $\underline{\theta}$ is the area $\underline{A}(D_x, D_L)$. For these cases the expressions for $\underline{A}(D_x, D_L)$ are as follows:

Figure 42 $T<0,\ \theta < |T|,\ A(D_x, D_L) = \pi r_L^{\,2};$ (A-1a)

43 $T>0,\ \theta < |T|,\ A(D_x, D_L) = \pi r_x^{\,2};$ (A-1b)

$$\left.\begin{matrix} 46 & T<0 \\ 47 & T>0 \end{matrix}\right\},\ \tan^{-1}\frac{r_L + r_x}{L-x} \le \theta \le \frac{\pi}{2},$$

$$A(D_x, D_L) = 0; \qquad \text{(A-1c)}$$

$$\left.\begin{matrix} 44 & T<0 \\ 45 & T>0 \end{matrix}\right\},\ |T| \le \theta \le \tan^{-1}\frac{r_L + r_x}{L-x},$$

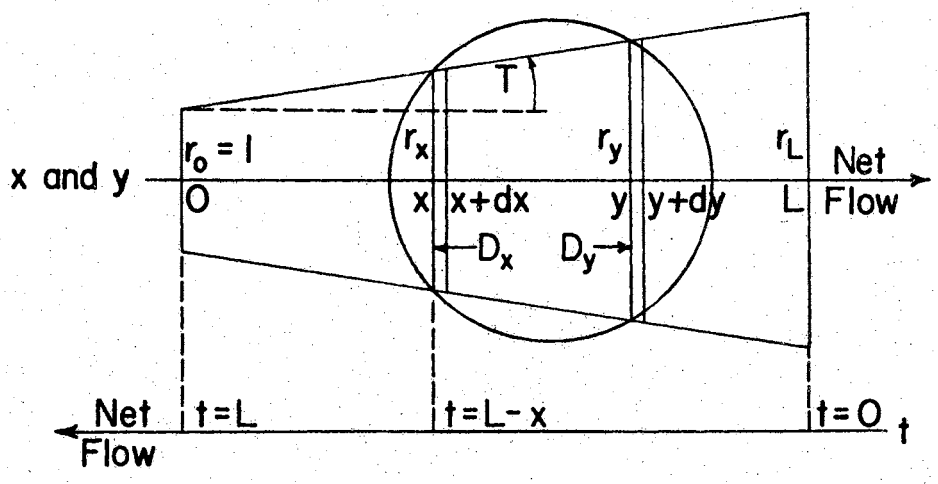

Figure 41. The Generalized Conical Orifice

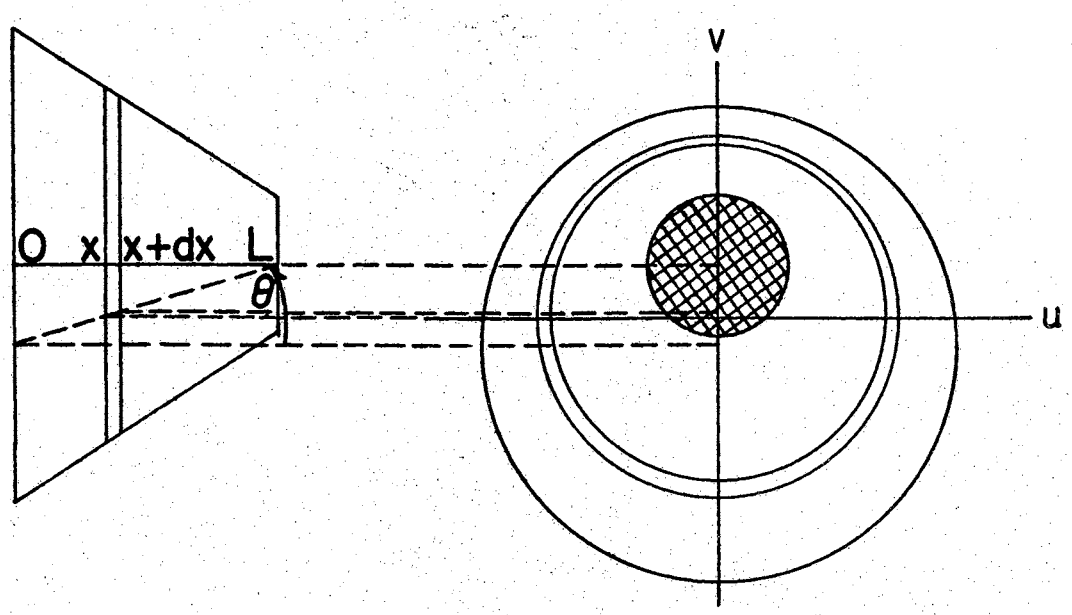

Figure 42. Projection at Angle $\underline{\theta}$ of the Disc $\underline{D}_x$ at $\underline{x}$ onto the Plane of the Disc $\underline{D}_L$ at L for the Case: $T < 0;\ 0 \leqslant \theta \leqslant |T|$

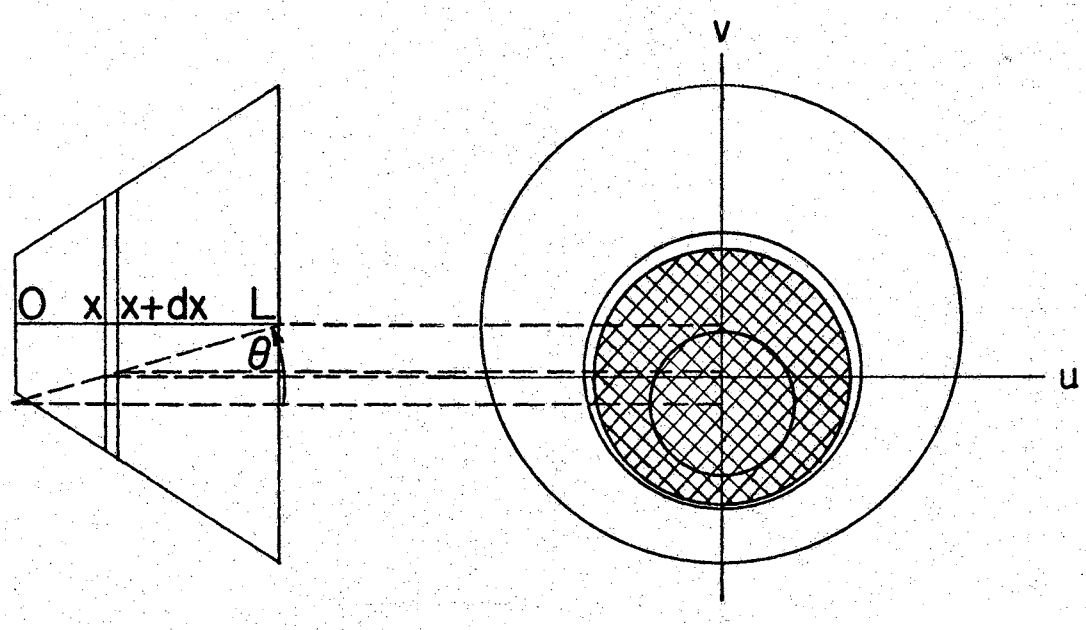

Figure 43. Projection at Angle $\underline{\theta}$ of the Disc $\underline{D}_x$ at $\underline{x}$ onto the Plane of the Disc $\underline{D}_L$ at $\underline{L}$ for the Case: $T > 0;\ 0 \leqslant \theta \leqslant |T|$

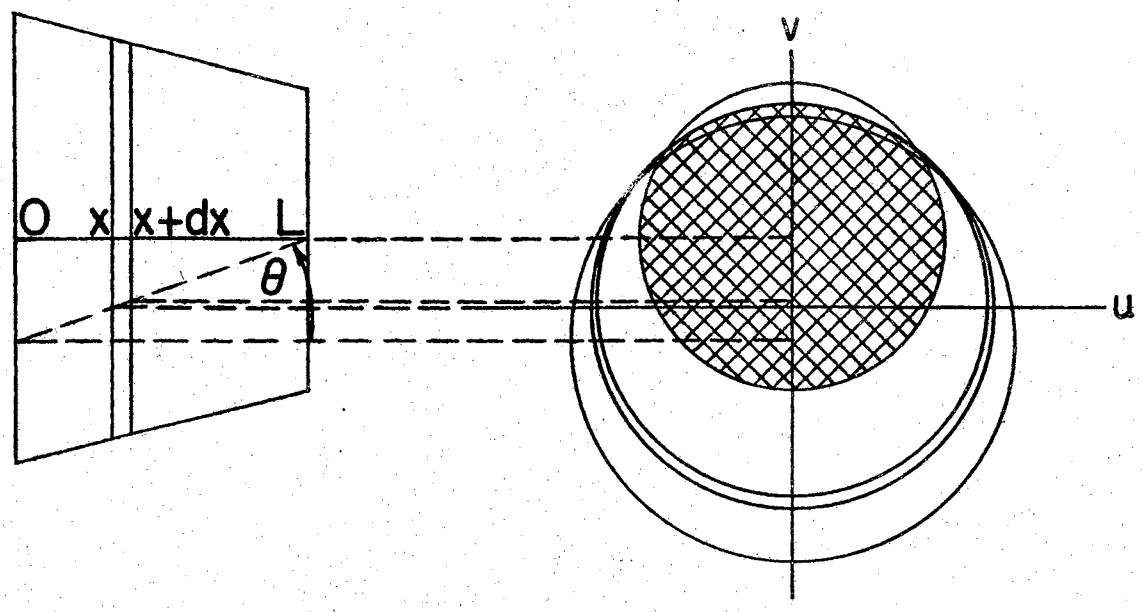

Figure 44. Projection at Angle $\underline{\theta}$ of the Disc at $\underline{x}$ onto the Plane of the Disc $\underline{D}_L$ at $\underline{L}$ for the Case: $T < 0$; $|T| \leqslant \theta \leqslant \tan^{-1}(r_L + r_x)/L-x)$

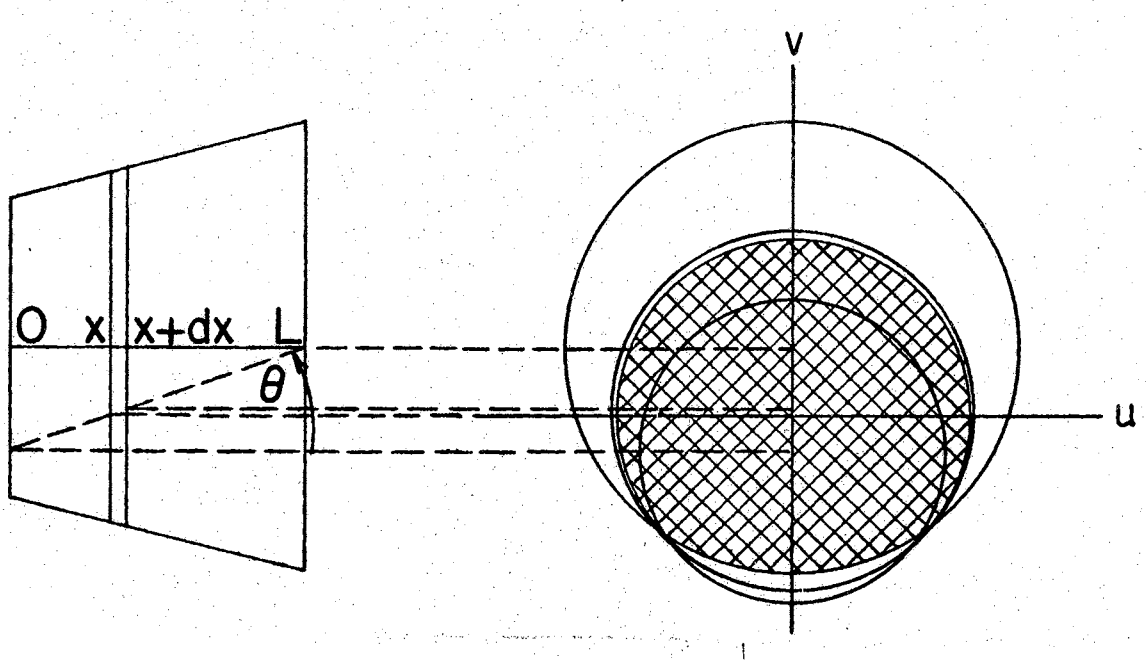

Figure 45. Projection at Angle $\underline{\theta}$ of the Disc $\underline{D}_x$ at $\underline{x}$ onto the Plane of the Disc $\underline{D}_L$ at $\underline{L}$ for the Case: $T > 0$; $|T| \leqslant \theta \leqslant \tan^{-1}(r_L + r_x)/(L-x)$

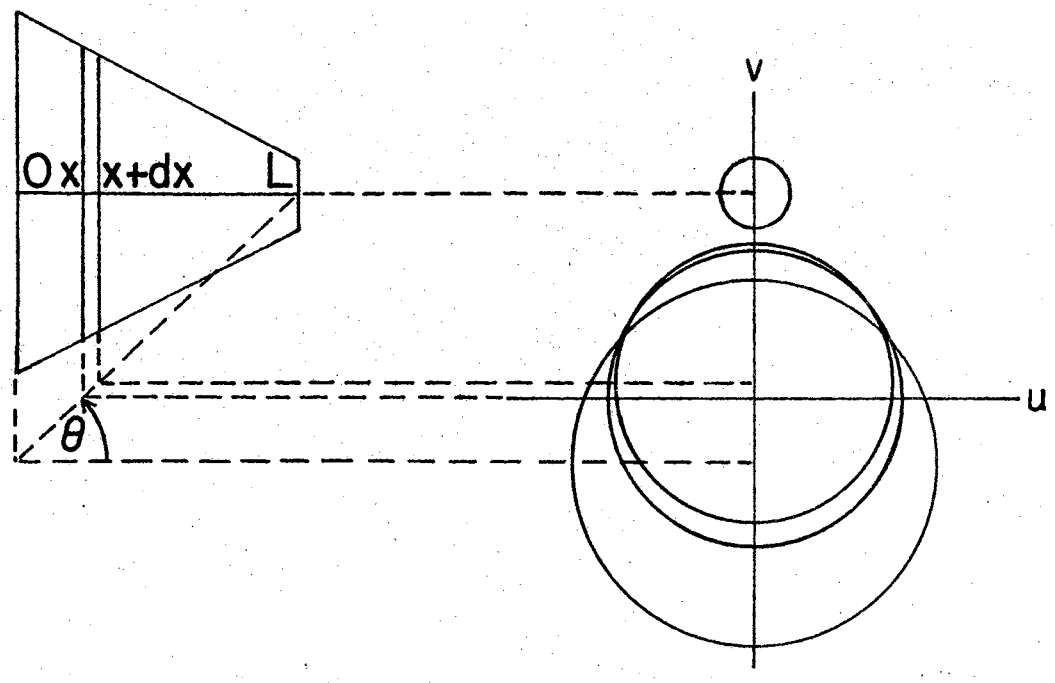

Figure 46. Projection at Angle $\underline{\theta}$ of the Disc $\underline{D}_x$ at $\underline{x}$ onto the Plane of the Disc $\underline{D}_L$ at $\underline{L}$ for the Case: $T < 0$; $\tan^{-1}(r_L + r_x)/(L-x) \leqslant \theta \leqslant \pi/2$

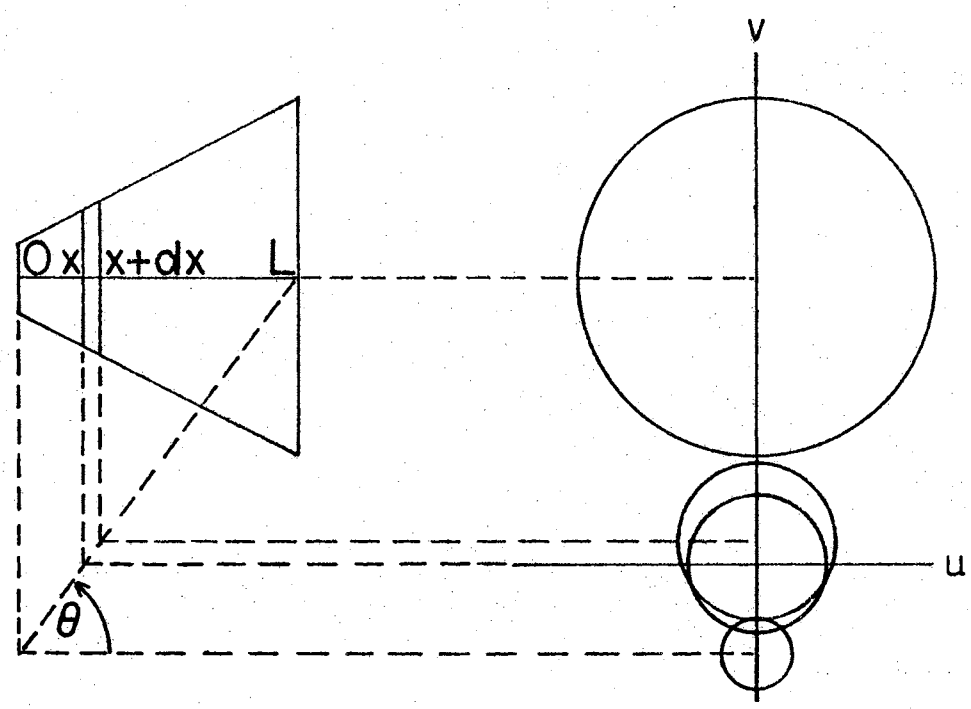

Figure 47. Projection at Angle $\underline{\theta}$ of the Disc $\underline{D}_x$ at $\underline{x}$ onto the Plane of the Disc $\underline{D}_L$ at $\underline{L}$ for the Case: $T > 0$; $\tan^{-1}(r_L + r_x)/(L-x) \leqslant \theta \leqslant \pi/2$

$$A(D_x;D_L) = (t-s)\ [r_L^{\ 2}-(t-s)^2]^{\frac{1}{2}} +$$

$$r_L^{\ 2}\ \sin^{-1}\ [(t-s)/r_L] + \pi r_L^{\ 2}/s +$$

$$\pi r_x^{\ 2}/2 - t(r_x^{\ 2}-t^2)^{\frac{1}{2}} - r_x^{\ 2}\ \sin^{-1}(t/r_x); \qquad \text{(A-1d)}$$

where $t = [(L-x)\tan^2\theta - (r_x + r_L)\tan T]/(2\ \tan\theta)$

and $s = (L-x)\tan\theta$.

The derivation of equation A-1 is accomplished by an extention of the method used by Clausing[9] and by Freeman[17] and is given in detail by Edwards.[16]

APPENDIX B

THE DEFINITION OF $\psi(x)$

The function $\psi(x)$ is defined by $\psi(x) = \mu_x/\mu_o$, with

μ_x = incident molecular density on the ring at x (Figure 41), and

μ_o = incident molecular density on a surface in the source cell, and hence, on a plane through the orifice entrance at $x = 0$.

Then $\psi(x)$ is the molecular flux incident on the wall at x normalized with respect to the entrance flux. Plots of $\psi(x)$ with x for various orifice show the density distribution changes that occur along the wall in the theoretical treatment. By modifying $\psi(x)$ one can simulate a process which involves a wall density change, such as surface diffusion does.

The derivation of the expression to calculate $\psi(x)$ and the calculation method used has been reported in detail earlier.[16,21]

APPENDIX C

THE TRANSMISSION COEFFICIENT, $\underline{W}$

The transmission coefficient, $\underline{W}$, is the probability that a molecule entering the orifice from the source cell will escape from the other end. In other words, of those molecules that enter the orifice from the cell, $\underline{W}$ is the fraction which escape from the other end of the orifice. The total number entering per second from the cell is $\underline{\pi r_o^2 \mu_o}$ (Chapter II). The number of molecules effusing per second into $\underline{dV_\theta}$ at θ is the sum of those molecules going straight through the orifice from the cell into $\underline{dV_\theta}$ and those molecules which strike the wall before effusing into this incremental volume. The sum of these two contributions is $\underline{dN_\theta}(L)$ (equation 1, Chapter II). Since the numerator of $\underline{W}$ includes the molecules leaving the orifice at all possible angles, $\underline{dN_\theta}(L)$ is integrated over $0 \leq \theta \leq \pi/2$.

$$W = \frac{1}{\pi r_o^2 \mu_o} \int_{\theta = 0}^{\theta = \pi/2} dN_\theta(L).$$

Contributions are made to $\underline{W}$ over the three ranges of $\underline{\theta}$ discussed in Chapter II.

APPENDIX D

THE EXPERIMENTAL DATA

The normalized angular intensities taken from the strip chart record of each experimental run are plotted in Figures 48-100. A smooth curve was drawn through the experimental data points for each run. From this smooth curve intensity values at 5° increments from 0° to 90° were obtained. The points read from the smooth curve were used in all calculations (Chapter IV).

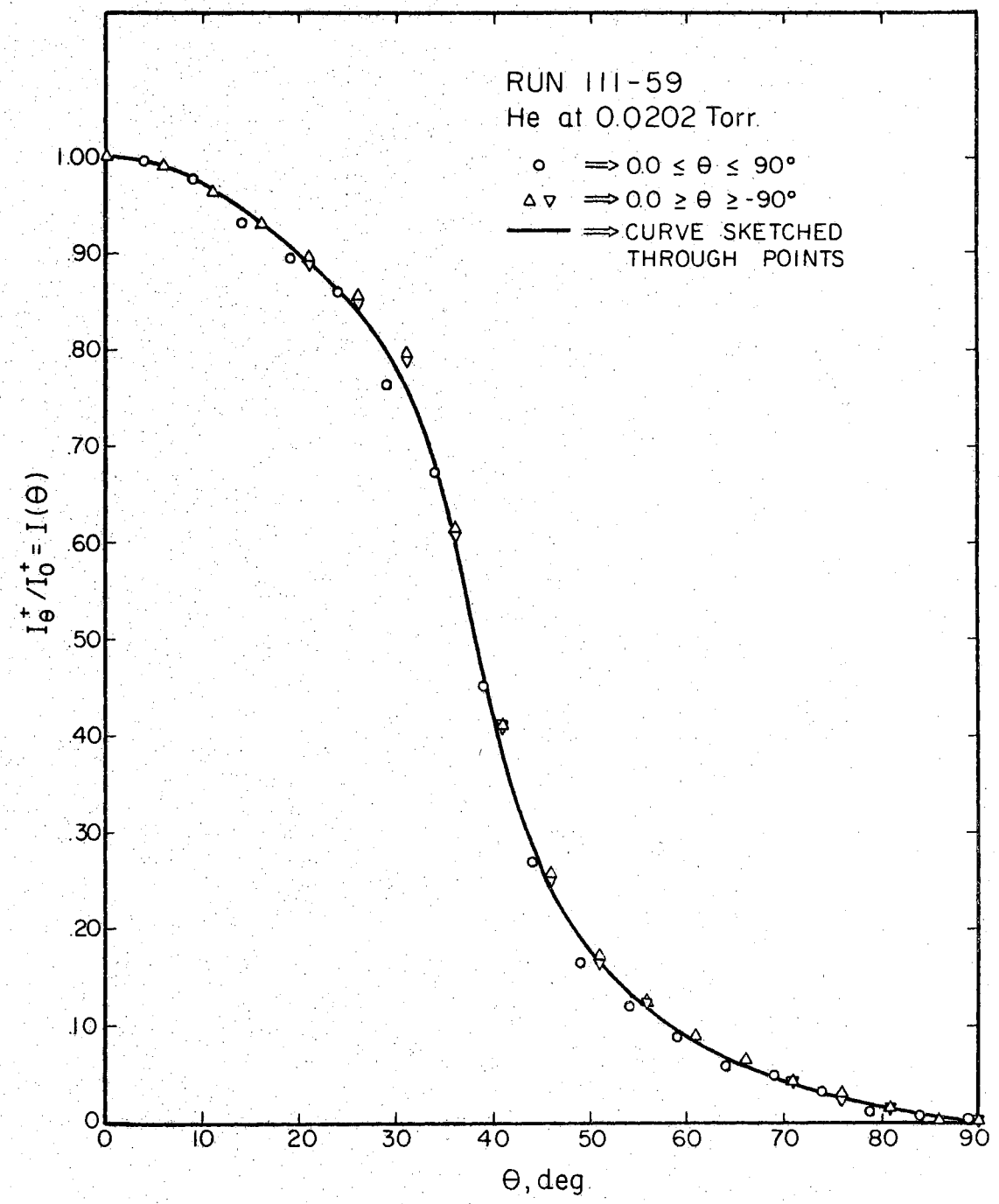

Figure 48. Normalized Experimental Intensities for Run 111-59

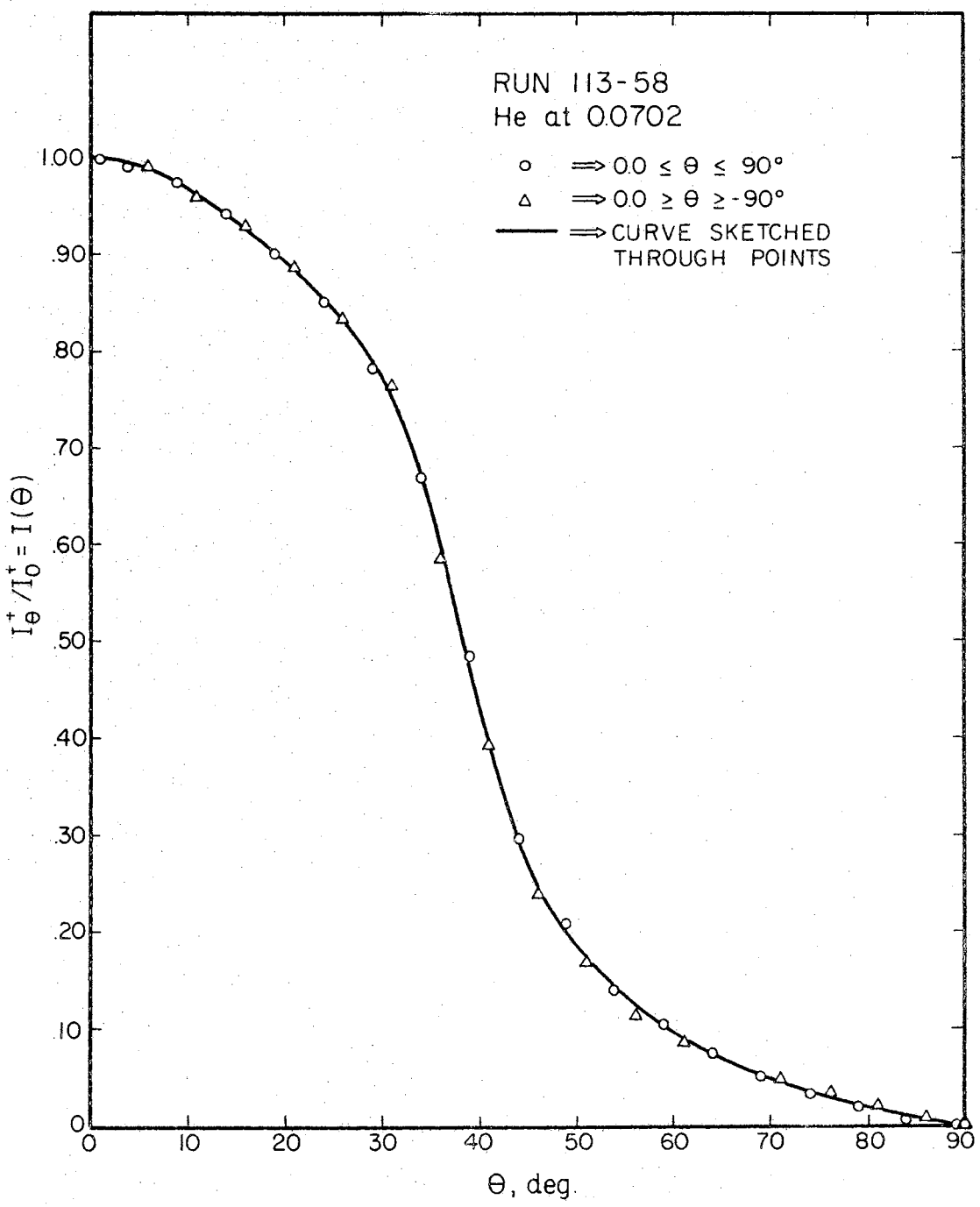

Figure 49. Normalized Experimental Intensities for Run 113-58

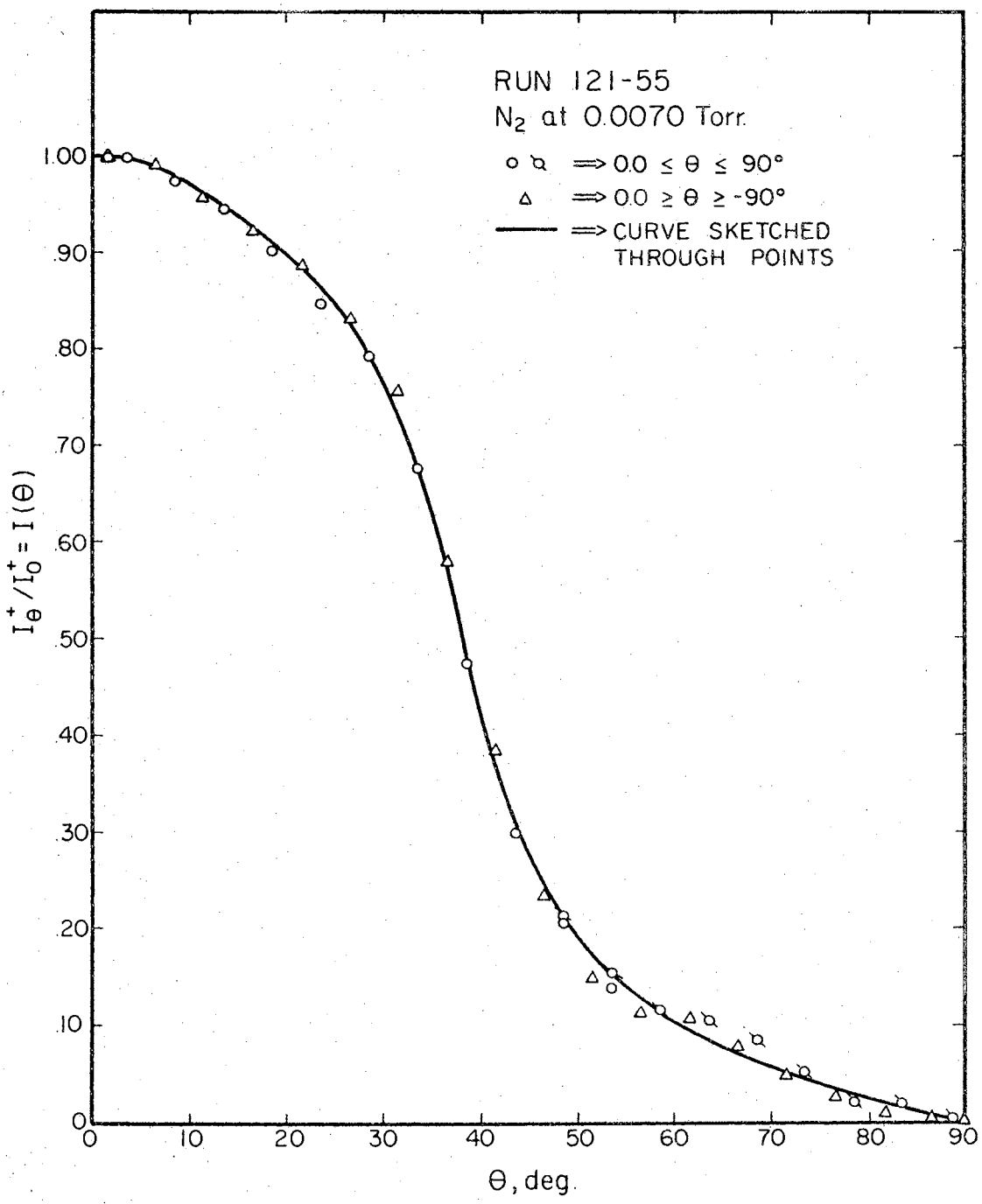

Figure 50. Normalized Experimental Intensities for Run 121-55

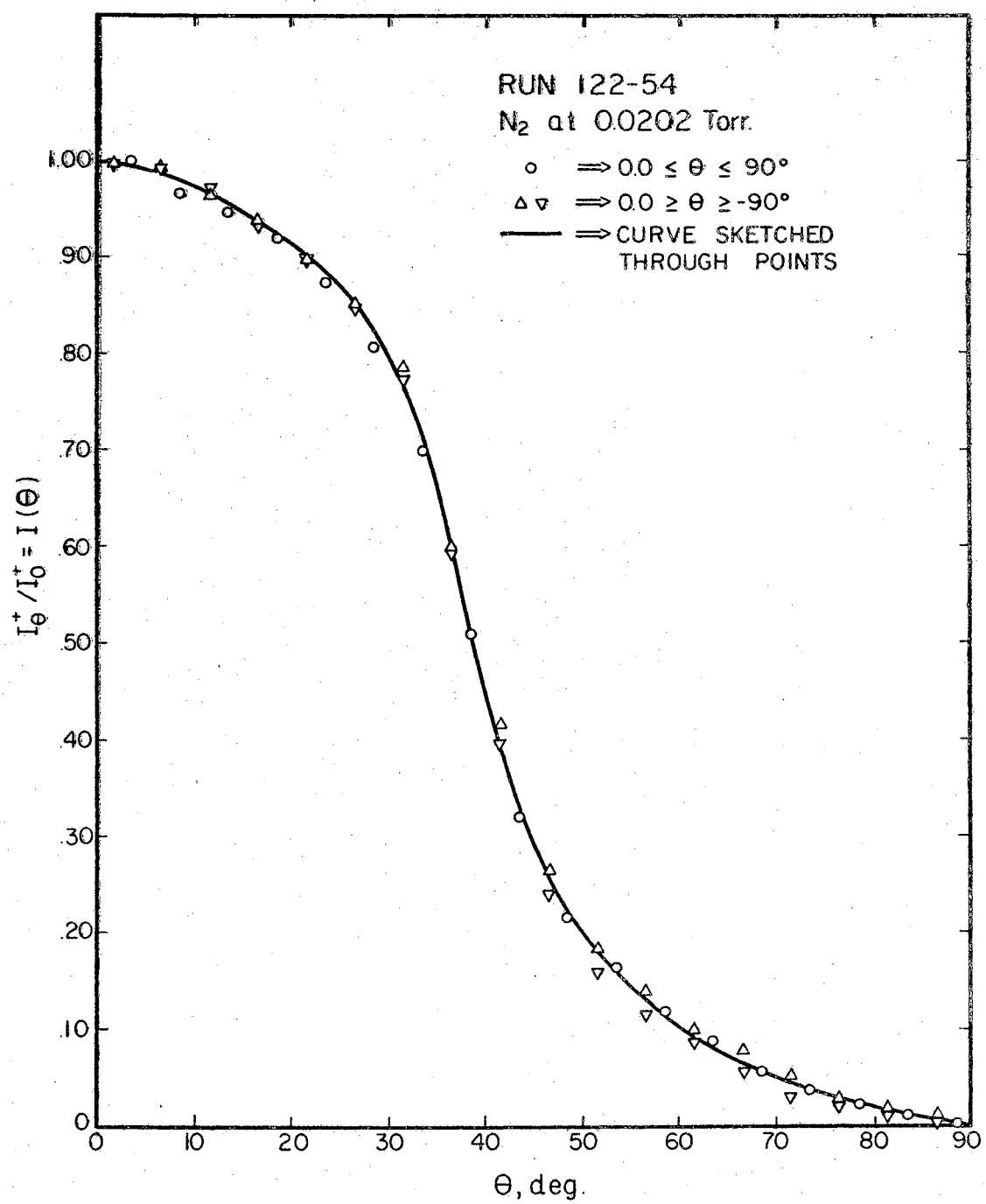

Figure 51. Normalized Experimental Intensities for Run 122-54

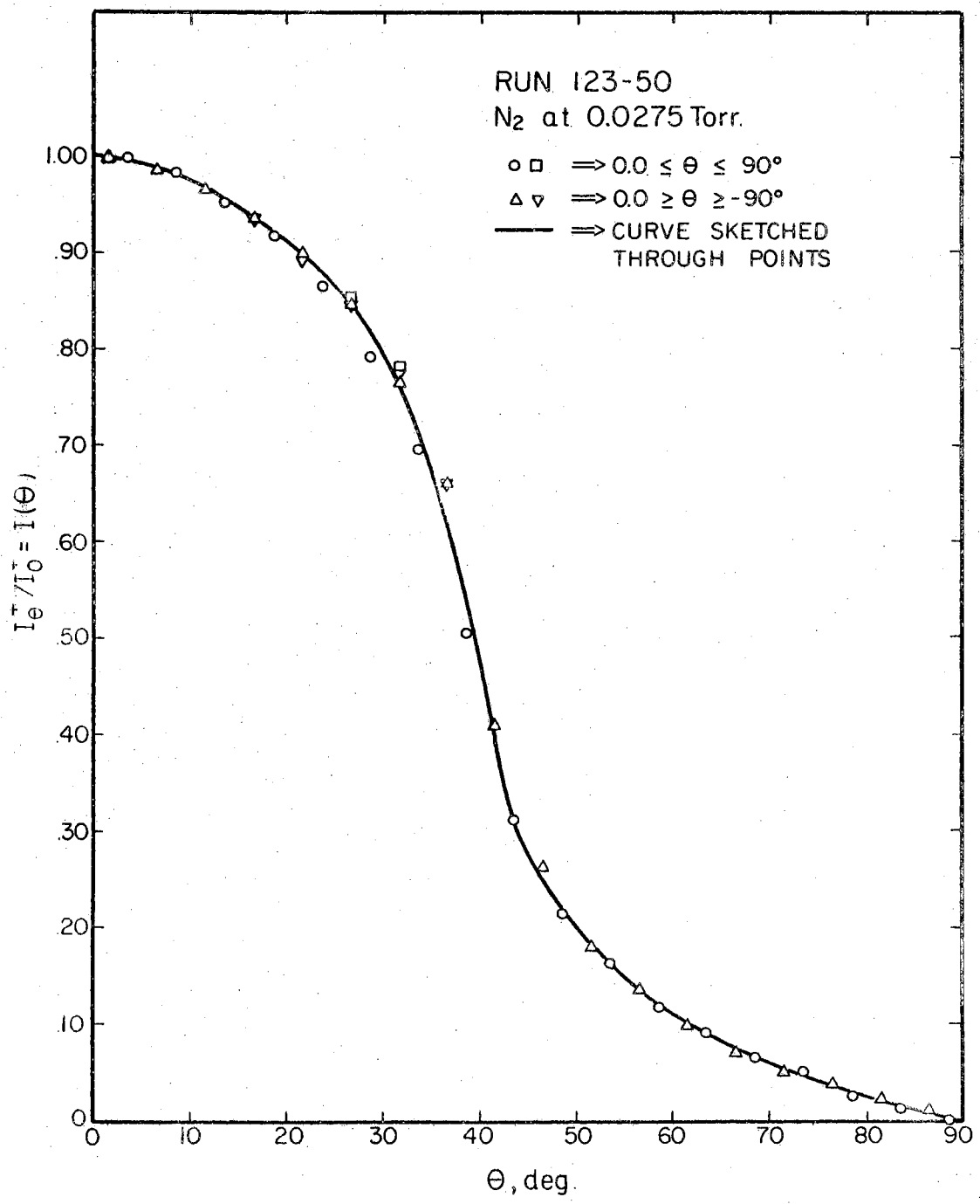

Figure 52. Normalized Experimental Intensities for Run 123-50

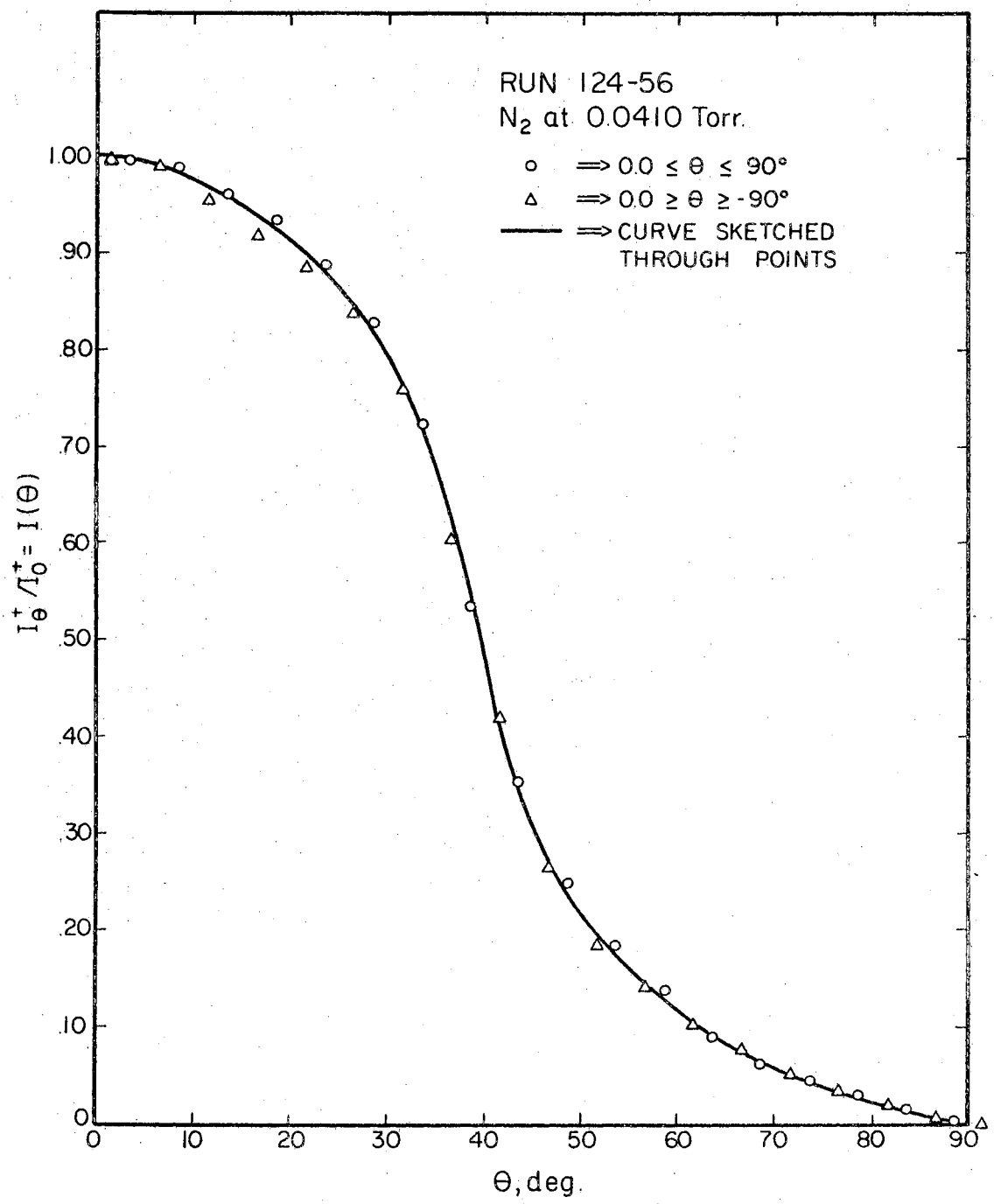

Figure 53. Normalized Experimental Intensities for Run 124-56

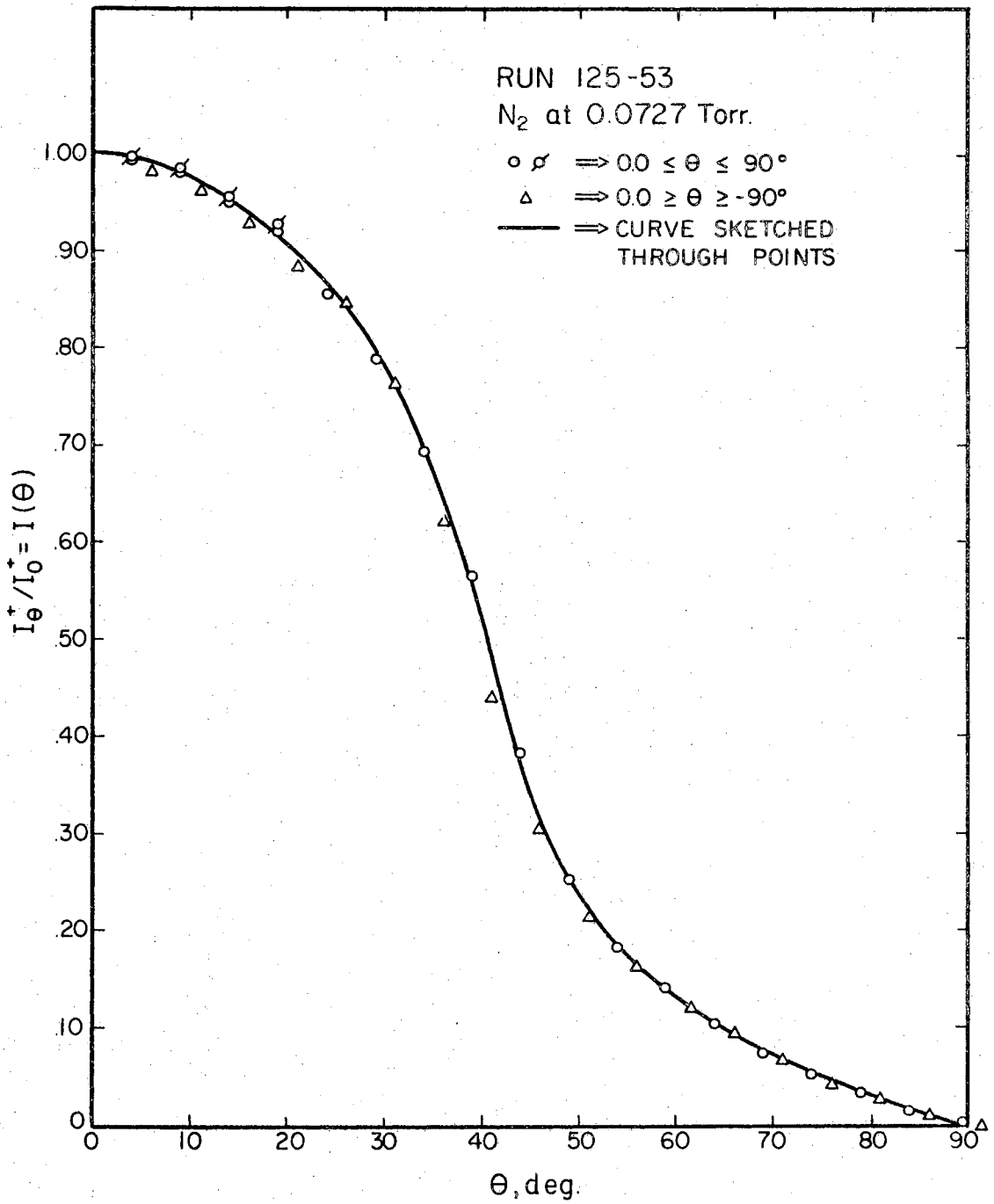

Figure 54. Normalized Experimental Intensities for Run 125-53

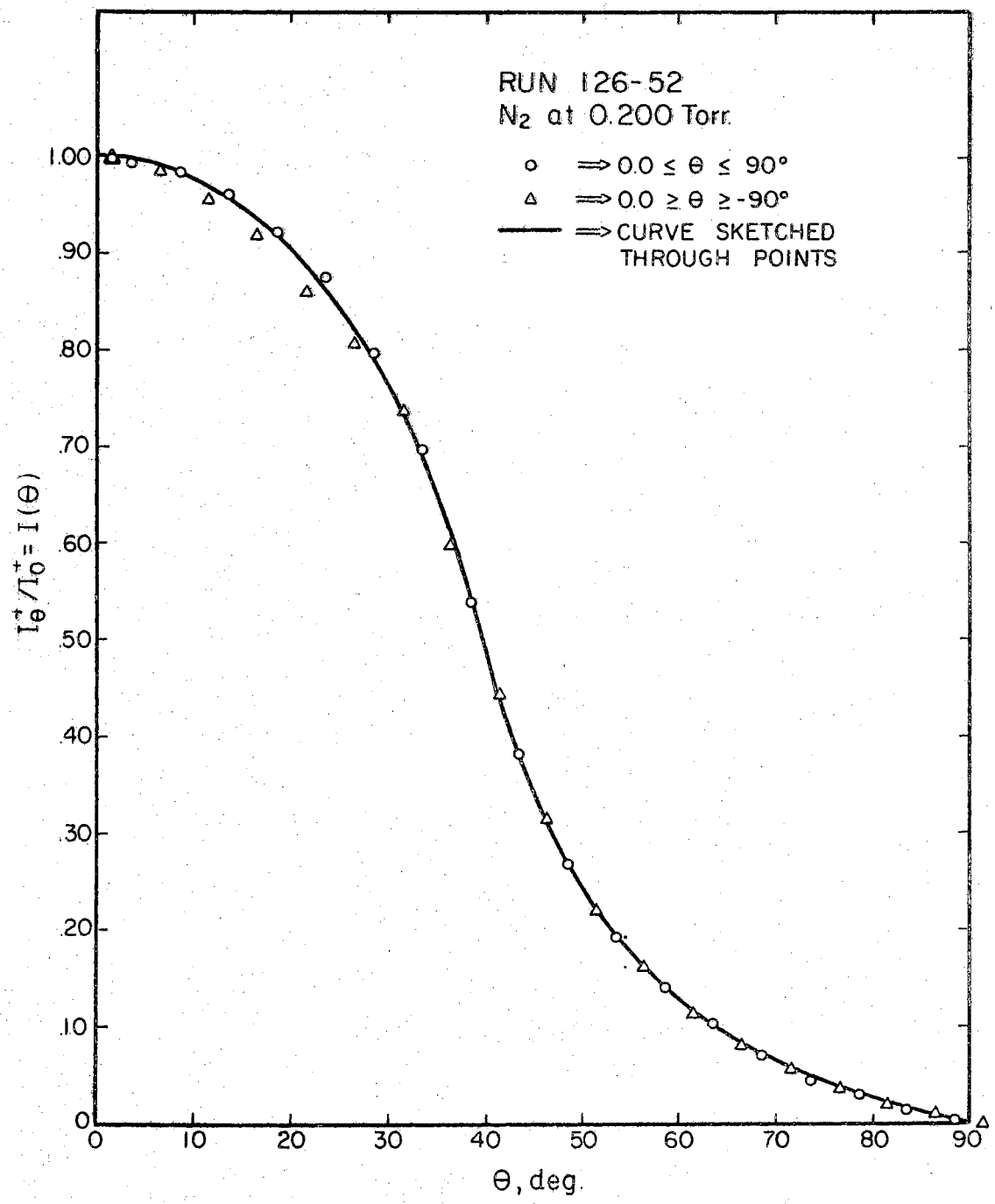

Figure 55. Normalized Experimental Intensities for Run 126-52

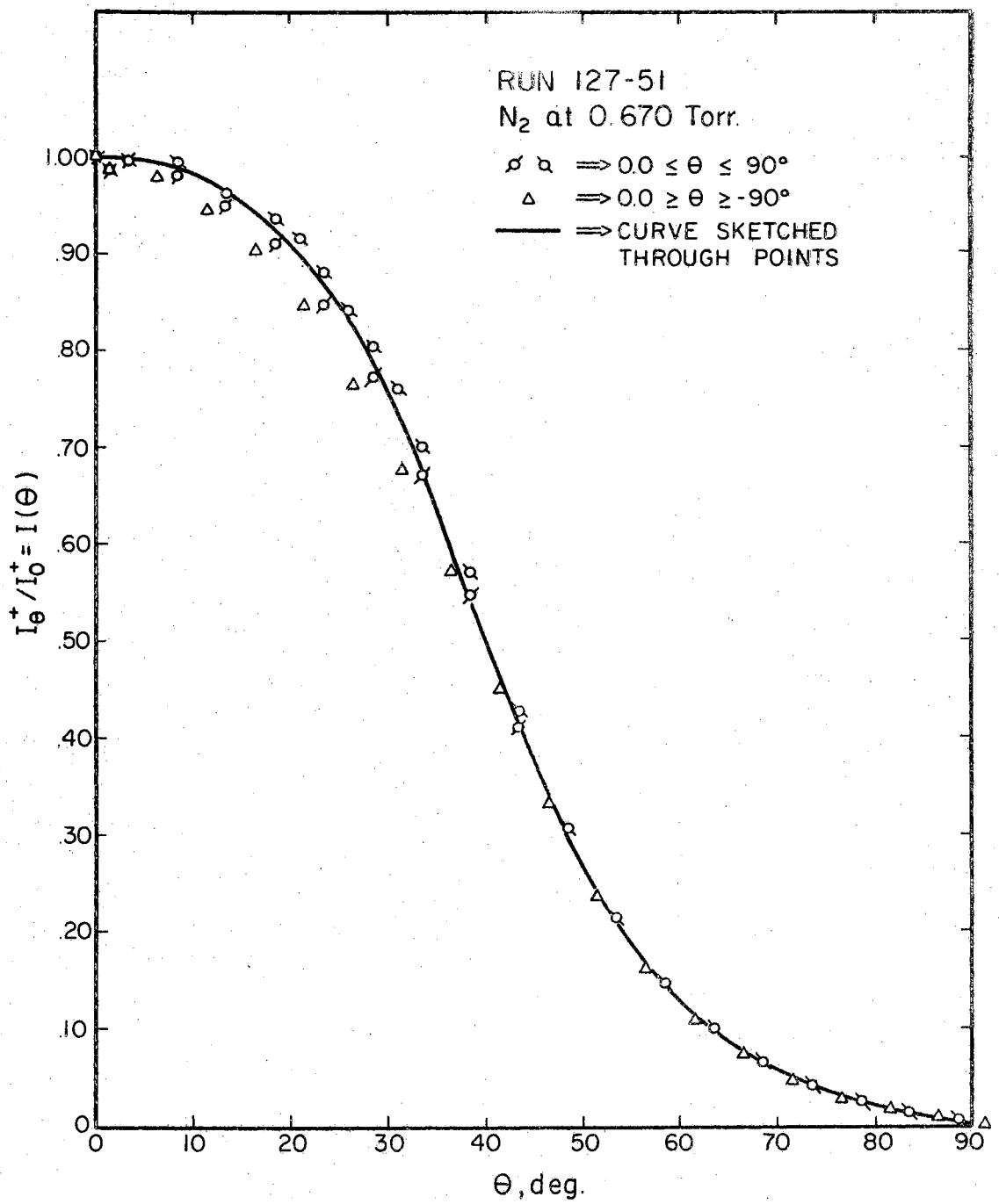

Figure 56. Normalized Experimental Intensities for Run 127-51

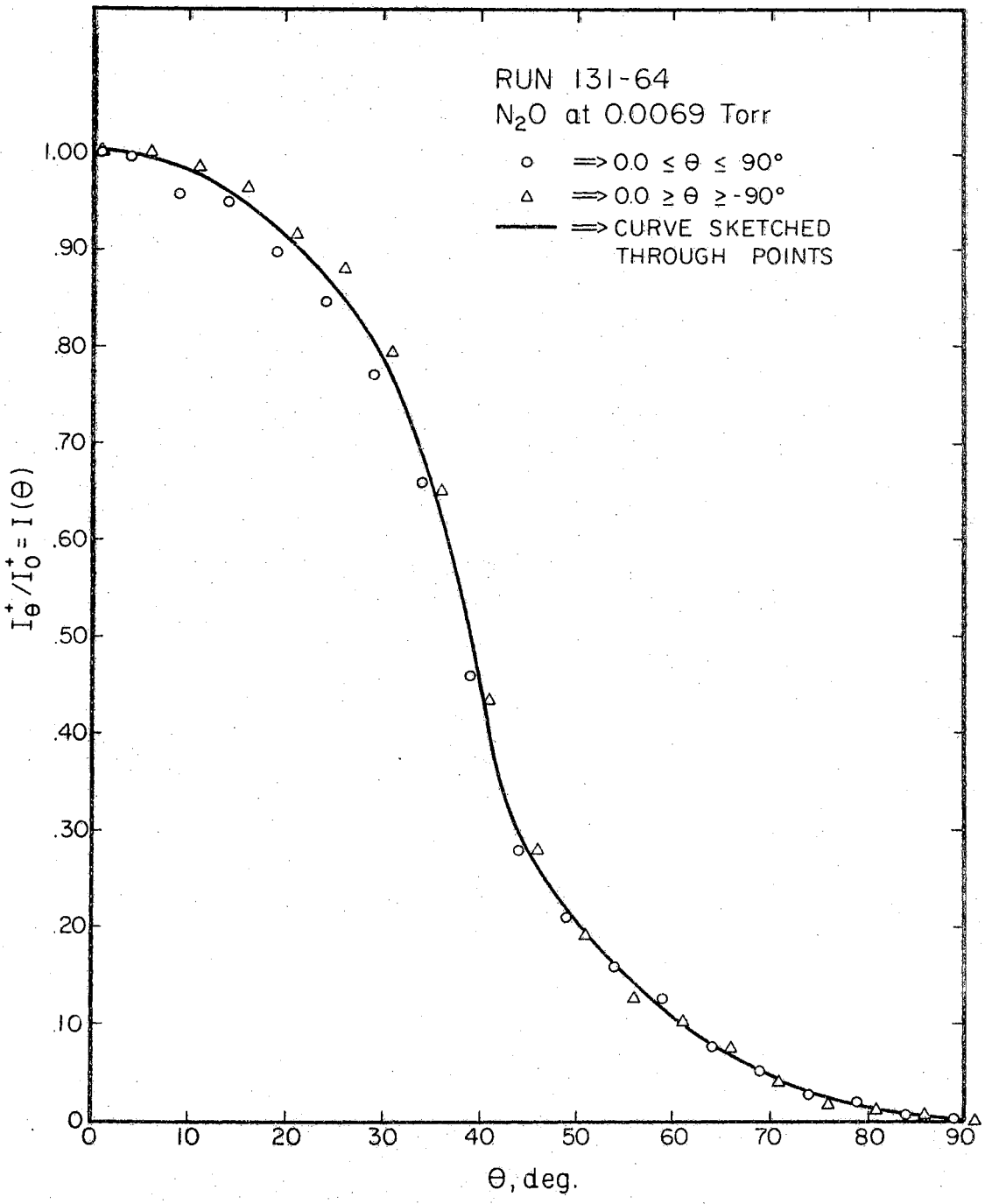

Figure 57. Normalized Experimental Intensities for Run 131-64

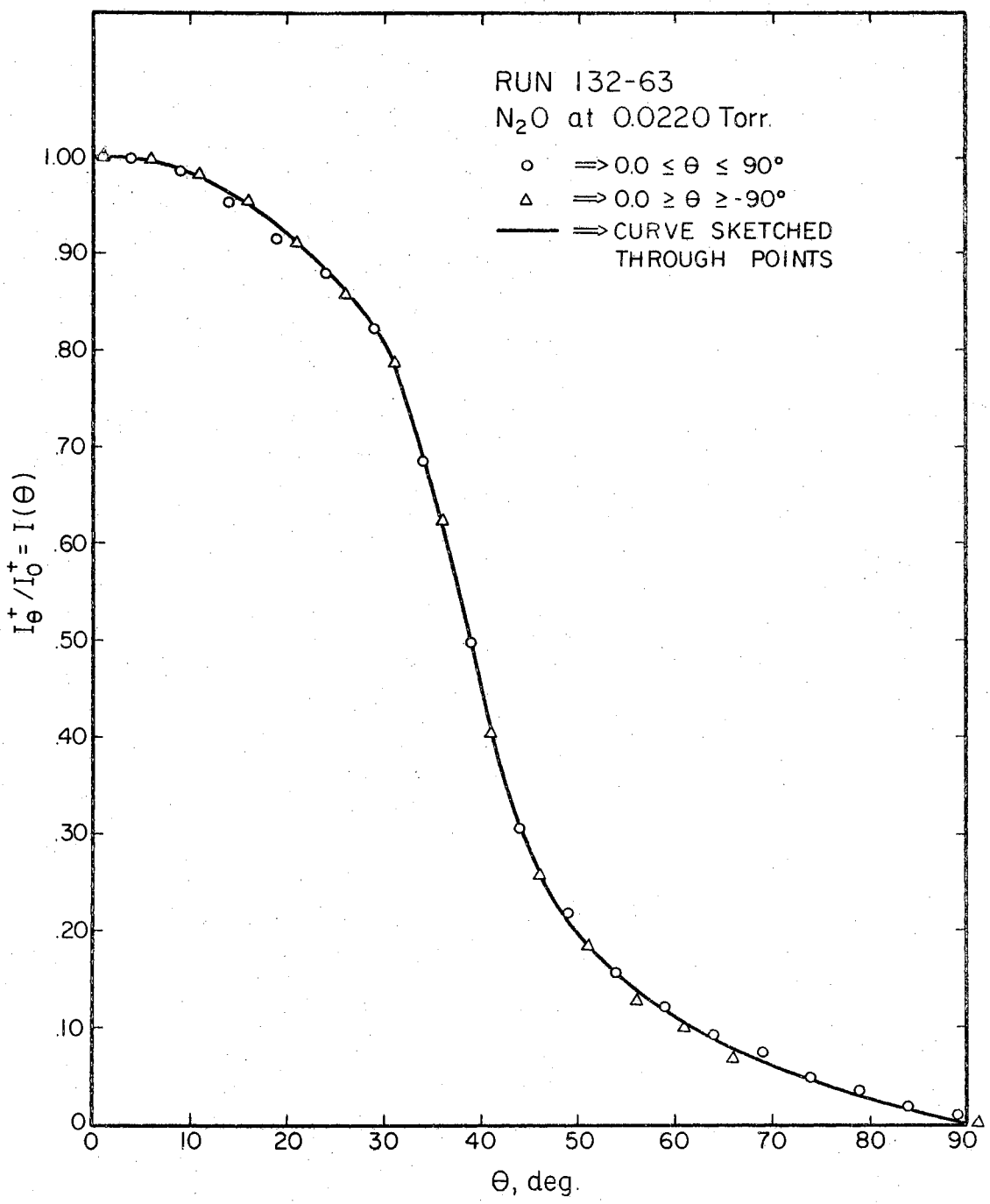

Figure 58. Normalized Experimental Intensities for Run 132-63

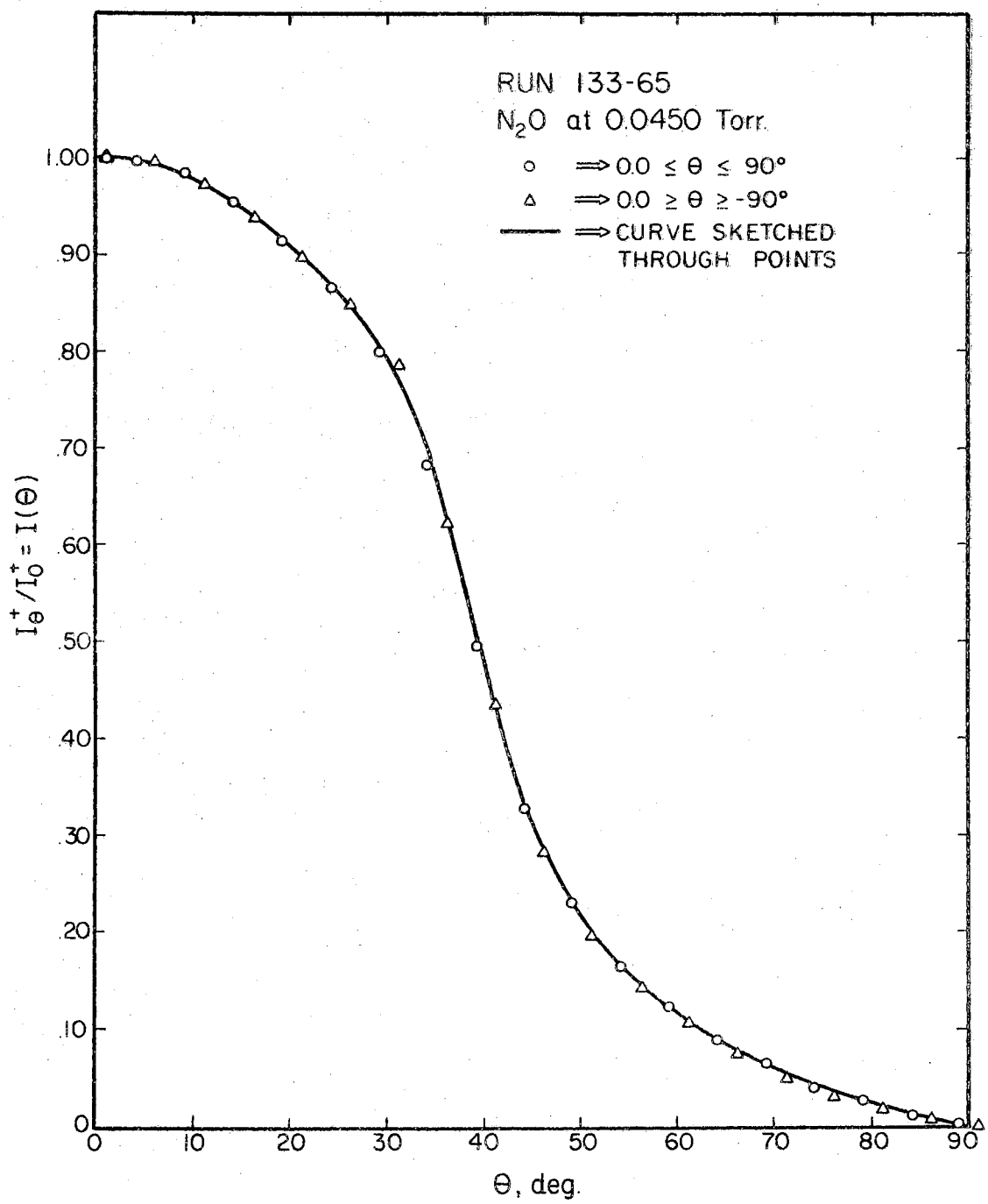

Figure 59. Normalized Experimental Intensities for Run 133-65

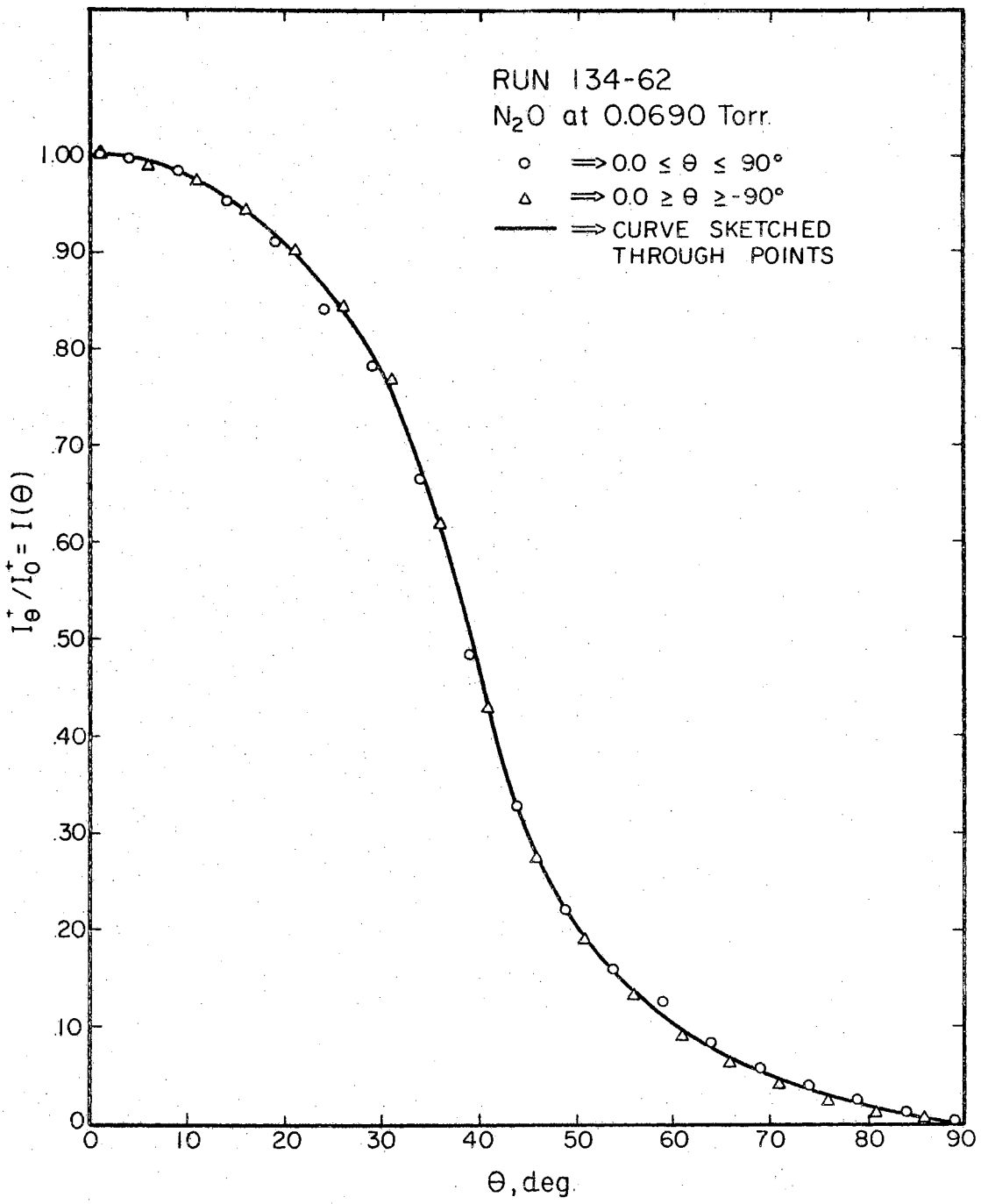

Figure 60. Normalized Experimental Intensities for Run 134-62

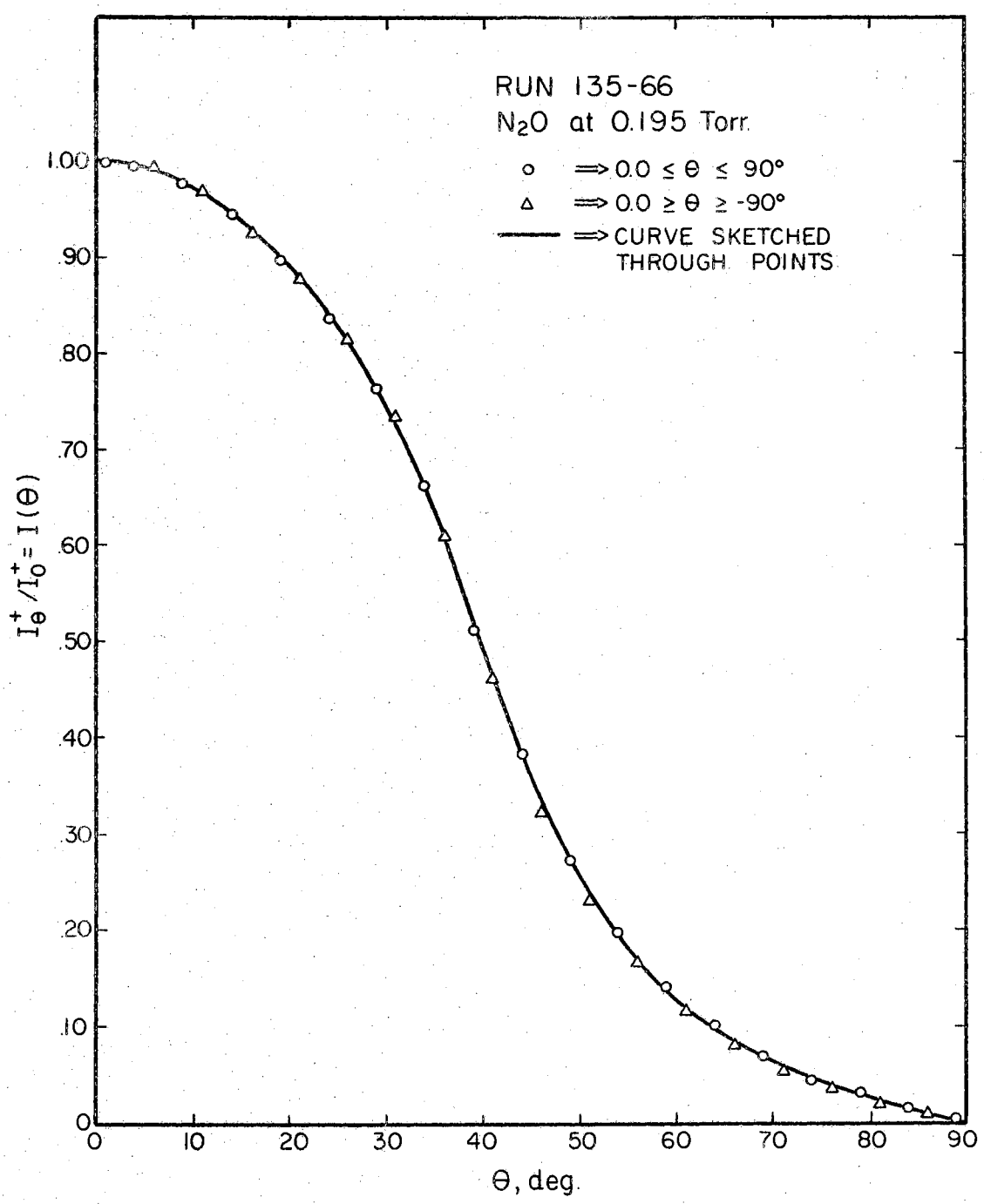

Figure 61. Normalized Experimental Intensities for Run 135-66

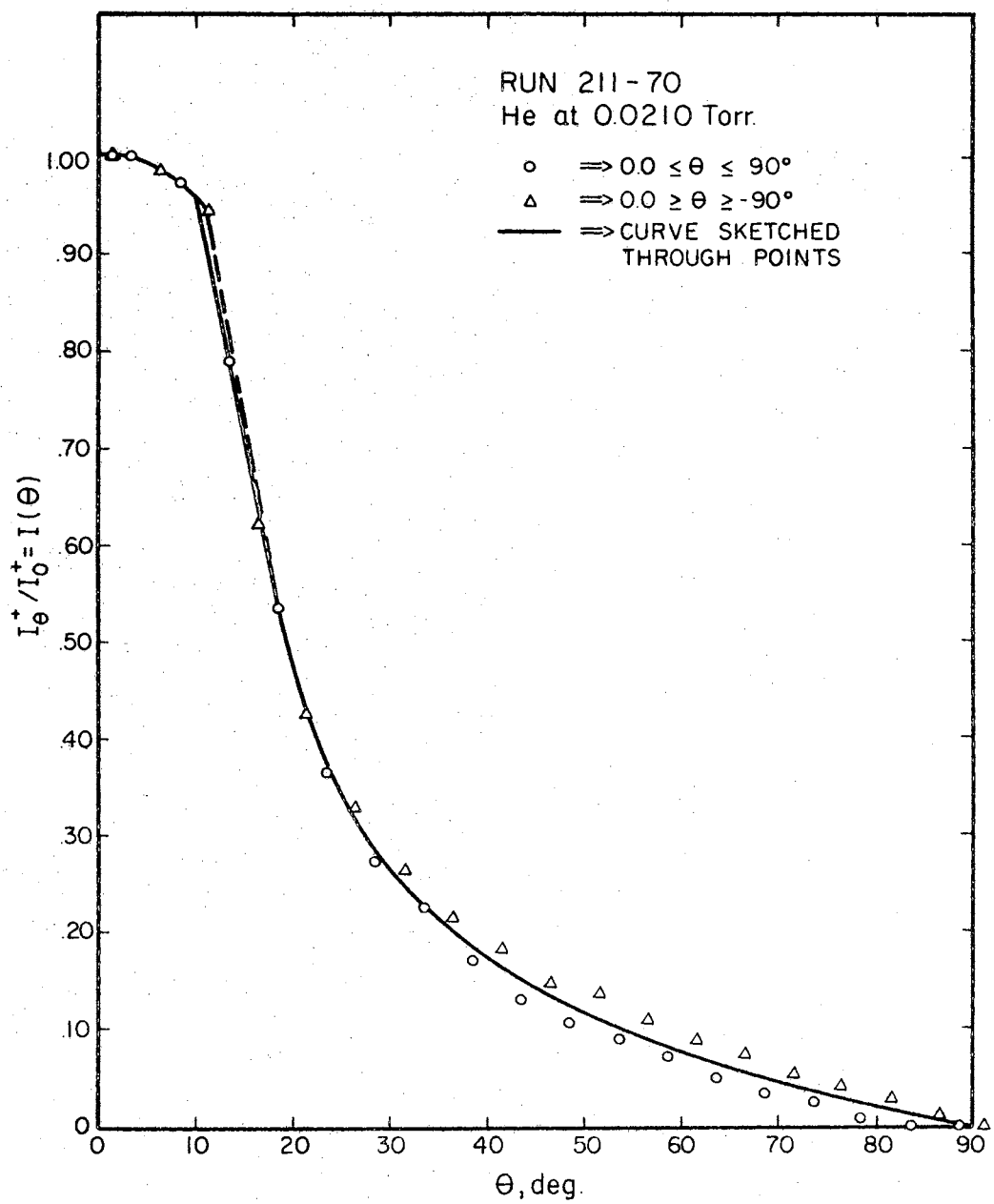

Figure 62. Normalized Experimental Intensities for Run 211-70

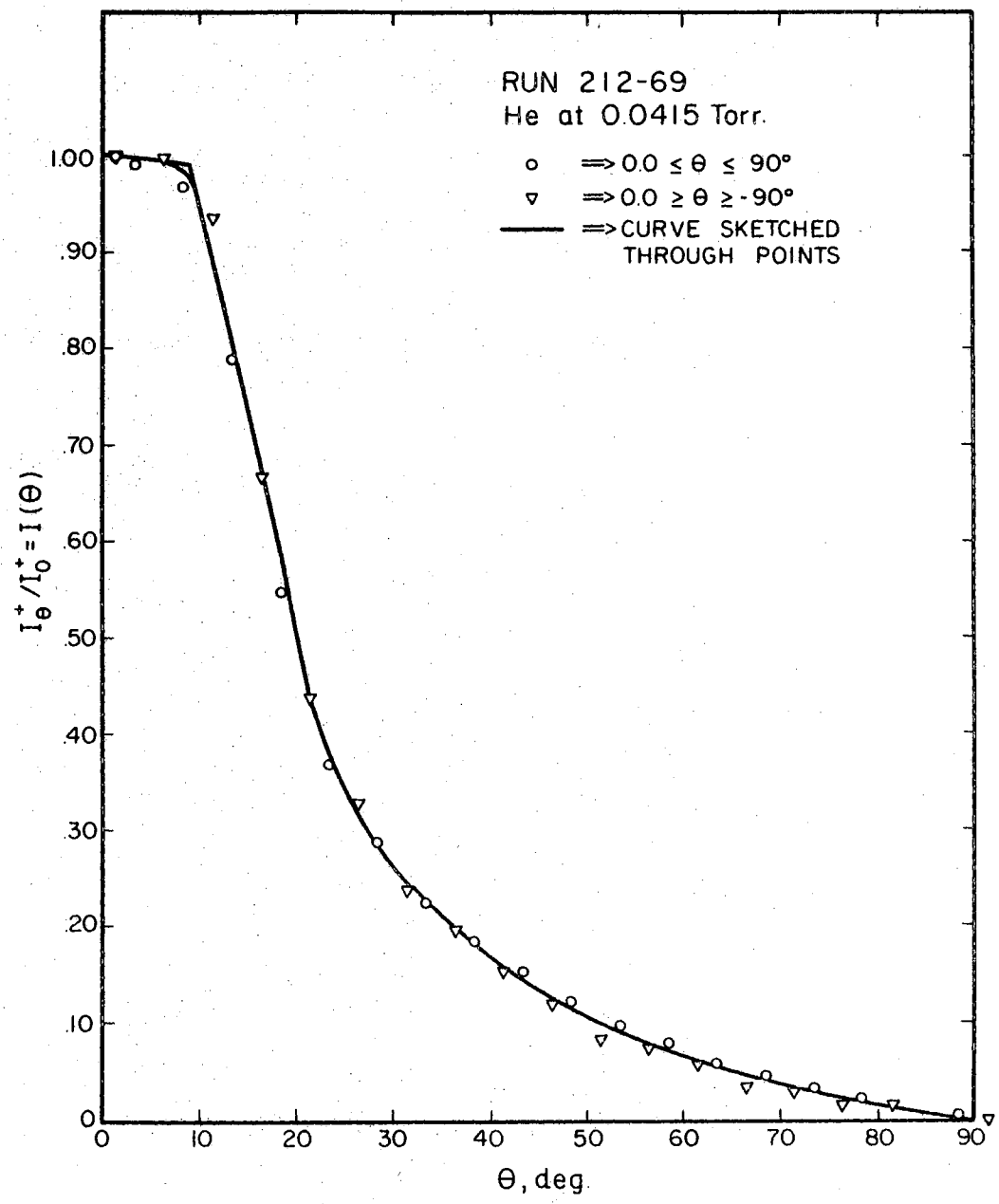

Figure 63. Normalized Experimental Intensities for Run 212-69

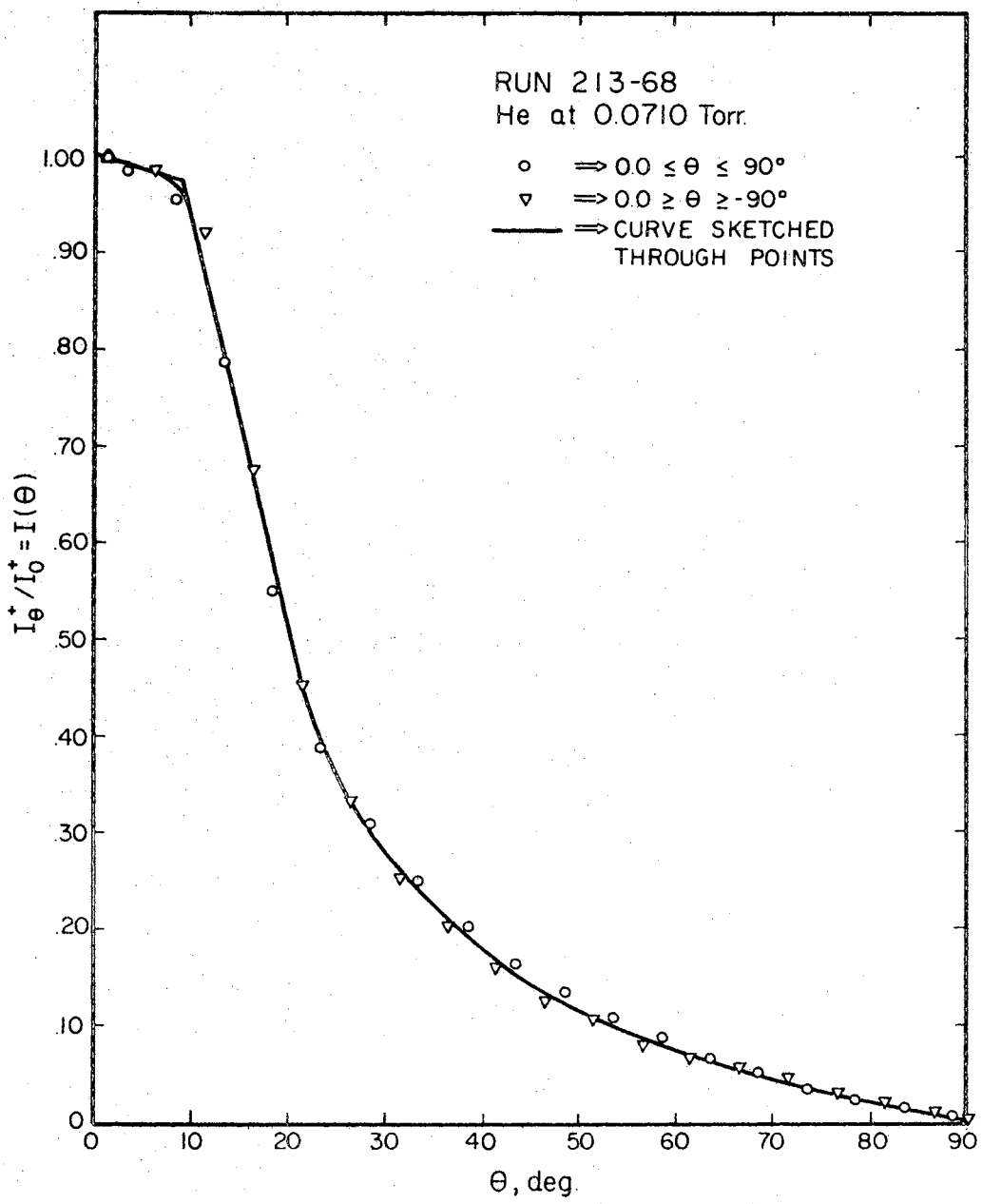

Figure 64. Normalized Experimental Intensities for Run 213-68

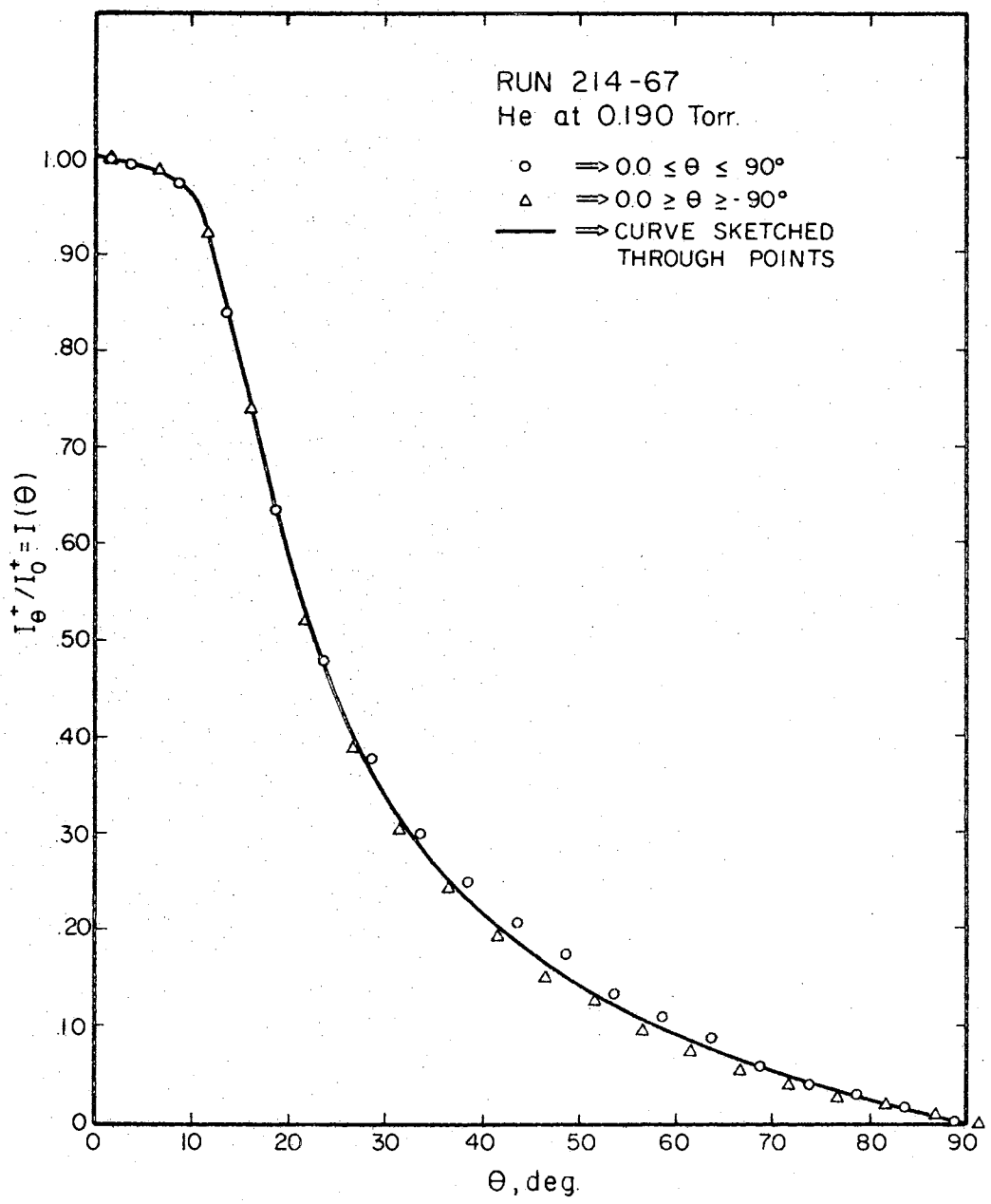

Figure 65. Normalized Experimental Intensities for Run 214-67

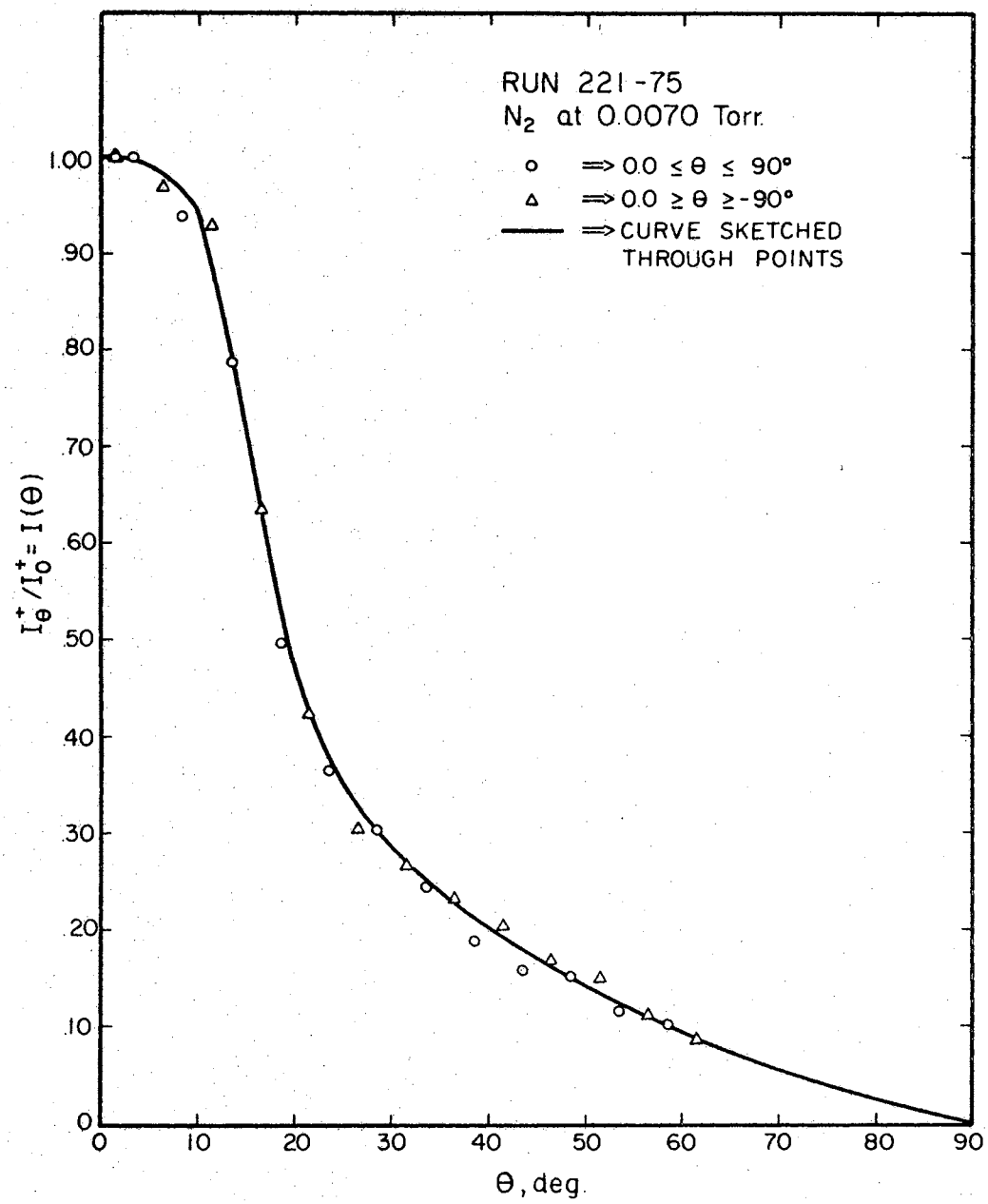

Figure 66. Normalized Experimental Intensities for Run 221-75

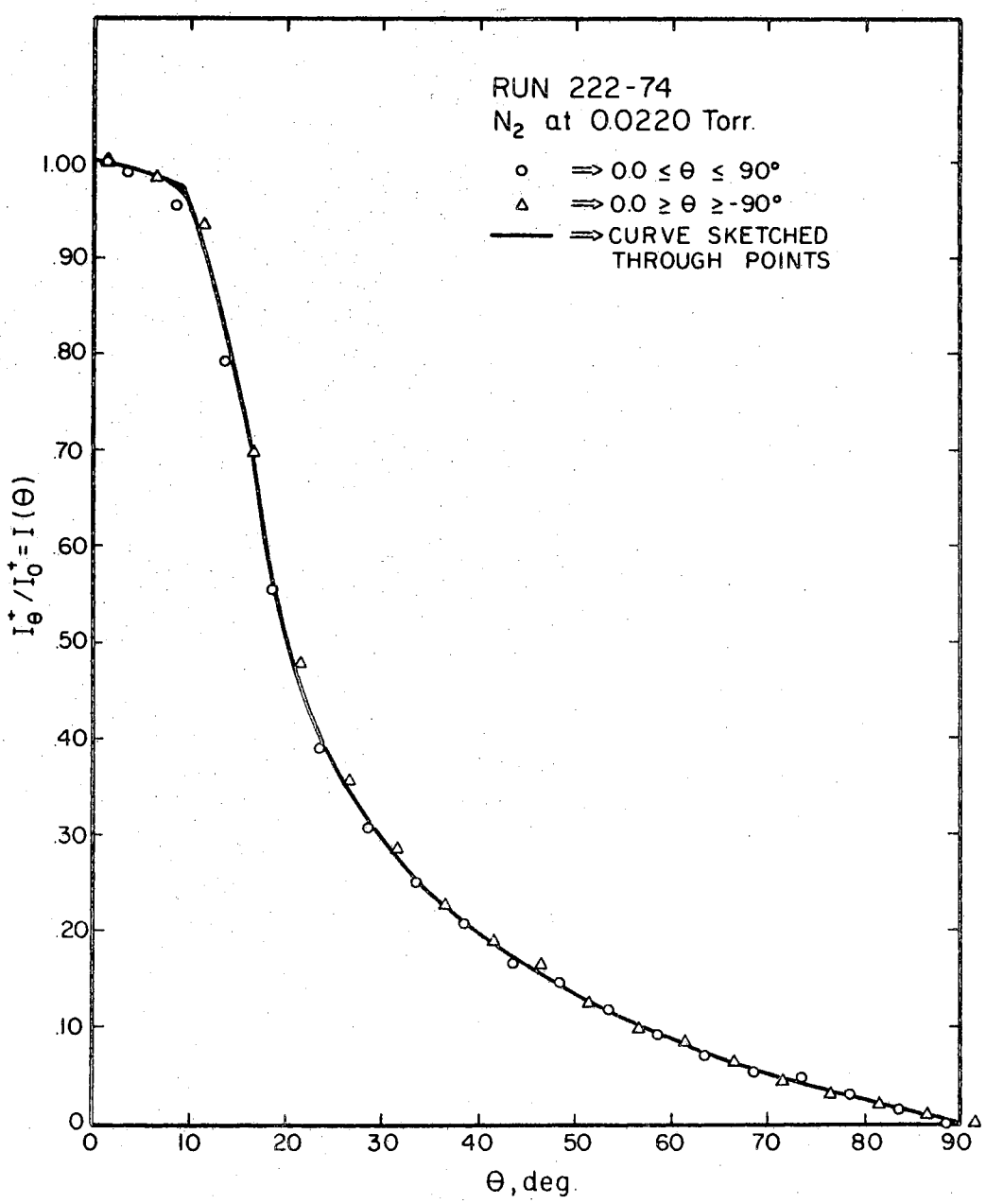

Figure 67. Normalized Experimental Intensities for for Run 222-74

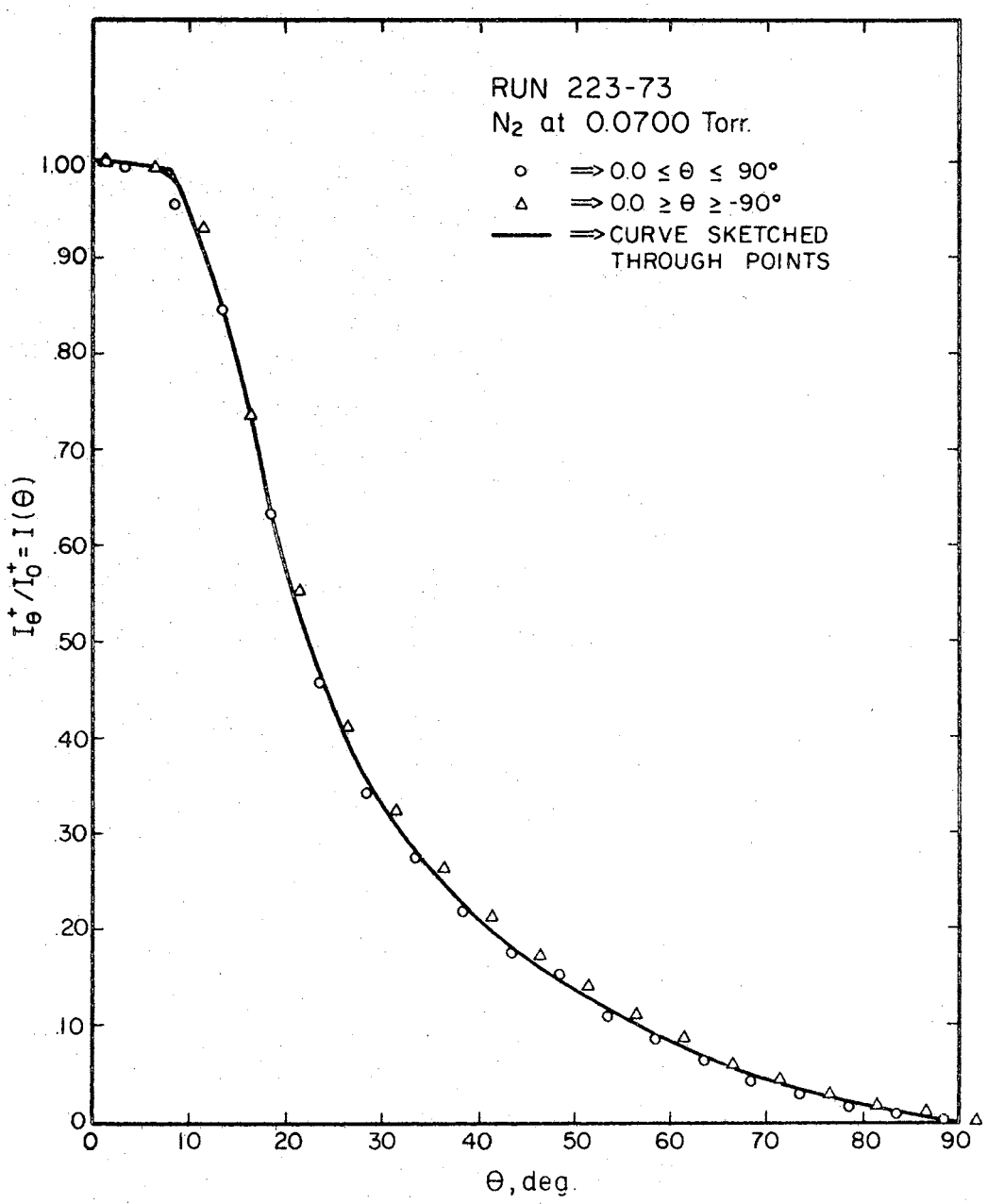

Figure 68. Normalized Experimental Intensities for Run 223-73

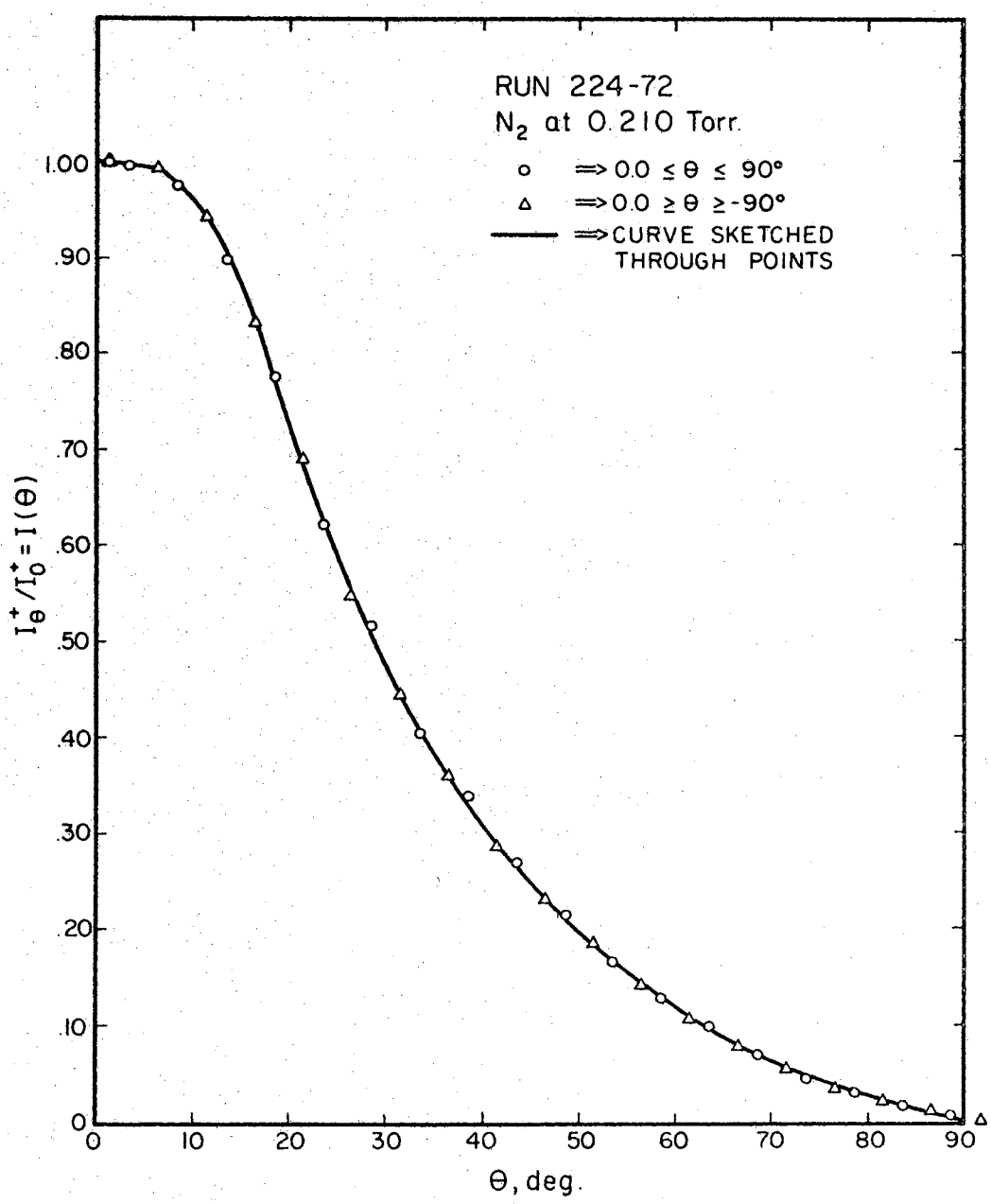

Figure 69. Normalized Experimental Intensities for Run 224-72

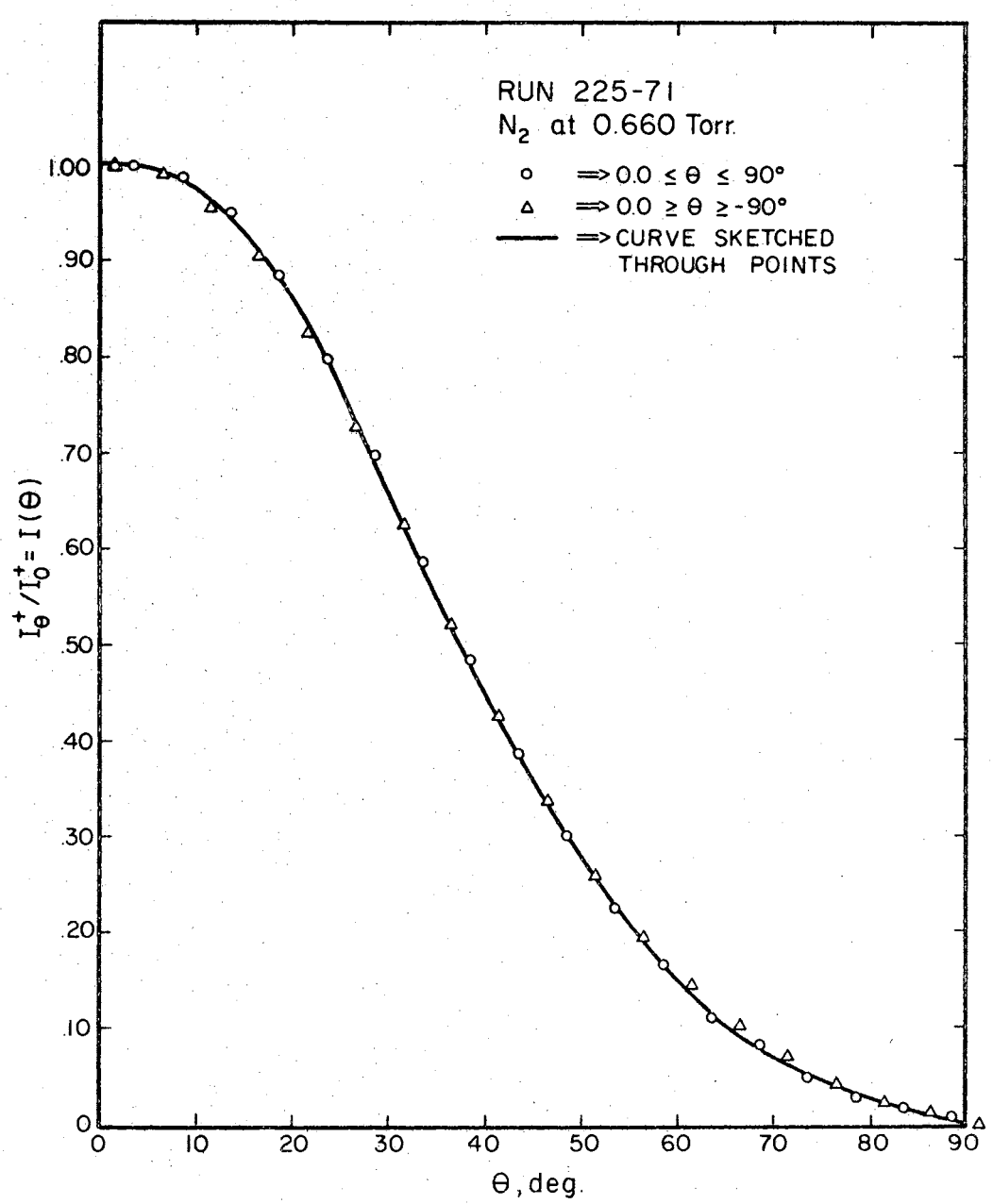

Figure 70. Normalized Experimental Intensities for Run 225-71

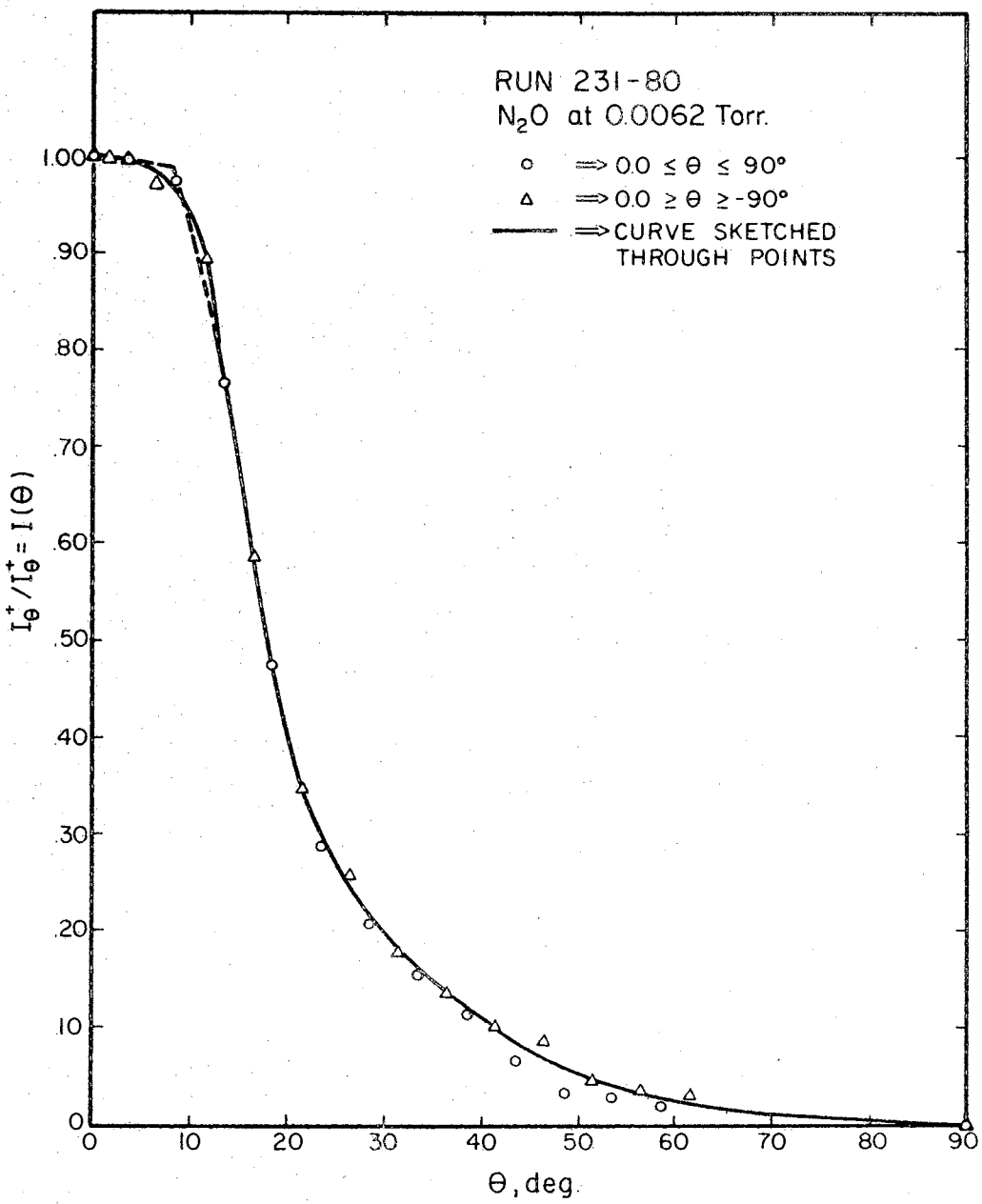

Figure 71. Normalized Experimental Intensities for Run 231-80

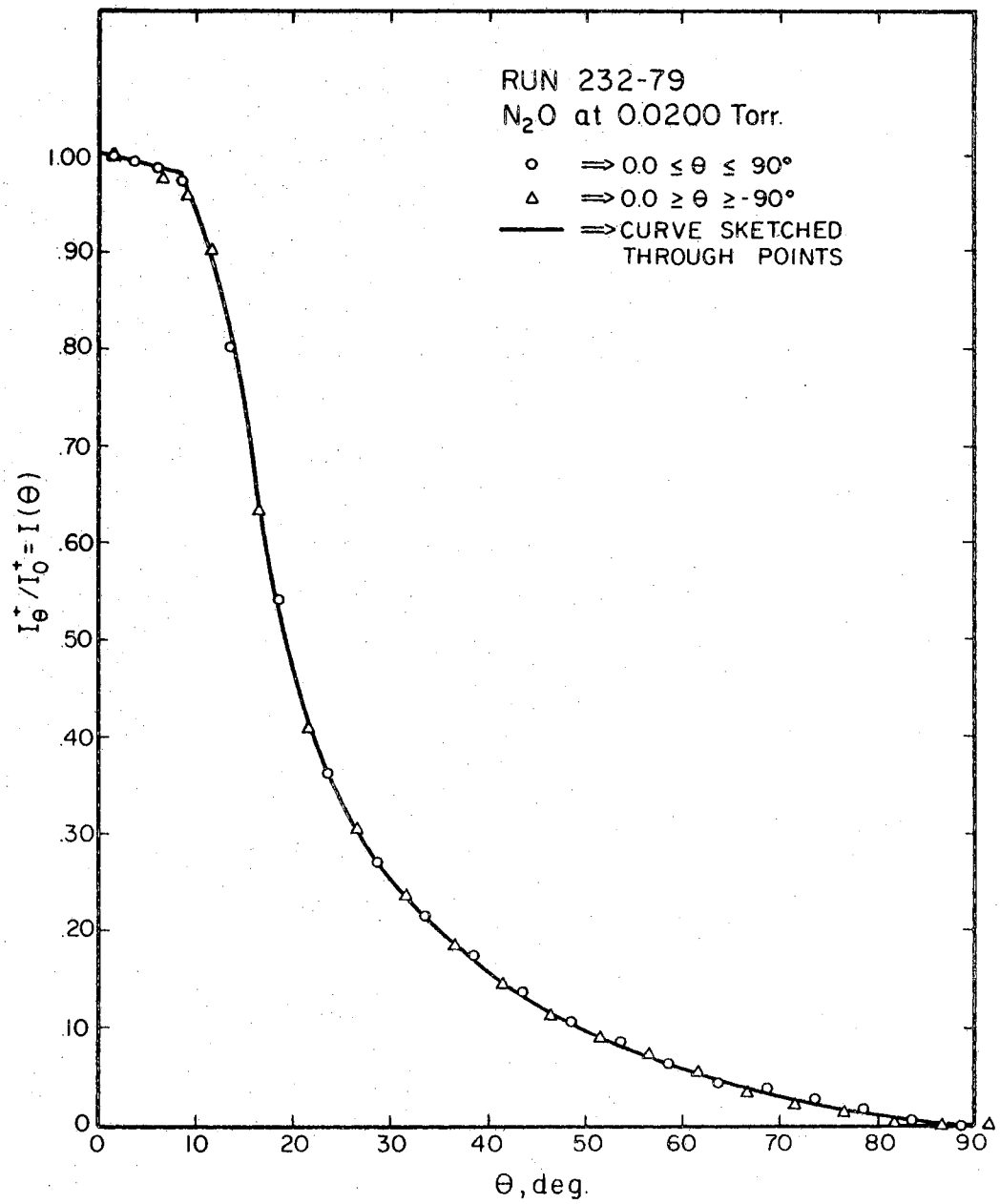

Figure 72. Normalized Experimental Intensities for Run 232-79

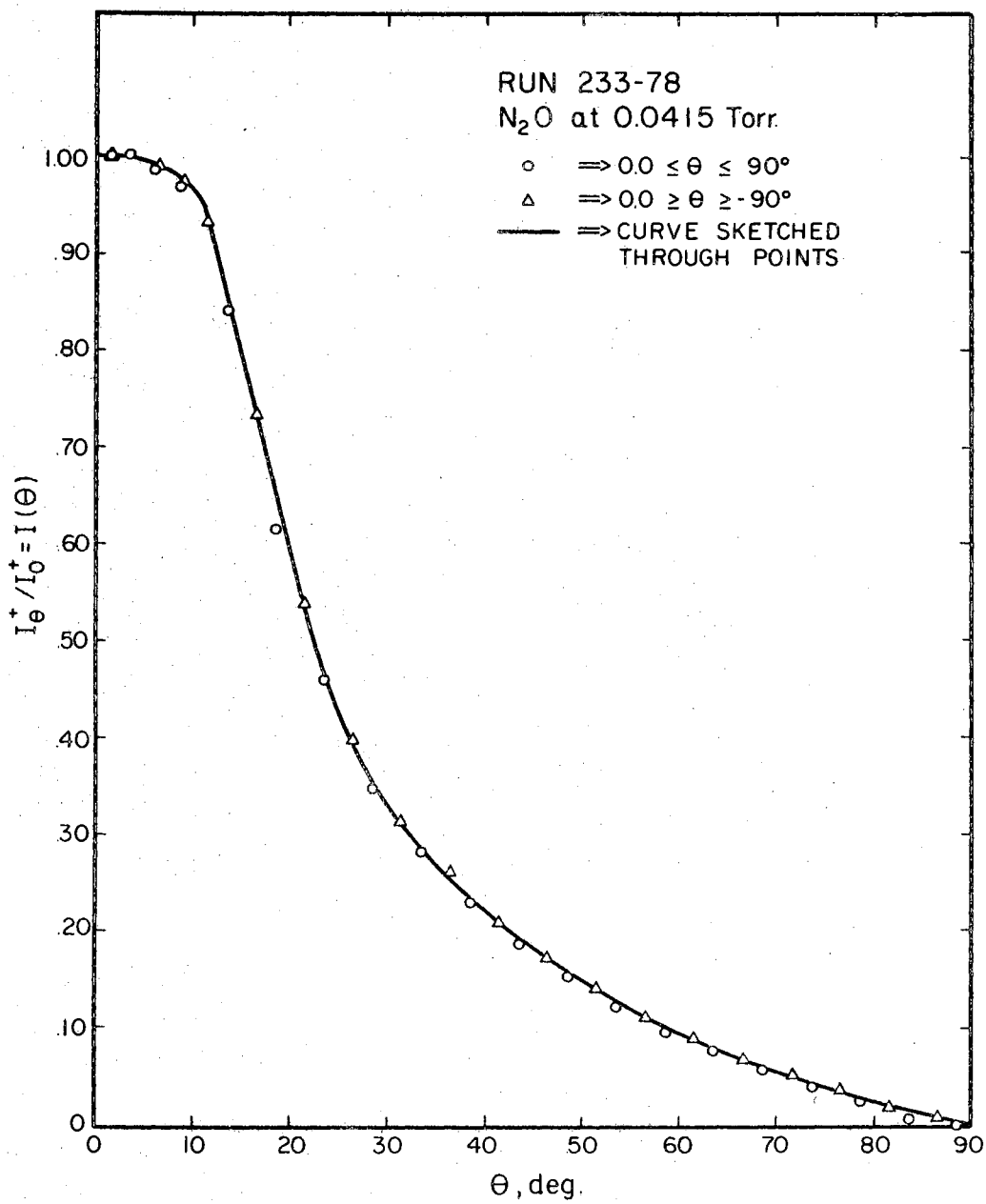

Figure 73. Normalized Experimental Intensities for Run 233-78

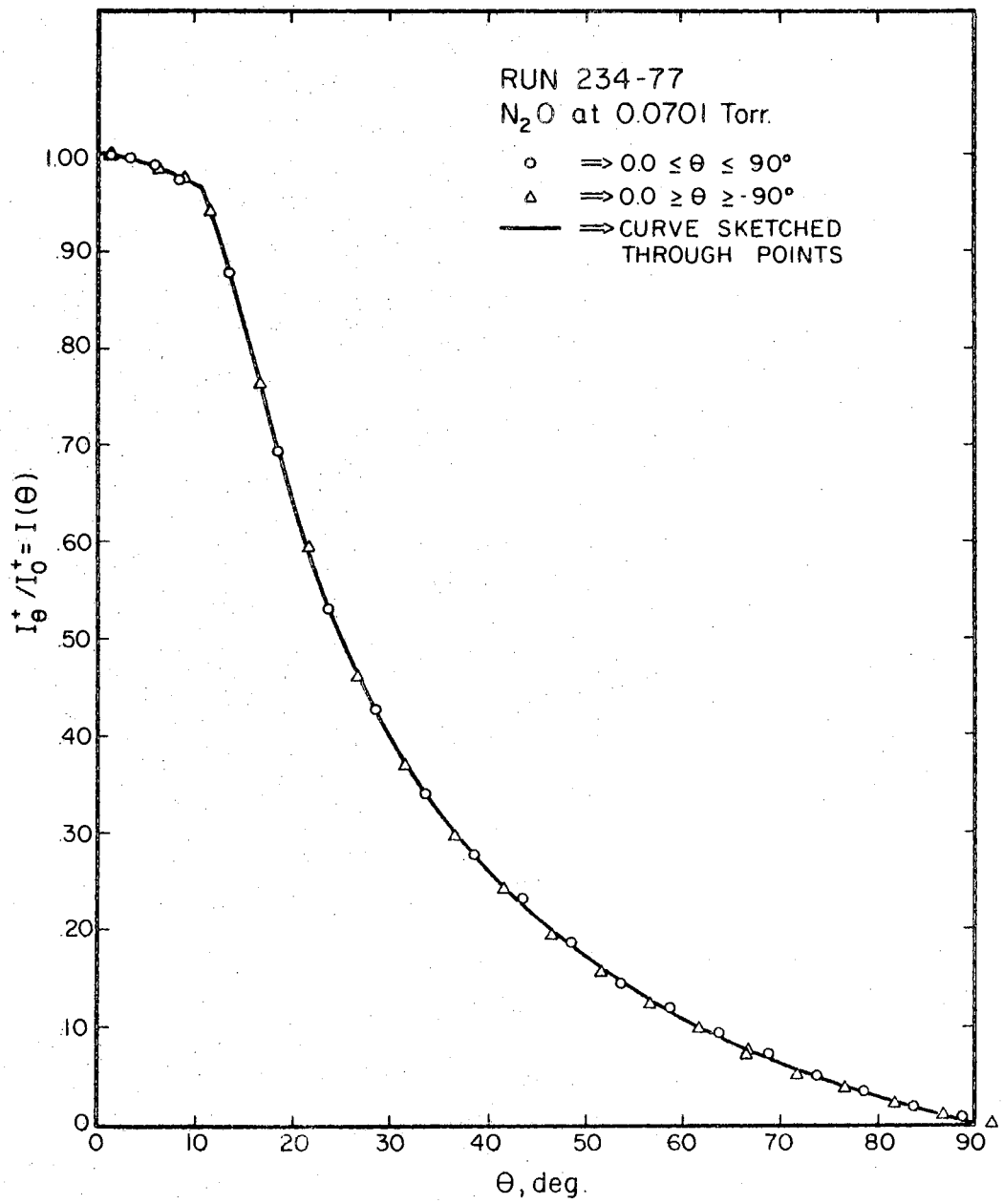

Figure 74. Normalized Experimental Intensities for Run 234-77

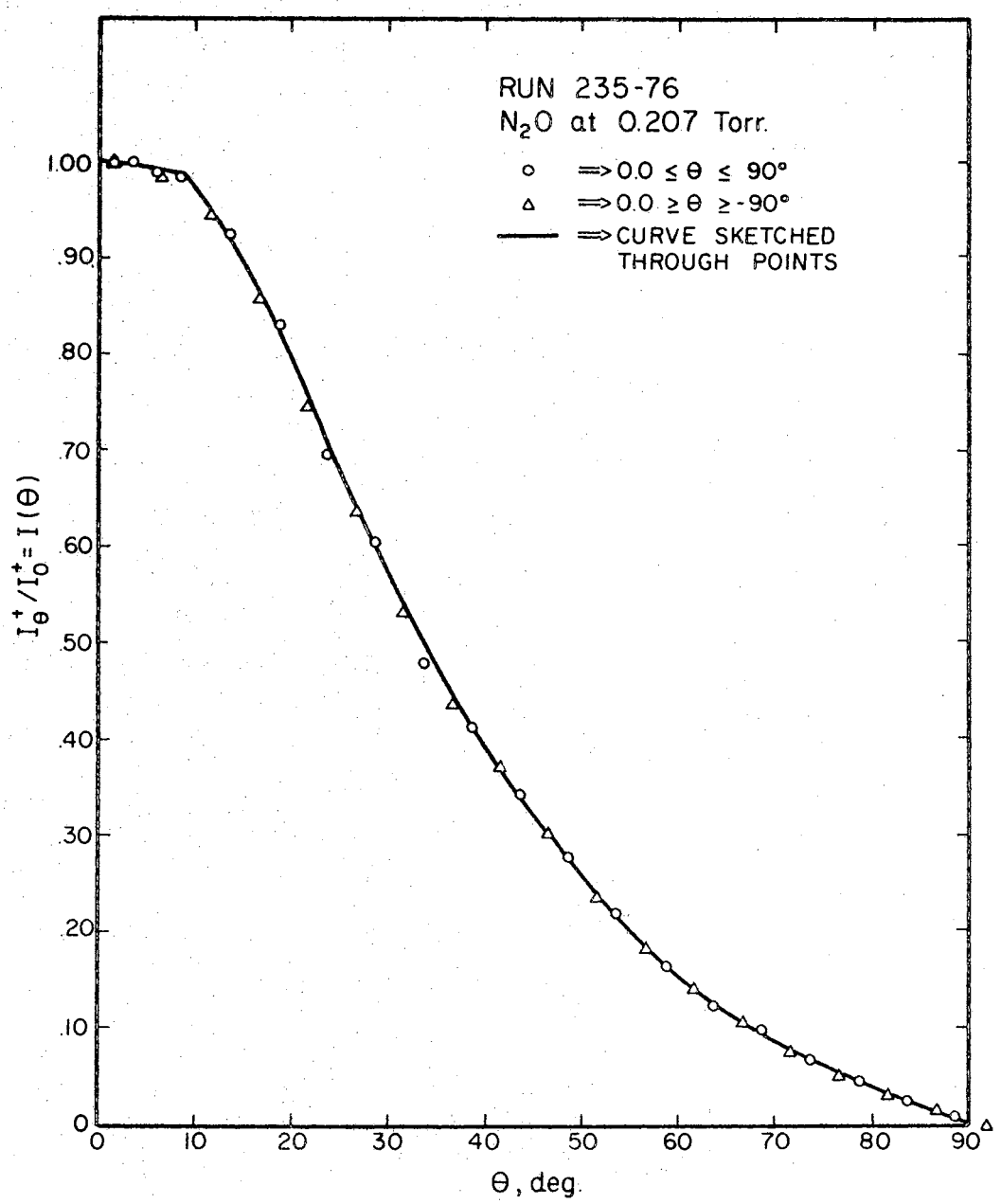

Figure 75. Normalized Experimental Intensities for Run 235-76

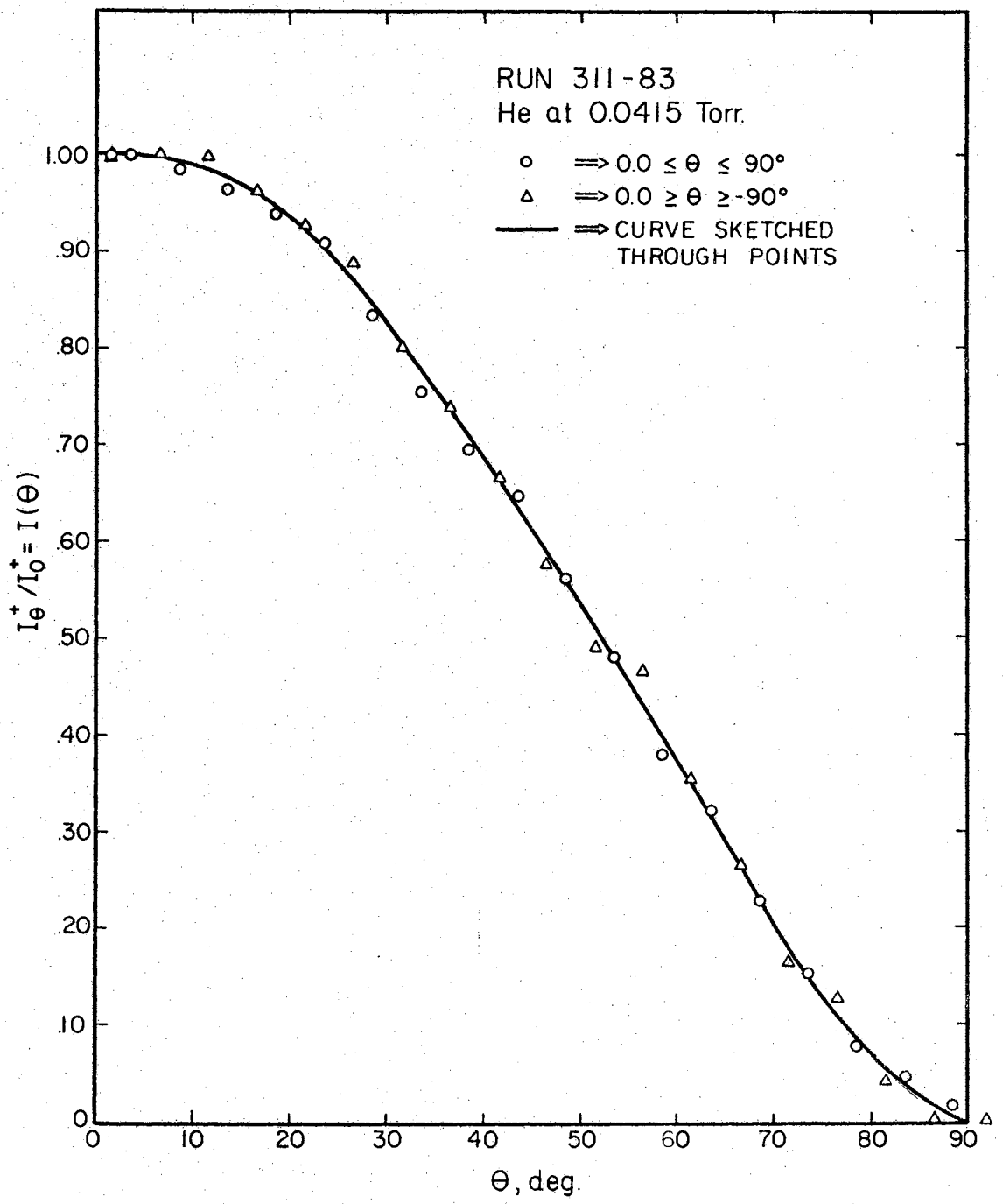

Figure 76. Normalized Experimental Intensities for Run 311-83

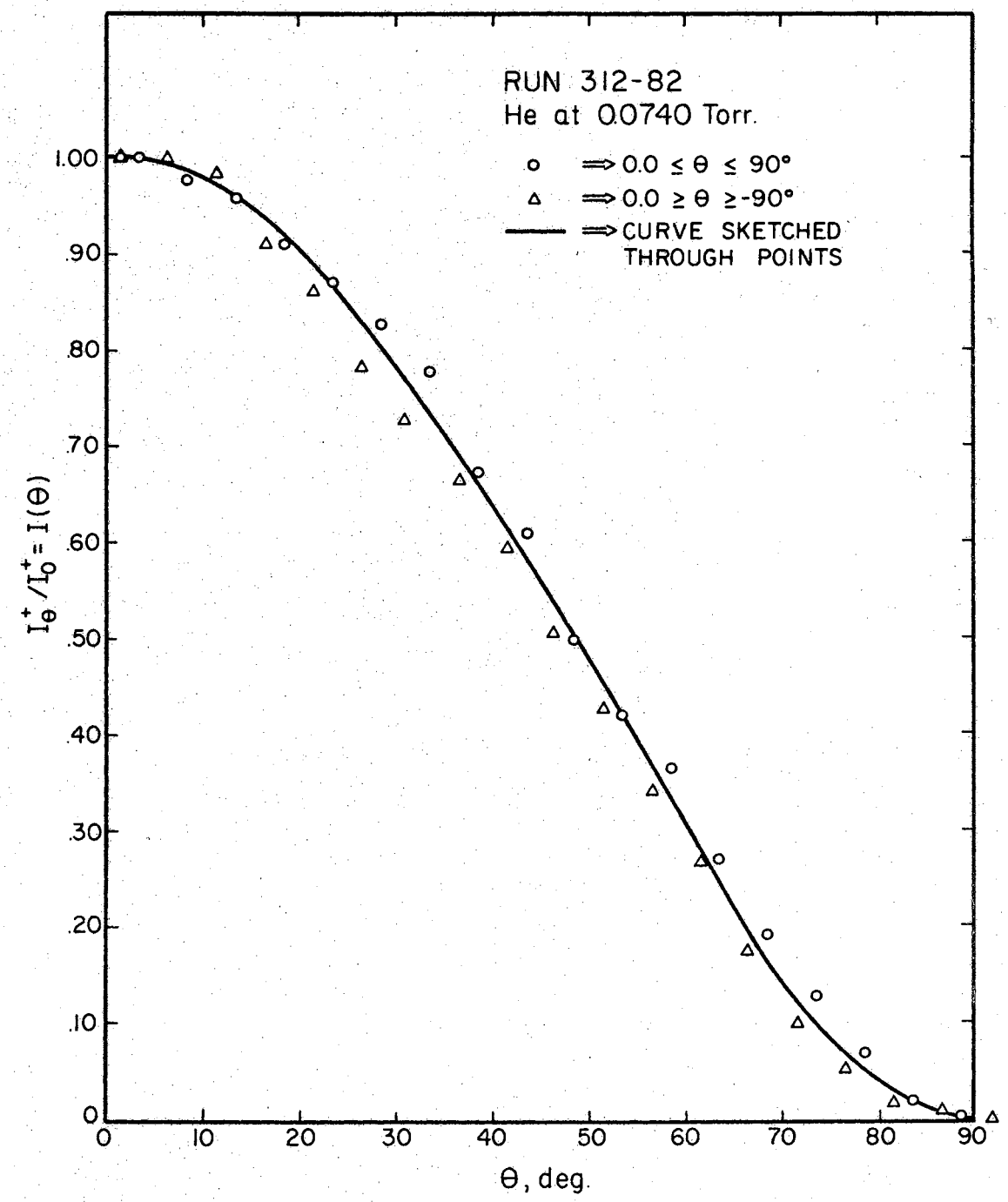

Figure 77. Normalized Experimental Intensities for Run 312-82

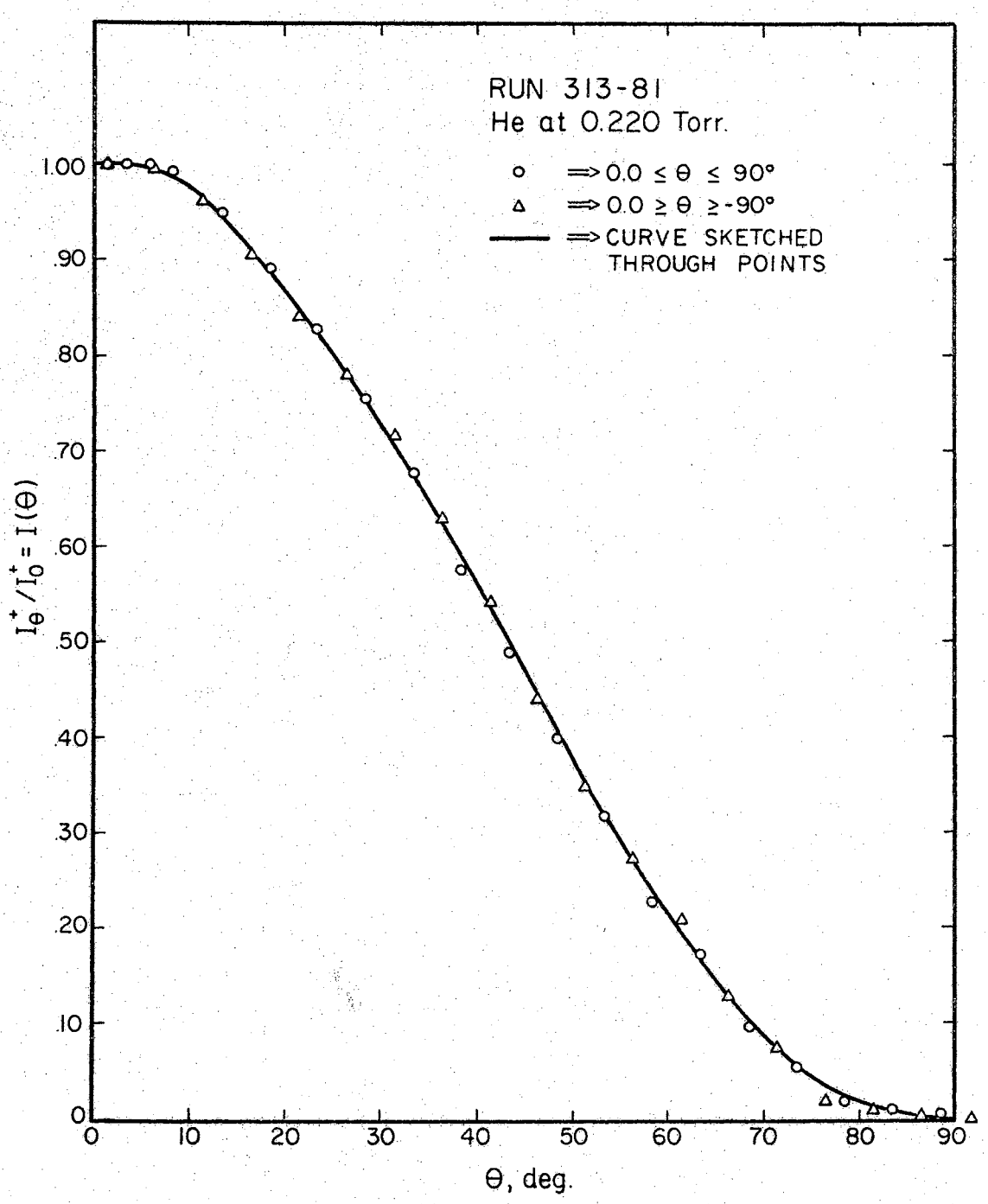

Figure 78. Normalized Experimental Intensities for Run 313-81

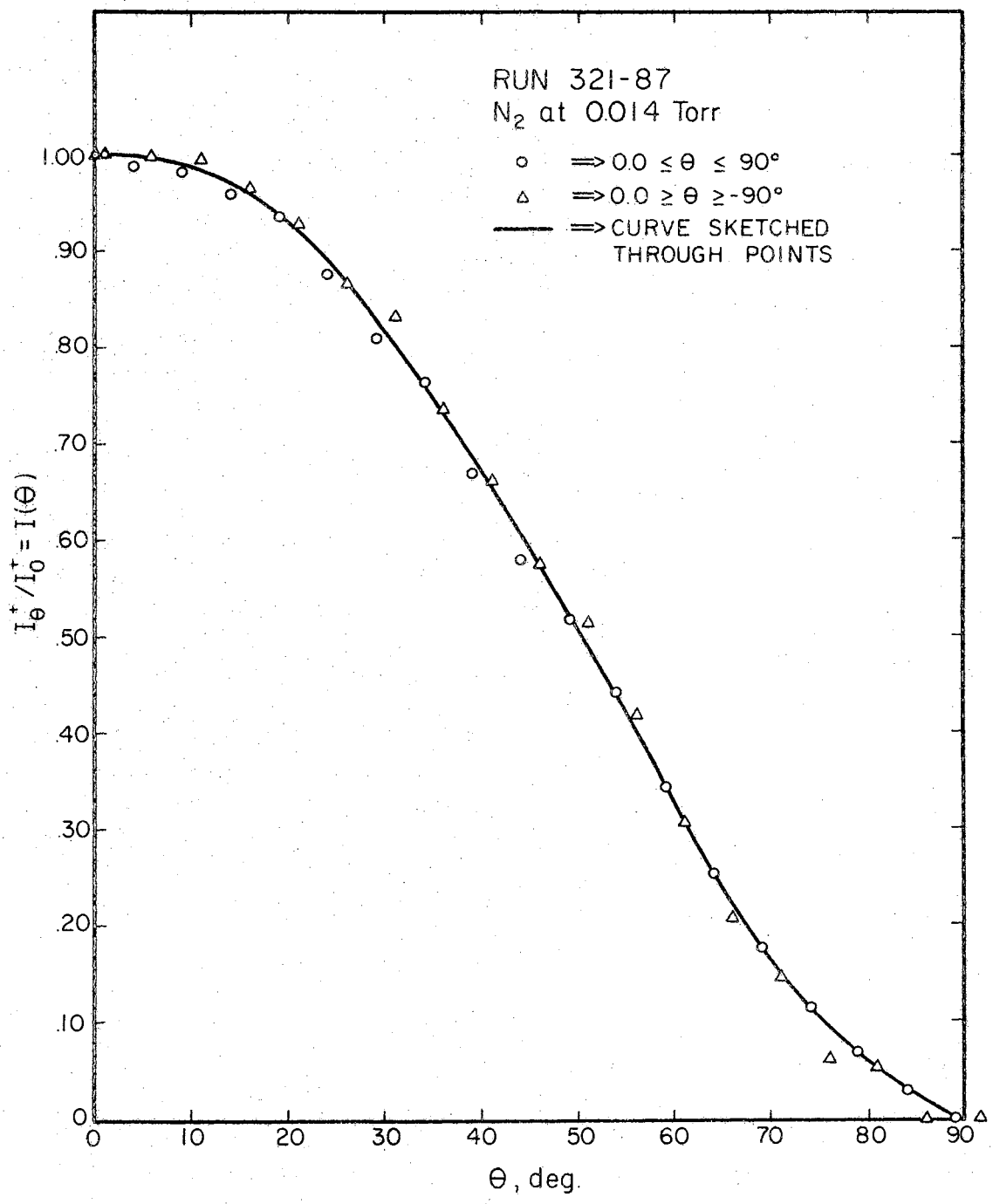

Figure 79. Normalized Experimental Intensities for Run 321-87

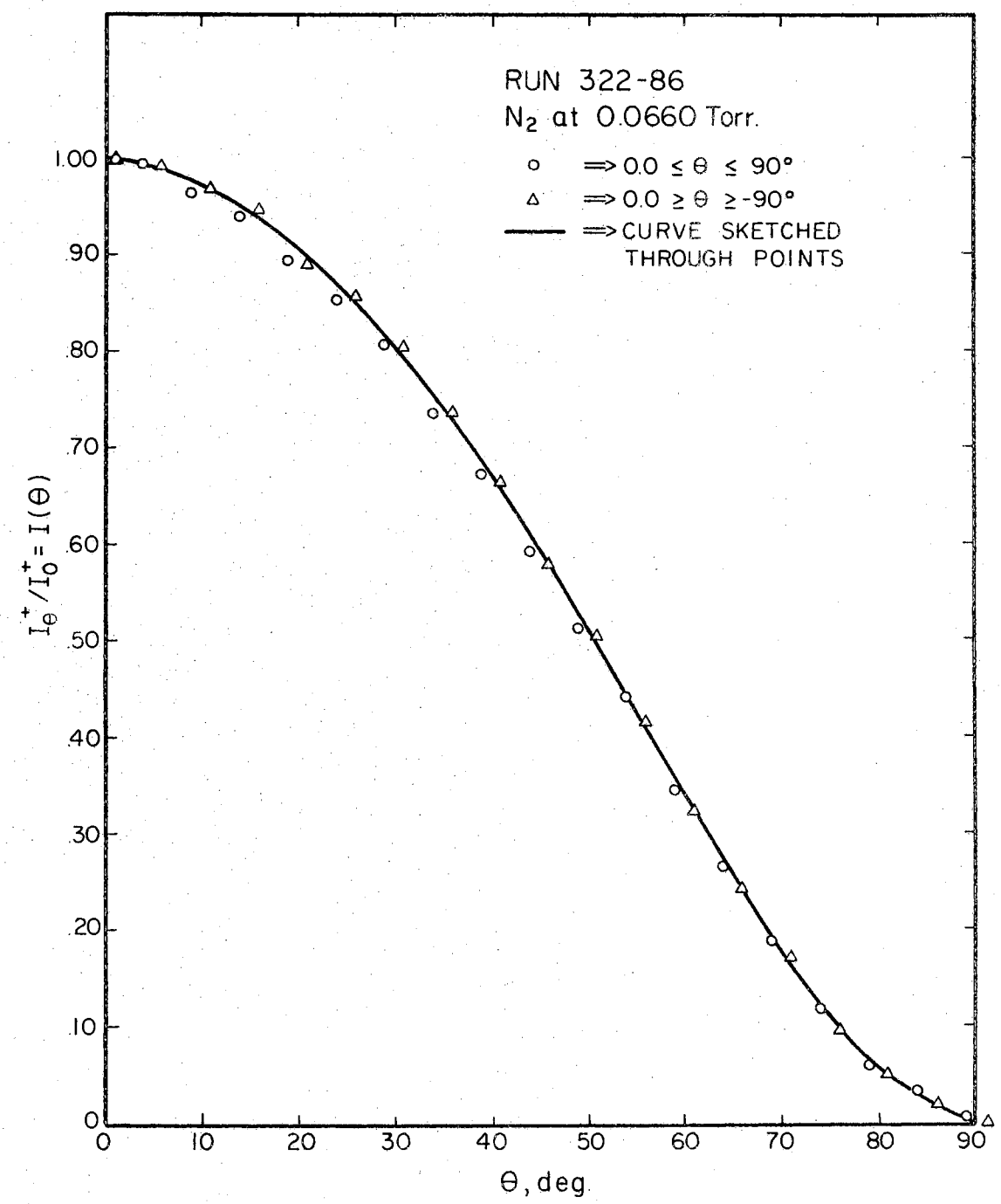

Figure 80. Normalized Experimental Intensities for Run 322-86

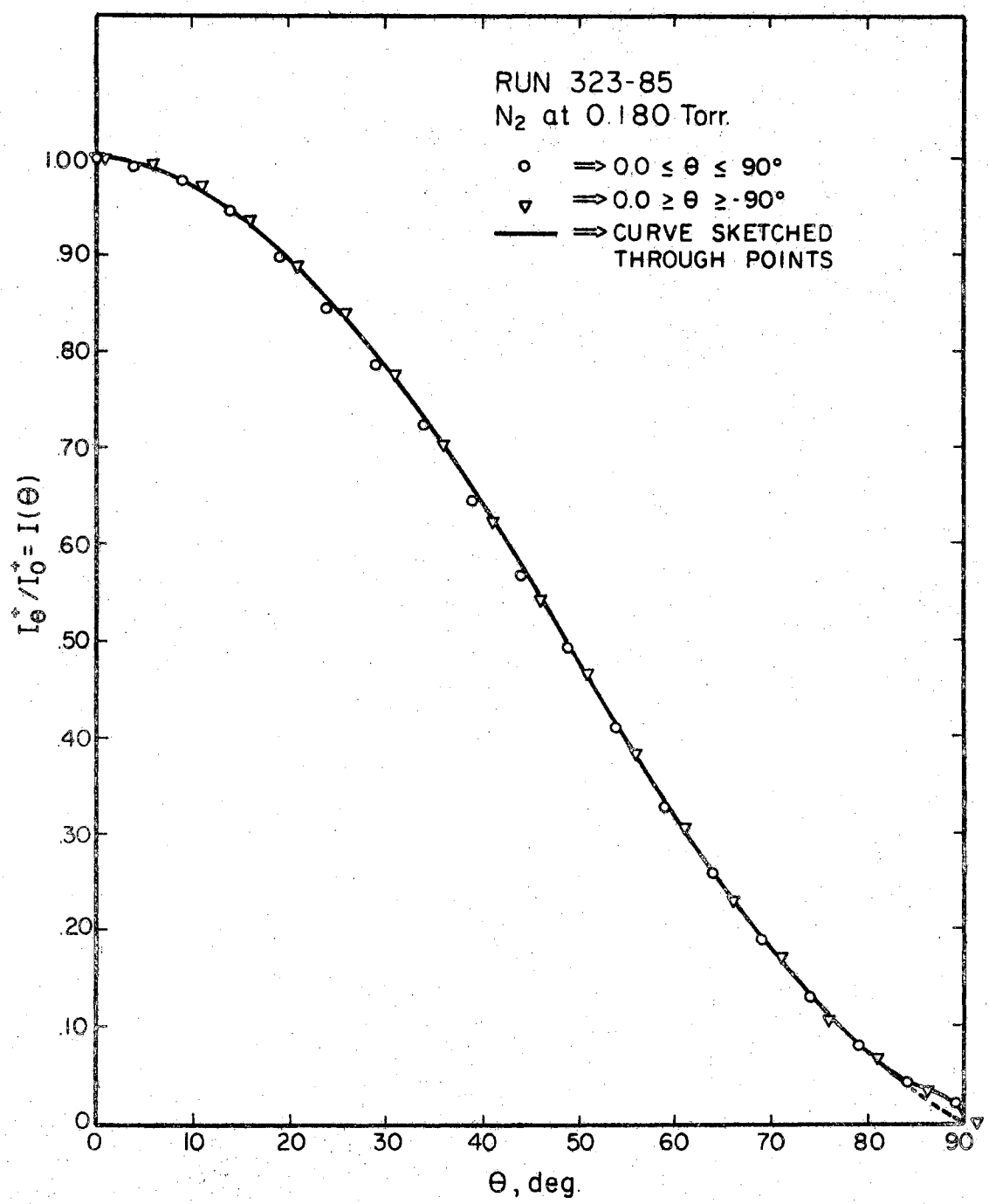

Figure 81. Normalized Experimental Intensities for Run 323-85

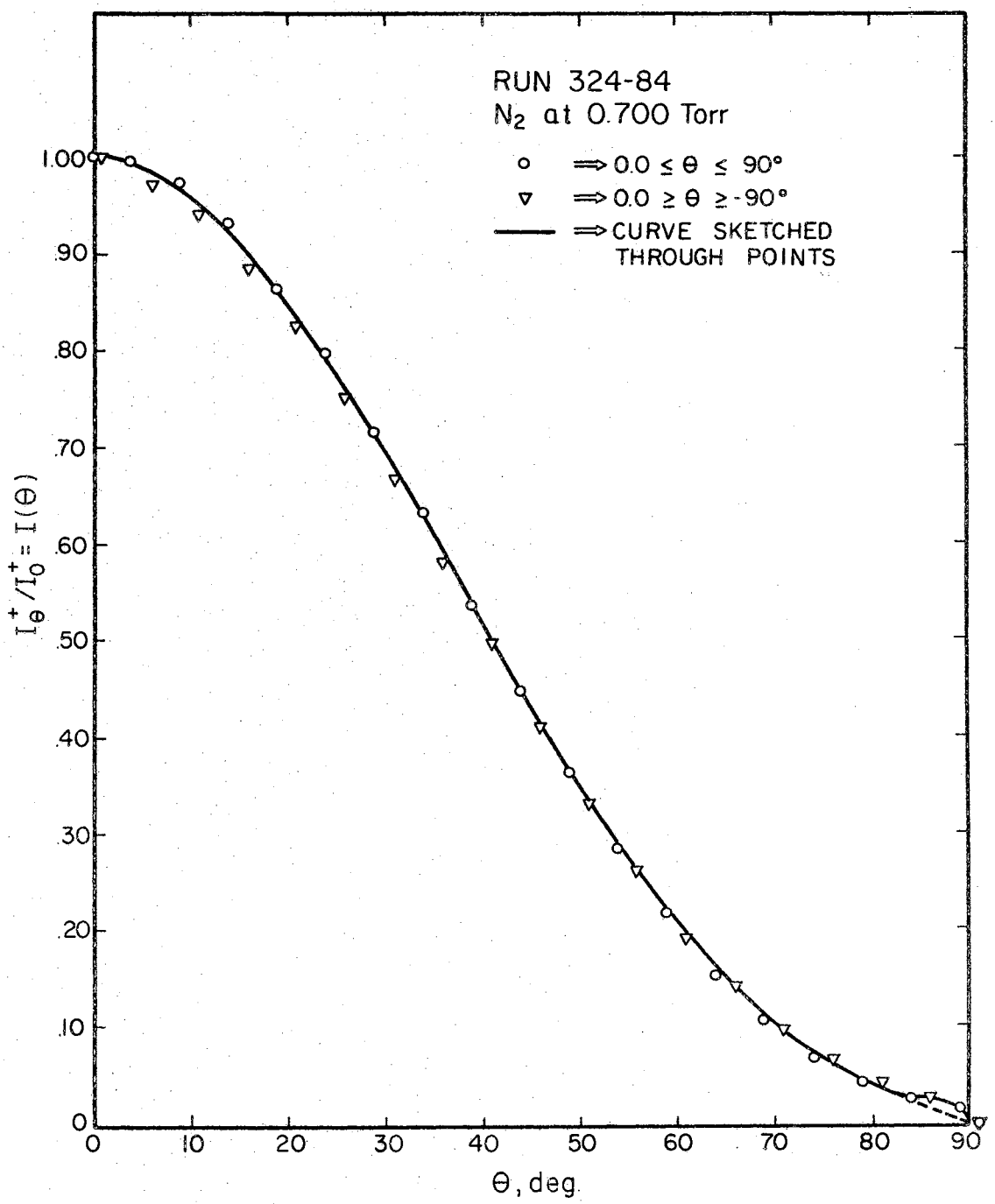

Figure 82. Normalized Experimental Intensities for Run 324-84

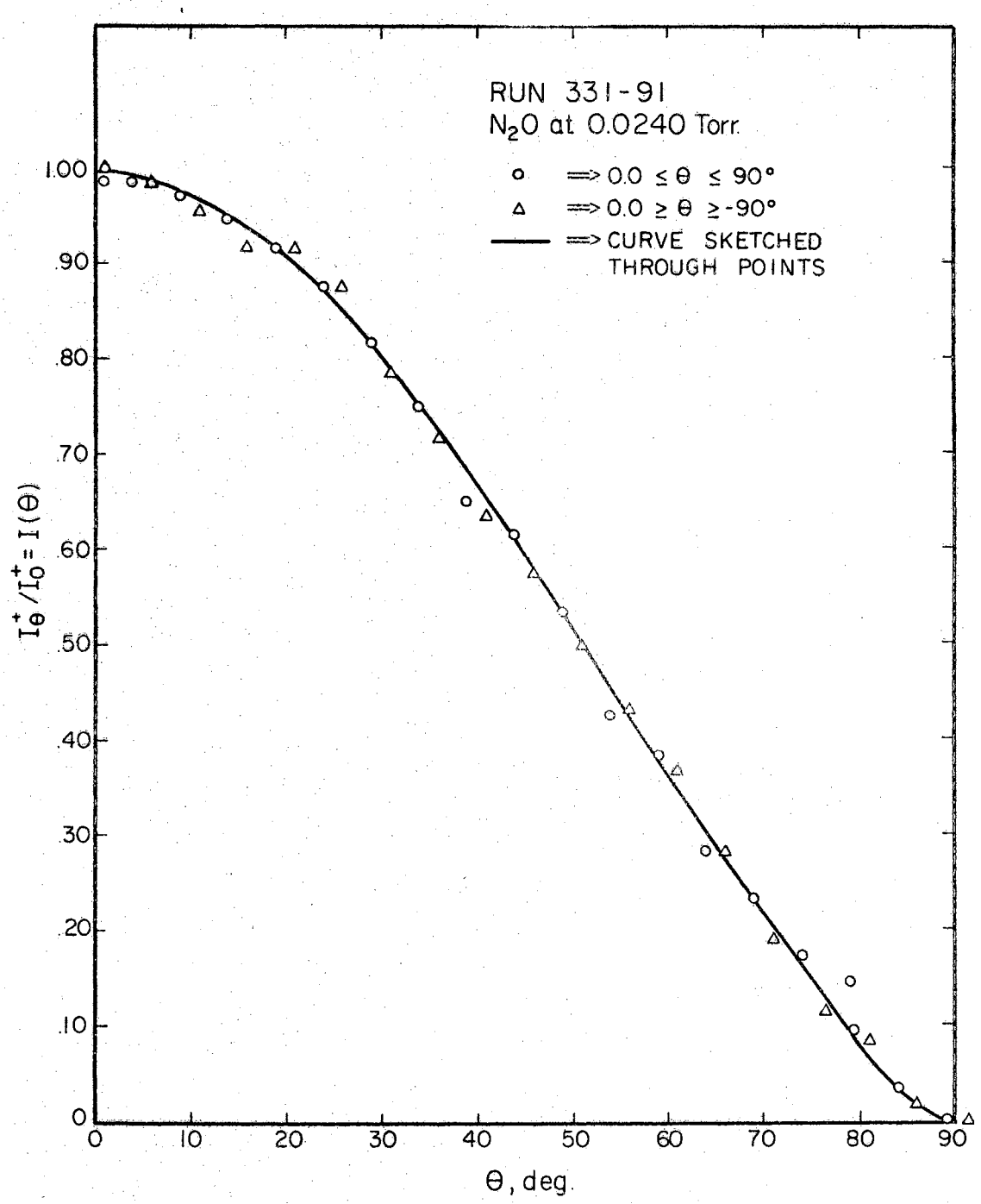

Figure 83. Normalized Experimental Intensities for Run 331-91.

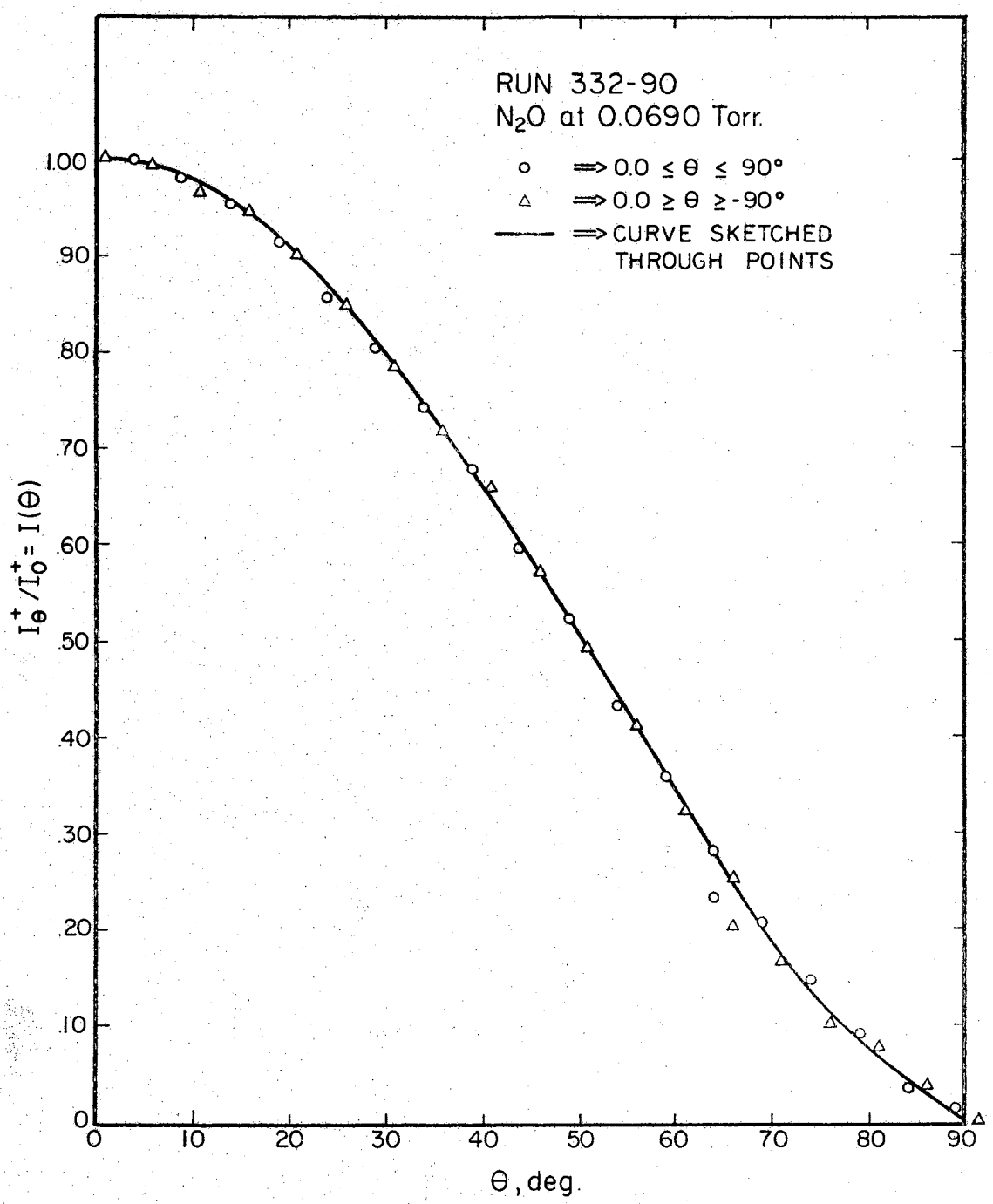

Figure 84. Normalized Experimental Intensities for Run 332-90

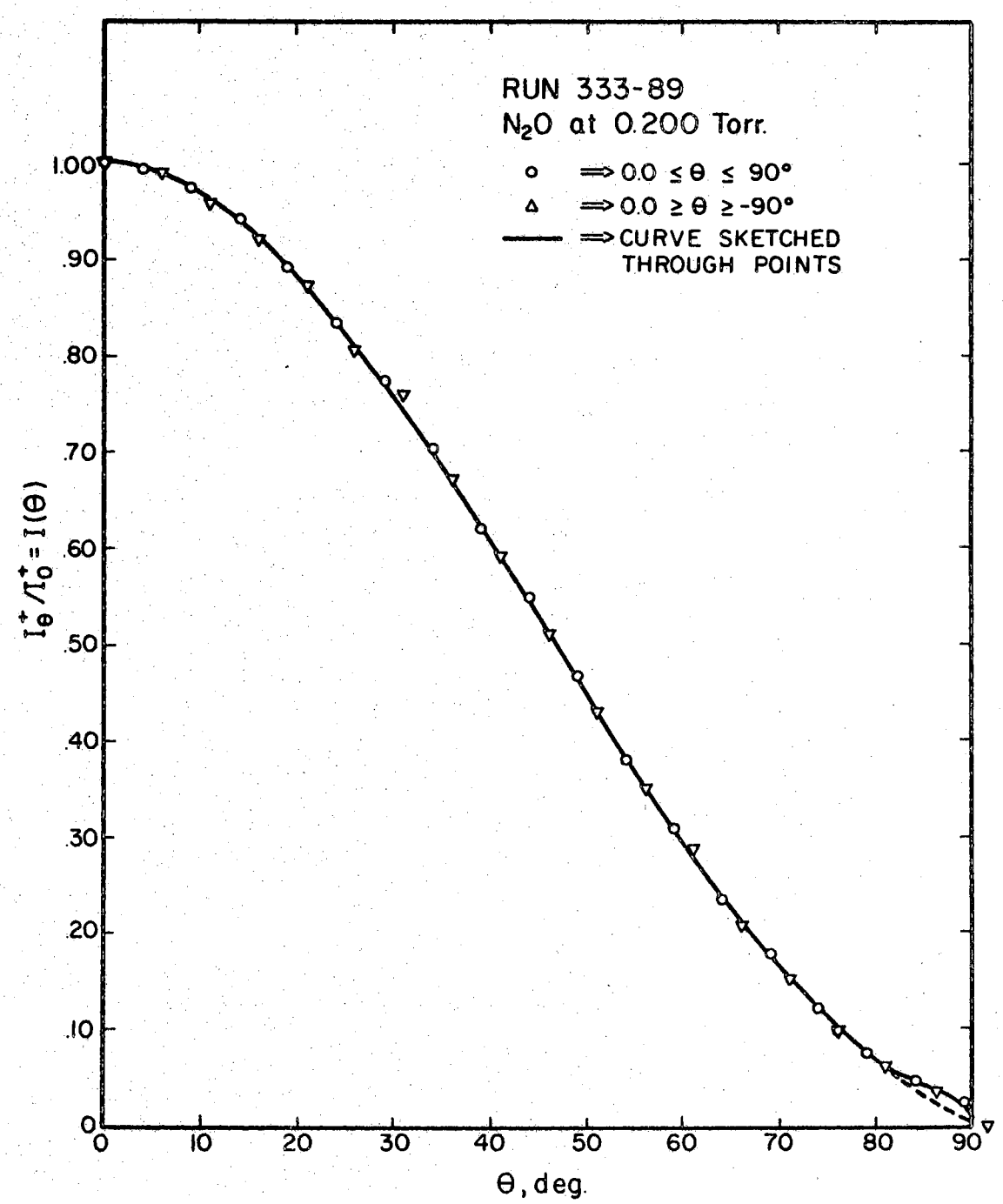

Figure 85. Normalized Experimental Intensities for Run 333-89

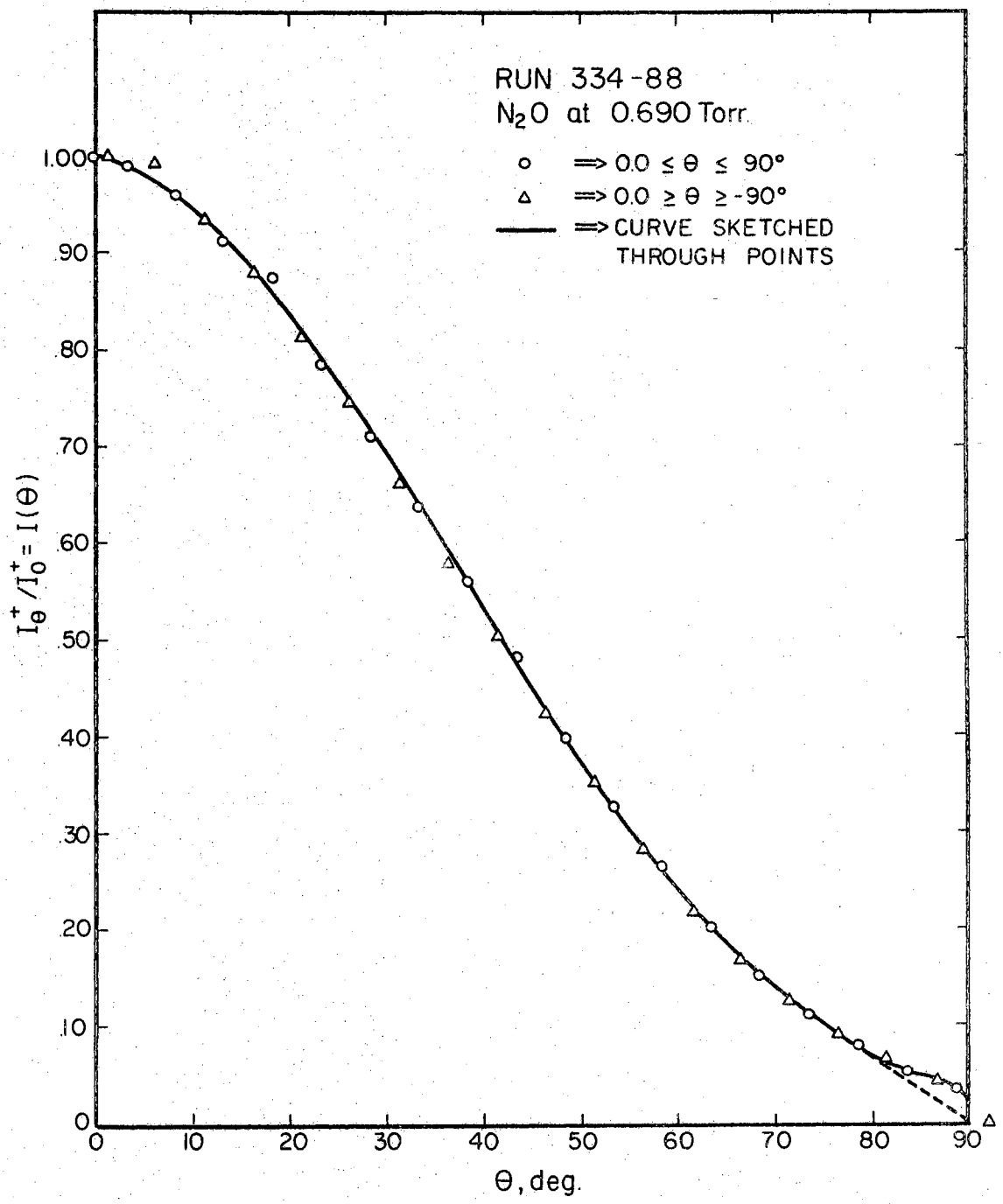

Figure 86. Normalized Experimental Intensities for Run 334-88

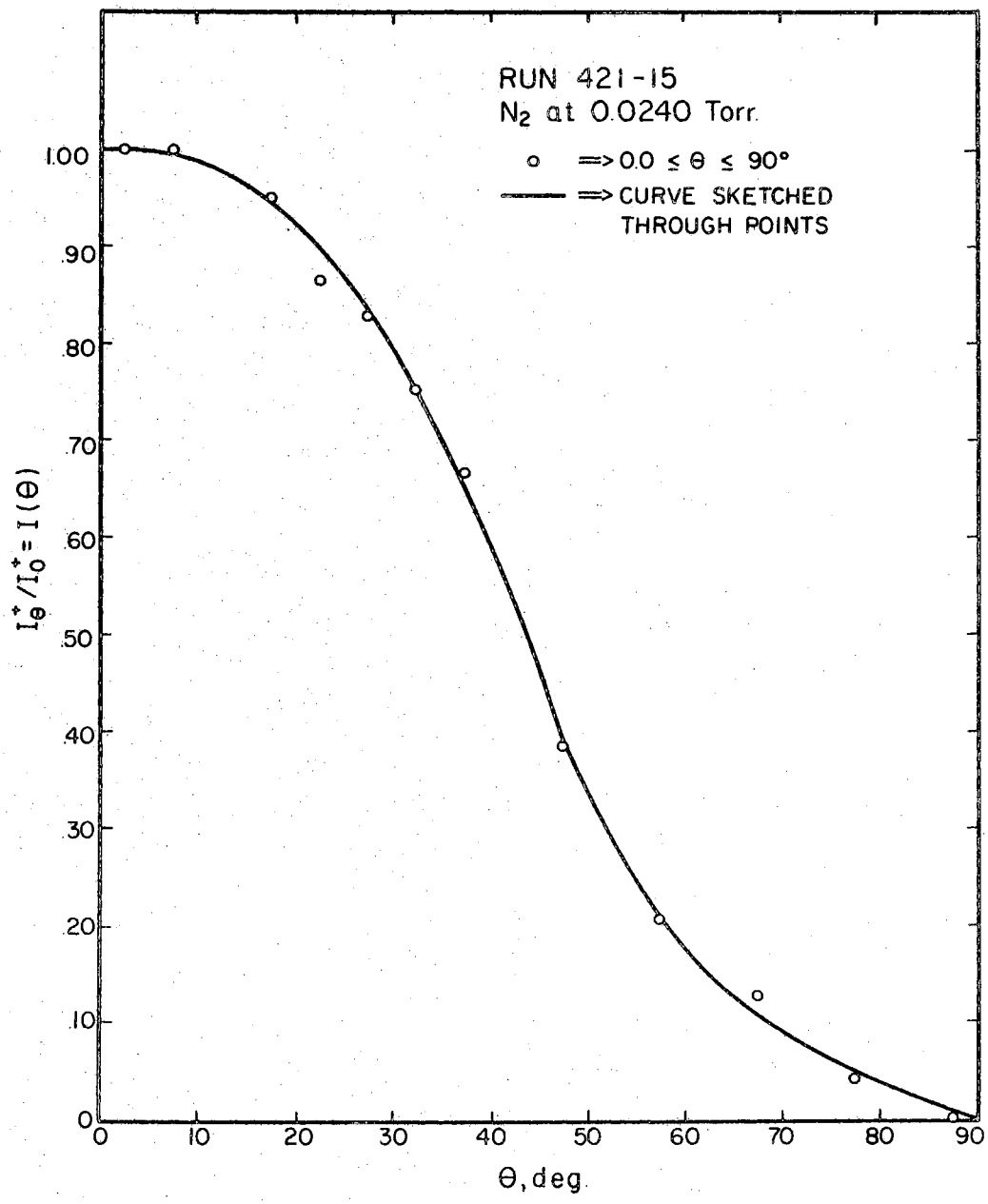

Figure 87. Normalized Experimental Intensities for Run 421-15

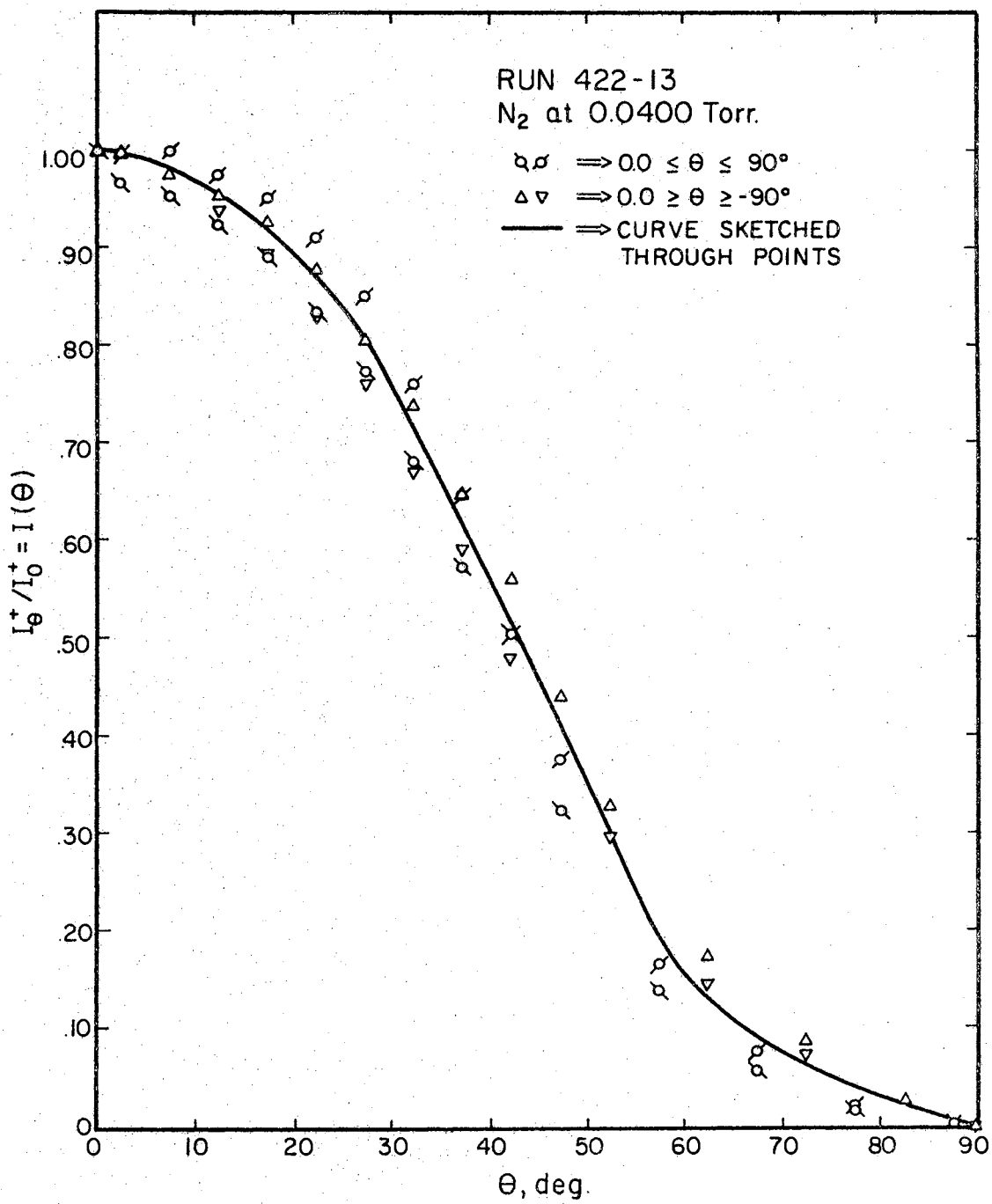

Figure 88. Normalized Experimental Intensities for Run 422-13

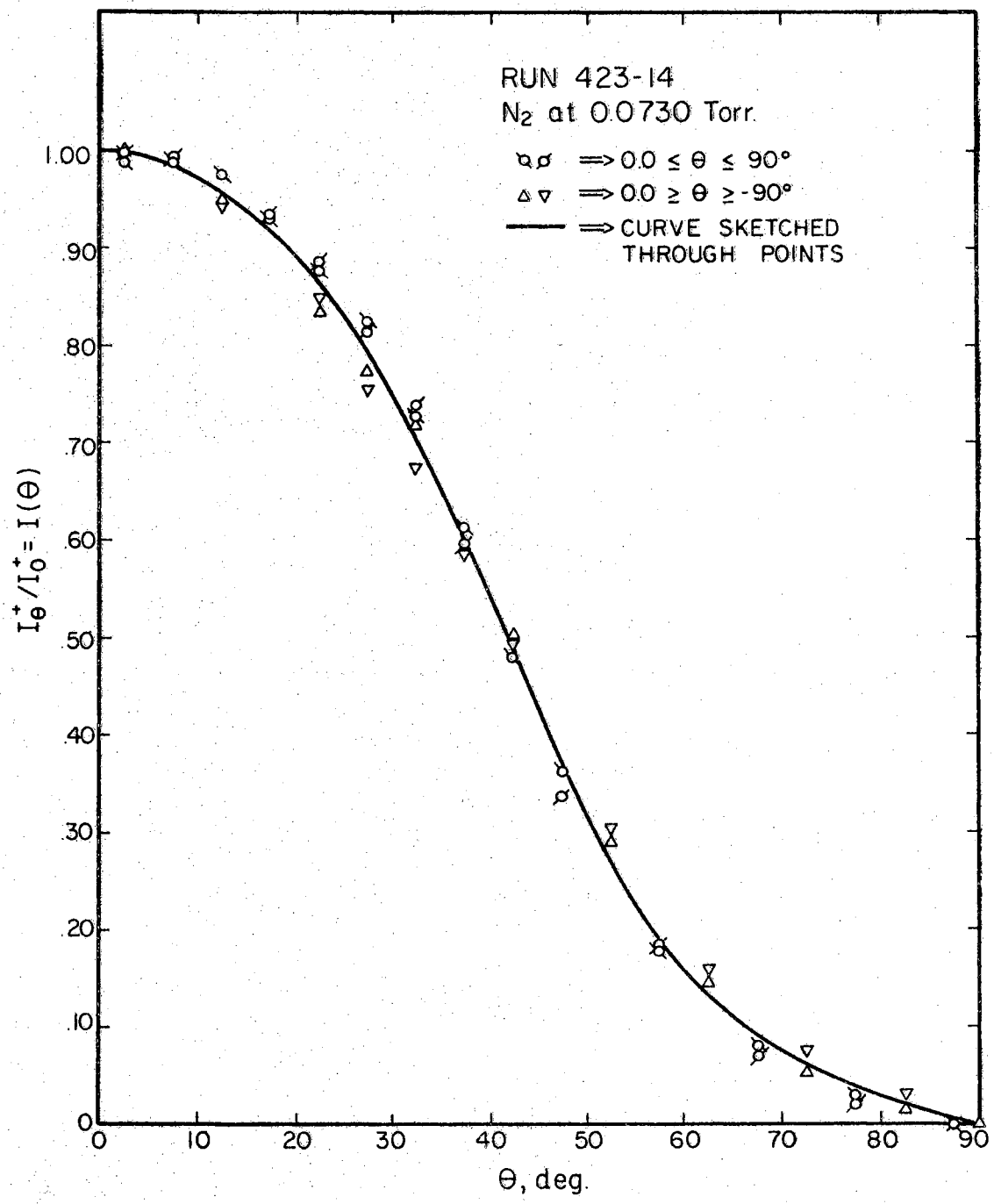

Figure 89. Normalized Experimental Intensities for Run 423-14

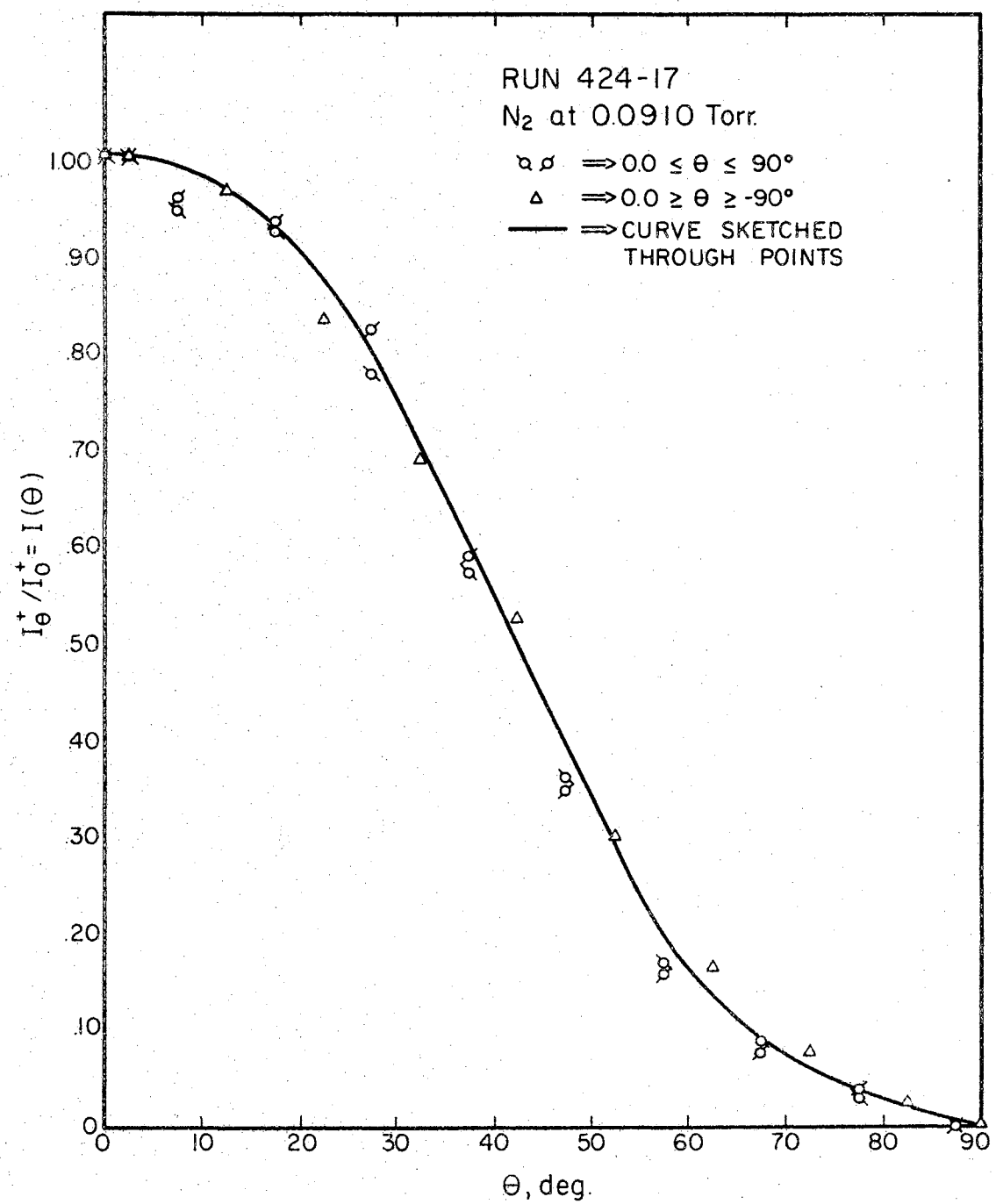

Figure 90. Normalized Experimental Intensities for Run 424-17

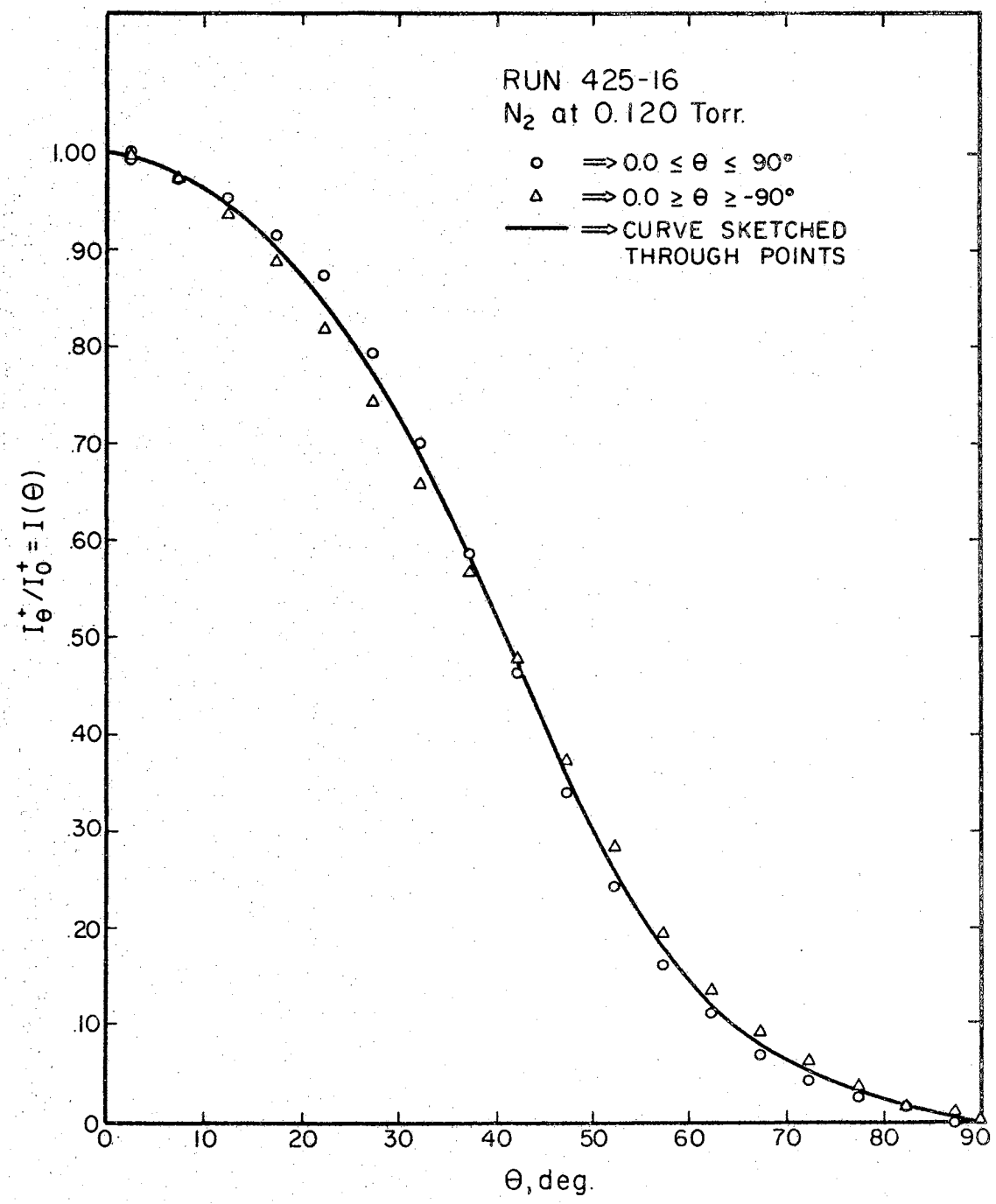

Figure 91. Normalized Experimental Intensities for Run 425-16

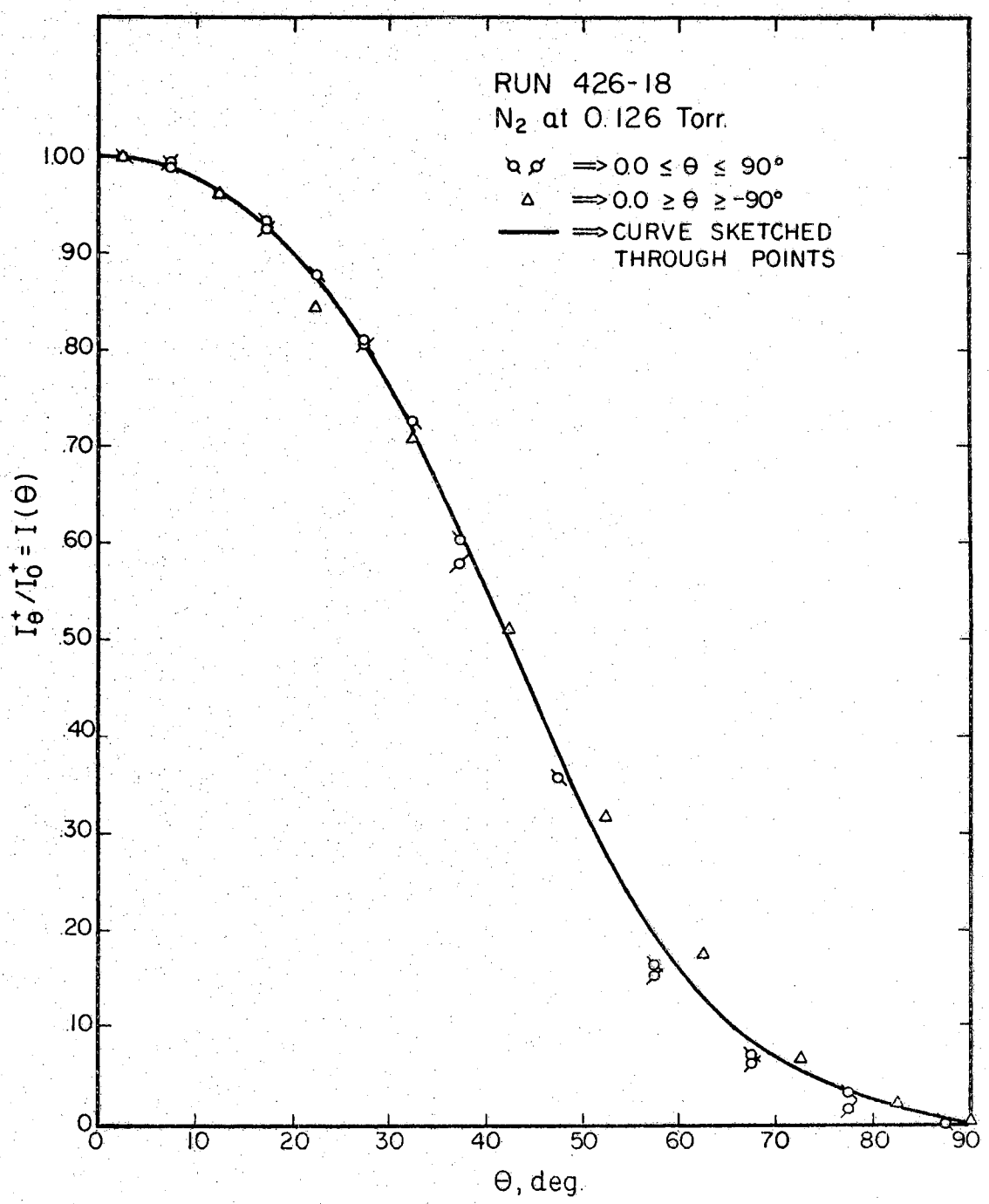

Figure 92. Normalized Experimental Intensities for Run 426-18

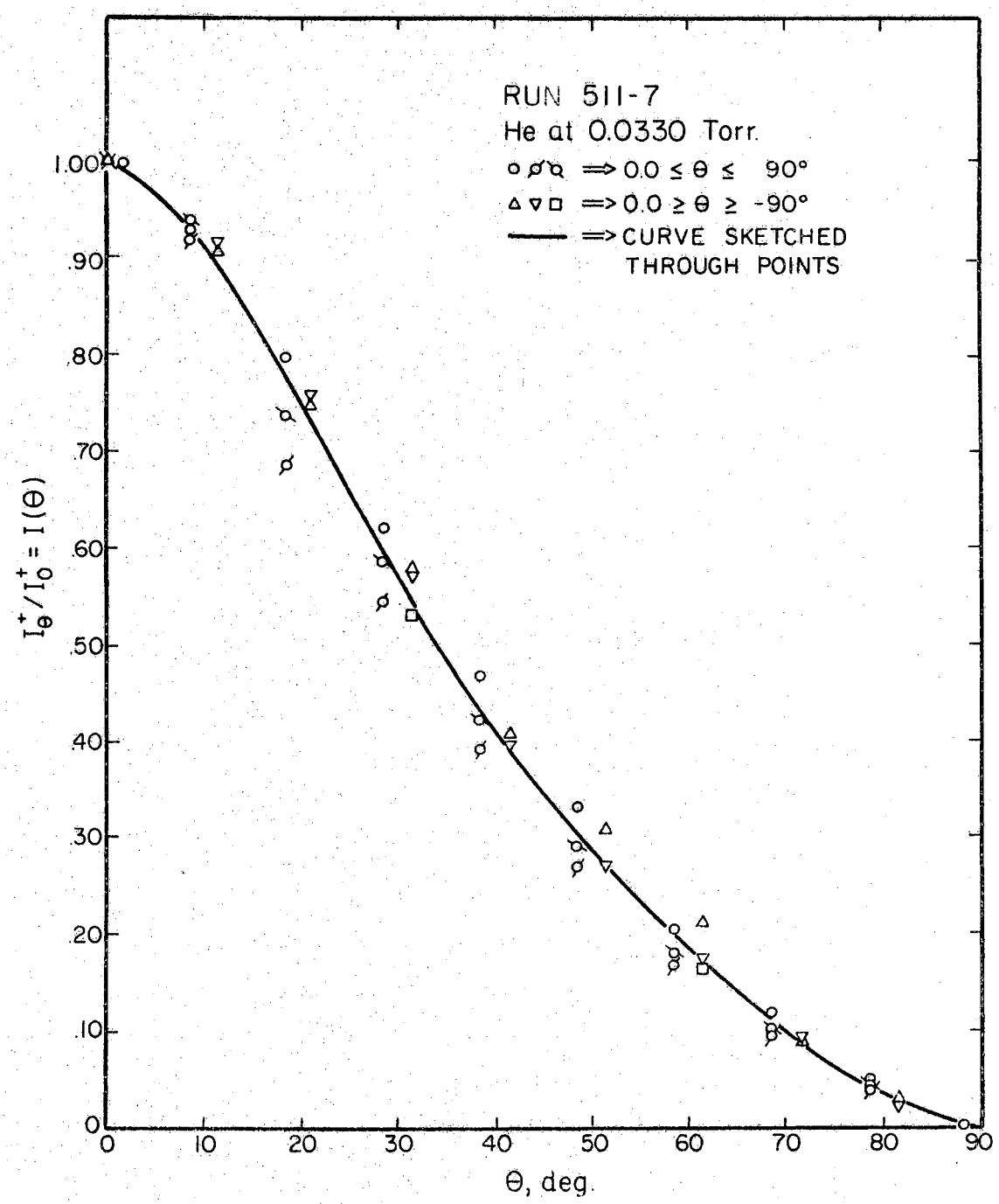

Figure 93. Normalized Experimental Intensities for Run 511-7

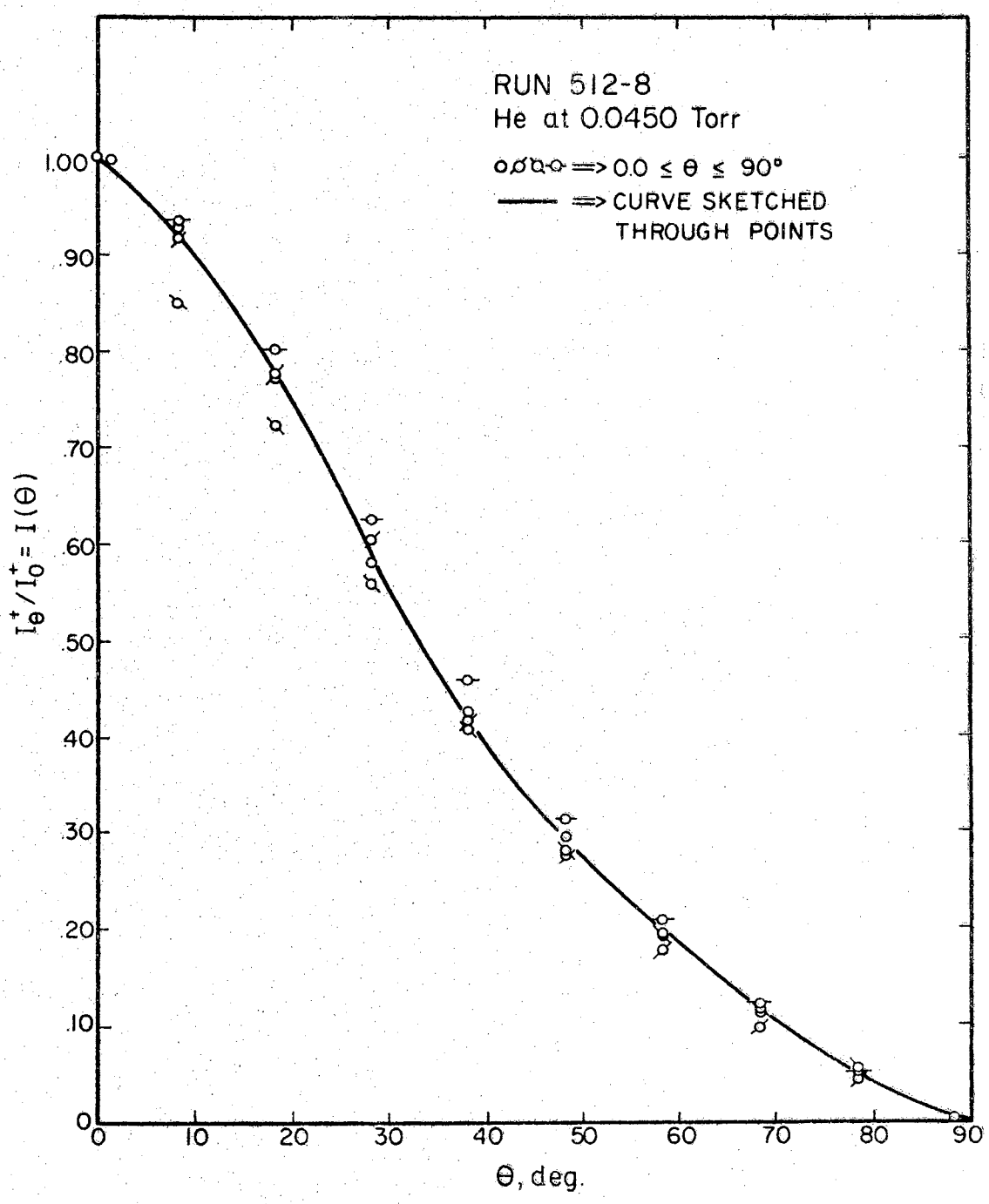

Figure 94. Normalized Experimental Intensities for Run 512-8

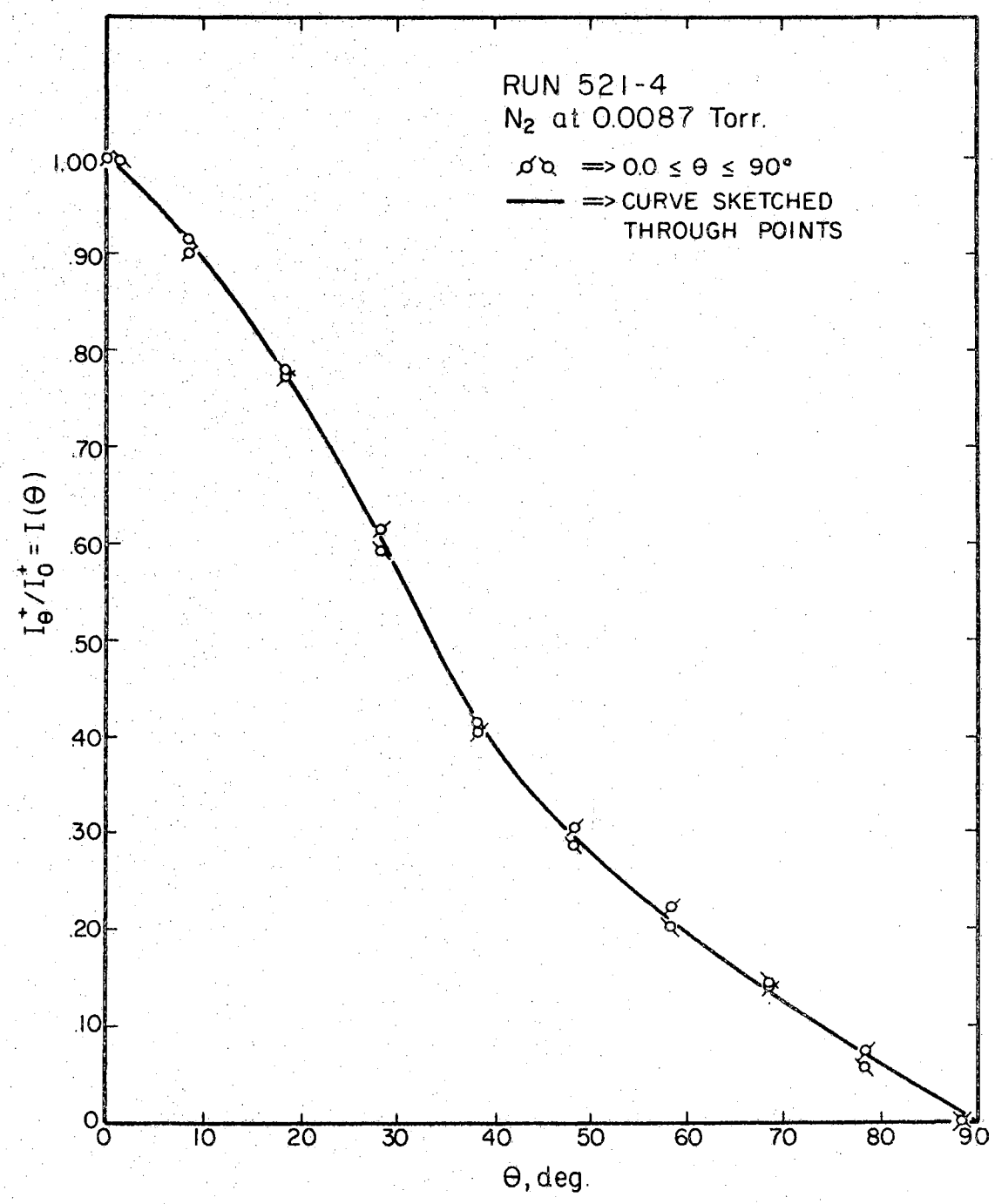

Figure 95. Normalized Experimental Intensities for Run 521-4

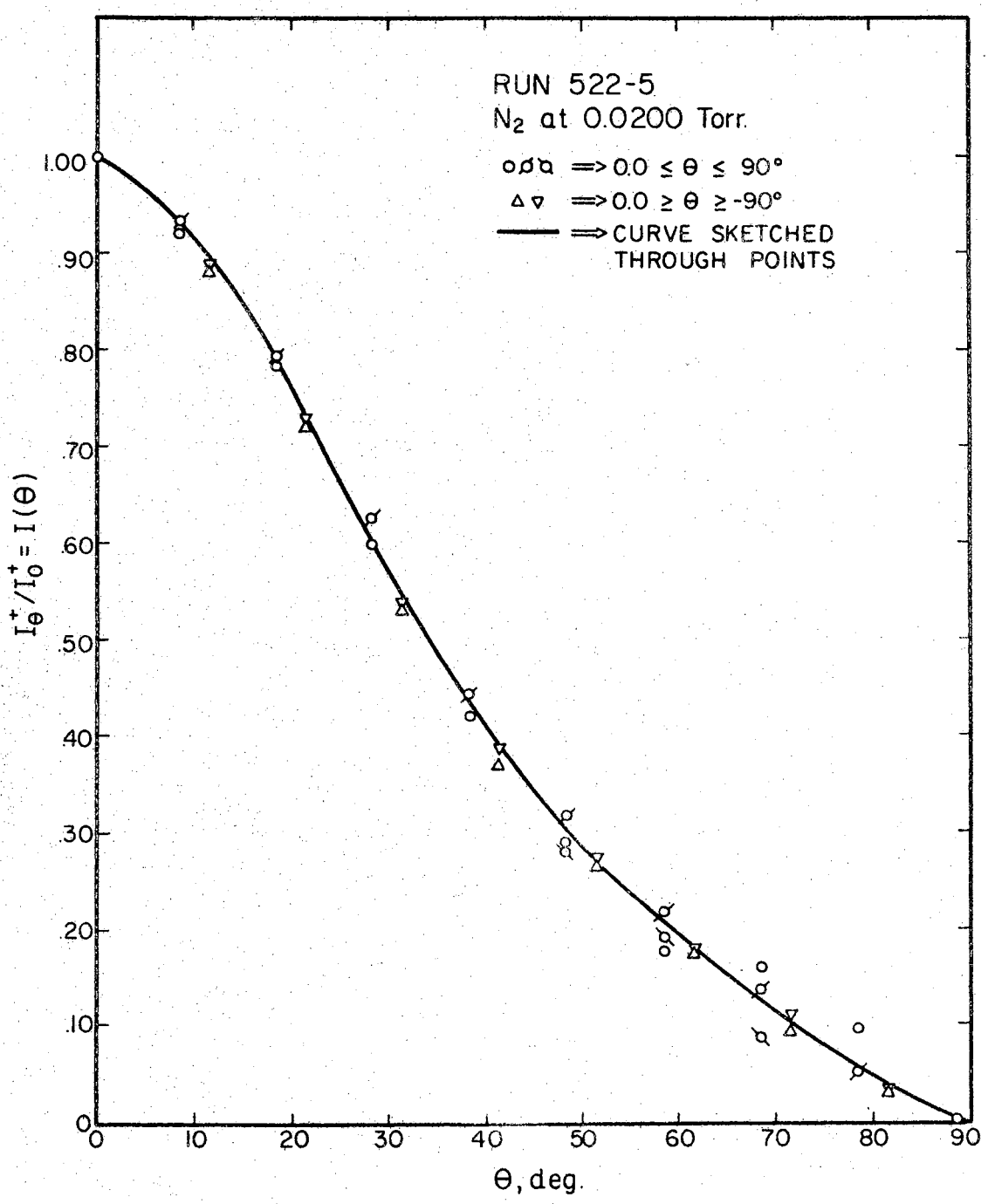

Figure 96. Normalized Experimental Intensities for Run 522-5

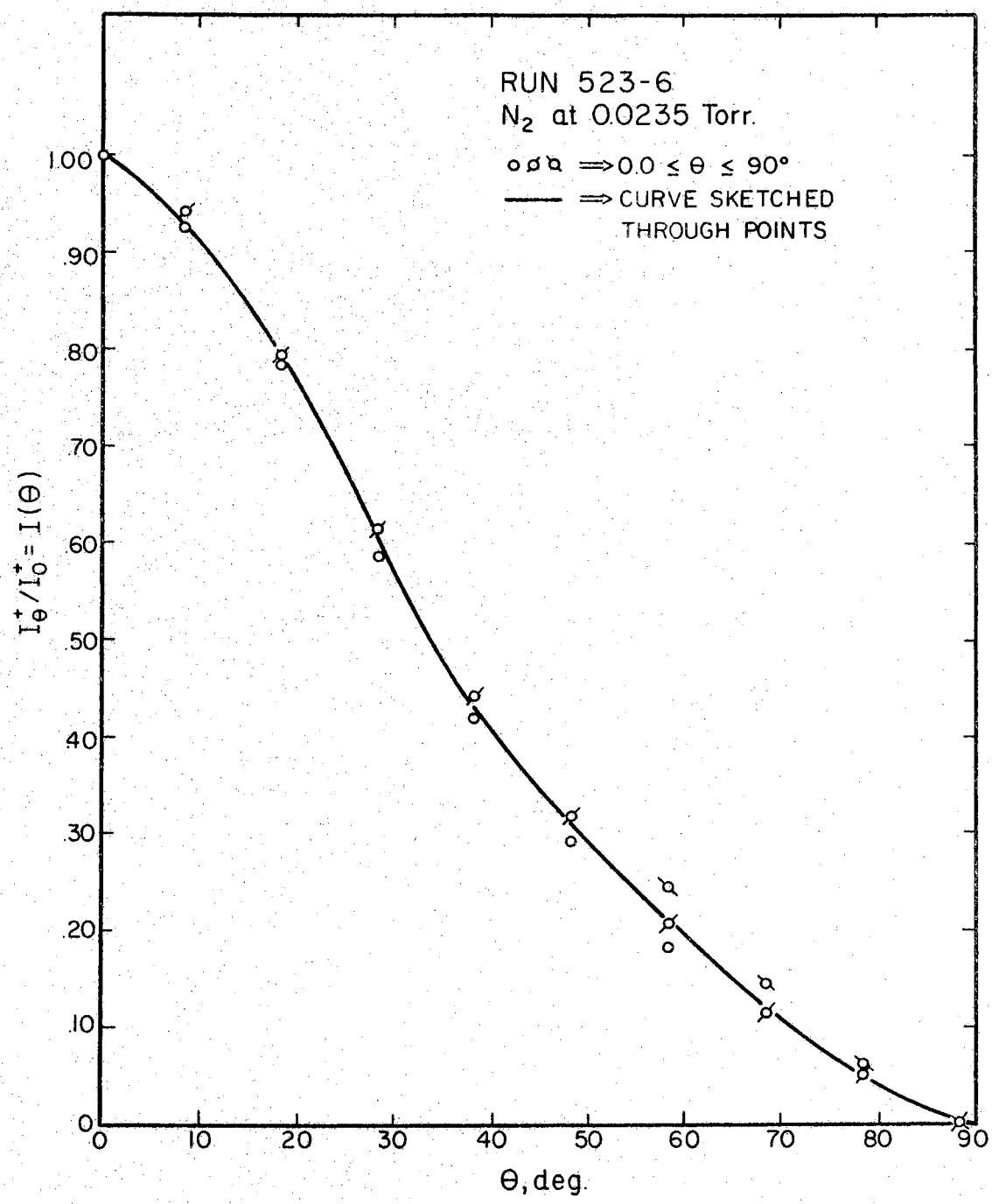

Figure 97. Normalized Experimental Intensities for Run 523-6

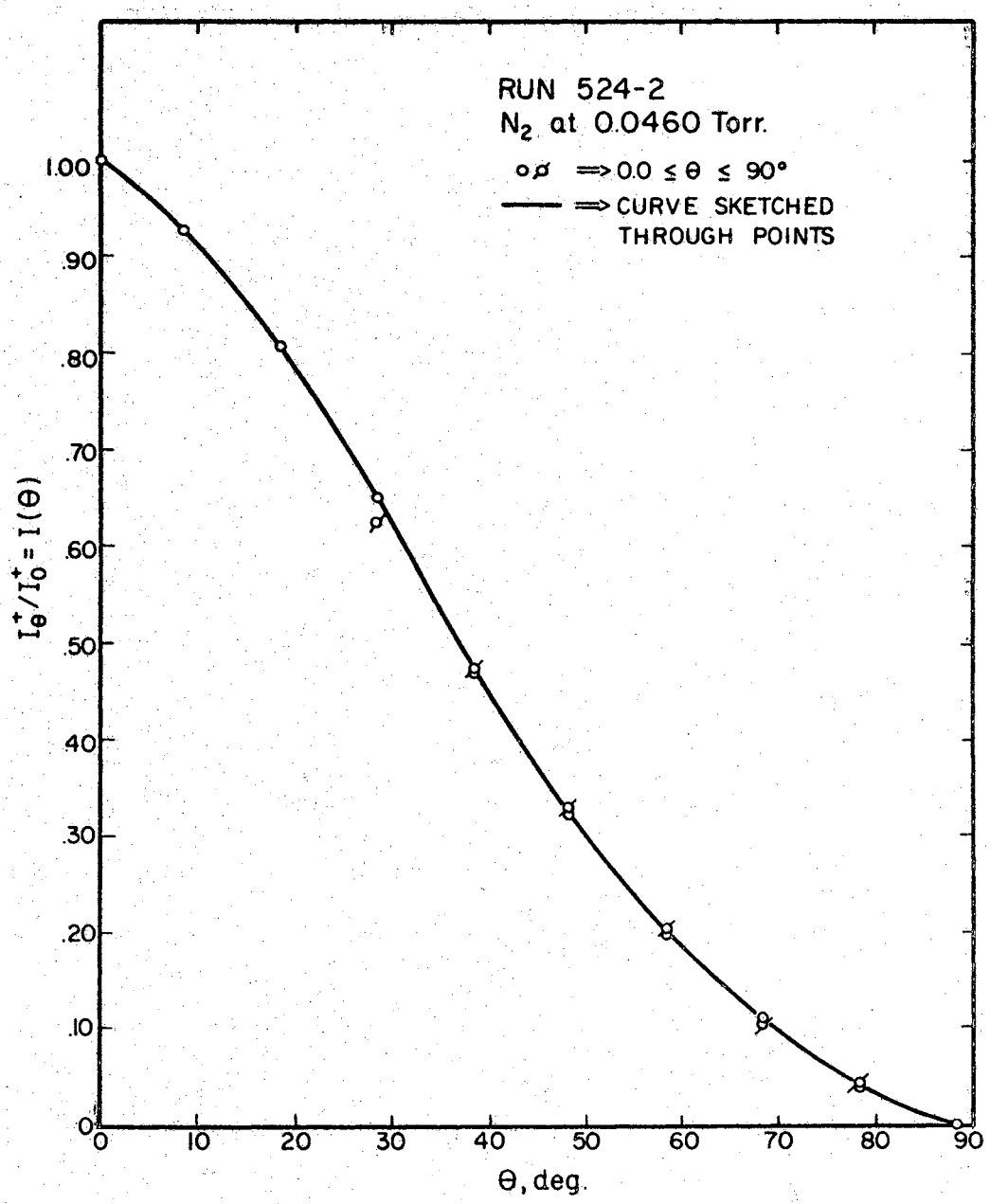

Figure 98. Normalized Experimental Intensities for Run 524-2

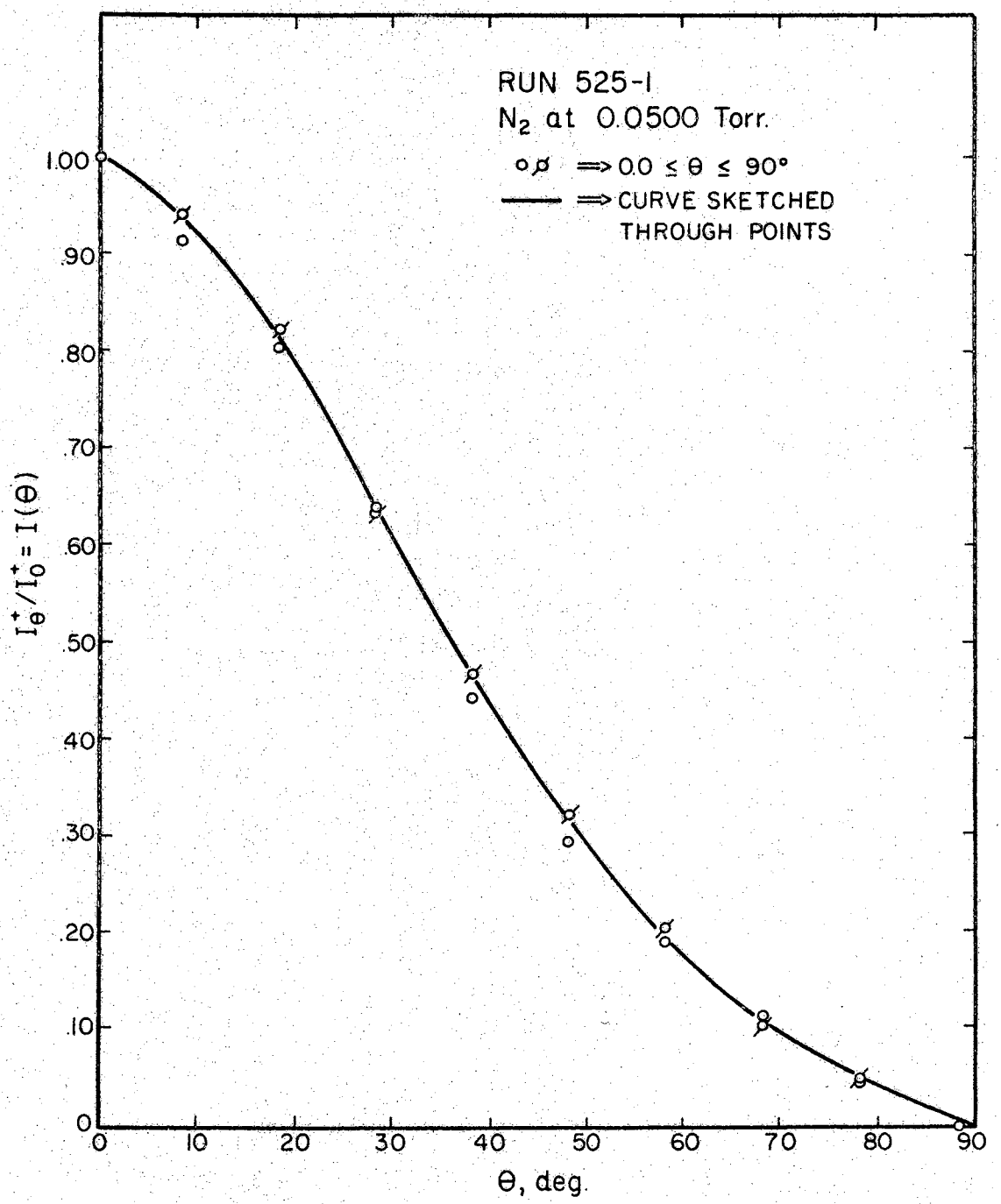

Figure 99. Normalized Experimental Intensities for Run 525-1

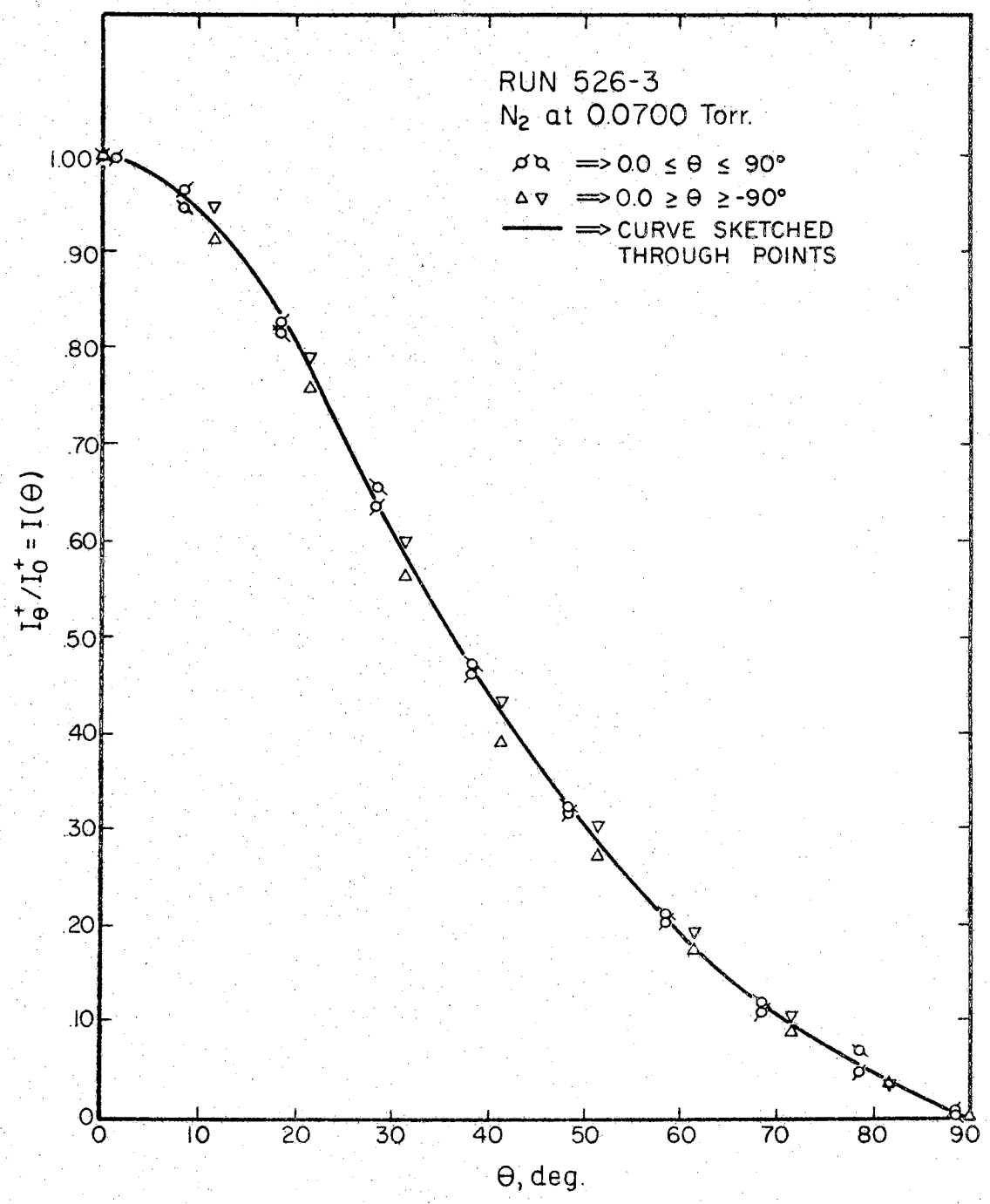

Figure 100. Normalized Experimental Intensities for Run 526-3

VITA

3

Ruth Campbell Erbar

Candidate for the Degree of

Doctor of Philosophy

Thesis: ANGULAR DISTRIBUTIONS OF MOLECULES EFFUSING FROM CONICAL ORIFICES

Major Field: Chemistry

Biographical:

Personal Data: Born near Claremore, Oklahoma, January 19, 1936, daughter of William David and Beatrice Johnson Campbell; married to John Harold Erbar, August 29, 1959; mother of John Harold, III and Kathleen Elizabeth Erbar.

Education: Received all elementary and secondary education in the Stillwater public school system; graduated from Stillwater High School in 1954; received the Bachelor of Science degree with a major in Chemical Engineering from Oklahoma State University in May, 1958; received the Master of Science degree with a major in Chemical Engineering from Oklahoma State University in May, 1960; completed requirements for the Doctor of Philosophy degree at the Oklahoma State University in August, 1969; membership in scholarly or professional societies includes Sigma Tau, Sigma Xi (assoc.), American Chemical Society, American Institute of Chemical Engineers, and the Society of Women Engineers.

Professional Experience: Summer Engineer, Esso Research and Engineering, Linden, New Jersey, 1957; Dow Fellow, Oklahoma State University, 1958-59; Process Engineer, California Research Corporation, Richmond, California 1960-63; Graduate Research Assistant, Oklahoma State University, 1963-66; Welch Foundation Fellow, Rice University, 1966-67.